BEILSTEIN JOURNAL OF NANOTECHNOLOGY

New directions for nanoporous materials

Edited by Cafer T. Yavuz

Generated on 12 November 2026, 11:43

Imprint

Beilstein Journal of Nanotechnology
www.bjnano.org
ISSN 2190-4286
Email: journals-support@beilstein-institut.de

The *Beilstein Journal of Nanotechnology* is published by the Beilstein-Institut zur Förderung der Chemischen Wissenschaften.

Beilstein-Institut zur Förderung der Chemischen Wissenschaften
Trakehner Straße 7–9
60487 Frankfurt am Main
Germany
www.beilstein-institut.de

The copyright to this document as a whole, which is published in the *Beilstein Journal of Nanotechnology*, is held by the Beilstein-Institut zur Förderung der Chemischen Wissenschaften. The copyright to the individual articles in this document is held by the respective authors, subject to a Creative Commons Attribution license.

BEILSTEIN JOURNAL OF NANOTECHNOLOGY

The impact of crystal size and temperature on the adsorption-induced flexibility of the Zr-based metal–organic framework DUT-98

Simon Krause[*1,2], Volodymyr Bon[1], Hongchu Du[3,4], Rafal E. Dunin-Borkowski[3], Ulrich Stoeck[1], Irena Senkovska[1] and Stefan Kaskel[*1]

Full Research Paper

Open Access

Address:
[1]Chair of Inorganic Chemistry, Technische Universität Dresden, Bergstrasse 66, 01062 Dresden, Germany, [2]Centre for Systems Chemistry, Stratingh Institute for Chemistry, University of Groningen, Nijenborgh 4, 9747 AG Groningen, The Netherlands, [3]Ernst Ruska-Centre for Microscopy and Spectroscopy with Electrons, Forschungszentrum Juelich GmbH, 52425 Juelich, Germany and [4]Central Facility for Electron Microscopy (GFE), RWTH Aachen University, 52074 Aachen, Germany

Email:
Simon Krause[*] - simon.krause@rug.nl; Stefan Kaskel[*] - Stefan.kaskel@tu-dresden.de

* Corresponding author

Keywords:
crystal engineering; crystal size; flexible metal–organic frameworks; MOFs; water adsorption

Beilstein J. Nanotechnol. **2019,** *10,* 1737–1744.
doi:10.3762/bjnano.10.169

Received: 28 June 2019
Accepted: 06 August 2019
Published: 20 August 2019

This article is part of the thematic issue "New directions for nanoporous materials".

Guest Editor: C. T. Yavuz

© 2019 Krause et al.; licensee Beilstein-Institut.
License and terms: see end of document.

Abstract

In this contribution we analyze the influence of adsorption cycling, crystal size, and temperature on the switching behavior of the flexible Zr-based metal–organic framework DUT-98. We observe a shift in the gate-opening pressure upon cycling of adsorption experiments for micrometer-sized crystals and assign this to a fragmentation of the crystals. In a series of samples, the average crystal size of DUT-98 crystals was varied from 120 µm to 50 nm and the obtained solids were characterized by X-ray diffraction, infrared spectroscopy, as well as scanning and transmission electron microscopy. We analyzed the adsorption behavior by nitrogen and water adsorption at 77 K and 298 K, respectively, and show that adsorption-induced flexibility is only observed for micrometer-sized crystals. Nanometer-sized crystals were found to exhibit reversible type I adsorption behavior upon adsorption of nitrogen and exhibit a crystal-size-dependent steep water uptake of up to 20 mmol g^{-1} at 0.5 p/p_0 with potential for water harvesting and heat pump applications. We furthermore investigate the temperature-induced structural transition by in situ powder X-ray diffraction. At temperatures beyond 110 °C, the open-pore state of the nanometer-sized DUT-98 crystals is found to irreversibly transform to a closed-pore state. The connection of crystal fragmentation upon adsorption cycling and the crystal size dependence of the adsorption-induced flexibility is an important finding for evaluation of these materials in future adsorption-based applications. This work thus extends the limited amount of studies on crystal size effects in flexible MOFs and hopefully motivates further investigations in this field.

Introduction

In the past 20 years, research in the area of metal–organic frameworks (MOFs) has delivered various record-holding materials in terms of surface area [1] and gas storage [2] and has also given rise to unprecedented adsorption phenomena [3] often associated with structural transitions. An increasing number of the so-called flexible MOFs are being reported and their use in the areas of storage [4], separation [5] and sensing [6] of gases is being evaluated; their structural flexibility and adsorption behavior can be manipulated by applying chemical functionalization to the ligand [7] and metal cluster [8]. However, recent examples progressively illustrate the manipulation of the adsorption properties of switching adsorbents by variation of size [9-13] and morphology [14] of the crystals, without changing the composition of the MOF. The reports on the MOF MIL-53 indicate an impact of crystal morphology and size on the structural contraction upon solvent removal [15,16]. In a recent report, we demonstrated the suppression of adsorption-induced contraction in the MOF DUT-49 (where the name DUT is derived from Dresden University of Technology) upon downsizing of the crystals below 1 μm [9] and loss of flexibility upon downsizing of DUT-8(Ni) crystals [17,18]. In a similar fashion, the suppression of gate opening in ZIF-8 upon crystal downsizing was previously reported [10-13] and Kitagawa and co-workers reported on a shape–memory effect of the gate-opening transition upon crystal downsizing in a pillared-layer MOF [19]. Although these reports demonstrate the influence of crystal size on the structural behavior of flexible MOFs, the materials for which this phenomenon was reported differ in terms of topology, the nature of the structural transitions and the resulting adsorption behavior. In fact, it appears to be possible that some reported nonflexible MOFs can exhibit flexibility if their crystals are synthesized at a specific size or with a specific morphology. It is thus of crucial importance to extend investigations on the crystal size effects in flexible and nonflexible MOFs to further define these phenomena and potentially postulate a global mechanism.

Results and Discussion

In this contribution we report on the impact of crystal size on adsorption- and temperature-induced structural transitions of DUT-98, a flexible Zr-based MOF. The structure of DUT-98 is comprised of 1D supramolecular building blocks (SBBs), which consist of Zr_6 clusters interconnected by 3,6-carbazole dicarboxylate ligands [20]. An additional benzoate functionality of the ligand connects the SBB into a 3D framework with a structure (Figure 1) similar to MIL-53 [21,22].

Upon removal of the solvent molecules from the pore channels by supercritical activation, the wine-rack-type channels of DUT-98 are contracted almost completely, reducing the gas-accessible pore volume by 98%. By adsorption of various guest molecules, including N_2 (at 77 K), CO_2 (at 195 K), *n*-butane (at 273 K), and various alcohols (at 298 K), the pores of the DUT-98*cp* (*cp* = closed pore) MOF reopen at a defined gate-opening pressure (p_{go}), giving rise to an isotherm with distinct steps that are typical for gate-opening MOFs. Upon cyclic adsorption/desorption, the structural transition and the structure of the corresponding *op* and *cp* phase remains (Supporting Information File 1, Figure S3); however, a shift of p_{go} towards a lower pressure is observed, indicating that the material properties change upon adsorption and desorption of various gases and vapors (Figure 2).

Only few reports on the cycling behavior of flexible MOFs can be found in the literature. Shi et al. reported on a shift of the gate pressure towards higher pressures upon cycling of the nitrogen adsorption/desorption at 77 K in $Zn_2(tdc)_2(pvq)$ (H_2tdc = 2,5-thiophenedicarboxylic acid, pvq = 5-(2-(pyridin-4-yl)vinyl)quinoline) [24]. Similar results are reported by Su et al. on a redox-active flexible MOF [25]. Nitrogen isotherms at 77 K of both materials show a pronounced pressure reduction upon structural opening referred to by the authors as “negative gas pressure”. Such artificial pressure reduction upon structural

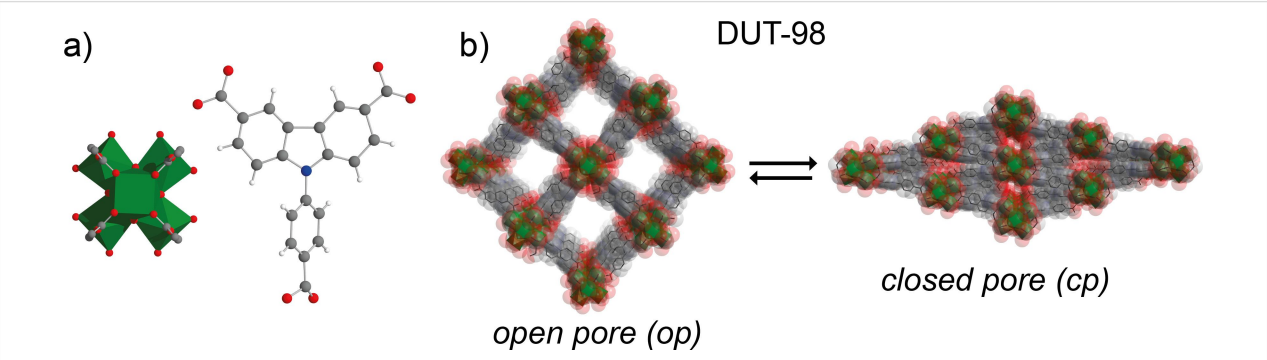


Figure 1: a) Zr-oxo cluster (green) and organic ligand CPCDC (9-(4-carboxyphenyl)-9*H*-carbazole-3,6-dicarboxylate) applied in the construction of DUT-98; b) crystal structure transformation of DUT-98 open pore (*op*) to closed pore (*cp*) configuration.

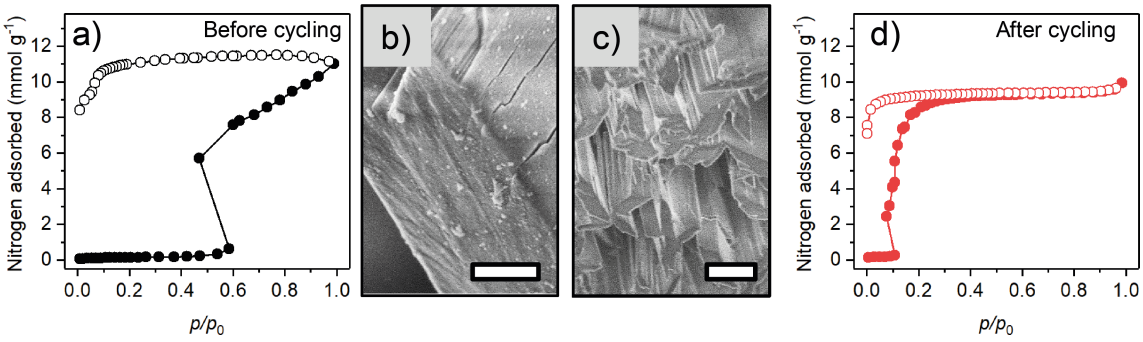


Figure 2: Nitrogen adsorption isotherms at 77 K (a,d) and SEM images (scale bars 1 µm) (b,c) of DUT-98(1) before (a,b) and after (c,d) adsorption experiments with nitrogen, CO_2, *n*-butane, and vapors of alcohols and hydrocarbons (for details on the adsorption experiments see [23]). Closed symbols: adsorption, open symbols: desorption.

expansion is also observed in DUT-98 and a few other examples in the literature [23,25-27] and is a clear indication of a metastable adsorption state, as previously described by Kitagawa and co-workers [28].

In a previous work, we addressed changes in the adsorption behavior in flexible MOFs upon cycled *n*-butane adsorption experiments on a series of flexible MOFs with predominantly one-dimensional channels [29]. In that investigation, the p_{go} in DUT-8(Ni) and SNU-9 isotherms was found to be shifted to higher pressures upon cycling. In contrast, the cycling of MIL-53 and ELM-11 was found to only slightly impact the adsorption behavior. The analysis of the SNU-9 and DUT-8(Ni) crystals before and after cycling showed deformation and fragmentation of the relatively large crystals compared to the microcrystals of MIL-53 and ELM-11, which were not affected by the cycling. This indicates that larger crystals are more prone to undergo deformation and fragmentation upon repeated contraction/expansion due to the higher number of unit cells merged in a single crystal that have to collectively switch upon structural transition. However, in all reported cases, p_{go} was shifted to higher pressures upon cycling in contrast to DUT-98, for which the gate pressure is found to be shifted to lower pressures. The SEM images of the DUT-98 crystals before and after cycling (Supporting Information File 1, Figures S1,S2, Figure 2) show that the rod-shaped crystals of DUT-98*cp* are fragmented into smaller needle-like pieces. Structurally, this indicates a fragmentation along the pore channels, which run along the rods and crystallographic *b*-axis in DUT-98*cp*. Thus, bond cleavage upon fragmentation is expected to occur at the edges of the SBB in DUT-98, which runs in parallel to the pore channels. This fragmentation is likely caused by the stress upon structural reopening during adsorption and contraction during desorption in which the unit cell volume changes by over 140%. The change in the adsorption isotherm as well as the crystal morphology and fragmentation indicate that the adsorption behavior depends on the size of the crystal domains. The question is whether this behavior can also be observed if the crystals were initially synthesized smaller in size?

Recently it has been shown that the crystal size of Zr-based MOFs can easily be controlled by adding acidic modulators [30,31] or water [32,33] to the reaction mixture in the solvothermal synthesis, which increase or decreases the crystal size, respectively. By changing the solvent, reaction time, concentration of acetic acid, and water content of the reaction mixture, four DUT-98 samples containing particles of different size, namely DUT-98(1)–(4) could be obtained (Figure 3).

All solvated samples were analyzed by powder X-ray diffraction (PXRD), illustrating the phase purity of the desired DUT-98*op* (open pore) phase (Figure 4). A significant peak broadening is observed for samples 3 and 4, which is indicative of the presence of nanometer-sized crystals. Quantitative analysis of the mean crystal size by applying the Debye–Scherrer method was unsuccessful due to peak overlap and coexistence of multiple phases as described later. The samples were further activated according to the procedure previously reported for DUT-98(1) [20]. Solvent-free white powders, and in the case of DUT-98(4), low-density monolithic structures (similar to aerogels recently reported for gel-like Zr MOFs [34,35]), were obtained. The SEM analysis shows a rod-like crystal morphology with crystal length in the range of 120 µm for DUT-98(1), 10 µm for DUT-98(2), 500 nm for DUT-98(3), and 50 nm for DUT-98(4) (Supporting Information File 1, Figures S4–S7). Thermogravimetric analysis (TGA) of activated DUT-98 samples shows a decrease in the decomposition temperature from 440–420 °C with decreasing crystal size (Supporting Information File 1, Figure S11). However, the general shape of the TGA curves is very similar, indicating the phase purity of the powders. PXRD analysis of the supercritically activated samples shows again peak broadening upon downsizing. However,

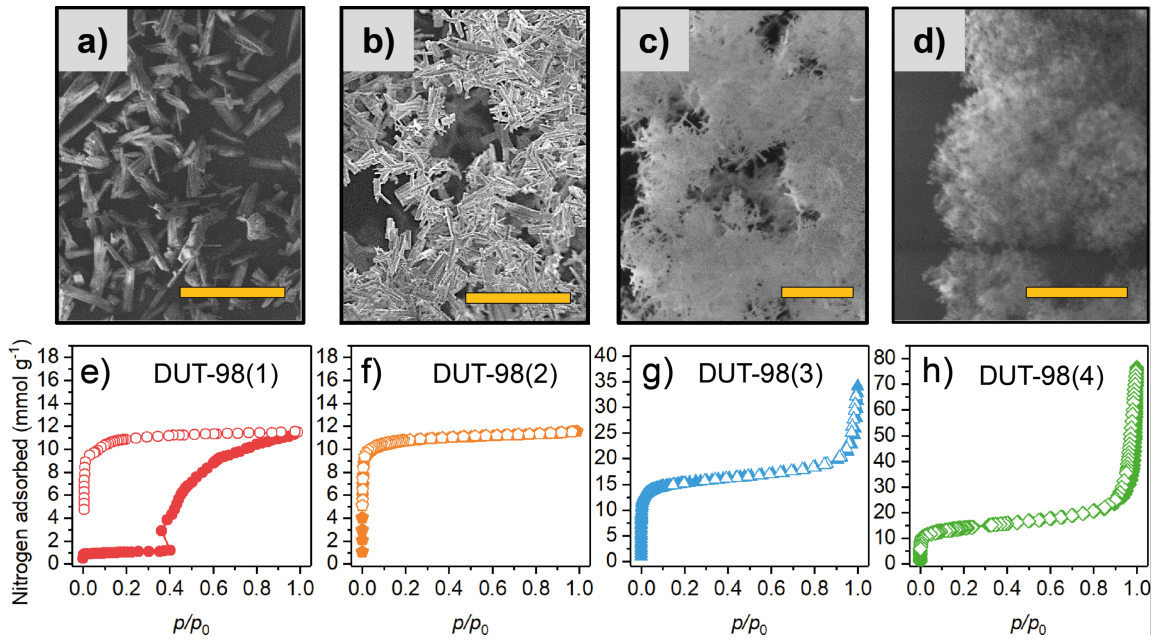


Figure 3: a–d) SEM images and e–h) nitrogen adsorption–desorption isotherms at 77 K for samples DUT-98(1) (a,e), DUT-98(2) (b,f), DUT-98(3) (c,g), and DUT-98(4) (d,h). Scale bars: a) 200 µm, b) 50 µm, c) 1 µm, and d) 500 nm. Closed symbols: adsorption, open symbols: desorption.

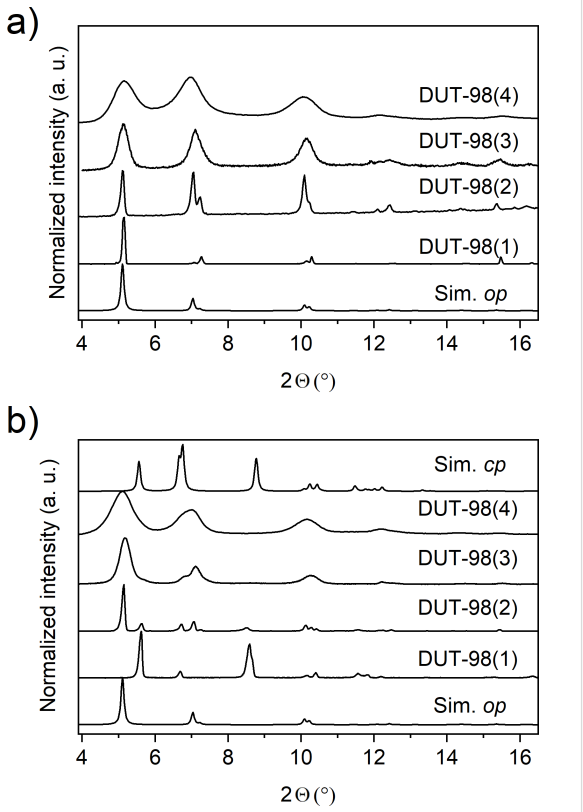


Figure 4: Powder XRD patterns of DUT-98 with varying crystal size a) as-synthesized and b) activated by supercritical solvent removal.

for DUT-98(1)–(3) samples, a shift in the reflection positions and appearance of new peaks, different from that of the *op* phase, are observed (Figure 4), which was previously assigned to the contraction of DUT-98*op* into DUT-98*cp*.

Interestingly, only DUT-98(1) exhibits complete contraction of the whole bulk, while the other three samples only exhibit peaks of low intensity of the DUT-98*cp* phase and primarily remaining peaks of the *op* phase. Consequently, in the samples with smaller crystals, the majority of crystals or crystal domains remain in the *op* phase and only part of the sample undergoes contraction upon solvent removal by supercritical activation. A quantitative phase analysis of the *op*–*cp* mixture by Rietveld refinement was not possible due to the anisotropy of the crystals and the large peak broadening, leading to an overlap of the reflections of the two phases. To further analyze the nature of the phase mixture, we performed high-resolution transmission electron microscopy (HRTEM) analysis on DUT-98(4). HRTEM was previously applied for the microscopic analysis of defects in Zr-MOFs [36]. Unfortunately, the nanocrystals of DUT-98(3) decomposed during the measurement. By reproducing the synthesis using Hf instead of Zr we obtained DUT-98(Hf) with a crystal length of 130 nm, which demonstrated the same structure as shown by PXRD (Supporting Information File 1, Figure S9). Interestingly, DUT-98(Hf) showed enhanced stability towards the electron beam allowing for detailed microscopic analysis of the nanocrystals and their structure.

HRTEM analysis shows uniform pore channels along the rod-shaped nanocrystals with a spacing of the Hf cluster of 1.5 nm, which is in good agreement with the lattice parameter and the inter-cluster distance of the DUT-98*op* crystal structure (Supporting Information File 1, Figure S8). The regular arrangement of the clusters indicates a high symmetry that matches the tetragonal symmetry in DUT-98*op*. In contrast, the DUT-98*cp* phase would exhibit a different microscopic structure due to the lower, monoclinic symmetry. In addition, no missing cluster or linker defects could be detected that are well-known for Zr-MOFs [36,37], demonstrating that the observed behavior does not depend on increasing concentration of lattice defects. Thus, all investigated DUT-98(Hf) crystals exhibited a structure expected for the open phase, which supports the results obtained from PXRD and nitrogen adsorption at 77 K in which the *op* phase is the dominant phase. We thus assume that the presence of the *cp* phase is based on a physical mixture of crystals exhibiting either *op* or *cp* phase and that these phases do not co-exist as domains within a single crystal. This supports the assumption that structural contraction is a cooperative phenomenon that propagates through the whole crystal. To further analyze the porosity and adsorption-induced flexibility, N_2 adsorption–desorption isotherms at 77 K were recorded on DUT-98(2)–(4) and compared to the initial isotherm of DUT-98(1) (Figure 3e–h).

Interestingly, only DUT-98(1) exhibits a flexible behavior evident by the stepped isotherm and wide hysteresis. DUT-98(2) exhibits type I isotherm, reflecting the microporosity of the MOF. DUT-98(3) and (4) show type I behavior at lower relative pressures and type IV behavior at higher relative pressures, reflecting the microporous nature of the MOF and additional interparticle mesoporosity, respectively. This assumption is supported by comparing the specific micropore volume and specific BET surface area (Supporting Information File 1, Table S2) of DUT-98(2)–(4), which exhibit comparable values with DUT-98(3), showing the highest values of 0.53 $cm^3\ g^{-1}$ and 1303 $m^2\ g^{-1}$, respectively. Interestingly, neither of the materials reach the pore volume value calculated theoretically from the crystal structure of DUT-98*op,* indicating that the *cp* fraction observed in the PXRD pattern does not reopen upon adsorption of nitrogen at 77 K. In this regard, DUT-98(Hf) is found to exhibit similar adsorption properties (Supporting Information File 1, Figure S10) compared to DUT-98(3), which further supports the observations made by PXRD and HRTEM. In fact, neither of the isotherms of DUT-98(Hf) nor DUT-98(2)–(4) show any indication of adsorption-induced flexible behavior, evident by steps or hysteresis in the isotherm. Thus, nitrogen, known to be a rather weakly interacting adsorbate, cannot initiate a structural contraction in downsized crystals of DUT-98.

The contraction mechanism in DUT-98(1) was previously shown to depend on pore shrinkage along a reorganization of water molecules within the structure close to the Zr cluster [23]. The diffuse reflectance Fourier transform (DRIFT) spectroscopy results show typical vibrations corresponding to the linker and OH groups of the MOFs in all materials (Supporting Information File 1, Figure S12). To analyze whether adsorption of water can promote contraction in small crystals of DUT-98*op*, water adsorption experiments were conducted at 298 K for DUT-98(2)–(4) (Figure 5a).

In DUT-98(1), no significant adsorption of water can be observed, indicating that structural opening cannot be induced via water adsorption. On the other hand, in DUT-98(2), an increase in uptake is observed around a relative pressure of 0.5, indicating increased adsorption ability. In contrast to other Zr-based MOFs [38], this is a rather high relative pressure for water adsorption, indicating a hydrophobic character of the pore inner surface. In DUT-98(3), a steep increase in water adsorption is observed again at around a relative pressure of 0.5, however the uptake is found to be almost three times higher compared to DUT-98(2). DUT-98(4) exhibits the same steep increase but a wide hysteresis at higher pressure, indicating the dominant contribution of interparticle mesoporosity over the microporosity of the pore channels. Repeated water adsorption experiments on DUT-98(3) show near identical isotherms, supporting the absence of structural transitions and cycling stability under these conditions. The high cycling stability and steep uptake at a relative pressure around 0.5 might make this material an interesting candidate for water capture applications [39-41].

In the original report on DUT-98, an irreversible contraction of the pores upon thermal activation at 80 °C in vacuum was described. An unknown structural transition, different from the contraction to DUT-98*cp*, takes place, and the formation of a high-temperature (DUT-98*ht)* phase was proposed. Although the structure of this phase could not be refined from PXRD and single crystal diffraction data, the obtained PXRD patterns were found to be very similar to the *cp* phase. In addition, DRIFT analysis indicates that the transition is supported by the loss of lattice water molecules [23]. Because the crystal downsizing allows for the preservation of the desolvated DUT-98*op* phase, we investigated the impact of elevated temperature on the structural transition in DUT-98*op* via in situ variable-temperature PXRD. The experiments were conducted under vacuum on supercritically activated DUT-98(2) in the temperature range of 30–350 °C. These conditions are often used for the thermal activation of MOFs and were previously applied in the analysis of DUT-98(1) [23]. In the range of 30–75 °C, no change in the PXRD patterns could be observed and the material could be heated and cooled down within this rage without any indication

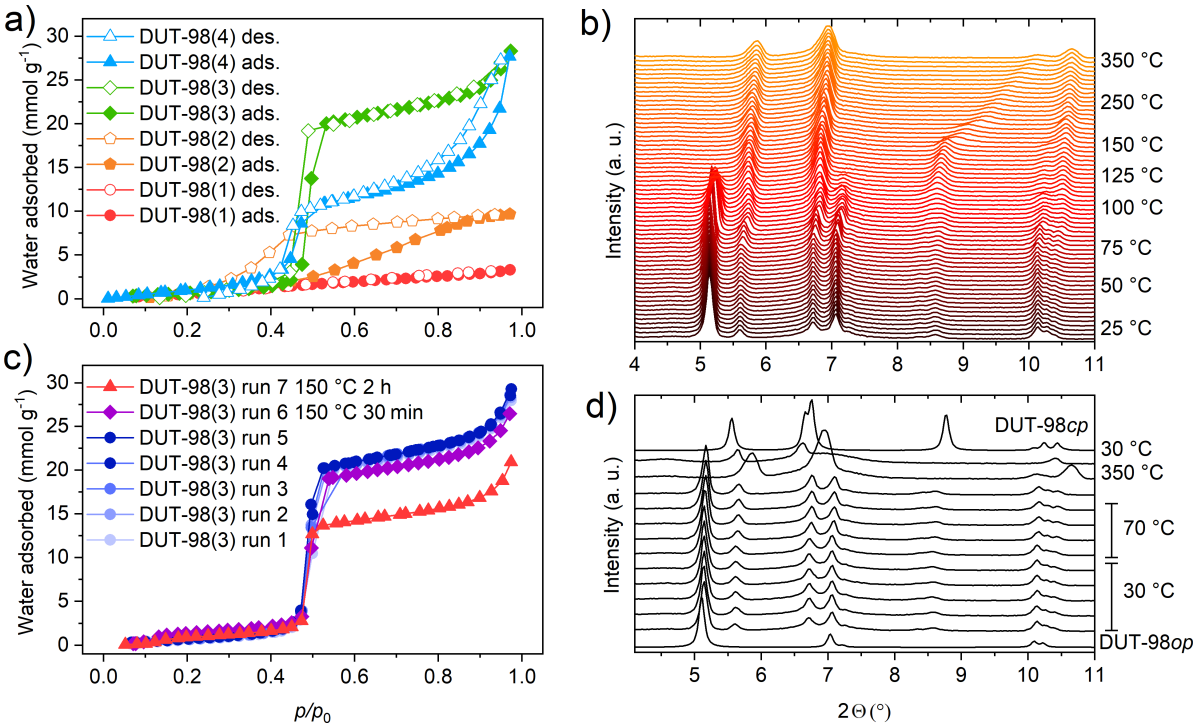


Figure 5: Water physisorption experiments at 298 K on: a) DUT-98(1)–(4) and c) DUT-98(3) after cycling and after thermal treatment. (Filled symbols: adsorption, open symbols: desorption). In situ temperature-variable PXRD of: b) DUT-98(2) and d) DUt-98(2) cycled at lower temperature.

of structural changes (Figure 5). However, upon further heating, a clear increase in the peak intensity assigned to reflections of DUT-98*ht* is observed. At around 100 °C, the peaks of the *op* phase disappear and a phase-pure *ht*-phase is obtained. At temperatures beyond 150 °C, the peaks at 8.5 and 11.5° exhibit a gradual shift towards a higher diffraction angle, indicating a reduction of the lateral intercluster distance. This would support the proposed enhanced contraction upon heating that is potentially supported by the loss of lattice water not evident in the DRIFT spectra after heating (Supporting Information File 1, Figure S13). Such a *ht*-phase has also been observed for MIL-53, which corresponds to the loss of water from the structure. Attempts to index the obtained patterns failed potentially due to a change in symmetry and the high crystal anisotropy. Nevertheless, the variable-temperature PXRD analysis clearly shows that elevated temperatures initiate a temperature-irreversible structural transition in DUT-98(2), which was also previously observed for DUT-98(1) [20]. This is well reflected in water adsorption experiments carried out on DUT-98(3) in which the uptake is found to decrease upon heating of the powder at 80 °C in dynamic vacuum (Figure 5c). Although no adsorption-induced transitions could be observed in downsized DUT-98 crystals, the samples showed a high sensitivity towards elevated temperature in vacuum – conditions found to initiate an irreversible structural contraction. This finding implicates that guest-free DUT-98*op* is a metastable phase and DUT-98*cp* or *ht* phase is the thermodynamic stable phase observed upon solvent removal in DUT-98(1) and partially in DUT-98(2)–(4). Thus, smaller crystal sizes seem to stabilize the presence of a metastable *op* phase by impacting the activation barrier, presumably due to the contribution of the surface energy and other factors. This observation was previously made for DUT-8 for which the guest-free metastable *op* phase was also found to be stabilized upon crystal downsizing. The reports on shape–memory effects [19,42] in flexible MOFs found to be intrinsically connected to the formation of metastable states indicate that crystal size and morphology are in fact parameters that significantly alter the free energy landscape of bistable adsorbents and therefore also impact the adsorption behavior.

Conclusion

In conclusion we demonstrated that the adsorption behavior and structural transition of the flexible Zr-MOF DUT-98 strongly depends on the size of the crystals. In addition, we demonstrate that cycled adsorption experiments can have a large impact on the properties of flexible MOFs by altering the crystal morphology, size and mosaicity. In many regards, DUT-98 is found to behave similar to DUT-8(Ni) and the applied methods indicate changes in the activation energy upon crystal downsizing to be responsible for the observed behavior. The lack of adsorption-induced structural transition for nanometer-sized crystals was previously described also for ZIF-8 [13] and DUT-49 [9]. How-

ever, the mechanism and structural transition in these flexible MOFs are of a different nature and therefore cannot be directly compared with DUT-98. After all, there might not be a single theory for explaining the effects of crystal size variation on the adsorption behavior of flexible MOFs. Only further crystal-size-dependence analysis of novel flexible MOFs with different transition and structures can solidify the presented observations and help to postulate a detailed mechanism. Furthermore, the effect of microscopic defects upon changes in the synthesis procedure should not be neglected as an increasing number of defects has been demonstrated to strongly alter the mechanical stability of MOFs [43-45]. In accordance, novel experimental investigations on flexible MOFs should consider crystal size and cycling effects and include these in experiments and discussion. In addition, we would like to motivate computational chemists to extend recent efforts [46] in developing strategies to analyze these phenomena in silico.

Supporting Information

Supporting Information File 1

Synthetic procedures and additional characterization of the discussed compounds.
[https://www.beilstein-journals.org/bjnano/content/supplementary/2190-4286-10-169-S1.pdf]

Acknowledgements

The authors would like to thank Annika Leifert for the SEM analysis. Simon Krause would like to thank the Alexander von Humboldt-Foundation for funding. Hongchu Du acknowledges the support from the Deutsche Forschungsgemeinschaft (DFG) under Grant SFB 917 Nanoswitches and under the core facilities Grant MA 1280/40-1. Stefan Kaskel acknowledges the support from DFG under Grant FOR 2433.

ORCID® iDs

Simon Krause - https://orcid.org/0000-0001-9504-8514
Volodymyr Bon - https://orcid.org/0000-0002-9851-5031
Hongchu Du - https://orcid.org/0000-0002-4661-4644
Rafal E. Dunin-Borkowski - https://orcid.org/0000-0001-8082-0647
Irena Senkovska - https://orcid.org/0000-0001-7052-1029

Preprint

A non-peer-reviewed version of this article has been previously published as a preprint doi:10.3762/bxiv.2019.52.v1

References

1. Hönicke, I. M.; Senkovska, I.; Bon, V.; Baburin, I. A.; Bönisch, N.; Raschke, S.; Evans, J. D.; Kaskel, S. *Angew. Chem., Int. Ed.* **2018,** *57,* 13780–13783. doi:10.1002/anie.201808240
2. Li, H.; Wang, K.; Sun, Y.; Lollar, C. T.; Li, J.; Zhou, H.-C. *Mater. Today* **2018,** *21,* 108–121. doi:10.1016/j.mattod.2017.07.006
3. Krause, S.; Bon, V.; Senkovska, I.; Stoeck, U.; Wallacher, D.; Többens, D. M.; Zander, S.; Pillai, R. S.; Maurin, G.; Coudert, F.-X.; Kaskel, S. *Nature* **2016,** *532,* 348–352. doi:10.1038/nature17430
4. Mason, J. A.; Oktawiec, J.; Taylor, M. K.; Hudson, M. R.; Rodriguez, J.; Bachman, J. E.; Gonzalez, M. I.; Cervellino, A.; Guagliardi, A.; Brown, C. M.; Llewellyn, P. L.; Masciocchi, N.; Long, J. R. *Nature* **2015,** *527,* 357–361. doi:10.1038/nature15732
5. Chang, Z.; Yang, D.-H.; Xu, J.; Hu, T.-L.; Bu, X.-H. *Adv. Mater. (Weinheim, Ger.)* **2015,** *27,* 5432–5441. doi:10.1002/adma.201501523
6. Zhang, X.; Zhang, Q.; Yue, D.; Zhang, J.; Wang, J.; Li, B.; Yang, Y.; Cui, Y.; Qian, G. *Small* **2018,** *14,* 1801563. doi:10.1002/smll.201801563
7. Biswas, S.; Ahnfeldt, T.; Stock, N. *Inorg. Chem.* **2011,** *50,* 9518–9526. doi:10.1021/ic201219g
8. Yot, P. G.; Yang, K.; Guillerm, V.; Ragon, F.; Dmitriev, V.; Parisiades, P.; Elkaïm, E.; Devic, T.; Horcajada, P.; Serre, C.; Stock, N.; Mowat, J. P. S.; Wright, P. A.; Férey, G.; Maurin, G. *Eur. J. Inorg. Chem.* **2016,** 4424–4429. doi:10.1002/ejic.201600263
9. Krause, S.; Bon, V.; Senkovska, I.; Többens, D. M.; Wallacher, D.; Pillai, R. S.; Maurin, G.; Kaskel, S. *Nat. Commun.* **2018,** *9,* 1573. doi:10.1038/s41467-018-03979-2
10. Tanaka, H.; Ohsaki, S.; Hiraide, S.; Yamamoto, D.; Watanabe, S.; Miyahara, M. T. *J. Phys. Chem. C* **2014,** *118,* 8445–8454. doi:10.1021/jp500931g
11. Gallaba, D. H.; Albesa, A. G.; Migone, A. D. *J. Phys. Chem. C* **2016,** *120,* 16649–16657. doi:10.1021/acs.jpcc.6b03481
12. Tanaka, S.; Fujita, K.; Miyake, Y.; Miyamoto, M.; Hasegawa, Y.; Makino, T.; Van der Perre, S.; Cousin Saint Remi, J.; Van Assche, T.; Baron, G. V.; Denayer, J. F. M. *J. Phys. Chem. C* **2015,** *119,* 28430–28439. doi:10.1021/acs.jpcc.5b09520
13. Zhang, C.; Gee, J. A.; Sholl, D. S.; Lively, R. P. *J. Phys. Chem. C* **2014,** *118,* 20727–20733. doi:10.1021/jp5081466
14. Yang, F.; Mu, H.; Wang, C.; Xiang, L.; Yao, K. X.; Liu, L.; Yang, Y.; Han, Y.; Li, Y.; Pan, Y. *Chem. Mater.* **2018,** *30,* 3467–3473. doi:10.1021/acs.chemmater.8b01073
15. Cheng, X.; Zhang, A.; Hou, K.; Liu, M.; Wang, Y.; Song, C.; Zhang, G.; Guo, X. *Dalton Trans.* **2013,** *42,* 13698–13705. doi:10.1039/c3dt51322j
16. Kundu, T.; Wahiduzzaman, M.; Shah, B. B.; Maurin, G.; Zhao, D. *Angew. Chem., Int. Ed.* **2019,** *58,* 8073–8077. doi:10.1002/anie.201902738
17. Kavoosi, N.; Bon, V.; Senkovska, I.; Krause, S.; Atzori, C.; Bonino, F.; Pallmann, J.; Paasch, S.; Brunner, E.; Kaskel, S. *Dalton Trans.* **2017,** *46,* 4685–4695. doi:10.1039/c7dt00015d
18. Miura, H.; Bon, V.; Senkovska, I.; Ehrling, S.; Watanabe, S.; Ohba, M.; Kaskel, S. *Dalton Trans.* **2017,** *46,* 14002–14011. doi:10.1039/c7dt02809a
19. Sakata, Y.; Furukawa, S.; Kondo, M.; Hirai, K.; Horike, N.; Takashima, Y.; Uehara, H.; Louvain, N.; Meilikhov, M.; Tsuruoka, T.; Isoda, S.; Kosaka, W.; Sakata, O.; Kitagawa, S. *Science* **2013,** *339,* 193–196. doi:10.1126/science.1231451
20. Schaber, J.; Krause, S.; Paasch, S.; Senkovska, I.; Bon, V.; Többens, D. M.; Wallacher, D.; Kaskel, S.; Brunner, E. *J. Phys. Chem. C* **2017,** *121,* 5195–5200. doi:10.1021/acs.jpcc.7b01204
21. Férey, G.; Serre, C. *Chem. Soc. Rev.* **2009,** *38,* 1380–1399. doi:10.1039/b804302g

22. Millange, F.; Serre, C.; Férey, G. *Chem. Commun.* **2002,** 822–823. doi:10.1039/b201381a
23. Krause, S.; Bon, V.; Stoeck, U.; Senkovska, I.; Többens, D. M.; Wallacher, D.; Kaskel, S. *Angew. Chem., Int. Ed.* **2017,** *56,* 10676–10680. doi:10.1002/anie.201702357
24. Shi, Y.-X.; Li, W.-X.; Zhang, W.-H.; Lang, J.-P. *Inorg. Chem.* **2018,** *57,* 8627–8633. doi:10.1021/acs.inorgchem.8b01408
25. Su, J.; Yuan, S.; Wang, H.-Y.; Huang, L.; Ge, J.-Y.; Joseph, E.; Qin, J.; Cagin, T.; Zuo, J.-L.; Zhou, H.-C. *Nat. Commun.* **2017,** *8,* 2008. doi:10.1038/s41467-017-02256-y
26. Li, X.; Chen, X.; Jiang, F.; Chen, L.; Lu, S.; Chen, Q.; Wu, M.; Yuan, D.; Hong, M. *Chem. Commun.* **2016,** *52,* 2277–2280. doi:10.1039/c5cc09461e
27. Maji, T. K.; Mostafa, G.; Matsuda, R.; Kitagawa, S. *J. Am. Chem. Soc.* **2005,** *127,* 17152–17153. doi:10.1021/ja0561439
28. Tanaka, D.; Nakagawa, K.; Higuchi, M.; Horike, S.; Kubota, Y.; Kobayashi, T.; Takata, M.; Kitagawa, S. *Angew. Chem., Int. Ed.* **2008,** *47,* 3914–3918. doi:10.1002/anie.200705822
29. Bon, V.; Kavoosi, N.; Senkovska, I.; Kaskel, S. *ACS Appl. Mater. Interfaces* **2015,** *7,* 22292–22300. doi:10.1021/acsami.5b05456
30. Schaate, A.; Roy, P.; Godt, A.; Lippke, J.; Waltz, F.; Wiebcke, M.; Behrens, P. *Chem. – Eur. J.* **2011,** *17,* 6643–6651. doi:10.1002/chem.201003211
31. Morris, W.; Wang, S.; Cho, D.; Auyeung, E.; Li, P.; Farha, O. K.; Mirkin, C. A. *ACS Appl. Mater. Interfaces* **2017,** *9,* 33413–33418. doi:10.1021/acsami.7b01040
32. Hu, Z.; Castano, I.; Wang, S.; Wang, Y.; Peng, Y.; Qian, Y.; Chi, C.; Wang, X.; Zhao, D. *Cryst. Growth Des.* **2016,** *16,* 2295–2301. doi:10.1021/acs.cgd.6b00076
33. Zahn, G.; Schulze, H. A.; Lippke, J.; König, S.; Sazama, U.; Fröba, M.; Behrens, P. *Microporous Mesoporous Mater.* **2015,** *203,* 186–194. doi:10.1016/j.micromeso.2014.10.034
34. Bueken, B.; Van Velthoven, N.; Willhammar, T.; Stassin, T.; Stassen, I.; Keen, D. A.; Baron, G. V.; Denayer, J. F. M.; Ameloot, R.; Bals, S.; De Vos, D.; Bennett, T. D. *Chem. Sci.* **2017,** *8,* 3939–3948. doi:10.1039/c6sc05602d
35. Liu, L.; Zhang, J.; Fang, H.; Chen, L.; Su, C.-Y. *Chem. – Asian J.* **2016,** *11,* 2278–2283. doi:10.1002/asia.201600698
36. Liu, L.; Chen, Z.; Wang, J.; Zhang, D.; Zhu, Y.; Ling, S.; Huang, K.-W.; Belmabkhout, Y.; Adil, K.; Zhang, Y.; Slater, B.; Eddaoudi, M.; Han, Y. *Nat. Chem.* **2019,** *11,* 622–628. doi:10.1038/s41557-019-0263-4
37. Øien, S.; Wragg, D.; Reinsch, H.; Svelle, S.; Bordiga, S.; Lamberti, C.; Lillerud, K. P. *Cryst. Growth Des.* **2014,** *14,* 5370–5372. doi:10.1021/cg501386j
38. Furukawa, H.; Gándara, F.; Zhang, Y.-B.; Jiang, J.; Queen, W. L.; Hudson, M. R.; Yaghi, O. M. *J. Am. Chem. Soc.* **2014,** *136,* 4369–4381. doi:10.1021/ja500330a
39. Kim, H.; Yang, S.; Rao, S. R.; Narayanan, S.; Kapustin, E. A.; Furukawa, H.; Umans, A. S.; Yaghi, O. M.; Wang, E. N. *Science* **2017,** *356,* 430–434. doi:10.1126/science.aam8743
40. Kim, H.; Rao, S. R.; Kapustin, E. A.; Zhao, L.; Yang, S.; Yaghi, O. M.; Wang, E. N. *Nat. Commun.* **2018,** *9,* 1191. doi:10.1038/s41467-018-03162-7
41. Kalmutzki, M. J.; Diercks, C. S.; Yaghi, O. M. *Adv. Mater. (Weinheim, Ger.)* **2018,** *30,* 1704304. doi:10.1002/adma.201704304
42. Shivanna, M.; Yang, Q.-Y.; Bajpai, A.; Sen, S.; Hosono, N.; Kusaka, S.; Pham, T.; Forrest, K. A.; Space, B.; Kitagawa, S.; Zaworotko, M. J. *Sci. Adv.* **2018,** *4,* eaaq1636. doi:10.1126/sciadv.aaq1636
43. Zheng, B.; Fu, F.; Wang, L. L.; Wang, J.; Du, L.; Du, H. *J. Phys. Chem. C* **2018,** *122,* 4300–4306. doi:10.1021/acs.jpcc.7b10928
44. Thornton, A. W.; Babarao, R.; Jain, A.; Trousselet, F.; Coudert, F.-X. *Dalton Trans.* **2016,** *45,* 4352–4359. doi:10.1039/c5dt04330a
45. Dissegna, S.; Vervoorts, P.; Hobday, C. L.; Düren, T.; Daisenberger, D.; Smith, A. J.; Fischer, R. A.; Kieslich, G. *J. Am. Chem. Soc.* **2018,** *140,* 11581–11584. doi:10.1021/jacs.8b07098
46. Keupp, J.; Schmid, R. *ChemRxiv* **2019**. doi:10.26434/chemrxiv.8281082.v1

License and Terms

This is an Open Access article under the terms of the Creative Commons Attribution License (http://creativecommons.org/licenses/by/4.0). Please note that the reuse, redistribution and reproduction in particular requires that the authors and source are credited.

The license is subject to the *Beilstein Journal of Nanotechnology* terms and conditions: (https://www.beilstein-journals.org/bjnano)

The definitive version of this article is the electronic one which can be found at: doi:10.3762/bjnano.10.169

BEILSTEIN JOURNAL OF NANOTECHNOLOGY

Processing nanoporous organic polymers in liquid amines

Jeehye Byun*[1], Damien Thirion[2] and Cafer T. Yavuz[2,3]

Full Research Paper

Open Access

Address:
[1]Water Cycle Research Center, Korea Institute of Science and Technology (KIST), 5 Hwarang-ro 14, Seoul, 02792, Korea, [2]Graduate School of Energy, Environment, Water and Sustainability (EEWS), Korea Advanced Institute of Science and Technology (KAIST), 291 Daehak-ro, Yuseong-gu, Daejeon, 34141, Korea and [3]Department of Chemical and Biomolecular Engineering, Korea Advanced Institute of Science and Technology (KAIST), 291 Daehak-ro, Yuseong-gu, Daejeon, 34141, Korea

Email:
Jeehye Byun* - jbyun@kist.re.kr

* Corresponding author

Keywords:
film; liquid amine; nanoparticles; nanoporous polymer; processibility

Beilstein J. Nanotechnol. **2019,** *10,* 1844–1850.
doi:10.3762/bjnano.10.179

Received: 29 June 2019
Accepted: 28 August 2019
Published: 09 September 2019

Associate Editor: J. Lahann

© 2019 Byun et al.; licensee Beilstein-Institut.
License and terms: see end of document.

Abstract

Rigid network structures of nanoporous organic polymers provide high porosity, which is beneficial for applications such as gas sorption, gas separation, heterogeneous (photo)catalysis, sensing, and (opto)electronics. However, the network structures are practically insoluble. Thus, the processing of nanoporous polymers into nanoparticles or films remains challenging. Herein, we report that nanoporous polymers made via a Knoevenagel-like condensation can be easily processed into nanoparticles (115.7 ± 40.8 nm) or a flawless film by using liquid amines as a solvent at elevated temperatures. FTIR spectra revealed that the carboxyl groups in the nanoporous polymers act as reactive sites for amines, forming new functionalities and spacing the polymeric chains to be dissolved in the liquid amines. The processed film was found to be CO_2-philic despite the low surface area, and further able to be transformed into a fine carbon film by thermal treatment.

Introduction

Nanoporous polymers offer permanent porosity along with robust and light-weight frameworks. The building-block approach for nanoporous polymers allows for a nearly infinite variety of architectures by changing chemistry and geometry of the monomers [1]. New discoveries on nanoporous polymers have been made based on different combinations of monomers yielding unique properties to the polymer structures. In particular, the high porosity of nanoporous polymers has gained significant attention in various applications such as gas adsorption and storage [2], water purification [3], energy storage [4], and catalysis [5], where the large and permanent voids in nanoporous polymers provide room to accommodate target substrates and guest molecules. A series of nanoporous polymers have been reported, namely covalent organic frameworks [6], conjugated microporous polymers [7], covalent triazine frameworks [8], porous aromatic frameworks [9], porous polymer networks [10], and polymers of intrinsic microporosity [11]. We have been working on nanoporous covalent organic polymers (COP), focusing on structural durability and economic sustainability for gas capture [12] and water treatment applications [13].

Nanoporous polymers are classified as network polymers, and such network polymers do not dissolve in common organic solvents but rather swell. Despite the advantages of network structures, the nanoporous polymers can be hardly processed into the desired morphologies such as small particulates, films, and membranes because of the insolubility. So far, the generation of nanoparticles and films made out of nanoporous polymers have been mostly done through initial synthetic controls such as miniemulsion polymerization [14], ionic complexation [15], and electrochemical polymerization [16], which require sophisticated techniques. There are only a few reports that show the processing of nanoporous polymers into the desired morphologies, for instance, the nanoporous polymers were directly processed into nanoparticles with different sizes [17]. However, extremely harsh conditions (piranha solution, 160 °C) were necessary to break the polymeric chains, indicating that the processing of nanoporous polymers is still challenging. Obviously, more applications were possible, if the nanoporous polymers could be fabricated into nanoparticles and films.

In this work, nanoporous polymers built via Knoevenagel-like condensations are made to be soluble in liquid amines and show structural processibility. At elevated temperatures (ca. 100 °C), the condensate nanoporous polymers were completely dissolved in neat liquid amines in a few seconds, and the resulting polymer solution was able to be transformed into either nanoparticles or flawless films. This new feature of processibility was underpinned by FTIR, in which the formation of amide groups between the carbonyl units on nanoporous polymers and the alkylamines was responsible for the dissolution of polymers. The obtained polymer film exhibited high CO_2-philicity by having nitrogen-rich surfaces. The film could be also turned into a fine carbon film by heat treatment in inert atmosphere.

Results and Discussion

Processing COP-100 in liquid amines

COP-100 is a network polymer that can be synthesized in one step from 1,3,5-benzenetriacetonitrile and terephthaldehyde via Knoevenagel-like condensation [18] (synthesis details can be found in Supporting Information File 1). The reaction proceeded smoothly at room temperature in the presence of potassium *tert*-butoxide with short reaction time (less than 3 h) and almost quantitative yield (>95%). A typical Knoevenagel reaction is known to form fully conjugated structures by two steps, where the nucleophilic addition of carbonyl takes place on the deprotonated α-CN position, further followed by the deprotonation of second α-CN proton and the successive dehydration [19,20]. COP-100, however, was intended to have a hydroxylated structure by using a bulky base (*t*-BuOK) and an aprotic solvent (THF), where the second deprotonation and the concomitant dehydration does not occur as the bulky base cannot easily access inside the polymer network. From our previous findings, the hydroxylated COP-100 exhibited the highest surface area of 82.3 $m^2 \cdot g^{-1}$ among all the tested combinations of base and solvent [18]. The mild reaction conditions of COP-100 further left carbonyl units in the structure to be reactive sites for further processing. These reactive sites could be unreacted aldehyde or carboxylic acid generated by disproportionation of aldehyde units [21], which can quickly react with amines to form imine or amide bonds, respectively. When ethylenediamine (EDA) was added to COP-100 under elevated temperatures, the short amine chains penetrated into COP-100 and formed the new functionalities with carbonyl units, creating room between the polymeric backbones to be dissolved in liquid amines. The amine-induced solubility of COP-100 facilitated the formation of small nanoparticles or polymeric film layers to give COP-100-NP and COP-100-Film, respectively (Figure 1).

COP-100 is sparingly soluble in common polar aprotic solvents including DMF, DMSO, DMAc, and NMP (Figure 2a). Intriguingly, when COP-100 was treated with EDA, there was an instant color change from light yellow to deep red (Figure 2b). Under thermal treatment at 100 °C, the whole powder dissolved in the amine within a few seconds, forming a red solution (Figure 2c). The solution was further turned into a film within a few minutes under elevated temperatures (Figure 2d). The polymer solution in EDA was highly polar, and it was miscible with common polar solvents but not with non-polar solvents. The COP-100-Film, on the other hand, was not soluble in any solvents despite its brittle nature.

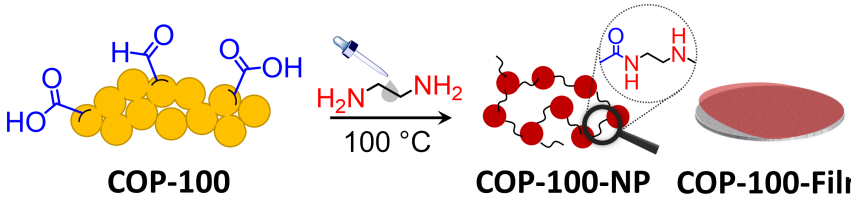


Figure 1: Schematic illustration of processible COP-100 in EDA to form either nanoparticles (COP-100-NP) or films (COP-100-Film) at 100 °C. The terminal groups of carboxylic acids and unreacted aldehydes are responsible for interparticle connections.

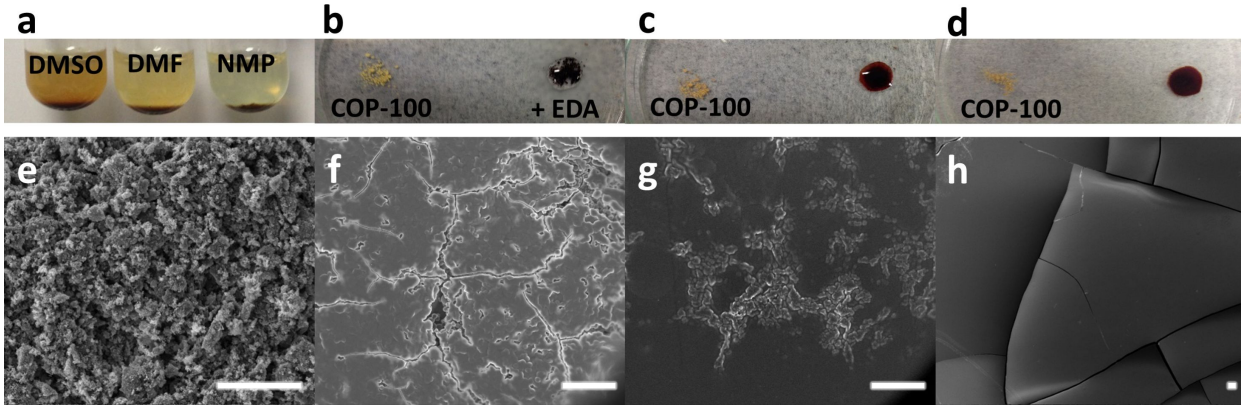


Figure 2: (a) Low solubility of COP-100 in polar aprotic solvents. (b) Instant color change of COP-100 by the addition of EDA dropwise at r.t., (c) dissolution of COP-100 in EDA at 100 °C in a few seconds, and (d) formation of COP-100 film at 100 °C in a few minutes (less than 5 min). SEM image of (e) pristine COP-100 powder, and EDA-treated COP-100 at 100 °C for (f) 1 min, (g) 3 min, and (h) 5 min (scale bar = 10 μm).

COP-100 in EDA was monitored using microscopic tools to understand its rapid phase change. As shown in Figure 2e, the original COP-100 consists of large polymeric granules aggregated with each other, and the size of each granule ranged from 100 to 300 nm. A TEM image of the COP-100 solution in EDA treated for a few seconds at 100 °C (Supporting Information File 1, Figure S1) shows that COP-100 granules were torn apart and separated from each other. In addition, the granules were covered with organic layers, presumably excess EDA. The solution was transferred on a silicon wafer to analyze the morphology changes by SEM as function of the heating time. When treated at high temperature for a short period of time (ca. 1 min), the granules were combined in a heap to form a cracked film surface (Figure 2f). The boundary layers between the granules were not demarcated as the heat treatment went on for 3 min (Figure 2g). After 5 min, as all the pieces were combined and covered with excess EDA, the surface became very clean, leading to a flawless film (Figure 2h). Since the film itself was thin and brittle, it was easily cracked, but the film did not show any polymeric granules exposed on the surface. The dissolution of polymer chains in a solvent is known to involve two transport processes; (i) solvent diffusion and (ii) chain disentanglement [22]. When the COP-100 was reacted with EDA, there was a color change of the COP, indicating the formation of an infiltration layer of EDA on the polymeric surface. As the treatment time progressed, further penetration of the EDA made the surface layer swollen so that bulk polymer cracked into smaller units that can behave like liquids.

During processing COP-100, the amount of EDA varied according to the molar ratio between the nitrogen content of COP-100 and the molecular weight of EDA. Interestingly, even a tiny amount of EDA can dissolve COP-100, showing significant solubility COP-100 in liquid amines. The amount of EDA, however, mattered when the further process went on. For instance, when only a little amount of EDA was added to COP-100, the mixture became a red polymeric solution, but the COP-100 polymer precipitated (COP-100-Precip.) if a polar solvent, i.e., ethanol, was added (Figure 3a). It may be attributed that the

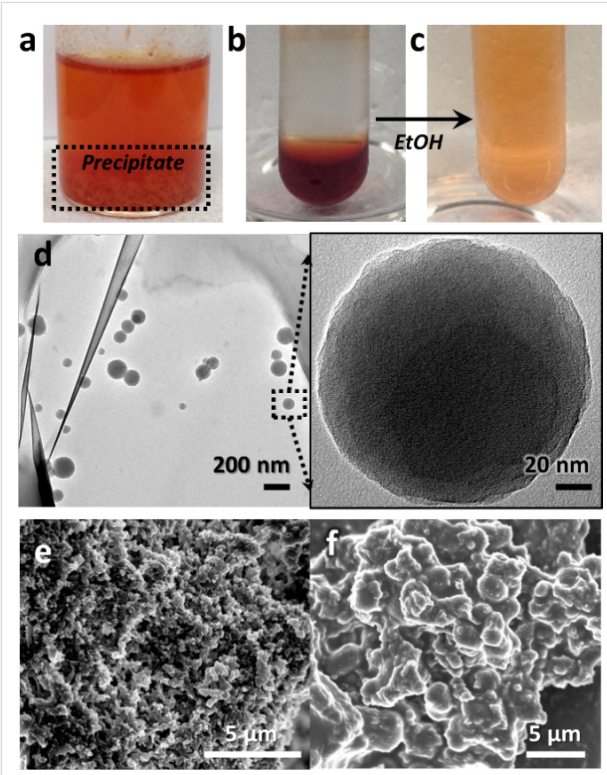


Figure 3: Effect of amine equivalence in solubilizing COP-100. (a) COP-100 dissolved in 8 equivalent EDA which precipitated by the addition of ethanol, (b) COP-100 dissolved in 50 equivalent EDA, and (c) diluted solution of (b) in ethanol. (d) TEM image of COP-100-NP obtained from the solution (b). SEM image of COP-100 precipitates after the addition of (e) 5 equivalent EDA and (f) 8 equivalent EDA.

amount of EDA was not enough to react with all COP-100. Thus, the unreacted COP-100, which is technically insoluble in any solvent, precipitated. When the amount of EDA was in large excess, the COP-100-Film became partially soluble in polar solvents. In order to make a stable polymer solution that does not form a polymer precipitate after the addition of polar solvents, the molar ratio between EDA and nitrogen content of COP-100 needs to be at least 10:1. At the same time, the critical molar ratio for the formation of an insoluble film in polar solvents was thus about 50:1 or less for EDA/COP-100.

A typical COP-100 solution with 50 equiv EDA, showing a clear red color (Figure 3b), could be easily mixed and diluted with ethanol (Figure 3c). When the diluted polymer solution was analyzed with TEM, separated polymer nanoparticles were observed showing an average size of 115.7 ± 40.8 nm (Figure 3d). The spherical shape of the polymer nanoparticles resulted from the split COP-100 granules covered with EDA. COP-100 precipitates with a lower amount of EDA, on the other hand, exhibited the aggregated form similarly to the original COP-100 (Figure 3e). After the addition of 8 equiv EDA, the COP-100 granules were fully covered with EDA layers, which is in the middle of a transformation into a film (Figure 3f).

Possible mechanism of the processibility

The instant color change of COP-100 with EDA indicated a chemical reaction between COP-100 and EDA. Our initial hypothesis was the addition of EDA on the nitrile groups by a nucleophilic attack [23], so that the alkylamine chain connected to the nitrile functionality can increase the polarity of the polymeric chains, making COP-100 soluble. However, as shown in Figure 4, FTIR spectra of COP-100, COP-100-Film, and COP-100-Precip. showed no drastic change in the nitrile region (2200 cm^{-1}). Moreover, the addition of an amine on a nitrile group cannot be achieved in a few seconds without catalyst despite the high temperature. The existence of carbonyl units at around 1700 cm^{-1} in COP-100 drew our attention. The carbonyl groups could originate either from unreacted terephthaldehyde or from the carboxylic acid generated during the work-up process with acid through the disproportionation of two adjacent aldehydes [21]. Aldehyde groups are known to generate imine bonds by the reaction with amines, however, a fast imine formation is most likely when an acid catalyst is present [24]. Alternatively, carboxylic acid could react with amines to form amide linkages at high temperatures [25], which corresponds to new peaks shown on the FTIR spectra of both COP-100-Film and COP-100-Precip. at 3300 cm^{-1}, 1660 cm^{-1}, and 1560 cm^{-1} for amide N–H, C=O, and C–N–H stretching vibrations, respectively [26]. The strong peak at 1365 cm^{-1} in both COP-100-Film and COP-100-Precip. spectra were attributed to the ethylene C–H stretching vibration of EDA. The direct formation of the amide functionality could be possibly due to the easy condensation with the hydrophobic nanoporous polymer at high temperature [27]. The COP-100-Film was formed much slower when the temperature was below 80 °C, supporting that the amide formation by the condensation reaction was crucial for processing the nanoporous polymer. The quick amide formation made the COP-100 granules torn apart through the interpenetration of EDA molecules into the polymeric chains. Consequently, as the EDA layers covered the COP-100 particles, a film could be generated with a clean surface.

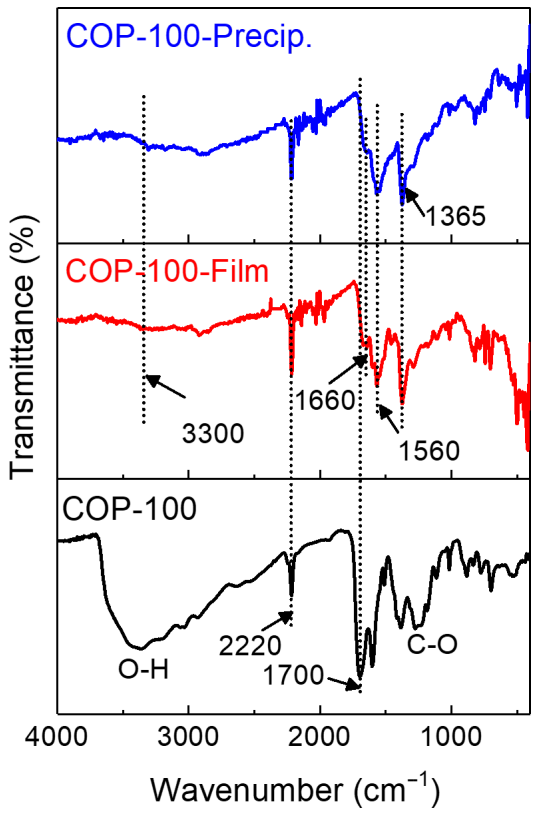


Figure 4: FTIR spectra of COP-100, COP-100-Film, and COP-100-Precip. COP-100 exhibited two peaks at 3400 cm^{-1} and 1375 cm^{-1} of O–H and C–O stretching vibrations of the hydroxylated structure, respectively.

The amine-induced solubility was not restricted to only COP-100. COP-600 (Figure 5a), produced by the Knoevenagel-like condensation of 1,3,5-benzenetriacetonitrile and 1,3,5-tris(4-formylphenyl)benzene, was also solubilized in EDA at elevated temperatures. COP-600 was not soluble in organic solvents even at high temperatures but it was in the presence of EDA. COP-600 has an almost pore-free structure, thus the dissolution in the liquid amine took much longer compared to COP-100 due to the slower penetration of EDA. The rigid backbone of COP-600 with the triphenylbenzene core also contributed to the

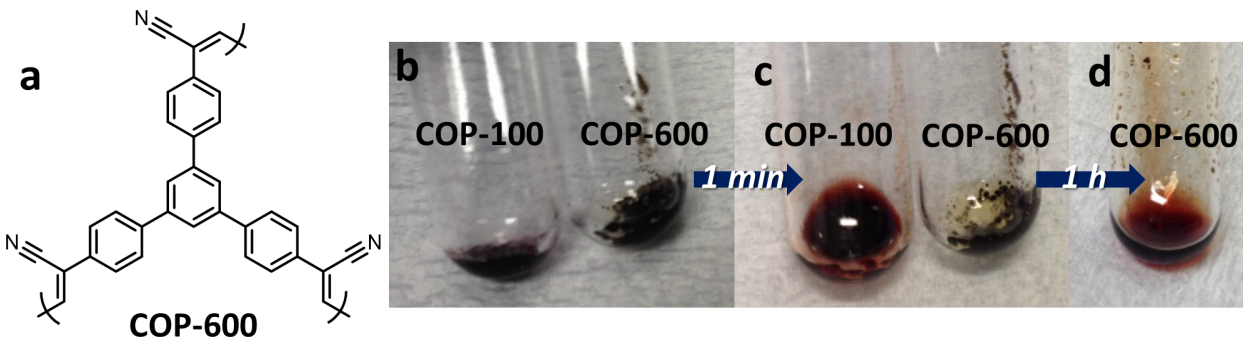


Figure 5: (a) Structure of COP-600 synthesized by Knoevenagel-like condensation. Solubility of COP-600 in EDA compared to COP-100; (b) addition of EDA at r.t., (c) heat treatment at 100 °C for 1 min and (d) for 1 h.

slower dissolution of polymer in EDA. As shown in Figure 5b, a red polymer solution of COP-600 could be obtained after 1 h of thermal treatment at 100 °C. The type of liquid amines could also be varied for solubilizing polymer structures (Supporting Information File 1, Figure S2). Among a series of common liquid amines, alkylamines, i.e., benzylamine and triethylenetetramine (TETA), were able to solubilize COP-100 at 100 °C. Allylamine, despite the amine structure, has a low boiling point (ca. 53 °C), which was not suitable for the high-temperature processing. Tertiary amines, i.e., triethylamine, did not solubilize COP-100 under the given conditions, confirming that the formation of the amide group was responsible for the polymer dissolution. The two control experiments with COP-600 and different liquid amines implied that nanoporous polymers made by Knoevenagel(-like) condensations can be easily processed in alkylamines, showing the wide applicability of the amine-induced processing method in terms of the structural variety of nanoporous polymers and amines.

Properties of COP-100-Film

Once COP-100-Film formed, it did not dissolve in any common organic solvents as long as the amount of EDA was within the threshold range, from 10 to 50 equiv of COP-100. The amount of nitrogen in COP-100-Film varied as the EDA amount changed. Typically, after addition of 10 equiv EDA, the COP-100-Film exhibited a nitrogen content of 20% by elemental analysis, indicating about an increase of nitrogen content by about 76% compared to the original COP-100. The COP-100-Film with higher nitrogen content might be eligible for CO_2 adsorption [28]. In a customized gravimetric analysis setup (Supporting Information File 1, Figure S3), COP-100 and COP-100-Film were tested for CO_2 uptake, where 9% and 2.4% of CO_2 sorption were observed in 3 h at 40 °C, respectively (Figure 6a). Despite the far worse CO_2 adsorption performance compared to COP-100, COP-100-Film exhibited a moderate CO_2 capture behavior even with the non-porous structure, owing to the nitrogen-rich surface.

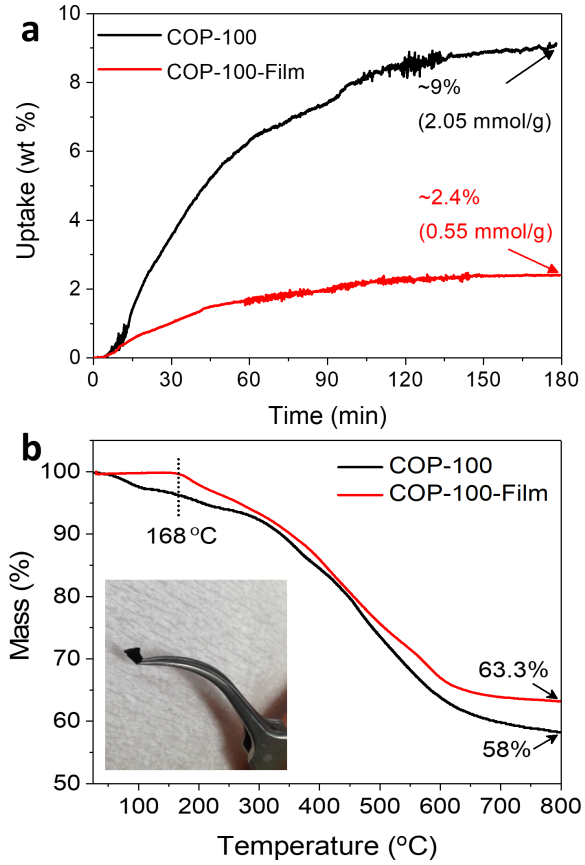


Figure 6: (a) Gravimetric CO_2 adsorption isotherm of COP-100 and COP-100-Film at 40 °C. (b) Thermogravimetric analysis of COP-100 and COP-100-Film under N_2 atmosphere. Inset displays a photograph of the carbonized COP-100-Film.

Thermogravimetric analysis of COP-100-Film (Figure 6b) showed that there was an initial mass loss at around 165 °C, possibly due to the evaporation of unassociated EDA residue incorporated within the film. The final mass of the film at 800 °C was about 63%, which corresponds to the 5% mass gain compared to that of COP-100 at 800 °C (58%), indicating that the

actual amount of EDA reacted with COP-100 was about 5% in mass. The film treated at 800 °C under inert conditions maintained its original shape, and the rigid texture of the annealed COP-100-Film indicated its high potential for fabricating a flat carbon surface on a variety of substrates (Figure 6b, inset) [29].

Conclusion

In this study, a new phenomenon is discovered to nanoporous polymer networks. The nanoporous covalent organic polymer (COP-100) was dissolved in liquid amines via simple heat treatment, and the polymer solution could be processed into either nanoparticles or films. FTIR revealed that the carbonyl groups in the polymers were reactive sites that helped to solubilize the structures in liquid amines by forming amide functionality. The control experiment with COP-600 further confirmed that amine-induced processing method can be widely applied to nanoporous network polymers having carbonyl units, especially for structures produced via a Knoevenagel-like condensation. Future research will be focused on the in-depth characterization of porosity and chemical functionalities of the processed polymers. Nanosized porous polymers would yield a better surface area, and size control would be of interest for applications in which size matters such as heterogeneous catalysis [30]. The films and membranes processed from nanoporous polymers should be tested for gas/liquid adsorption applications [31], as the functionalities of nanoporous polymers remain intact even after the processing. The remaining amines and newly formed amide functionalities in the nanoporous polymers would provide an additional advantage for favorable interaction toward target sorbate molecules. A control in thickness and composition of the film should also be achieved when varying the type and the concentration of nanoporous polymers, which will affect the permeability and selectivity of polymer films for adsorption applications.

Supporting Information

Synthetic details and methods. A TEM image and a photograph of dissolved polymers in liquid amines. A schematic illustration of gravimetric gas adsorption set-up.

Supporting Information File 1

Additional experimental details.
[https://www.beilstein-journals.org/bjnano/content/supplementary/2190-4286-10-179-S1.pdf]

Acknowledgements

This work was partly supported by an institutional program grant (Project No.: 2E29660) from the Korea Institute of Science and Technology.

ORCID® iDs

Jeehye Byun - https://orcid.org/0000-0003-1548-2017

References

1. Wu, D.; Xu, F.; Sun, B.; Fu, R.; He, H.; Matyjaszewski, K. *Chem. Rev.* **2012,** *112,* 3959–4015. doi:10.1021/cr200440z
2. Zhu, Y.; Long, H.; Zhang, W. *Chem. Mater.* **2013,** *25,* 1630–1635. doi:10.1021/cm400019f
3. Alsbaiee, A.; Smith, B. J.; Xiao, L.; Ling, Y.; Helbling, D. E.; Dichtel, W. R. *Nature* **2016,** *529,* 190–194. doi:10.1038/nature16185
4. Thomas, A.; Kuhn, P.; Weber, J.; Titirici, M.-M.; Antonietti, M. *Macromol. Rapid Commun.* **2009,** *30,* 221–236. doi:10.1002/marc.200800642
5. Kaur, P.; Hupp, J. T.; Nguyen, S. T. *ACS Catal.* **2011,** *1,* 819–835. doi:10.1021/cs200131g
6. Côté, A. P.; Benin, A. I.; Ockwig, N. W.; O'Keeffe, M.; Matzger, A. J.; Yaghi, O. M. *Science* **2005,** *310,* 1166–1170. doi:10.1126/science.1120411
7. Xu, Y.; Jin, S.; Xu, H.; Nagai, A.; Jiang, D. *Chem. Soc. Rev.* **2013,** *42,* 8012–8031. doi:10.1039/c3cs60160a
8. Kuhn, P.; Antonietti, M.; Thomas, A. *Angew. Chem., Int. Ed.* **2008,** *47,* 3450–3453. doi:10.1002/anie.200705710
9. Ben, T.; Ren, H.; Ma, S.; Cao, D.; Lan, J.; Jing, X.; Wang, W.; Xu, J.; Deng, F.; Simmons, J. M.; Qiu, S.; Zhu, G. *Angew. Chem., Int. Ed.* **2009,** *48,* 9457–9460. doi:10.1002/anie.200904637
10. Lu, W.; Yuan, D.; Zhao, D.; Schilling, C. I.; Plietzsch, O.; Muller, T.; Bräse, S.; Guenther, J.; Blümel, J.; Krishna, R.; Li, Z.; Zhou, H.-C. *Chem. Mater.* **2010,** *22,* 5964–5972. doi:10.1021/cm1021068
11. McKeown, N. B.; Budd, P. M. *Chem. Soc. Rev.* **2006,** *35,* 675–683. doi:10.1039/b600349d
12. Patel, H. A.; Karadas, F.; Canlier, A.; Park, J.; Deniz, E.; Jung, Y.; Atilhan, M.; Yavuz, C. T. *J. Mater. Chem.* **2012,** *22,* 8431–8437. doi:10.1039/c2jm30761h
13. Byun, J.; Patel, H. A.; Thirion, D.; Yavuz, C. T. *Nat. Commun.* **2016,** *7,* 13377. doi:10.1038/ncomms13377
14. Ma, B. C.; Ghasimi, S.; Landfester, K.; Zhang, K. A. I. *J. Mater. Chem. B* **2016,** *4,* 5112–5118. doi:10.1039/c6tb00943c
15. Zhao, Q.; Dunlop, J. W. C.; Qiu, X.; Huang, F.; Zhang, Z.; Heyda, J.; Dzubiella, J.; Antonietti, M.; Yuan, J. *Nat. Commun.* **2014,** *5,* 4293. doi:10.1038/ncomms5293
16. Gu, C.; Huang, N.; Gao, J.; Xu, F.; Xu, Y.; Jiang, D. *Angew. Chem., Int. Ed.* **2014,** *53,* 4850–4855. doi:10.1002/anie.201402141
17. Zhu, Y.; Qiao, M.; Peng, W.; Li, Y.; Zhang, G.; Zhang, F.; Li, Y.; Fan, X. *J. Mater. Chem. A* **2017,** *5,* 9272–9278. doi:10.1039/c7ta01438d
18. Özdemir, E.; Thirion, D.; Yavuz, C. T. *RSC Adv.* **2015,** *5,* 69010–69015. doi:10.1039/c5ra10697d
19. Bi, S.; Lan, Z.-A.; Paasch, S.; Zhang, W.; He, Y.; Zhang, C.; Liu, F.; Wu, D.; Zhuang, X.; Brunner, E.; Wang, X.; Zhang, F. *Adv. Funct. Mater.* **2017,** *27,* 1703146. doi:10.1002/adfm.201703146
20. Thirion, D.; Lee, J. S.; Özdemir, E.; Yavuz, C. T. *Beilstein J. Org. Chem.* **2016,** *12,* 2274–2279. doi:10.3762/bjoc.12.220
21. Chung, S.-K. *J. Chem. Soc., Chem. Commun.* **1982,** 480–481. doi:10.1039/c39820000480
22. Rao, J. P.; Geckeler, K. E. *Prog. Polym. Sci.* **2011,** *36,* 887–913. doi:10.1016/j.progpolymsci.2011.01.001
23. Wang, J.; Xu, F.; Cai, T.; Shen, Q. *Org. Lett.* **2008,** *10,* 445–448. doi:10.1021/ol702739c

24. Ciaccia, M.; Di Stefano, S. *Org. Biomol. Chem.* **2015,** *13,* 646–654. doi:10.1039/c4ob02110j
25. Rahman, M.; Kundu, D.; Hajra, A.; Majee, A. *Tetrahedron Lett.* **2010,** *51,* 2896–2899. doi:10.1016/j.tetlet.2010.03.097
26. Larkin, P. J. *Infrared and Raman Spectroscopy: Principles and Spectral Interpretation,* 2nd ed.; Elsevier: Amsterdam, Netherlands, 2018. doi:10.1016/c2015-0-00806-1
27. Ojeda-Porras, A.; Hernández-Santana, A.; Gamba-Sánchez, D. *Green Chem.* **2015,** *17,* 3157–3163. doi:10.1039/c5gc00189g
28. Byun, J.; Je, S.-H.; Patel, H. A.; Coskun, A.; Yavuz, C. T. *J. Mater. Chem. A* **2014,** *2,* 12507–12512. doi:10.1039/c4ta00698d
29. Yeo, K.; Kim, J.; Kim, J. *J. Nanosci. Nanotechnol.* **2018,** *18,* 6278–6282. doi:10.1166/jnn.2018.15642
30. Bond, G. C. *Surf. Sci.* **1985,** *156,* 966–981. doi:10.1016/0039-6028(85)90273-0
31. Budd, P. M.; Msayib, K. J.; Tattershall, C. E.; Ghanem, B. S.; Reynolds, K. J.; McKeown, N. B.; Fritsch, D. *J. Membr. Sci.* **2005,** *251,* 263–269. doi:10.1016/j.memsci.2005.01.009

License and Terms

This is an Open Access article under the terms of the Creative Commons Attribution License (http://creativecommons.org/licenses/by/4.0). Please note that the reuse, redistribution and reproduction in particular requires that the authors and source are credited.

The license is subject to the *Beilstein Journal of Nanotechnology* terms and conditions: (https://www.beilstein-journals.org/bjnano)

The definitive version of this article is the electronic one which can be found at: doi:10.3762/bjnano.10.179

BEILSTEIN JOURNAL OF NANOTECHNOLOGY

Long-term entrapment and temperature-controlled-release of SF_6 gas in metal–organic frameworks (MOFs)

Hana Bunzen*[1,2], Andreas Kalytta-Mewes[1], Leo van Wüllen[3] and Dirk Volkmer*[1]

Full Research Paper

Open Access

Address:
[1]Chair of Solid State and Materials Chemistry, Institute of Physics, University of Augsburg, Universitätsstraße 1, D-86159 Augsburg, Germany, [2]Institute of Materials Resource Management, University of Augsburg, Universitätsstraße 1, D-86159 Augsburg, Germany and [3]Chair of Chemical Physics and Materials Science, Institute of Physics, University of Augsburg, Universitätsstraße 1, D-86159 Augsburg, Germany

Email:
Hana Bunzen* - hana.bunzen@physik.uni-augsburg.de;
Dirk Volkmer* - dirk.volkmer@physik.uni-augsburg.de

* Corresponding author

Keywords:
benzobistriazole; gas storage; kinetic trapping; metal–organic frameworks (MOFs); sulfur hexafluoride

Beilstein J. Nanotechnol. **2019,** *10,* 1851–1859.
doi:10.3762/bjnano.10.180

Received: 29 June 2019
Accepted: 21 August 2019
Published: 10 September 2019

This article is part of the thematic issue "New directions for nanoporous materials".

Guest Editor: C. T. Yavuz

© 2019 Bunzen et al.; licensee Beilstein-Institut.
License and terms: see end of document.

Abstract

In this work, a metal–organic framework (MOF), namely MFU-4, which is comprised of zinc cations and benzotriazolate ligands, was used to entrap SF_6 gas molecules inside its pores, and thus a new scheme for long-term leakproof storage of dangerous gasses is demonstrated. The SF_6 gas was introduced into the pores at an elevated gas pressure and temperature. Upon cooling down and release of the gas pressure, we discovered that the gas was well-trapped inside the pores and did not leak out – not even after two months of exposure to air at room temperature. The material was thoroughly analyzed before and after the loading as well as after given periods of time (1, 3, 7, 14 or 60 days) after the loading. The studies included powder X-ray diffraction measurements, thermogravimetric analysis, Fourier-transform infrared spectroscopy, scanning electron microscopy, ^{19}F nuclear magnetic resonance spectroscopy and computational simulations. In addition, the possibility to release the gas guest by applying elevated temperature, vacuum and acid-induced framework decomposition was also investigated. The controlled gas release using elevated temperature has the additional benefit that the host MOF can be reused for further gas capture cycles.

Introduction

Metal–organic frameworks (MOFs) are coordination polymers with organic ligands containing (potential) voids [1]. Their porosity and high surface area make them attractive materials for adsorption-based applications [2-5]. MOFs have been suggested as promising materials for gas storage of attractive fuel gases such as hydrogen [6-8] or methane [9-11]. In these applications the gas is adsorbed inside the pores. To enhance the guest adsorption in MOFs, several different approaches have

been introduced over the last few years. These include tuning the pore properties, such as polarity, or introducing open metal sides for a better interaction between the guest and host material [5,7,11]. Recently, we reported on an alternative approach which dealt with kinetic trapping of gas molecules in MOFs [12]. This approach is based on using MOFs with ultranarrow pore apertures. Under elevated pressure and temperature, the gas molecules enter the pores, but they are not released immediately when normal conditions are re-established. This is due to the activation energy barrier for gas diffusion of the entrapped sorbate within the pores connected via ultranarrow pore apertures.

As a proof-of-principle study, we used a MOF called MFU-4 (where MFU-4 stands for Metal−Organic Framework Ulm University-4) to trap xenon gas inside the pores [12]. MFU-4 is comprised of zinc cations and benzotriazolate ions (Scheme 1) [13]. It crystallizes in the cubic crystal system and contains two types of cavities with diameters of 3.88 and 11.94 Å, which are connected by narrow (only 2.52 Å) pore apertures. This made the MOF a promising candidate for kinetic trapping of gases. In our recent work we were able to show that it was possible to trap over 40 wt % of xenon (kinetic diameter: 3.96 Å) [14] inside the pores despite its diameter being larger than the pore aperture [12]. Upon exposure of the sample to air under normal conditions, we observed that the gas was slowly released. For instance, after three days approximately 20% of the guest gas was released and after one month more than 67% was lost. Keeping these results in mind we were curious if it was possible to permanently trap (i.e., imprison) gas inside the MOF without observing any leaking at normal conditions, thus enabling the use of MOFs as a gas storage container for dangerous gases.

In this work we selected sulfur hexafluoride (kinetic diameter: 5.50 Å) [14] as a guest, which has a much larger kinetic diameter than the previously reported entrapment of xenon gas (kinetic diameter: 3.96 Å) [14]. Additionally, its presence inside the pores can be easily followed by Fourier-transform infrared (FTIR) and ^{19}F nuclear magnetic resonance (NMR) spectroscopy. SF_6 is an inert, nonflammable and nontoxic gas, which is known to be an excellent dielectric gas for high-voltage applications [15,16]. At the same time, it is also known as one of the most severe greenhouse gases [17,18]. Therefore, there is currently much interest in finding effective materials to allow its capture that provide safe storage as well as re-use. Various porous materials have been tested for this purpose including carbons [19,20], zeolites [21-23], MOFs [24-27] and porous organic cages [28,29]. Herein we present a study applying the approach of kinetic trapping of gases in MOFs and characterize the loading of SF_6 into MFU-4 and its release from the MOF at normal conditions over a period of two months.

Results and Discussion

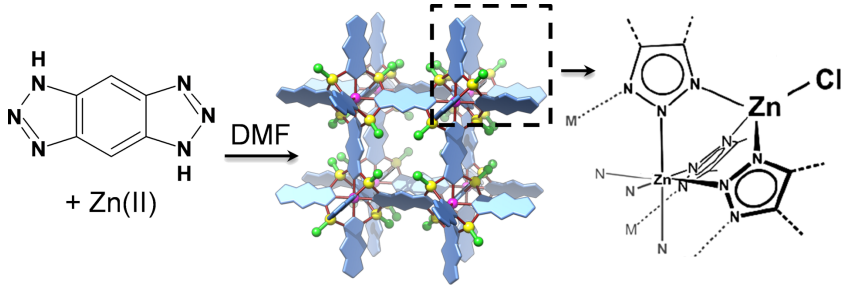
Materials synthesis

The MOF MFU-4 (Scheme 1) was synthetized according to the procedure reported previously [12]. By carrying out the reported microwave-assisted synthesis, ≈2–10 μm cubic crystals were obtained (Figure S1 in Supporting Information File 1). Prior to guest loading, the sample was kept under vacuum at 320 °C overnight to make sure that there were no solvent molecules left in the pores, thus ensuring that the whole pore volume was available for trapping the SF_6 guest. The bulk sample was analyzed before and after the gas loading by conventional analytical methods, including FTIR, powder X-ray diffraction (XRD) and thermogravimetric analysis (TGA).

SF_6-loading experiments

The SF_6-loading was carried out at elevated pressure and temperature. To incorporate the highest amount of the guest molecules inside the pores, we tested various loading conditions. We used a pressure of 20 bar and varied the loading temperature and time. From all tested conditions (Table 1), the highest loading was achieved after 18 hours at 250 °C (sample 3). Prolonging the loading time did not lead to a higher loading. Therefore, sample 3 was used in the following studies.

To estimate the amount of the guest loaded into the MOF, we used TGA (Figure 1 and Figure S2 in Supporting Information



Scheme 1: Synthesis of MFU-4.

Table 1: SF_6-loading into MFU-4 under various conditions.

Sample	SF_6 pressure (bar)	Temp. (°C)	Time (h)	SF_6 loaded (wt %)[a]	Calc. no. of SF_6 molecules per unit cell/void of MFU-4[b]
1	20	150	18	2.16	1.14 / 0.29
2	20	200	18	2.37	1.25 / 0.31
3a	20	250	18	3.09	1.65 / 0.41
3b	20	250	18	3.07	1.63 / 0.41
3c	20	250	18	3.13	1.67 / 0.42
4	20	250	48	3.04	1.62 / 0.40

[a]Mass loss in the temperature range from 150 to 390 °C determined from TGA data (see Supporting Information File 1, Figure S2). [b]Assuming all SF_6 molecules are located in the larger void (with four larger voids per unit cell of MFU-4).

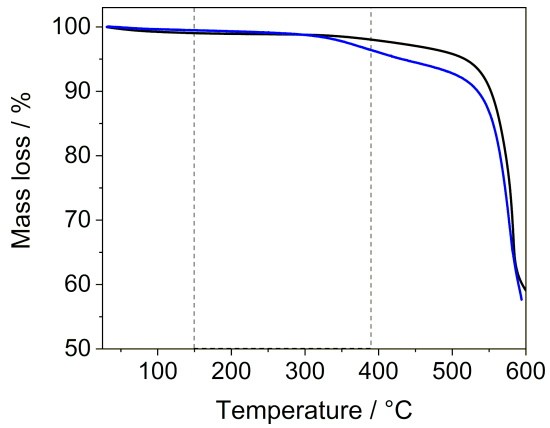


Figure 1: Thermogravimetric analysis of MFU-4 before (black) and after (Sample 3a, blue) the loading of SF_6 measured under a nitrogen atmosphere at a heating rate of 10 K min^{-1}.

File 1). The analysis revealed a gradual mass loss between 150–500 °C. When heated above 500 °C, a second mass loss was observed which corresponded to the framework decomposition. By utilizing mass spectrometry, we analyzed the gaseous products that were released during sample heating. We recorded that SF_6 was gradually released from 150 to 390 °C (Figure S3 in Supporting Information File 1). Therefore, this temperature range was used to quantify the amount of loaded SF_6 from the TGA data (Table 1).

The activation energy for the guest release was estimated by temperature-modulated TGA to be as high as approximately +135 kJ·mol^{-1} (Figure S4 in Supporting Information File 1). Modulated TGA (MTGA^{TM} by TA instruments) is an analytical technique used for obtaining continuous kinetic information for decomposition and volatilization reactions. The method makes use of an oscillation temperature program to obtain kinetic parameters during a mass loss [30,31]. Until now it has been mainly used to study organic polymers (e.g., poly(ethylene) and poly(styrene)) and simple inorganic compounds (e.g., calcium carbonate and calcium oxalate) [31]. Here we used the method to estimate the activation energy of a guest released from a porous material. The determined value of the activation energy was further compared to the results obtained from computational simulations (see the dedicated section later in the text).

To qualify the guest, we used FTIR spectroscopy (Figure 2 and Figure S5 in Supporting Information File 1). The FTIR spectrum revealed, beside the bands originating from MFU-4, three additional bands at 610.8, 935.4 and 991.6 cm^{-1}. These bands can be assigned to the ν_4 (liquid: 610.8 cm^{-1}; gas: 614.5 cm^{-1}), ν_3 (liquid: 914.9 cm^{-1}; gas: 948.0 cm^{-1}) and $\nu_2 + \nu_6$ (liquid: ≈990 cm^{-1}; gas: 984.2 cm^{-1}) vibrational modes in SF_6 [32].

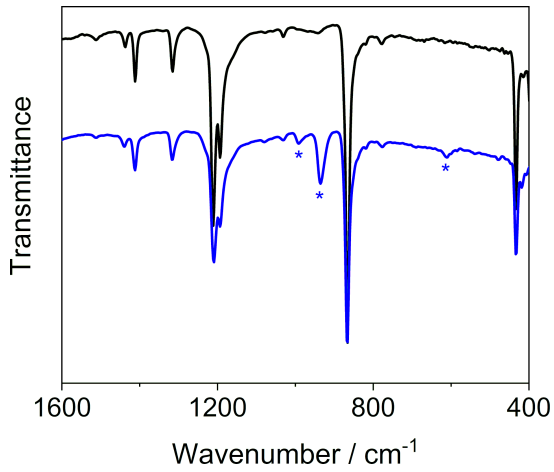


Figure 2: FTIR spectra of MFU-4 before (black) and after (Sample 3a, blue) the loading of SF_6. Bands attributed to SF_6 are marked with an asterisk.

To check that the sample crystallinity was preserved, we measured powder XRD patterns before and after the loading (Figure 3). The recorded powder XRD patterns did not reveal any changes in the diffraction peak positions, but there were differences in the peak intensities. Similar variations in the peak intensities of MOF samples have been previously described and

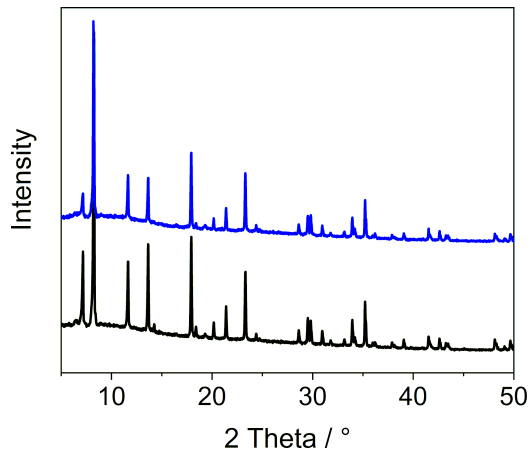


Figure 3: Powder X-ray diffraction analysis of MFU-4 before (black) and after (Sample 3a, blue) the loading of SF_6.

assigned to the presence of solvent molecules inside the pores [33]. Therefore, here the changes in intensities can be seen as a sign of SF_6 molecules being successfully included into the pores. Last but not least, scanning electron microscopy (SEM) images of the sample (taken before and after the guest loading) did not reveal any detectable changes in the crystal surface and morphology, confirming that the MOF crystals remained intact during the loading (Supporting Information File 1, Figure S1).

The presence of SF_6 could be further confirmed by NMR measurements. The ^{19}F MAS NMR spectrum, obtained at a MAS frequency of 8 kHz, revealed one singlet signal at 52.7 ppm, which can be assigned to the ^{19}F nuclei of the SF_6 guest (Figure 4). The line position is approximately 5 ppm upfield from the resonance of gaseous SF_6 (57.42 ppm) [34]. Additionally, small signals (marked by asterisks in Figure 4) to the left and right side of the main singlet represent spinning sidebands,

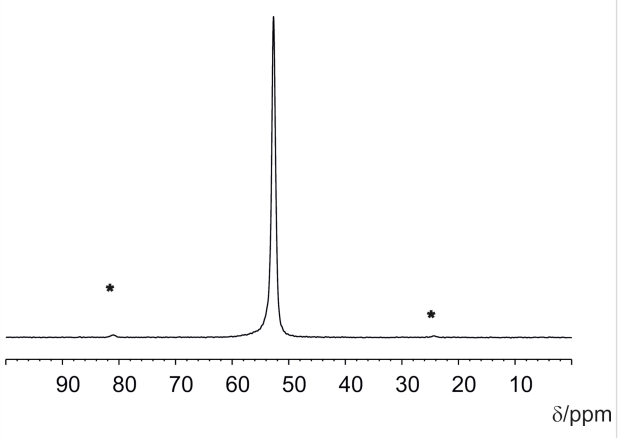


Figure 4: ^{19}F MAS NMR spectrum of MFU-4 (Sample 3b) loaded with SF_6 recorded at room temperature. The spectrum was referenced against $CFCl_3$.

which illustrates that the SF_6 molecule is not completely freely rotating and that there is an interaction with the MOF host lattice.

Computational simulations

Theoretical calculations were performed in order to determine the activation energy parameters from atomistic simulation data. Briefly, the approach previously described for scanning the minimum energy path of xenon atoms crossing the small pore in MFU-4 [13] was adapted and further refined in order to account for the multiatomic nature of the diffusant, i.e., SF_6. The linear transition path of SF_6 passing through a single unit cell of MFU-4 is shown in Figure 5a, which shows the start and

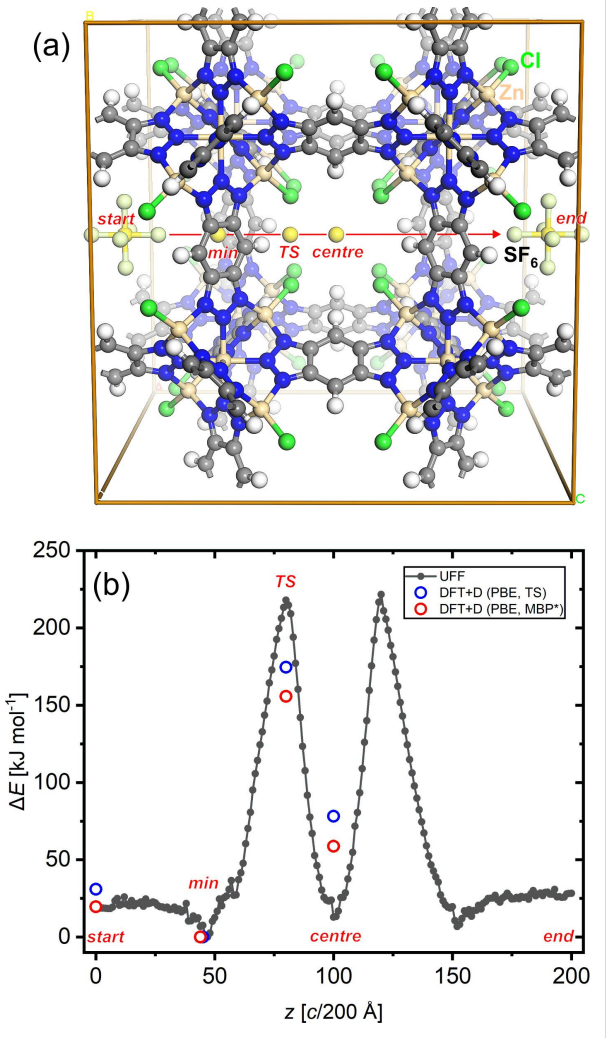


Figure 5: (a) MFU-4 unit cell showing the linear transition scan path for SF_6 crossing a single small pore. (b) Black curve and filled circles: differences of UFF total energy values of 200 configurations of SF_6@MFU-4 scanned along the linear path displayed in (a). Open circles: differences of DFT total energy values for selected configurations and different dispersion correction methods (for explanations see text).

end position of a SF_6 molecule, serving as a probe for scanning the potential energy of the system along the displayed path. To obtain a rough estimate for the energy changes along the path, molecular mechanics calculations were performed, employing the universal force field (UFF) [35] parameters as included in the GULP code [36]. In order to prevent an origin shift of the framework during transition path sampling, the fractional atom coordinates of four framework hydrogen atoms were fixed. In addition, the geometry of the linear F–S–F group (as part of SF_6) parallel to the transition path was restrained to the UFF equilibrium bond distance values. During transition path sampling all unit cell parameters were held constant. All other atom positions were allowed to relax freely during the simulation. An example input file is provided as part of the Supporting Information File 1.

The change of the total energy of all 200 configurations sampled during the linear transition of SF_6 through the unit cell of MFU-4 is shown as the black curve in Figure 5b. The potential energy curve is symmetric, showing two pronounced energy maxima at the transition path scan coordinates *c*/80 (marked by "TS") and *c*/120, respectively. At these coordinates the SF_6 molecule experiences the highest repulsive interaction energy, thus leading to a strong geometric distortion of the small pores of MFU-4. The energy minima are located at *c*/47 (marked by "min") and *c*/152; According to force field calculations, another (local) energy minimum is found in the middle of the pore (*c*/100, "centre"), which is surprising in light of the close-packed arrangement of coordinated chloride ligands in the framework structure. According to the potential energy curve, an activation energy of approximately +218 kJ·mol^{-1} can be estimated, which is significantly higher than the experimental value of +135 kJ·mol^{-1}, as gleaned from the temperature-modulated thermogravimetric analysis.

In order to obtain more realistic energy values, constrained geometry plane wave DFT+D calculations were performed for four different configurations ("min", "TS", "centre" and "start/end") as marked in Figure 5a. For this, the starting configurations were extracted from the previous force field scan trajectory and all atomic positions were allowed to relax during subsequent optimization steps, except for the position of the sulfur atom of SF_6, which was fixed at the corresponding *c*/N coordinate of the transition path. The PW-DFT+D calculations were performed with the CASTEP code [37] employing the PBE functional [38] and on-the-fly generated ultrasoft pseudopotentials (energy cutoff: 570 eV). Two different correction methods were included in all DFT calculations in order to account for dispersion interactions. The total energy values of these are shown in Figure 5b as blue (TS dispersion correction [39]) and red circles (MBD* dispersion correction [40]). The latter dispersion correction scheme leads to an approximate DFT-calculated activation energy of +156 kJ·mol^{-1}, which is in good agreement with the experimentally determined value, taking into account the fact that all calculated values formally correspond to a temperature of zero Kelvin. In the future, metadynamic MD simulation studies might be performed, which should take into account both the effects of different gas loading conditions as well as temperature-dependent lattice vibrations and distortions. For this purpose, a well-parametrized force field for the MFU-4 host lattice and the diffusant will have to be developed.

SF_6-release experiments

The SF_6-loaded MFU-4 sample was stored in air at room temperature. After a certain period (0, 1, 3, 7, 14 and 60 days) the sample was analyzed by TGA (to quantify the amount of the guest in MFU-4, Figure 6), powder XRD measurements (Figure S6 in Supporting Information File 1) and FTIR spectroscopy (Figure 7 and Figure S7 in Supporting Information File 1). Based on the results of these measurements, it can be concluded that there was no leaking of the guest. Both TGA (Figure 6 and Table 2) and FTIR spectroscopy (Figure 7, and Figure S8 and Table S1 in Supporting Information File 1) showed that SF_6 remained inside the pores over the entire investigated period. The analyses also revealed that upon exposure of the sample to air, a small amount of water was adsorbed onto the surface of the MFU-4 crystals.

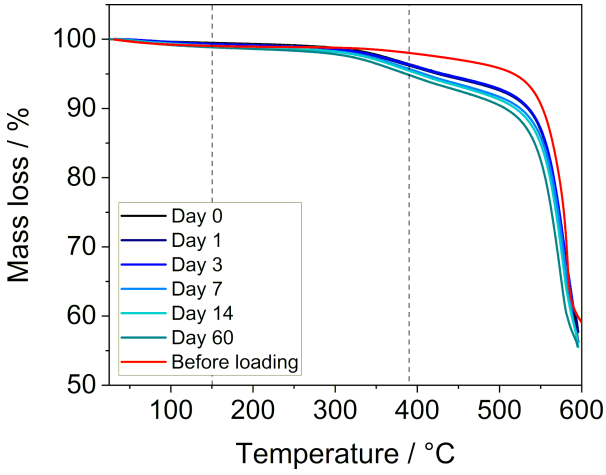


Figure 6: Thermogravimetric analysis of MFU-4 loaded with SF_6 (Sample 3a) after 0, 1, 3, 7, 14, and 60 days measured under a nitrogen atmosphere at a heating rate of 10 K min^{-1}.

As indicated by the results of the thermogravimetric analysis (Figure 1), if needed, the guest gas can be released in a controlled manner by heating the sample without decomposing the framework. This was proven by a variable temperature powder

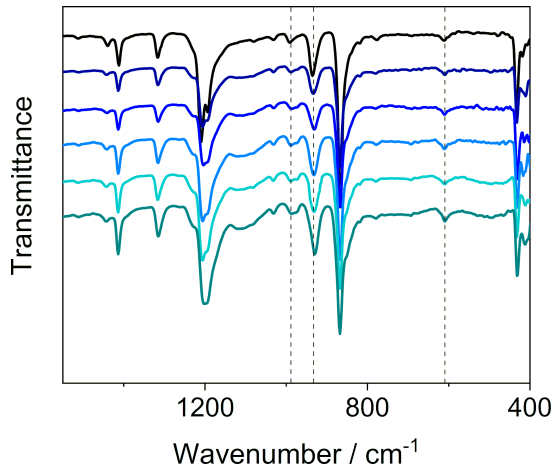


Figure 7: FTIR spectra of MFU-4 loaded with SF_6 (Sample 3a) after 0, 1, 3, 7, 14, and 60 days. Bands attributed to SF_6 are marked with dotted vertical lines.

XRD measurement (Figure S9 in Supporting Information File 1), which confirmed that MFU-4 was stable up to 500 °C. This temperature is higher than that needed for the SF_6 release, enabling the host material to be reused for further guest storage. To show that SF_6 can be released without its decomposition, a study of temperature-induced gas release followed by mass spectrometry was carried out. In this measurement only signals corresponding to the SF_6 fragments (such as $SF_5^{\cdot}$ and $SF_4^{\cdot}$) [41] and no signals of its thermal decomposition products [42] could be detected, confirming that the gas release from the host material was possible (for details see Figure S3 in Supporting Information File 1).

In another experiment, we examined if it was possible to release the gas guest at room temperature by applying vacuum. We kept a sample of MFU-4 loaded with SF_6 (Sample 3c) under vacuum at 25 °C for a certain period of time and then analyzed it by FTIR and TGA (Figure S10 and S11 in Supporting Information File 1). Even after 24 h of applying high vacuum ($p = 2.8 \times 10^{-7}$ mbar), we could still detect a substantial amount of SF_6 which corresponded to approximately 90% of the originally loaded amount (determined by TGA; see Figure S11 in Supporting Information File 1). Furthermore, we studied the possibility to release SF_6 from the pores of MFU-4 by decomposing the framework. To do so, we treated a sample of the MOF loaded with SF_6 with an acid, namely concentrated sulfuric acid, and analyzed the gas phase by mass spectrometry (Figure S12 in Supporting Information File 1). As expected, upon adding the acid to the reaction vessel, the framework decomposed and an immediate evolution of gas bubbles was observed. The SF_6 release could be followed by mass spectrometry; however, a precise quantification was not possible with the experimental set-up used. SF_6 is a heavy gas (MW: 146.06 $g \cdot mol^{-1}$), and thus some of the gas remained in the bottom of the reaction vessel and possibly also dispersed as bubbles in the viscous reaction solution.

Conclusion

In this study we were able to show that it was possible to trap SF_6 gas in a MOF and that the gas guest remained inside the MOF upon exposing the sample at room temperature to air. Even after two months we did not observe any measurable leaking of the guest gas from the host. Furthermore, even under high-vacuum conditions, most (90%) of the gas remained entrapped in the pores. This finding could lead to a new gas storage method for dangerous gasses. We also showed that it was possible to release the gas guest in a controlled manner by applying elevated temperature or by decomposing the material by acid digestion. For gas release by elevated temperature, the host MOF can be recycled for further gas-capture cycles. In the future we plan to study the influence of the material crystal size on the loading capacity and focus on engineering structural properties of MFU-4 in order to prepare its analogues with different pore aperture sizes. We believe that such materials could find potential application in gas storage and separation.

Experimental

Benzobistriazole was synthetized according to the previously reported procedure [43]. Anhydrous $ZnCl_2$ and DMF were of analytical grade and used as-received from commercial

Table 2: SF_6 release from MFU-4 (Sample 3a) stored in air at room temperature for 0–60 days as evaluated by thermogravimetric analysis (Figure 6).

Time (days)	H_2O adsorbed (wt %)[a] (25–150 °C)	SF_6 loaded (wt %)[a] (150–390 °C)	Calc. no. of SF_6 molecules per unit cell/void of MFU-4[b]
0	0.53	3.09	1.65 / 0.41
1	0.67	3.08	1.64 / 0.41
3	0.75	3.03	1.61 / 0.40
7	0.91	3.10	1.65 / 0.41
14	0.95	3.00	1.60 / 0.40
60	1.22	3.29	1.76 / 0.44

[a]Determined by TGA (Figure 6). [b]Assuming all SF_6 molecules are located in the larger void (with four larger voids per unit cell of MFU-4).

suppliers. SF_6 (≥99.995+%) was also used as-received from a commercial supplier (Linde). FTIR spectra were recorded in the range of 400–4000 cm^{-1} on a Bruker Equinox 55 FTIR spectrometer equipped with an ATR unit. Thermogravimetric analysis (TGA) was measured on a TA Instruments Q500 device over a temperature range of 25–600 °C under a nitrogen atmosphere at a heating rate of 10 K min^{-1}. Temperature-modulated TGA was measured on a TA Instruments Q500 device in the temperature range of 25–550 °C under helium atmosphere at a heating rate of 1.5 K min^{-1}, amplitude of ±5 °C and period of 200 s. The temperature-induced gas release was followed by a BelCat-B catalyst analyzer (Bel Japan, Inc.) coupled with a mass spectrometer (OmniStar GSD 320, Pfeiffer Vacuum). The sample was placed between two plugs of quartz wool in a quartz glass reactor and heated up to 500 °C (10 K·min^{-1}) under a flow of helium (30 mL·min^{-1}). The composition of the exhaust gas was analyzed by a mass spectrometer. The acid-induced gas release was carried out in a round-bottom flask purged with a flow of argon (100 mL·min^{-1}) and connected to a BelCat-B catalyst analyzer (Bel Japan, Inc.) attached to a mass spectrometer (OmniStar GSD 320, Pfeiffer Vacuum). To a solid sample (20 mg), 1 mL of concentrated sulfuric acid (95–98 wt %) was added and the gas phase was analyzed by the mass spectrometer. Powder XRD data were collected in the 5–50° 2θ range using a Seifert XRD 3003 TT powder diffractometer with a Meteor1D detector operating at room temperature using Cu $K\alpha_1$ radiation (λ = 1.54187 Å). Variable-temperature powder XRD data were measured in the 5–50° 2θ range under nitrogen atmosphere with an Empyrean (PANalytical) diffractometer equipped with a Bragg–Brentano HD mirror and a PIXcel3D 2×2 detector. The temperature program was carried out at 50 °C steps up 600 °C at a heating rate of 0.5 °C s^{-1} and held for 10 min between the measurements. SEM micrographs were recorded on a Zeiss Gemini 2 (Crossbeam 550) instrument operating at 30 kV. The ^{19}F MAS NMR spectrum was recorded at a frequency of 282.5 MHz employing a Bruker Avance III spectrometer at a field of 7 T equipped with a 4 mm Bruker MAS probe. The MAS frequency was set to 8 kHz, and a repetition rate of 2 s (T_1 = 0.37 s at room temperature) was used to collect the signal. The spectrum was referenced against $CFCl_3$.

MFU-4 synthesis

MFU-4 was prepared by a microwave-assisted synthesis following the previously reported procedure [13]. Briefly, a mixture of benzobistriazole (100 mg, 0.624 mmol) and anhydrous $ZnCl_2$ (340 mg, 2.495 mmol) in DMF (5 mL) was placed in a pyrex tube (30 mL). The reaction mixture was heated in a microwave synthesizer (CEM, Discover S) to 155 °C at 300 W and kept under these conditions for 10 min and then cooled to room temperature. The formed precipitate was isolated by centrifugation, washed well with DMF (3 × 5 mL) and dried in air at ambient conditions to give an off-white crystalline material (166 mg). Prior to the SF_6-loading experiments, the material was kept under vacuum at 320 °C overnight to remove any solvent molecules from the voids.

SF_6-loading experiments

Analogous as described in [12], in each experiment, 50−100 mg of MFU-4 was placed in a steel vessel constructed from metal tubing attached to a manometer. The vessel was filled with SF_6 gas and kept at the desired pressure and temperature for a desired period of time. Upon cooling, the gas pressure was released, and the sample was immediately analyzed with TGA, FTIR and XRPD methods.

SF_6-release experiments

In a similar manner as described in [12], the SF_6-loaded sample was stored in a container opened to air, and after a certain period of time (0, 1, 3, 7, 14 or 60 days) a small amount (≈10 mg) was taken and analyzed by TGA, FTIR and XRPD methods.

Computational simulations

To obtain a rough estimate of the energy changes along the linear transition path of SF_6 passing through a single unit cell of MFU-4 (Figure 5a), molecular mechanics calculations were performed, employing the universal force field (UFF) [35] parameters as included in the GULP code [36]. Force field atom types were assigned automatically within Material Studio's Visualizer GUI [37]. The cell parameters for the cubic unit cell of MFU-4 were taken from the published single crystal structural data, with a = 21.697 Å [13], which was kept at the experimental value in all subsequent calculations. The electrostatic-potential-derived partial (ESP) charges for the lattice atoms of MFU-4 and for SF_6 were obtained from discrete cluster DFT calculations, as described previously [44]. ESP values for the symmetry unique atoms of MFU-4 and SF_6 are displayed in the Supporting Information File 1 in Figure S13.

Prior to the potential energy scan, all atomic positions of the MFU-4 unit cell were fully relaxed at tight convergence settings. Next, a single SF_6 molecule was added to the unit cell, centered at a fractional atomic position 0.5a, 0.5b, 0.0c. The transition path of SF_6 was set to the length of one unit cell and a complete translation of SF_6 was performed in 200 steps, ending at fractional atomic positions 0.5a, 0.5b, 1.0c. The "translation" directive included in GULP was employed for automatizing the SF_6 linear transition task in a single run (setting: translate 0.0 0.0 1.0 200 noise 0.05), during which a geometry-constrained linear F–S–F fragment placed along the transition path (as part of SF_6) was moved in steps of c/200 Å in the <001> direction.

The lattice constants and some hydrogen atoms were fixed during the run, the latter constraints being required to avoid translation of the whole framework when approaching the transition state of the scan path. An example input file is provided as part of Supporting Information File 1. PW-DFT+D calculations were performed with the CASTEP code [37], employing the PBE functional [38] and on-the-fly generated ultrasoft pseudopotentials (energy cut-off: 570 eV). Geometry optimizations were performed in different symmetry-constrained unit cells of MFU-4 (tetragonal space group *P*4mm (no. 99) for those cells corresponding to "min", "TS", and "centre"; cubic space group *P*m−3m for the "start/end" configuration). Again, the experimental lattice parameter a = 21.697 Å was retained during all calculations. The two different correction methods were included in all DFT calculations in order to account for dispersion interactions.

Supporting Information

Supporting Information File 1

Additional results of SF_6-loading and SF_6-release experiments (TGA, FTIR and powder XRD measurements), and an example of an input file for the computation simulations.
[https://www.beilstein-journals.org/bjnano/content/supplementary/2190-4286-10-180-S1.pdf]

Acknowledgements

The authors are thankful to Prof. T. Meersmann (Sir Peter Mansfield Imaging Centre University of Nottingham) for valuable suggestions related to the capture of SF_6 in porous host materials.

ORCID® iDs

Hana Bunzen - https://orcid.org/0000-0003-1824-0291
Dirk Volkmer - https://orcid.org/0000-0002-8105-2157

References

1. Batten, S. R.; Champness, N. R.; Chen, X.-M.; Garcia-Martinez, J.; Kitagawa, S.; Öhrström, L.; O'Keeffe, M.; Paik Suh, M.; Reedijk, J. *Pure Appl. Chem.* **2013,** *85,* 1715–1724. doi:10.1351/pac-rec-12-11-20
2. Furukawa, H.; Cordova, K. E.; O'Keeffe, M.; Yaghi, O. M. *Science* **2013,** *341,* 1230444. doi:10.1126/science.1230444
3. Farha, O. K.; Özgür Yazaydın, A.; Eryazici, I.; Malliakas, C. D.; Hauser, B. G.; Kanatzidis, M. G.; Nguyen, S. T.; Snurr, R. Q.; Hupp, J. T. *Nat. Chem.* **2010,** *2,* 944–948. doi:10.1038/nchem.834
4. Ma, S.; Zhou, H.-C. *Chem. Commun.* **2010,** *46,* 44–53. doi:10.1039/b916295j
5. Li, H.; Wang, K.; Sun, Y.; Lollar, C. T.; Li, J.; Zhou, H.-C. *Mater. Today* **2018,** *21,* 108–121. doi:10.1016/j.mattod.2017.07.006
6. Sculley, J.; Yuan, D.; Zhou, H.-C. *Energy Environ. Sci.* **2011,** *4,* 2721–2735. doi:10.1039/c1ee01240a
7. Suh, M. P.; Park, H. J.; Prasad, T. K.; Lim, D.-W. *Chem. Rev.* **2012,** *112,* 782–835. doi:10.1021/cr200274s
8. García-Holley, P.; Schweitzer, B.; Islamoglu, T.; Liu, Y.; Lin, L.; Rodriguez, S.; Weston, M. H.; Hupp, J. T.; Gómez-Gualdrón, D. A.; Yildirim, T.; Farha, O. K. *ACS Energy Lett.* **2018,** *3,* 748–754. doi:10.1021/acsenergylett.8b00154
9. Makal, T. A.; Li, J.-R.; Lua, W.; Zhou, H.-C. *Chem. Soc. Rev.* **2012,** *41,* 7761–7779. doi:10.1039/c2cs35251f
10. He, Y.; Zhou, W.; Qian, G.; Chen, B. *Chem. Soc. Rev.* **2014,** *43,* 5657–5678. doi:10.1039/c4cs00032c
11. Eddaoudi, M.; Kim, J.; Rosi, N.; Vodak, D.; Wachter, J.; O'Keeffe, M.; Yaghi, O. M. *Science* **2002,** *295,* 469–472. doi:10.1126/science.1067208
12. Bunzen, H.; Kolbe, F.; Kalytta-Mewes, A.; Sastre, G.; Brunner, E.; Volkmer, D. *J. Am. Chem. Soc.* **2018,** *140,* 10191–10197. doi:10.1021/jacs.8b04582
13. Biswas, S.; Grzywa, M.; Nayek, H. P.; Dehnen, S.; Senkovska, I.; Kaskel, S.; Volkmer, D. *Dalton Trans.* **2009,** 6487–6495. doi:10.1039/b904280f
14. Breck, D. W. Recent Advances in Zeolite Science. In *Molecular Sieve Zeolites-I;* Flanigen, E. M.; Sand, L. B., Eds.; Advances in Chemistry, Vol. 101; American Chemical Society: Washington, DC, U.S.A., 1974; pp 1–19. doi:10.1021/ba-1971-0101.ch001
15. Christophorou, L. G.; Van Brunt, R. J. *IEEE Trans. Dielectr. Electr. Insul.* **1995,** *2,* 952–1003. doi:10.1109/94.469988
16. Xiao, S.; Zhang, X.; Tang, J.; Liu, S. *Energy Rep.* **2018,** *4,* 486–496. doi:10.1016/j.egyr.2018.07.006
17. Ravishankara, A. R.; Solomon, S.; Turnipseed, A. A.; Warren, R. F. *Science* **1993,** *259,* 194–199. doi:10.1126/science.259.5092.194
18. Fang, X.; Hu, X.; Janssens-Maenhout, G.; Wu, J.; Han, J.; Su, S.; Zhang, J.; Hu, J. *Environ. Sci. Technol.* **2013,** *47,* 3848–3855. doi:10.1021/es304348x
19. Chiang, Y.-C.; Wu, P.-Y. *J. Hazard. Mater.* **2010,** *178,* 729–738. doi:10.1016/j.jhazmat.2010.02.003
20. Takase, A.; Kanoh, H.; Ohba, T. *Sci. Rep.* **2015,** *5,* 11994. doi:10.1038/srep11994
21. Murase, H.; Imai, T.; Inohara, T.; Toyoda, M. *IEEE Trans. Dielectr. Electr. Insul.* **2004,** *11,* 166–173. doi:10.1109/tdei.2004.1266332
22. Toyoda, M.; Murase, H.; Imai, T.; Naotsuka, H.; Kobayashi, A.; Takano, K.; Ohkuma, K. *IEEE Trans. Power Delivery* **2003,** *18,* 442–448. doi:10.1109/tpwrd.2002.803691
23. Cao, D. V.; Sircar, S. *Ind. Eng. Chem. Res.* **2001,** *40,* 156–162. doi:10.1021/ie000650b
24. Senkovska, I.; Barea, E.; Navarro, J. A. R.; Kaskel, S. *Microporous Mesoporous Mater.* **2012,** *156,* 115–120. doi:10.1016/j.micromeso.2012.02.021
25. Kim, M.-B.; Lee, S.-J.; Lee, C. Y.; Bae, Y.-S. *Microporous Mesoporous Mater.* **2014,** *190,* 356–361. doi:10.1016/j.micromeso.2014.02.028
26. Skarmoutsos, I.; Eddaoudi, M.; Maurin, G. *Microporous Mesoporous Mater.* **2019,** *281,* 44–49. doi:10.1016/j.micromeso.2019.02.035
27. Han, L.; Guo, T.; Guo, Z.; Wang, C.; Zhang, W.; Shakya, S.; Ding, H.; Li, H.; Xu, X.; Ren, Y.; Zhang, J. *J. Phys. Chem. B* **2018,** *122,* 5225–5233. doi:10.1021/acs.jpcb.8b01420

28. Hasell, T.; Miklitz, M.; Stephenson, A.; Little, M. A.; Chong, S. Y.; Clowes, R.; Chen, L.; Holden, D.; Tribello, G. A.; Jelfs, K. E.; Cooper, A. I. *J. Am. Chem. Soc.* **2016,** *138,* 1653–1659. doi:10.1021/jacs.5b11797
29. Riddell, I. A.; Smulders, M. M. J.; Clegg, J. K.; Nitschke, J. R. *Chem. Commun.* **2011,** *47,* 457–459. doi:10.1039/c0cc02573a
30. Flynn, J. H.; Wall, L. A. *J. Polym. Sci., Part B: Polym. Lett.* **1966,** *4,* 323–328. doi:10.1002/pol.1966.110040504
31. Blaine, R. L.; Hahn, B. K. *J. Therm. Anal. Calorim.* **1998,** *54,* 695–704. doi:10.1023/a:1010171315715
32. Chapados, C.; Birnbaum, G. *J. Mol. Spectrosc.* **1988,** *132,* 323–351. doi:10.1016/0022-2852(88)90329-3
33. Chen, B.; Wang, X.; Zhang, Q.; Xi, X.; Cai, J.; Qi, H.; Shi, S.; Wang, J.; Yuan, D.; Fang, M. *J. Mater. Chem.* **2010,** *20,* 3758–3767. doi:10.1039/b922528e
34. Dungan, C. H.; van Wazer, J. R. *Compilation of reported F^{19} NMR chemical shifts, 1951 to mid-1967;* Wiley-Interscience: New York, NY, U.S.A., 1970.
35. Rappe, A. K.; Casewit, C. J.; Colwell, K. S.; Goddard, W. A.; Skiff, W. M. *J. Am. Chem. Soc.* **1992,** *114,* 10024–10035. doi:10.1021/ja00051a040
36. Gale, J. D.; Rohl, A. L. *Mol. Simul.* **2003,** *29,* 291–341. doi:10.1080/0892702031000104887
37. *BIOVIA Materials Studio,* 2019; .
38. Perdew, J. P.; Burke, K.; Ernzerhof, M. *Phys. Rev. Lett.* **1996,** *77,* 3865–3868. doi:10.1103/physrevlett.77.3865
39. Tkatchenko, A.; Scheffler, M. *Phys. Rev. Lett.* **2009,** *102,* 073005. doi:10.1103/physrevlett.102.073005
40. Ambrosetti, A.; Reilly, A. M.; Di Stasio, R. A., Jr.; Tkatchenko, A. *J. Chem. Phys.* **2014,** *140,* 18A508. doi:10.1063/1.4865104
41. Dibeler, V. H.; Mohler, F. L. *J. Res. Natl. Bur. Stand. (U. S.)* **1948,** *40,* 25–29. doi:10.6028/jres.040.014
42. Wang, J.; Ding, W.; Yan, J.; Wang, Y.; Wang, Y.; Li, Z.; Li, G. *IEEE Trans. Dielectr. Electr. Insul.* **2017,** *24,* 3405–3415. doi:10.1109/tdei.2017.006572
43. Hart, H.; Ok, D. *J. Org. Chem.* **1986,** *51,* 979–986. doi:10.1021/jo00357a005
44. Sastre, G.; van den Bergh, J.; Kapteijn, F.; Denysenko, D.; Volkmer, D. *Dalton Trans.* **2014,** *43,* 9612–9619. doi:10.1039/c4dt00365a

License and Terms

This is an Open Access article under the terms of the Creative Commons Attribution License (http://creativecommons.org/licenses/by/4.0). Please note that the reuse, redistribution and reproduction in particular requires that the authors and source are credited.

The license is subject to the *Beilstein Journal of Nanotechnology* terms and conditions: (https://www.beilstein-journals.org/bjnano)

The definitive version of this article is the electronic one which can be found at: doi:10.3762/bjnano.10.180

BEILSTEIN JOURNAL OF NANOTECHNOLOGY

Charge-transfer interactions between fullerenes and a mesoporous tetrathiafulvalene-based metal–organic framework

Manuel Souto*[1], Joaquín Calbo[2], Samuel Mañas-Valero[1], Aron Walsh[2] and Guillermo Mínguez Espallargas*[1]

Full Research Paper

Open Access

Address:
[1]Instituto de Ciencia Molecular (ICMol), Universidad de Valencia, C/ Catedrático José Beltrán 2, 46980 Paterna, Spain and [2]Department of Materials, Imperial College London, London SW7 2AZ, United Kingdom

Email:
Manuel Souto* - manuel.souto@uv.es;
Guillermo Mínguez Espallargas* - guillermo.minguez@uv.es

* Corresponding author

Keywords:
charge transfer; donor–acceptor; fullerene; metal–organic frameworks (MOFs); tetrathiafulvalene (TTF)

Beilstein J. Nanotechnol. **2019,** *10,* 1883–1893.
doi:10.3762/bjnano.10.183

Received: 28 June 2019
Accepted: 11 September 2019
Published: 18 September 2019

This article is part of the thematic issue "New directions for nanoporous materials".

Guest Editor: C. T. Yavuz

© 2019 Souto et al.; licensee Beilstein-Institut.
License and terms: see end of document.

Abstract

The design of metal–organic frameworks (MOFs) incorporating electroactive guest molecules in the pores has become a subject of great interest in order to obtain additional electrical functionalities within the framework while maintaining porosity. Understanding the charge-transfer (CT) process between the framework and the guest molecules is a crucial step towards the design of new electroactive MOFs. Herein, we present the encapsulation of fullerenes (C_{60}) in a mesoporous tetrathiafulvalene (TTF)-based MOF. The CT process between the electron-acceptor C_{60} guest and the electron-donor TTF ligand is studied in detail by means of different spectroscopic techniques and density functional theory (DFT) calculations. Importantly, gas sorption measurements demonstrate that sorption capacity is maintained after encapsulation of fullerenes, whereas the electrical conductivity is increased by two orders of magnitude due to the CT interactions between C_{60} and the TTF-based framework.

Introduction

Metal–organic frameworks (MOFs), which are crystalline porous materials constructed from metallic nodes and organic linkers, have been a major breakthrough in chemistry in the last decades [1,2]. Because of their immense structural and functional possibilities, this class of hybrid materials finds several applications in, for example, gas storage and separation, sensing or catalysis [3-5]. In addition, electroactive MOFs combining porosity and electrical conductivity [6-8] have also attracted much attention during the last years in view of their potential application, for example as chemiresistive sensors [9], field-effect transistors [10] or supercapacitors [11]. Whereas most MOFs are electrical insulators, some have shown to exhibit

excellent electrical conductivity and high charge mobility. This was achieved either by an appropriate choice of the building units to form electronically delocalised frameworks, or by incorporating electroactive guest molecules in the pores [6,12-14]. In this direction, the incorporation of redox-active moieties [15-18] as well as the understanding of charge-transfer (CT) processes in MOFs [19-24], are excellent pathways for the rational design of new electroactive frameworks exhibiting electrical conductivity and porosity at the same time.

Fullerenes (C_{60}) [25] have found numerous applications in different fields, ranging from molecular electronics and nanotechnology to biomedical applications, due to their exceptional electrochemical and photophysical properties [26,27]. In particular, understanding the CT processes between the electron-acceptor C_{60} and the electron-donor molecules is fundamental in order to optimise photovoltaics and develop efficient solar cells [28]. The encapsulation of C_{60} in MOFs [29] has become a very interesting strategy for the purification of fullerenes [30-32], or to incorporate additional functionalities within the MOF [33-35]. Very recently, Farha and co-workers have demonstrated that encapsulation of C_{60} in a zirconium-based MOF can lead to an enhancement of electrical conductivity due to donor–acceptor interactions between the pyrene-based ligand (donor) and fullerene (acceptor) without a significant decrease in the porosity [36].

Tetrathiafulvalene (TTF) and its numerous derivatives are redox-active electron-donor molecules with unique electronic properties that have been widely used as important building units in the field of molecular electronics as conductors, switches, sensors or rectifiers [37,38]. Several studies have also been devoted to the development of TTF-based macrocyclic systems for their use as molecular machines or for supramolecular host–guest recognition [39-41]. In this context, donor–acceptor interactions between C_{60} and discrete π-extended TTF molecules have been extensively studied in solution during the last years [42-47]. In contrast, much less is known about their supramolecular interactions in solid-state polymeric structures such as metal–organic frameworks.

MOFs using TTF as ligands have become an interesting new class of functional porous systems since they can incorporate additional electronic features to prepare new electrically conductive and redox-active MOFs [48-51]. Very recently, we have reported a hierarchical and highly stable TTF-based MOF, named **MUV-2**, which is based on the 6-connected trimeric cluster $[Fe_3(\mu_3O)(COO)_6]$ as secondary building unit (SBU) and tetratopic tetrathiafulvalene-tetrabenzoate ($TTFTB^{4-}$) ligands. This MOF shows a hierarchical structure with mesoporous channels of ≈3 nm and orthogonal microporous channels of ≈1 nm. In addition, it exhibits an enhanced catalytic activity for the aerobic oxidation of dibenzothiophene in diesel [52], and a reversible continuous breathing upon adsorption of different solvents [53]. Importantly, the planarity of the TTF ligands can be modulated by the breathing behaviour, which directly impacts on its electrochemical properties [53,54]. In view of the remarkable electron-donor character of the TTF-based ligands, herein we present the encapsulation of C_{60} in **MUV-2** (**C_{60}@MUV-2**) (Figure 1). A detailed study on the CT interactions between the electron-donor TTF ligands from the framework and the electron-acceptor fullerenes has been carried out by different spectroscopic techniques and theoretical calculations. Gas sorption measurements demonstrate that permanent porosity is retained, whereas electrical measurements show that conductivity is enhanced after C_{60} encapsulation.

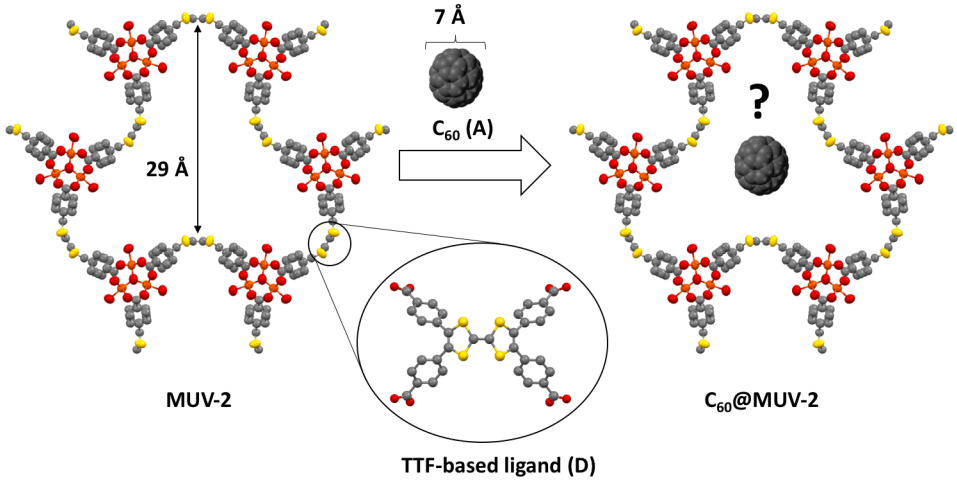


Figure 1: Schematic representation of the encapsulation of the electron-acceptor (A) C_{60} in the electron-donor (D) TTF-based **MUV-2**. Grey, yellow, orange and red spheres represent C, S, Fe and O atoms, respectively.

Results and Discussion

Synthesis and characterisation of C_{60}@MUV-2

Synthesis and encapsulation of C_{60} into MUV-2

MUV-2 was synthesised as previously described based on the solvothermal reaction of tetrathiafulvalene tetrabenzoic acid (H_4TTFTB), the preformed cluster $[Fe_3O(CH_3COO)_6]ClO_4$ and acetic acid as a modulator in dimethylformamide (DMF) [52]. In order to activate the material, **MUV-2** was exhaustively washed with DMF, methanol and heated at 150 °C for 2 h. Encapsulation of C_{60} was achieved adapting a reported procedure [36] by immersing the activated microcrystalline powder of **MUV-2** in a saturated solution of C_{60} in *o*-dichlorobenzene for three days at 60 °C. Then, the material was exhaustively washed with *o*-dichlorobenzene in order to remove the physisorbed C_{60} on the MOF surface, washed with methanol and dried at 150 °C for 2 h. The powder X-ray diffraction (PXRD) pattern of **C_{60}@MUV-2** shows that the principal peak remains at 3.4° confirming that crystallinity is maintained after encapsulation of C_{60} and removal of the solvent (Figure 2). It is important to note that the principal peak is slightly shifted when comparing the experimental and simulated PXRD patterns. This can be explained by the breathing behaviour of **MUV-2** [53]. The needle-like morphology of **C_{60}@MUV-2** also remained similar to the one of **MUV-2** as confirmed by scanning electron microscopy (SEM) (Figure S1, Supporting Information File 1).

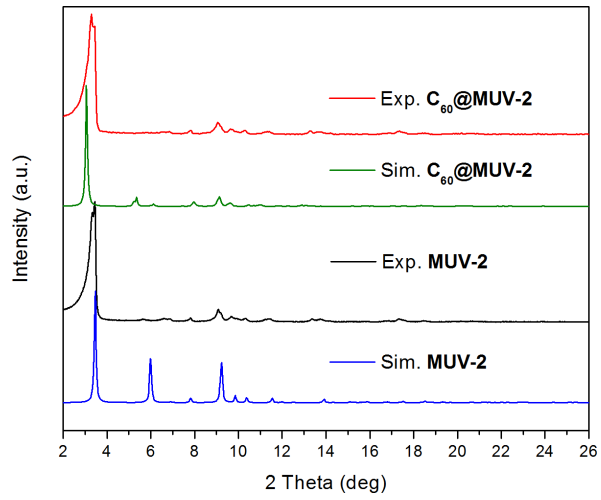


Figure 2: Powder X-ray diffraction (PXRD) patterns of simulated and experimental desolvated **MUV-2** and **C_{60}@MUV-2**.

Raman and UV–vis spectroscopy

Raman spectra of **C_{60}**, **MUV-2** and **C_{60}@MUV-2** crystals were measured using a Raman excitation wavelength of 785 nm (Figure 3a). The presence of Raman bands at 218, 284 and 490 cm^{-1} evidences the encapsulation of C_{60} in **MUV-2**, whereas the broadening and shifting of the bands towards higher frequencies are indicative of the charge-transfer (CT) interactions between the electron-acceptor C_{60} and the electron-donor TTF ligands of the framework [36,55]. On the other hand, the UV–vis spectrum of **C_{60}@MUV-2** crystals dispersed in KBr pellets (Figure 3b) shows the presence of two new bands around 260 and 350 nm, which can be assigned to C_{60}, whereas a broad band from 450 to 800 nm can be designated to an intermolecular CT excitation between the C_{60} and TTF ligands, as supported by theoretical calculations (see below). The experimental optical bandgap calculated from the onset is near 1.4 eV (885 nm), which is in agreement with the calculated electrochemical bandgap (1.43 eV) since the redox potential of TTF linkers was found to be 1.1 V (vs Ag/AgCl) [53] and the redox potential of C_{60} is −0.33 V (vs Ag/AgCl).

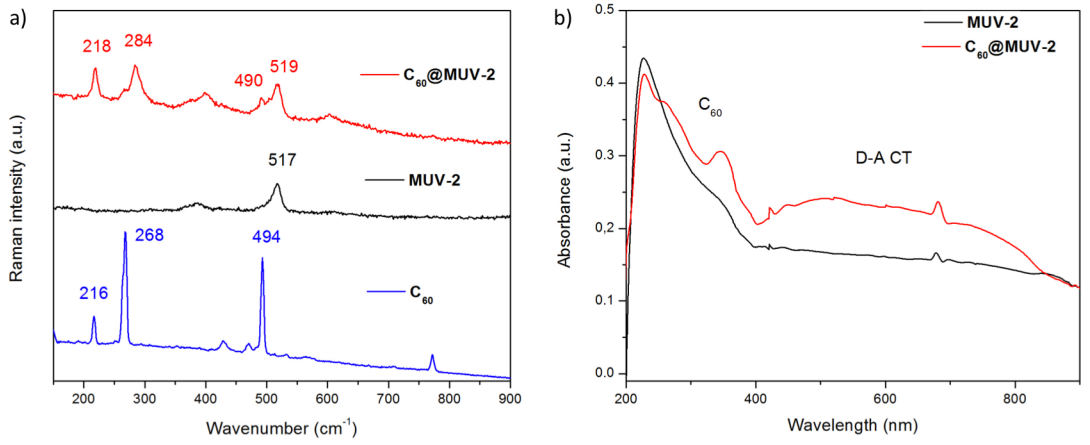


Figure 3: a) Raman spectra of **C_{60}**, **MUV-2** and **C_{60}@MUV-2**. b) Solid-state UV–vis spectra of **MUV-2** and **C_{60}@MUV-2**. The spectra were recorded by dispersing the samples in KBr pellets.

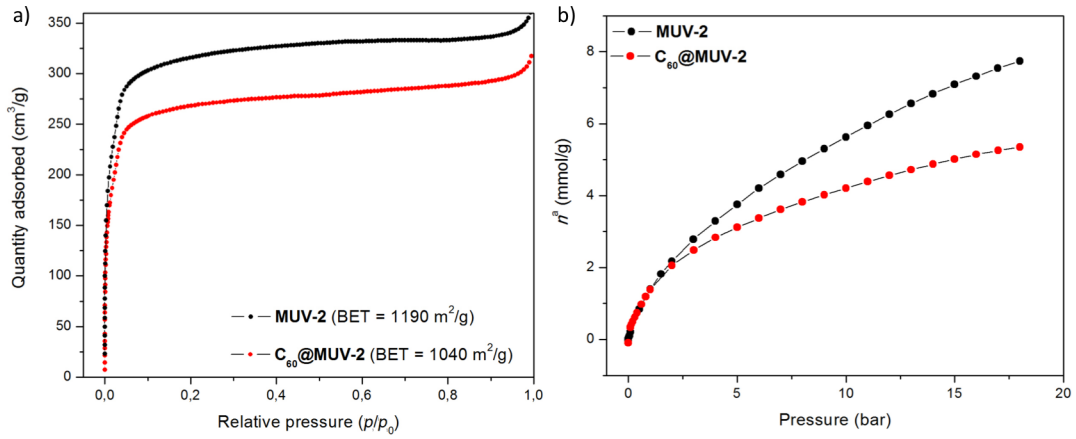


Figure 4: a) Nitrogen adsorption isotherms at 77 K and b) high-pressure CO_2 adsorption isotherms at 298 K, on **MUV-2** (black) and **C_{60}@MUV-2** (red).

Gas sorption measurements

The porosity of **C_{60}@MUV-2** was studied by means of N_2 and CO_2 adsorption isotherm measurements (Figure 4). The measurement of nitrogen at 77 K yielded a combination of type-I and type-IV isotherms (Figure 4a), as in the case of **MUV-2**, indicating the presence of micropores and mesopores in the framework. **C_{60}@MUV-2** has a Brunauer–Emmett–Teller (BET) surface area of 1040 m^2/g, which is slightly lower than that of **MUV-2** (1190 m^2/g). Thus, porosity is retained after encapsulation of C_{60}, in agreement with other reported examples [36,56]. The pore volume decreased from 0.53 cm^3/g to 0.44 cm^3/g after encapsulation of C_{60} in **MUV-2**, whereas the average pore diameter calculated by means of the Barret–Joyner–Halenda (BJH) method was found to be similar in both cases (≈35 Å). The quantity of fullerene encapsulated in **MUV-2** was estimated from the decrease in pore volume, obtaining a value of around 0.7 C_{60} per 3 TTF ligands, almost 1 fullerene per section of the void. This low encapsulation rate can be explained by diffusion issues or by weak interactions between the C_{60} and the framework, which are not strong enough to keep the C_{60} retained during the washing procedure. The CO_2 isotherm on **C_{60}@MUV-2** at 298 K also showed a small decrease in the gas sorption capacity (Figure 4b), especially at high pressures (7.7 and 5.3 mmol CO_2/g at 18 bar for **MUV-2** and **C_{60}@MUV-2**, respectively).

Theoretical calculations

In order to get further insight into the donor–acceptor interactions between **C_{60}** and the TTF-based MOF, theoretical calculations were performed under the density functional theory (DFT). The **MUV-2** framework was modelled as previously described [53], with a high-spin Fe(III) configuration and one fullerene C_{60} guest molecule per pore (according to the experimental encapsulation efficiency). The host–guest system **C_{60}@MUV-2** was fully optimized under periodic boundary conditions using the PBEsol functional with dispersion corrections (see the Experimental section for details). We initially modelled the fullerene C_{60} guest in the middle of the **MUV-2** mesopore. After several relaxation steps, the C_{60} was able to accommodate in one of the three cavities to interact favourably with the TTF-based ligand. We explored two possible conformations for the host–guest **C_{60}@MUV-2** system (A and B; Figure 5a, Supporting Information File 2). In conformer A, the fullerene ball remains in the void between two TTFTB ligands, approaching one of them with short C(C_{60})···S(TTFTB) and C(C_{60})···benzene(TTFTB) contacts calculated at 3.4 and 3.5 Å, respectively (Figure 5b). In conformer B, fullerene remains over the TTFTB ligand, promoting an efficient concave–convex complementarity with a large amount of noncovalent interactions between the C_{60} ball and the TTF core (C(C_{60})···S(TTFTB) distances of 3.6–3.8 Å), and stabilizing CH···π contacts between the benzene rings of TTFTB and the fullerene (2.5 Å, Figure 5). Analysis of the NCI index allows for the visualization of the noncovalent interactions between the TTFTB ligand and the C_{60} guest, showing a significantly larger NCI surface for conformer B compared to conformer A (Figure 5b).

Accurate hybrid DFT molecular calculations including dispersion corrections were performed to quantify the total stabilization gained when C_{60} interacts with **MUV-2** in arrangements A and B. Interaction energies (E_{int}) were calculated for the cluster **C_{60}@TTFTB** at the B3LYP-D3/6-31G** level of theory with counterpoise correction, using the minimum-energy geometry previously obtained under periodic boundary conditions (see Experimental section). Theoretical calculations indicate that C_{60} favourably interacts with the TTFTB ligand, with large $E_{int} < -20$ kcal/mol in both arrangements. Conformer B, in

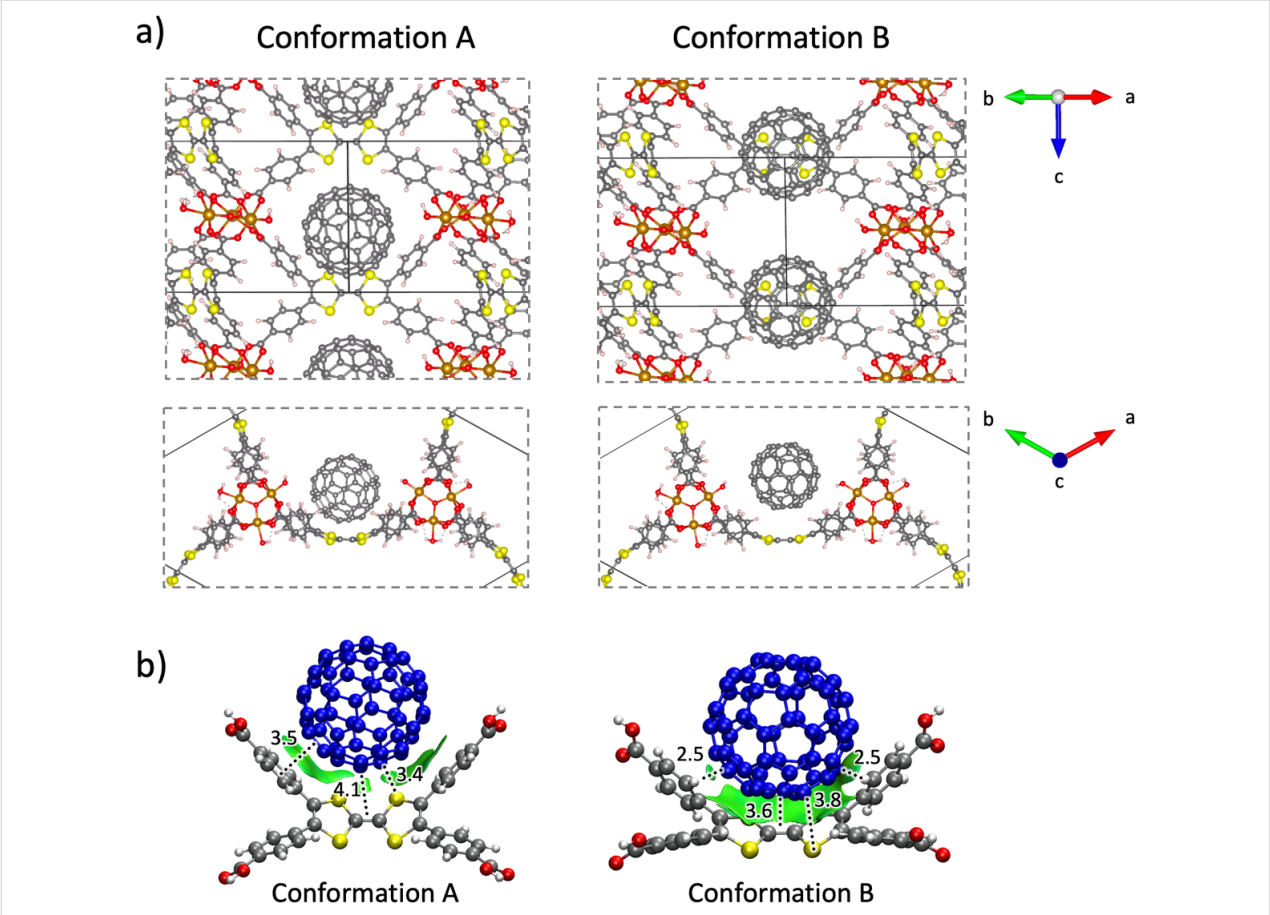


Figure 5: a) Minimum-energy crystal structure calculated for conformations A and B of host–guest **C_{60}@MUV-2** at the PBEsol level under periodic boundary conditions (PBC). b) Supramolecular assemblies of **C_{60}@TTFTB** extracted from the PBC-optimized **C_{60}@MUV-2** system in arrangements A and B. Intermolecular short contacts (in Å) and NCI surfaces (reduced density gradient isovalue = 0.3 a. u. (atomic units)) are displayed. Interaction energies (E_{int}) of −20.01 and −23.74 kcal/mol are calculated for **C_{60}@TTFTB** in conformer A and B, respectively. Fullerene C_{60} is coloured in blue for better viewing.

which the fullerene is placed over the TTF moiety promoting an efficient concave–convex complementarity (Figure 5), is predicted the most stable arrangement, with an E_{int} value of −23.74 kcal/mol (≈4 kcal/mol more stable than conformer A). Henceforth, we focus the subsequent analysis on conformation B.

Electronic structure calculations indicate that **C_{60}@MUV-2** presents a small bandgap calculated to be 0.90 eV in spin-up or α-channel, and 0.72 eV in spin-down or β-channel (Figure 6), slightly smaller than that predicted for pristine **MUV-2** (0.86 eV in β-channel) [53]. Analysis of the projected density of states (PDoS) indicates that the valence band maximum (VBM) in **C_{60}@MUV-2** corresponds to the electron-rich TTF unit (Figure 6a). The highest occupied crystal orbital (HOCO) displays the typical shape of the TTF HOMO and confirms the TTF-nature of the VBM (Figure 6b). In the α-channel, the conduction band minimum (CBM) is described by the fullerene moiety, being the lowest unoccupied crystal orbital (LUCO) completely localized on the C_{60} ball. Otherwise, the CBM in the β-channel is best described by the unoccupied Fe *d*-orbitals of the inorganic cluster of the MOF, the eigenstates corresponding to the fullerene being only 0.2 eV above in energy (Figure 6). Due to the relatively low bandgap, the nature of the frontier crystal orbitals and the close proximity between the electroactive donor TTF and acceptor C_{60} moieties, CT processes are expected upon light irradiation.

Donor–acceptor interactions in **C_{60}@MUV-2** were first assessed at the ground state electronic configuration. The electron density difference between the framework interacting with C_{60} (**C_{60}@MUV-2**) and the individual moieties (**C_{60} + MUV-2**) suggests a partial charge transfer from the TTF to the fullerene ball. Blue regions in Figure 7 indicate that the electron density is depleted from the TTF unit, especially from the S lone pairs, and is accumulated (yellow volumes) in the fullerene regions close to the TTFTB ligand. The partial charge transfer from the donor TTFTB ligand to the acceptor fullerene moiety

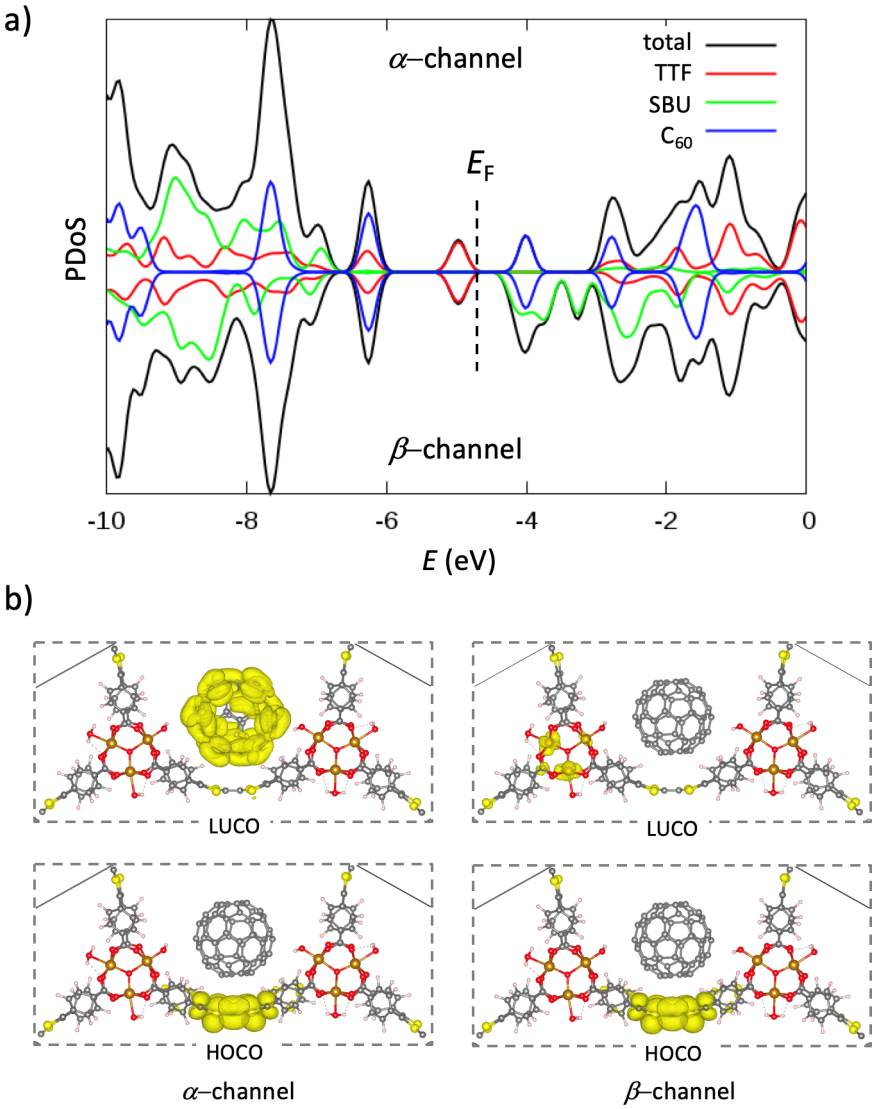


Figure 6: a) Projected density of states (PDoS) for the host–guest **C_{60}@MUV-2** system, with contributions from the TTF core, the secondary building unit (SBU), and the fullerene C_{60}. The Fermi level (E_F) is indicated, and the energy reference is set to vacuum. b) Highest occupied (HOCO) and lowest unoccupied (LUCO) crystal orbitals in the two spin channels for **C_{60}@MUV-2**.

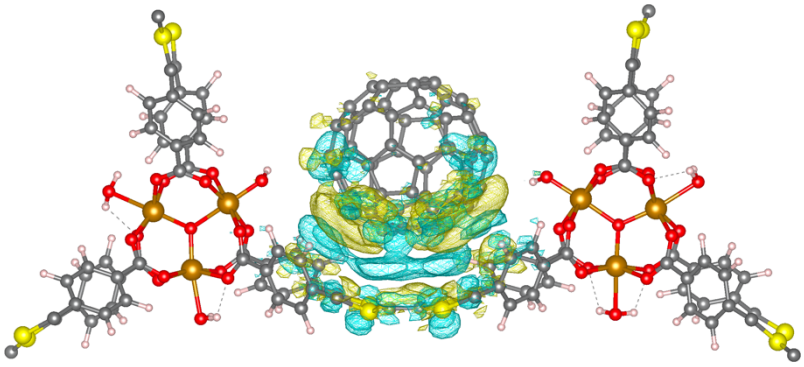


Figure 7: Electron density difference between host–guest **C_{60}@MUV-2** and the constituting moieties (**C_{60}** + **MUV-2**). Blue and yellow regions indicate charge depletion and accumulation, respectively.

in the ground state is calculated to be as small as 0.02e (and probably assigned to electronic polarization), with an exponential decay as a function of the C_{60}···TTF intermolecular distance (Table S2, Supporting Information File 1).

Time-dependent DFT molecular calculations were performed at the CAM-B3LYP/6-31G** level (see the Experimental section) to shed light onto the photoinduced CT process of **C_{60}@MUV-2**. Figure 8 displays the simulated absorption spectra predicted for the cluster **C_{60}@TTFTB** system in the most stable arrangement B, the TTFTB ligand, and the fullerene guest (the triplet excitation energies are indicated). The high-energy region (below 400 nm) of the experimental UV–vis absorption spectrum of **C_{60}@MUV-2** is dominated by the **MUV-2** framework (Figure 3b). Theoretical calculations predict several intense transitions in the region below 300 nm for the TTFTB ligand (Table S3, Supporting Information File 1) that explain the experimental wide band with maximum at ≈230 nm recorded for **MUV-2** and **C_{60}@MUV-2**. These transitions are described by π–π* electronic promotions involving the TTF and the peripheral carboxybenzene groups in the TTFTB ligand (Table S3, Supporting Information File 1). Singlet excited states S_1 and S_3 are predicted with less intensity (oscillator strength $f < 0.2$) and are described by TTF→benzene and TTF-centred monoexcitations, respectively, and give rise to the shoulder experimentally recorded at ≈350 nm for **C_{60}@MUV-2** (Table S3, Supporting Information File 1). On the other hand, the predicted singlet excited states of fullerene S_{37}–S_{39} ($f \approx 0.2$) and S_{52}–S_{54} ($f \approx 0.1$) in the region of 280 and 260 nm (Table S3, Supporting Information File 1), respectively, correlate with the experimental features that appear at 325 and 275 nm in host–guest **C_{60}@MUV-2** (Figure 3b).

Importantly, a new singlet excitation is computed for **C_{60}@TTFTB** (S_1) at 578 nm, which is not predicted either for the TTFTB ligand or the fullerene C_{60} (Figure 8). This transition has relatively small intensity ($f = 0.018$), and can be described by one-electron promotion from TTF to C_{60}, i.e., it has a CT nature (Figure 8b). The position of this CT excitation (578 nm) nicely agrees with the low-energy broad band that appears in the experimental absorption spectrum of **C_{60}@MUV-2,** centred at 550 nm and expanding up to 800 nm. In fact, theoretical calculations indicate that the intensity and energy of the S_1 CT transition in **C_{60}@TTFTB** is significantly affected by the intermolecular TTF···C_{60} distance and the characteristic TTF boat dihedral angle (Table S4, Supporting Information File 1). The charge transfer from the TTF to the fullerene ball in the S_1 CT excitation of **C_{60}@TTFTB** is calculated to be of nearly 1e (0.94e at the minimum-energy geometry, Table S2, Supporting Information File 1).

Electrical measurements

In order to analyse the possible enhancement of electrical conductivity after encapsulation of C_{60} in **MUV-2**, transport measurements for **MUV-2** and **C_{60}@MUV-2** were performed using two-contact probe pressed-pellet devices measured at room temperature (300 K) (Figure 9). Interestingly, the pellet of **C_{60}@MUV-2** shows an increase of around two orders of magnitude ($\sigma = 4.7 \cdot 10^{-9}$ S/cm) compared to the very resistive **MUV-2** ($\sigma = 3.7 \cdot 10^{-11}$ S/cm, Table 1). This enhancement of the electrical conductivity can be explained by the donor–acceptor charge transfer from the TTF linkers to C_{60} since the fullerene is acting as a dopant introducing charge carriers within the framework. However, this enhancement in conductivity is lower in comparison to other reported systems [14,35] probably due to the low ratio between C_{60} and TTF (1:4) and the long distances between the TTF moieties (9.6 Å along the *c*-axis), which could prevent the charge delocalisation along the framework.

Conclusion

In summary, we have reported for the first time the encapsulation of C_{60} in a mesoporous TTF-based MOF (**MUV-2**).

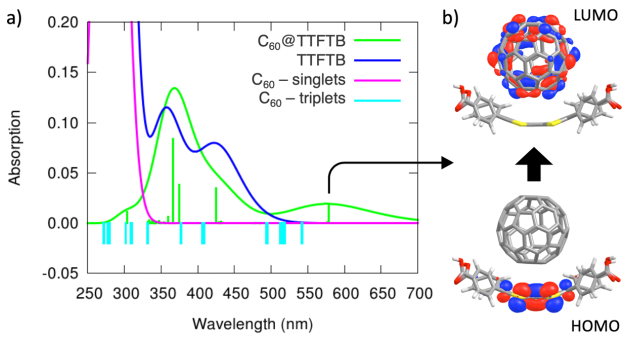


Figure 8: a) TDDFT absorption spectra calculated at the CAM-B3LYP/6-31G** level for host–guest **C_{60}@TTFTB** (including vertical excitation energies), TTFTB ligand, and fullerene C_{60} (singlets and triplet energies). b) Monoelectronic excitation that describes the nature of the lowest-lying singlet excited state S_1 of **C_{60}@TTFTB**.

Table 1: Geometrical factors (length *l*, width *w*, and thickness *t*), resistance obtained by the linear fit of the ohmic regime of the *I*–*V* curves and conductivity for **MUV-2** and **C_{60}@MUV-2**, at 300 K.

sample	*l* (μm)	*w* (μm)	*t* (μm)	*R* (Ω) at 300 K	σ (S/cm) at 300 K
MUV-2	110	480	65	$(9.5 \pm 0.6)\cdot10^{11}$	$3.7\cdot10^{-11}$
C_{60}@MUV-2	325	540	150	$(8.510 \pm 0.015)\cdot10^{9}$	$4.7\cdot10^{-9}$

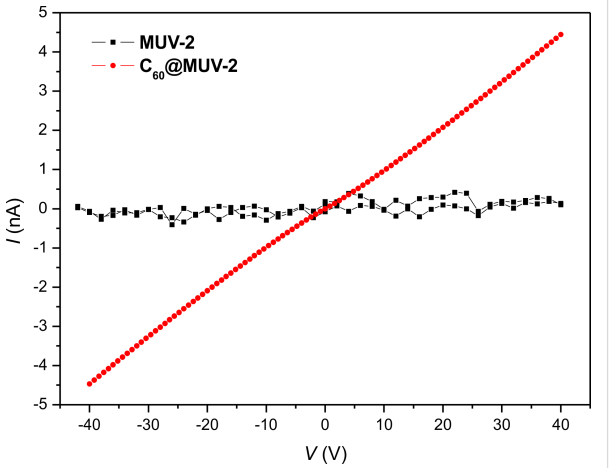


Figure 9: Current (*I*)–Voltage (*V*) plot for pressed pellets of **MUV-2** (black) and **C_{60}@MUV-2** (red) at 300 K.

Charge-transfer interactions between C_{60} and TTF ligands from the framework in **C_{60}@MUV-2** were confirmed by different spectroscopic techniques and theoretical calculations. Interestingly, after encapsulation of fullerenes, gas sorption measurements demonstrated that the mesoporosity of the MOF is maintained, and electrical measurements revealed an increase of around two orders of magnitude in conductivity, which can be explained by CT donor–acceptor (TTF→C_{60}) interactions. Current research is focused on the improvement of the electrical conductivity in **MUV-2** and the photophysical characterisation of the charge transfer process in **C_{60}@MUV-2**.

Experimental

General methods and materials: All reagents and solvents employed for the syntheses were of high purity and were purchased from Sigma-Aldrich Co., and TCI. Powder X-ray diffraction patterns were recorded using 0.7 mm borosilicate capillaries that were aligned on an Empyrean PANalytical powder diffractometer, using Cu Kα radiation (λ = 1.54056 Å). Raman spectra were acquired with a micro-Raman (model XploRA ONE from Horiba, Kyoto, Japan) with a grating of 1200 gr/mm and a wavelength of 785 nm. UV–vis absorption spectra were recorded on a Jasco V-670 spectrophotometer in baseline mode from 400 to 800 nm range. The absorption spectra were measured on the solid state by dispersing the crystals in KBr pellets. Nitrogen adsorption isotherms were measured using a TriStar II PLUS apparatus (Micromeritics) at 77 K. The BET surface area was calculated by using the Brunauer–Emmett–Teller equation. The high-pressure CO_2 adsorption isotherms were measured in a IGA-100 gravimetric sorption analyzer (Hiden Isochema) and the sample was degassed for 2 h at 150 °C in vacuum.

Synthesis of MUV-2 and encapsulation of C_{60}: MUV-2 was synthesised and characterised as previously reported [52]. Then, 30 mg of fullerene (C_{60}) was dissolved in 2 mL of *o*-dichlorobenzene and activated **MUV-2** (10 mg) was added to it. The vial was heated at 60 °C for 3 days and the MOF was then exhaustively washed with *o*-dichlorobenzene to remove any physisorbed C_{60} on the MOF surface, washed with methanol and finally dried at 150 °C for 2 h.

Computational details: Theoretical calculations were performed under the density functional theory framework. Periodic boundary conditions (PBC) calculations were carried out with the FHI-AIMS (Version 171221) software [57]. **MUV-2** was modelled as previously described, with Fe(III) ions in a high-spin d^5-configuration. The guest C_{60} molecule was rationally inserted into the bigger mesoporous channel of **MUV-2** in the most plausible sites, and the geometry of the host–guest **C_{60}@MUV-2** system was fully relaxed at the PBEsol functional [58] with tier-1 basis set. Dispersion corrections were added according to the Hirshfeld partitioning of the electron density (Tkatchenko–Scheffler method) [59]. Electronic structure calculations were performed for band structure analysis using the hybrid HSE06 functional [60] and tier-1 basis set. Energy reference was set to vacuum according to the protocol reported by Butler and co-workers [61]. Crystal structures, crystal orbitals and electron density differences were plotted by means of VESTA (version 3.4.6) software [62]. NonCovalent Index (NCI) calculations were performed under the NCIPLOT-3.0 software [63,64] using the default PROMOLECULAR atomic densities, and density and gradient thresholds. The intermolecular contribution to the NCI surfaces was calculated by means of the INTERMOLECULAR keyword, and the VMD-1.9.3 software [65] was employed for graphical display. Molecular DFT calculations were performed for the **C_{60}@TTFTB** system using the Gaussian-16.A03 suite of packages [66].

Hydrogen atoms were added in the terminal carboxylate groups for charge neutrality. Interaction energies were calculated for the previously PBC-optimized crystal structures as the energy difference between the dimer and the constituting monomers. The hybrid B3LYP [67] with the Grimme's D3 dispersion correction [68] (B3LYP-D3) was employed along with the 6-31G** basis set and half of the counterpoise correction (CP) [69]. The consistency of the interaction energy trends at the B3LYP-D3/6-31G**+½CP level was confirmed by using other basis set or CP weights (Table S1, Supporting Information File 1). Time-dependent DFT (TDDFT) calculations were performed using the coulomb-attenuating CAM-B3LYP approach [70] with the 6-31G** basis set for the lowest-lying excited states. The B3LYP functional was also tested, but the characteristic charge-transfer excitation was largely underestimated (Figure S4, Supporting Information File 1). Excitation energies were convoluted with Gaussian functions with full-width-at-half-maximum (FWHM) of 0.2 eV. Charge transfer was evaluated as the accumulated natural population analysis (NPA) [71] charges on each moiety. Molecular orbitals were represented by means of the Chemcraft 1.7 software [72].

Electrical measurements: Pressed pellets ($F \approx 5$ US tons) were cut in rectangular shapes and contacted with silver conductive paint (RS 123-9911) and platinum wires (Goodfellow, 99.99%, 25 μm of diameter) in a four-probe configuration (Figure S2 and Figure S3, Supporting Information File 1). The geometrical factors (thickness, width and length were measured using an optical microscope (width and length were determined from the top view, Figure S2a and Figure S3a, and the thickness from the lateral view, Figure S2b and Figure S3b). *I–V* curves were measured with a Keithley 6517B electrometer for ultra-high resistance/ultra-low current measurements in a two-probe configuration, i.e., applying a voltage bias between two leads and measuring the current between them.

Supporting Information

Supporting Information File 1

Additional figures and tables.
[https://www.beilstein-journals.org/bjnano/content/supplementary/2190-4286-10-183-S1.pdf]

Supporting Information File 2

CIF files of simulated structures of C_{60}@MUV-2.
The ZIP archive contains CIF files of the simulated structures of C60@MUV-2 in conformation A and in conformation B.
[https://www.beilstein-journals.org/bjnano/content/supplementary/2190-4286-10-183-S2.zip]

Acknowledgements

This work has been supported by the European Union (ERC-2016-CoG 724681-S-CAGE) and the Spanish MICINN (CTQ2017-89528-P). G.M.E. and M.S. thank MICINN for a Ramón y Cajal and a Juan de la Cierva-Formación fellowships, respectively. J.C. acknowledges the Generalitat Valenciana for the postdoctoral APOSTD/2017/081 fellowship. Via our membership of the UK's HEC Materials Chemistry Consortium, which is funded by EPSRC (EP/L000202), this work used the ARCHER UK National Supercomputing Service (http://www.archer.ac.uk).

ORCID® iDs

Manuel Souto - https://orcid.org/0000-0003-3491-6984
Joaquín Calbo - https://orcid.org/0000-0003-4729-0757
Samuel Mañas-Valero - https://orcid.org/0000-0001-6319-9238

Preprint

A non-peer-reviewed version of this article has been previously published as a preprint https://doi.org/10.26434/chemrxiv.8427047.v1

References

1. Zhou, H.-C.; Long, J. R.; Yaghi, O. M. *Chem. Rev.* **2012,** *112,* 673–674. doi:10.1021/cr300014x
2. Maurin, G.; Serre, C.; Cooper, A.; Férey, G. *Chem. Soc. Rev.* **2017,** *46,* 3104–3107. doi:10.1039/c7cs90049j
3. Furukawa, H.; Cordova, K. E.; O'Keeffe, M.; Yaghi, O. M. *Science* **2013,** *341,* No. 1230444. doi:10.1126/science.1230444
4. Slater, A. G.; Cooper, A. I. *Science* **2015,** *348,* aaa8075. doi:10.1126/science.aaa8075
5. Rogge, S. M. J.; Bavykina, A.; Hajek, J.; Garcia, H.; Olivos-Suarez, A. I.; Sepúlveda-Escribano, A.; Vimont, A.; Clet, G.; Bazin, P.; Kapteijn, F.; Daturi, M.; Ramos-Fernandez, E. V.; Llabrés i Xamena, F. X.; Van Speybroeck, V.; Gascon, J. *Chem. Soc. Rev.* **2017,** *46,* 3134–3184. doi:10.1039/c7cs00033b
6. Sun, L.; Campbell, M. G.; Dincă, M. *Angew. Chem., Int. Ed.* **2016,** *55,* 3566–3579. doi:10.1002/anie.201506219
7. Stassen, I.; Burtch, N.; Talin, A.; Falcaro, P.; Allendorf, M.; Ameloot, R. *Chem. Soc. Rev.* **2017,** *46,* 3185–3241. doi:10.1039/c7cs00122c
8. Medina, D. D.; Mähringer, A.; Bein, T. *Isr. J. Chem.* **2018,** *58,* 1089–1101. doi:10.1002/ijch.201800110
9. Campbell, M. G.; Sheberla, D.; Liu, S. F.; Swager, T. M.; Dincă, M. *Angew. Chem., Int. Ed.* **2015,** *54,* 4349–4352. doi:10.1002/anie.201411854
10. Wu, G.; Huang, J.; Zang, Y.; He, J.; Xu, G. *J. Am. Chem. Soc.* **2017,** *139,* 1360–1363. doi:10.1021/jacs.6b08511
11. Sheberla, D.; Bachman, J. C.; Elias, J. S.; Sun, C.-J.; Shao-Horn, Y.; Dincă, M. *Nat. Mater.* **2017,** *16,* 220–224. doi:10.1038/nmat4766
12. Talin, A. A.; Centrone, A.; Ford, A. C.; Foster, M. E.; Stavila, V.; Haney, P.; Kinney, R. A.; Szalai, V.; El Gabaly, F.; Yoon, H. P.; Léonard, F.; Allendorf, M. D. *Science* **2014,** *343,* 66–69. doi:10.1126/science.1246738
13. Bhardwaj, S. K.; Bhardwaj, N.; Kaur, R.; Mehta, J.; Sharma, A. L.; Kim, K.-H.; Deep, A. *J. Mater. Chem. A* **2018,** *6,* 14992–15009. doi:10.1039/c8ta04220a

14. Kung, C.-W.; Otake, K.; Buru, C. T.; Goswami, S.; Cui, Y.; Hupp, J. T.; Spokoyny, A. M.; Farha, O. K. *J. Am. Chem. Soc.* **2018,** *140,* 3871–3875. doi:10.1021/jacs.8b00605
15. D'Alessandro, D. M. *Chem. Commun.* **2016,** *52,* 8957–8971. doi:10.1039/c6cc00805d
16. Kung, C.-W.; Wang, T. C.; Mondloch, J. E.; Fairen-Jimenez, D.; Gardner, D. M.; Bury, W.; Klingsporn, J. M.; Barnes, J. C.; Van Duyne, R.; Stoddart, J. F.; Wasielewski, M. R.; Farha, O. K.; Hupp, J. T. *Chem. Mater.* **2013,** *25,* 5012–5017. doi:10.1021/cm403726v
17. Chen, Q.; Sun, J.; Li, P.; Hod, I.; Moghadam, P. Z.; Kean, Z. S.; Snurr, R. Q.; Hupp, J. T.; Farha, O. K.; Stoddart, J. F. *J. Am. Chem. Soc.* **2016,** *138,* 14242–14245. doi:10.1021/jacs.6b09880
18. Calbo, J.; Golomb, M. J.; Walsh, A. *J. Mater. Chem. A* **2019,** *7,* 16571–16597. doi:10.1039/c9ta04680a
19. Van Wyk, A.; Smith, T.; Park, J.; Deria, P. *J. Am. Chem. Soc.* **2018,** *140,* 2756–2760. doi:10.1021/jacs.7b13211
20. Hua, C.; Doheny, P. W.; Ding, B.; Chan, B.; Yu, M.; Kepert, C. J.; D'Alessandro, D. M. *J. Am. Chem. Soc.* **2018,** *140,* 6622–6630. doi:10.1021/jacs.8b02638
21. Miyasaka, H. *Acc. Chem. Res.* **2013,** *46,* 248–257. doi:10.1021/ar300102t
22. Xiao, J.-D.; Han, L.; Luo, J.; Yu, S.-H.; Jiang, H.-L. *Angew. Chem., Int. Ed.* **2018,** *57,* 1103–1107. doi:10.1002/anie.201711725
23. Fang, X.; Shang, Q.; Wang, Y.; Jiao, L.; Yao, T.; Li, Y.; Zhang, Q.; Luo, Y.; Jiang, H.-L. *Adv. Mater. (Weinheim, Ger.)* **2018,** *30,* 1705112. doi:10.1002/adma.201705112
24. Xiao, J.-D.; Jiang, H.-L. *Acc. Chem. Res.* **2019,** *52,* 356–366. doi:10.1021/acs.accounts.8b00521
25. Kroto, H. W.; Heath, J. R.; O'Brien, S. C.; Curl, R. F.; Smalley, R. E. *Nature* **1985,** *318,* 162–163. doi:10.1038/318162a0
26. Giacalone, F.; Martín, N. *Chem. Rev.* **2006,** *106,* 5136–5190. doi:10.1021/cr068389h
27. Martín, N. *Chem. Commun.* **2006,** 2093–2104. doi:10.1039/b601582b
28. Zieleniewska, A.; Lodermeyer, F.; Roth, A.; Guldi, D. M. *Chem. Soc. Rev.* **2018,** *47,* 702–714. doi:10.1039/c7cs00728k
29. Meng, H.; Wang, C.; Wang, T. *Gen. Chem.* **2018,** *4,* 180019. doi:10.21127/yaoyigc20180019
30. Inokuma, Y.; Arai, T.; Fujita, M. *Nat. Chem.* **2010,** *2,* 780–783. doi:10.1038/nchem.742
31. García-Simón, C.; Garcia-Borràs, M.; Gómez, L.; Parella, T.; Osuna, S.; Juanhuix, J.; Imaz, I.; Maspoch, D.; Costas, M.; Ribas, X. *Nat. Commun.* **2014,** *5,* 5557. doi:10.1038/ncomms6557
32. García-Simón, C.; Costas, M.; Ribas, X. *Chem. Soc. Rev.* **2016,** *45,* 40–62. doi:10.1039/c5cs00315f
33. Feng, Y.; Wang, T.; Li, Y.; Li, J.; Wu, J.; Wu, B.; Jiang, L.; Wang, C. *J. Am. Chem. Soc.* **2015,** *137,* 15055–15060. doi:10.1021/jacs.5b10796
34. Meng, H.; Zhao, C.; Nie, M.; Wang, C.; Wang, T. *J. Phys. Chem. C* **2019,** *123,* 6265–6269. doi:10.1021/acs.jpcc.8b11659
35. Liu, X.; Kozlowska, M.; Okkali, T.; Wagner, D.; Higashino, T.; Brenner-Weiß, G.; Marschner, S. M.; Fu, Z.; Zhang, Q.; Imahori, H.; Bräse, S.; Wenzel, W.; Wöll, C.; Heinke, L. *Angew. Chem., Int. Ed.* **2019,** *58,* 9590–9595. doi:10.1002/anie.201904475
36. Goswami, S.; Ray, D.; Otake, K.-i.; Kung, C.-W.; Garibay, S. J.; Islamoglu, T.; Atilgan, A.; Cui, Y.; Cramer, C. J.; Farha, O. K.; Hupp, J. T. *Chem. Sci.* **2018,** *9,* 4477–4482. doi:10.1039/c8sc00961a
37. Segura, J. L.; Martín, N. *Angew. Chem., Int. Ed.* **2001,** *40,* 1372–1409. doi:10.1002/1521-3773(20010417)40:8<1372::aid-anie1372>3.0.co;2-i
38. Martín, N. *Chem. Commun.* **2013,** *49,* 7025–7027. doi:10.1039/c3cc00240c
39. Jana, A.; Bähring, S.; Ishida, M.; Goeb, S.; Canevet, D.; Sallé, M.; Jeppesen, J. O.; Sessler, J. L. *Chem. Soc. Rev.* **2018,** *47,* 5614–5645. doi:10.1039/c8cs00035b
40. Spruell, J. M.; Coskun, A.; Friedman, D. C.; Forgan, R. S.; Sarjeant, A. A.; Trabolsi, A.; Fahrenbach, A. C.; Barin, G.; Paxton, W. F.; Dey, S. K.; Olson, M. A.; Benítez, D.; Tkatchouk, E.; Colvin, M. T.; Carmielli, R.; Caldwell, S. T.; Rosair, G. M.; Hewage, S. G.; Duclairoir, F.; Seymour, J. L.; Slawin, A. M. Z.; Goddard, W. A., III; Wasielewski, M. R.; Cooke, G.; Stoddart, J. F. *Nat. Chem.* **2010,** *2,* 870–879. doi:10.1038/nchem.749
41. Frasconi, M.; Kikuchi, T.; Cao, D.; Wu, Y.; Liu, W.-G.; Dyar, S. M.; Barin, G.; Sarjeant, A. A.; Stern, C. L.; Carmieli, R.; Wang, C.; Wasielewski, M. R.; Goddard, W. A., III; Stoddart, J. F. *J. Am. Chem. Soc.* **2014,** *136,* 11011–11026. doi:10.1021/ja504662a
42. Pérez, E. M.; Sánchez, L.; Fernández, G.; Martín, N. *J. Am. Chem. Soc.* **2006,** *128,* 7172–7173. doi:10.1021/ja0621389
43. Pérez, E. M.; Sierra, M.; Sánchez, L.; Torres, M. R.; Viruela, R.; Viruela, P. M.; Ortí, E.; Martín, N. *Angew. Chem., Int. Ed.* **2007,** *46,* 1847–1851. doi:10.1002/anie.200604327
44. Pérez, E. M.; Martín, N. *Chem. Soc. Rev.* **2008,** *37,* 1512–1519. doi:10.1039/b802589b
45. Canevet, D.; Pérez, E. M.; Martín, N. *Angew. Chem., Int. Ed.* **2011,** *50,* 9248–9259. doi:10.1002/anie.201101297
46. Goeb, S.; Bivaud, S.; Dron, P. I.; Balandier, J. Y.; Chas, M.; Sallé, M. *Chem. Commun.* **2012,** *48,* 3106–3108. doi:10.1039/c2cc00065b
47. Gallego, M.; Calbo, J.; Aragó, J.; Krickcalderon, R. M.; Liquido, F. H.; Iwamoto, T.; Greene, A. K.; Jackson, E. A.; Pérez, E. M.; Ortí, E.; Guldi, D. M.; Scott, L. T.; Martín, N. *Angew. Chem., Int. Ed.* **2014,** *53,* 2170–2175. doi:10.1002/anie.201309672
48. Wang, H.-Y.; Cui, L.; Xie, J.-Z.; Leong, C. F.; D'Alessandro, D. M.; Zuo, J.-L. *Coord. Chem. Rev.* **2017,** *345,* 342–361. doi:10.1016/j.ccr.2016.10.011
49. Park, S. S.; Hontz, E. R.; Sun, L.; Hendon, C. H.; Walsh, A.; Van Voorhis, T.; Dincă, M. *J. Am. Chem. Soc.* **2015,** *137,* 1774–1777. doi:10.1021/ja512437u
50. Su, J.; Yuan, S.; Wang, H.-Y.; Huang, L.; Ge, J.-Y.; Joseph, E.; Qin, J.; Cagin, T.; Zuo, J.-L.; Zhou, H.-C. *Nat. Commun.* **2017,** *8,* 2008. doi:10.1038/s41467-017-02256-y
51. Wang, H.-Y.; Ge, J.-Y.; Hua, C.; Jiao, C.-Q.; Wu, Y.; Leong, C. F.; D'Alessandro, D. M.; Liu, T.; Zuo, J.-L. *Angew. Chem., Int. Ed.* **2017,** *56,* 5465–5470. doi:10.1002/anie.201611824
52. Souto, M.; Santiago-Portillo, A.; Palomino, M.; Vitórica-Yrezábal, I. J.; Vieira, B. J. C.; Waerenborgh, J. C.; Valencia, S.; Navalón, S.; Rey, F.; García, H.; Mínguez Espallargas, G. *Chem. Sci.* **2018,** *9,* 2413–2418. doi:10.1039/c7sc04829g
53. Souto, M.; Romero, J.; Calbo, J.; Vitórica-Yrezábal, I. J.; Zafra, J. L.; Casado, J.; Ortí, E.; Walsh, A.; Mínguez Espallargas, G. *J. Am. Chem. Soc.* **2018,** *140,* 10562–10569. doi:10.1021/jacs.8b05890
54. Vicent-Morales, M.; Vitórica-Yrezábal, I. J.; Souto, M.; Mínguez Espallargas, G. *CrystEngComm* **2019,** *21,* 3031–3035. doi:10.1039/c9ce00233b
55. Chae, H. K.; Siberio-Pérez, D. Y.; Kim, J.; Go, Y.; Eddaoudi, M.; Matzger, A. J.; O'Keeffe, M.; Yaghi, O. M. *Nature* **2004,** *427,* 523–527. doi:10.1038/nature02311

56. Li, H.; Hill, M. R.; Huang, R.; Doblin, C.; Lim, S.; Hill, A. J.; Babarao, R.; Falcaro, P. *Chem. Commun.* **2016,** *52,* 5973–5976. doi:10.1039/c6cc01620k
57. Blum, V.; Gehrke, R.; Hanke, F.; Havu, P.; Havu, V.; Ren, X.; Reuter, K.; Scheffler, M. *Comput. Phys. Commun.* **2009,** *180,* 2175–2196. doi:10.1016/j.cpc.2009.06.022
58. Perdew, J. P.; Ruzsinszky, A.; Csonka, G. I.; Vydrov, O. A.; Scuseria, G. E.; Constantin, L. A.; Zhou, X.; Burke, K. *Phys. Rev. Lett.* **2008,** *100,* 136406. doi:10.1103/physrevlett.100.136406
59. Tkatchenko, A.; Scheffler, M. *Phys. Rev. Lett.* **2009,** *102,* 073005. doi:10.1103/physrevlett.102.073005
60. Heyd, J.; Scuseria, G. E.; Ernzerhof, M. *J. Chem. Phys.* **2003,** *118,* 8207–8215. doi:10.1063/1.1564060
61. Butler, K. T.; Hendon, C. H.; Walsh, A. *J. Am. Chem. Soc.* **2014,** *136,* 2703–2706. doi:10.1021/ja4110073
62. Momma, K.; Izumi, F. *J. Appl. Crystallogr.* **2011,** *44,* 1272–1276. doi:10.1107/s0021889811038970
63. Johnson, E. R.; Keinan, S.; Mori-Sanchez, P.; Contreras-Garcia, J.; Cohen, A. J.; Yang, W. *J. Am. Chem. Soc.* **2010,** *132,* 6498–6506. doi:10.1021/ja100936w
64. Contreras-García, J.; Johnson, E. R.; Keinan, S.; Chaudret, R.; Piquemal, J.-P.; Beratan, D. N.; Yang, W. *J. Chem. Theory Comput.* **2011,** *7,* 625–632. doi:10.1021/ct100641a
65. Humphrey, W.; Dalke, A.; Schulten, K. *J. Mol. Graphics* **1996,** *14,* 33–38. doi:10.1016/0263-7855(96)00018-5
66. *Gaussian 16,* Revision A.03; Gaussian, Inc.: Wallingford CT, USA, 2016.
67. Becke, A. D. *J. Chem. Phys.* **1993,** *98,* 5648–5652. doi:10.1063/1.464913
68. Grimme, S.; Ehrlich, S.; Goerigk, L. *J. Comput. Chem.* **2011,** *32,* 1456–1465. doi:10.1002/jcc.21759
69. Boys, S. F.; Bernardi, F. *Mol. Phys.* **1970,** *19,* 553–566. doi:10.1080/00268977000101561
70. Yanai, T.; Tew, D. P.; Handy, N. C. *Chem. Phys. Lett.* **2004,** *393,* 51–57. doi:10.1016/j.cplett.2004.06.011
71. Weinhold, F.; Carpenter, J. E. The Natural Bond Orbital Lewis Structure Concept for Molecules, Radicals and Radical Ions. In *The Structure of Small Molecules and Ions;* Naaman, R.; Vager, Z., Eds.; Springer: Boston, MA, USA, 1988; pp 227–236. doi:10.1007/978-1-4684-7424-4_24
72. Chemcraft - graphical software for visualization of quantum chemistry computations. https://www.chemcraftprog.com (accessed June 27, 2019).

License and Terms

This is an Open Access article under the terms of the Creative Commons Attribution License (http://creativecommons.org/licenses/by/4.0). Please note that the reuse, redistribution and reproduction in particular requires that the authors and source are credited.

The license is subject to the *Beilstein Journal of Nanotechnology* terms and conditions: (https://www.beilstein-journals.org/bjnano)

The definitive version of this article is the electronic one which can be found at:
doi:10.3762/bjnano.10.183

BEILSTEIN JOURNAL OF NANOTECHNOLOGY

The influence of porosity on nanoparticle formation in hierarchical aluminophosphates

Matthew E. Potter*[1], Lauren N. Riley[1], Alice E. Oakley[1], Panashe M. Mhembere[1], June Callison[2,3] and Robert Raja*[1]

Letter

Open Access

Address:
[1]Department of Chemistry, University of Southampton, Highfield Campus, Highfield, Southampton, SO17 1BJ, UK, [2]UK Catalysis Hub, Research Complex at Harwell, Rutherford Appleton Labs, Harwell Campus, OX11 0FA, UK and [3]Department of Chemistry, University College London, 20 Gordon Street, London, WC1H 0AJ, UK

Email:
Matthew E. Potter* - m.e.potter@soton.ac.uk; Robert Raja* - R.Raja@soton.ac.uk

* Corresponding author

Keywords:
aluminophosphate; catalysis; hierarchical catalysts; nanoparticles; porosity

Beilstein J. Nanotechnol. **2019,** *10,* 1952–1957.
doi:10.3762/bjnano.10.191

Received: 31 May 2019
Accepted: 11 September 2019
Published: 25 September 2019

This article is part of the thematic issue "New directions for nanoporous materials".

Guest Editor: C. T. Yavuz

© 2019 Potter et al.; licensee Beilstein-Institut.
License and terms: see end of document.

Abstract

In this work we explore the deposition of gold onto a silicoaluminophosphate, using a variety of known nanoparticle deposition techniques. By comparing the gold particles deposited on a traditional microporous aluminophosphate, with an analogous hierarchical species, containing both micropores and mesopores, we explore the influence of this dual porosity on nanoparticle deposition. We show that the presence of mesopores has limited influence on the nanoparticle properties, but allows the system to maintain porosity after nanoparticle deposition. This will aid diffusion of reagents through the system, allowing continued access to the active sites in hierarchical systems, which offers significant potential in catalytic oxidation/reduction reactions.

Findings

The controlled synthetic design of metallic nanoparticles has generated significant interest in recent decades due to their implementation in a range of fields, including medicine [1], optics [2] and catalysis [3]. Given the wide range of controllable properties, such as size, shape and charge, nanoparticle design is non-trivial, as specific procedures are constantly being developed to promote targeted features and behaviours [4]. Commonly, in catalysis nanoparticles are immobilised onto a solid support, preventing aggregation, leading to increased catalyst lifetime and performance [5]. Yet, immobilisation further complicates nanoparticle design by introducing surface–nanoparticle interactions, which have been shown to have a significant influence on the catalytic efficacy [6]. Commonly, the supports used are porous, which allows the nanoparticle to be

deposited, and yet sufficiently isolated from other particles, to hinder aggregation. Of the wide range of supports utilised in the literature, micro- and meso-porous species are the most common [7-10]. Microporous materials can achieve high levels of control in catalytic reactions, resulting in targeted product selectivity and hence are, in principle, excellent hosts for metal nanoparticles [11]. Similarly, zeotype materials such as zeolites and aluminophosphates (AlPOs) also possess a wide range of secondary functionalities that could synergise with the nanoparticles in a catalytic reaction [12]. However, due to the limited pore aperture and channels of these systems, even sub-nanometre particles can block the framework and hinder activity, thereby preventing reagents from accessing the internal active sites. In contrast, mesoporous species (pores greater than 2 nm) maintain a large portion of their porosity when hosting metal nanoparticles, although they lack the more subtle ability to control the space around the active site [13]. In our previous work we have shown that inclusion of a micellular agent, i.e., dimethyloctadecyl[3-(trimethoxysilyl)propyl]ammonium chloride (DMOD) in an AlPO synthesis, alongside a microporous template, allows silanol-lined mesopores to form simultaneously with the microporous network, yielding a hierarchically porous (HP) system [14]. In this work, we utilise both a HP silicoaluminophosphate (SAPO) system and a traditional microporous SAPO-5 species, to demonstrate the advantages of hierarchical systems for nanoparticle deposition. We selected SAPO-5 as our basic framework, as the AlPO-5 synthesis is robust and forms one of the largest AlPO frameworks (pore size 7.3 Å), which will aid nanoparticle deposition and maintain porosity. Specifically, we compare three known methods for nanoparticle preparation, incipient wetness (IW), wet impregnation (WI) and ammonia evaporation (AE), on the typical microporous (MP-SAPO-5) and corresponding hierarchically porous system (HP-SAPO-5) [15,16].

MP-SAPO-5 was synthesised according to our previous work [17], giving the expected phase-pure, crystalline, microporous AlPO-5 framework (Figure 1A and Figures S1–S3 and Table S2, Supporting Information File 1). Modifying the synthesis procedure by adding a small quantity of DMOD (Table S1, Supporting Information File 1) into the hydrothermal gel (HP-SAPO-5) preserved the phase purity, as only AlPO-5 features are present (Figure S1, Supporting Information File 1). Nitrogen physisorption measurements show that while the type-I isotherm of MP-SAPO-5 strongly indicates microporosity, HP-SAPO-5 has a type-IV isotherm, indicating the hierarchical nature of the sample (Figure S2, Supporting Information File 1), but with a disordered mesoporous region. This is typical of hierarchical materials prepared in this manner [12,14] as they contain a broad range of mesopore sizes. Subsequent pore-distribution plots show no textural features for MP-SAPO-5 in the region of 20–350 Å, but HP-SAPO-5 shows a discerning hysteresis, indicating mesopores which are 60 Å in size (Figure S3, Supporting Information File 1). This is also highlighted as both systems possess similar micropore pore volumes, though HP-SAPO-5 has a much larger mesopore pore volume. The particles of HP-SAPO-5 were notably less crystalline than MP-SAPO-5 (Figure 1). HP-SAPO-5 showed crystalline features with smaller crystalline particles aggregating, forming part of a platelet morphology. The features of HP-SAPO-5 are attributed to the DMOD used in the synthesis. DMOD is believed to modify the crystallisation rate, which allows mesopores to form. In doing so, it also increases the disorder in the system, leading to agglomeration and different crystalline phases. Overall, we concluded that bare HP-SAPO-5 and MP-SAPO-5 systems were successfully synthesised. They were then used as supports for gold deposition in order to explore the influence that the microporous and hierarchical systems had on the nanoparticles characteristics.

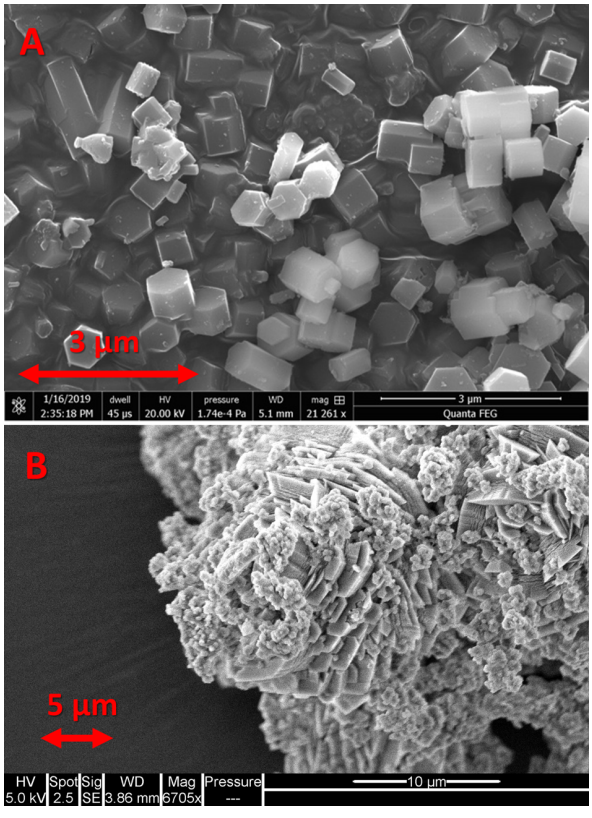


Figure 1: SEM images of microporous MP-SAPO-5 (A) and hierarchical HP-SAPO-5 (B).

All three deposition methods (IW, WI and AE) were carried out on both HP-SAPO-5 and MP-SAPO-5 with an intended theoretical loading of 1 wt % Au. Metal analysis on the deposited MP-SAPO-5 (Table S3, Supporting Information File 1) shows

that the gold loadings vary significantly depending on the immobilisation strategy used, with IW being the most effective (0.66 wt % Au) and WI being the least (0.10 wt % Au). Likely the minimal amount of solvent used in the IW method increases support–metal interactions leading to more rapid deposition. The minimal amount of solvent will also be readily adsorbed into the internal pores of the material by capillary action, encouraging the metal to deposit on the micropores and mesopores and not just on the external surface. In contrast, the excess solvent used in WI will promote deposition primarily on the external surface. AE results in a reasonable deposition efficiency (0.49 wt % Au). Likely the evaporation stage of this process also encourages limited capillary action, similar to IW. Excellent agreement is seen between analogous MP-SAPO-5 and HP-SAPO-5 systems (Table S3, Supporting Information File 1), suggesting that the inclusion of silanol-lined mesopores neither encourages nor hinders nanoparticle deposition.

Following nanoparticle deposition, all samples maintained a phase-pure AlPO-5 framework, with the powder XRD patterns showing no significant variation in crystallinity or signal width (Figure 2 and Figure S4 and Figure S5, Supporting Information File 1). Nanoparticle deposition was found to greatly reduce the porosity of both the hierarchical and microporous supports. For MP-SAPO-5 the surface area decreases from 254 m^2/g to just 72 m^2/g, on depositing 0.10 wt % of Au through WI (Figure S6 and Table S4, Supporting Information File 1). This is accompanied by a significant decrease in pore volume (Table S4, Supporting Information File 1). Given that the framework integrity is maintained (Figure S4 and Figure S5, Supporting Information File 1), the decrease in porosity suggests that the 1D channels are blocked, restricting access to the internal micropores. As pore mouths are known to produce high-energy defect sites [18], they are more likely to encourage nanoparticle deposition, thus blocking the AlPO-5 channels. The IW and AE methods decrease the surface area to a greater extent due to increased Au deposition. The surface area follows a similar trend for HP-SAPO-5, with bare support > WI > AE > IW, again in agreement with the Au loadings (Figure 2B, Tables S3 and Table S4, Supporting Information File 1). Notably, a higher proportion of porosity is maintained in the hierarchical systems, where equivalent loadings of gold give surface areas above 110 m^2/g. The surface areas for the Au-doped MP systems were difficult to estimate due to a loss of data at the very lowest pressures. However, the measurements here provide a reasonable estimate (Table S4, Supporting Information File 1). Further qualitative comparison of the isotherms for the Au-doped MP and HP at low pressure confirms the significantly lower surface area in the MP systems. The total pore volume follows a similar trend, with higher Au loadings prompting lower pore volumes. However, for the hierarchical system a higher proportion of the pore volume still remains on deposition (Table S4, Supporting Information File 1). Thus the introduction of mesopores into the hierarchical system (Figure S7, Supporting Information File 1) helps the systems maintain higher pore volumes and surface areas after nanoparticle inclusion. In principle this should translate into the hierarchical systems being improved catalysts with better diffusion.

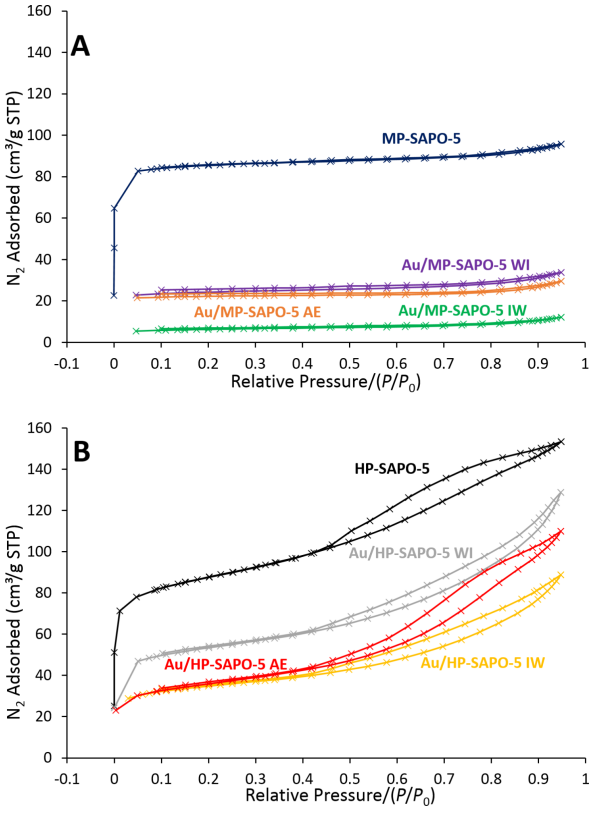


Figure 2: Nitrogen physisorption isotherms of gold-deposited microporous (A) and hierarchical (B) SAPO-5 systems showing that porosity is maintained in hierarchical HP-SAPO-5, but not in microporous MP-SAPO-5.

To probe the influence of the support on the deposited metal, a range of characterisation techniques were used to explore the nature of the Au species. UV–vis measurements show signals attributed to localised surface plasmon resonance for both Au/MP-SAPO-5 (Figure S8, Supporting Information File 1) and Au/HP-SAPO-5 (Figure S9, Supporting Information File 1) systems suggesting that nanoparticles have indeed formed via the IW and AE procedures [19]. However, no signals are seen for WI samples due to the low (0.10 wt %) Au loadings. The peak positions are in good agreement for the Au/MP-SAPO-5 species between the two techniques (IW 514 nm, AE 517 nm), though the hierarchical system shows a greater disparity (IW 511 nm, AE 529 nm). This is likely due to the wider range of

possible deposition sites and environments, though overall the systems are in good agreement. X-ray adsorption spectroscopy (XAS) was used to probe the gold species, but only subtle variations between the systems was observed (Figure 3 and Figures S10–S15, Supporting Information File 1). There was good agreement with the Au foil, suggesting the gold has been successfully reduced to metallic gold particles. The Au/MP-SAPO-5 systems show a lower-energy X-ray absorption near edge structure (XANES), suggesting a higher average oxidation state ($Au^{\delta+}$, Figure S11, Supporting Information File 1) than the Au foil (Au^0) [20]. In all cases the data was satisfactorily fit with a single Au–Au path, at a bond distance of 2.85–2.86 Å (Figure 3 and Table 1). The Au coordination number for all Au/SAPO-5 systems was found to be lower than the theoretical value of 12 for bulk Au foil, suggesting the formation of non-bulk Au systems. In both systems the coordination number was found to vary as AE < IW < WI, indicating AE produces smaller sized nanoparticles [21], despite WI having significantly lower Au loading. This again emphasises the influence of synthesis protocols on active site design.

X-ray photoelectron spectroscopy (XPS) data (Figure 4) was in good agreement with the XAS data, as Au/HP-SAPO-5 IW and Au/HP-SAPO-5 AE systems were exclusively fit with Au^0 features (Figure 4B). However, the corresponding microporous systems required additional Au^1 features to be accurately fit, in agreement with the $Au^{\delta+}$ species observed from XANES (Figure 4A). As XPS has a limited penetration depth, it will accentuate surface species, which are more likely to contain Au^1 species, over the bulk [22]. In both cases the weak signal from the low loading of the WI systems makes fitting infeasible. These measurements confirm that the different porosity of the two systems has only a subtle influence on the nanoparticle environment and coordination. A potential cause of this being the lack of porosity in the Au/MP-SAPO-5 species, hindering the complete reduction of the Au species, during the activation (calcination/reduction) process.

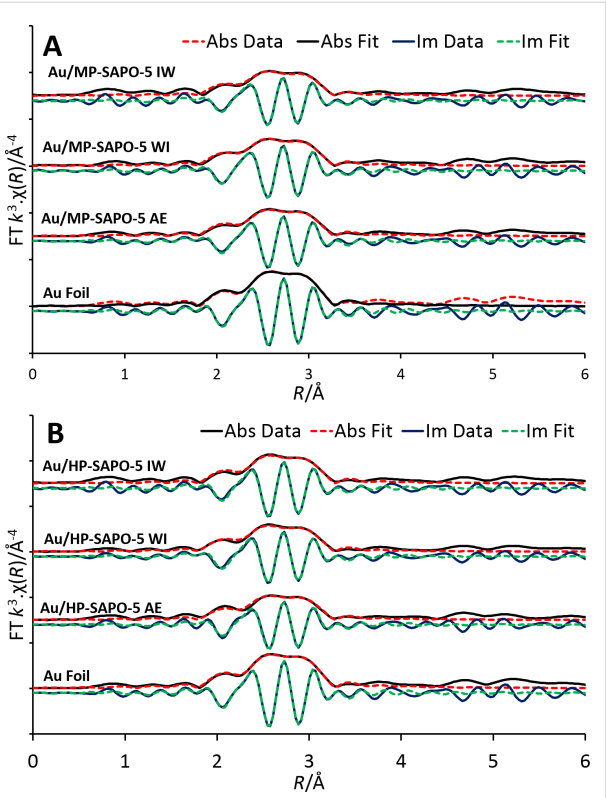


Figure 3: The magnitude and imaginary component of the k^3-weighted Fourier transform for the XAS data of the Au-deposited microporous MP-SAPO-5 (A) and hierarchical HP-SAPO-5 (B) compared to the Au foil. Associated scattering paths, with a single Au–Au feature are included.

We have thus shown that pore blockage can be minimised by immobilising metal nanoparticles onto hierarchical systems, allowing tailored zeotype catalysts to act as hosts through the

Table 1: XAS fitting paths of Au-doped SAPO systems and Au foil.[a]

sample	abs–sc	*N*	*R*/Å	$2\sigma^2$/Å^2	R_{factor}
Au/MP-SAPO-5 IW	Au–Au	10.0 (5)	2.849 (5)	0.0088 (5)	0.019
Au/MP-SAPO-5 WI	Au–Au	11.2 (3)	2.850 (3)	0.0089 (4)	0.006
Au/MP-SAPO-5 AE	Au–Au	10.1 (3)	2.852 (3)	0.0083 (3)	0.007
Au/HP-SAPO-5 IW	Au–Au	10.7 (4)	2.855 (5)	0.0082 (4)	0.015
Au/HP-SAPO-5 WI	Au–Au	10.8 (4)	2.851 (4)	0.0087 (5)	0.012
Au/HP-SAPO-5 AE	Au–Au	9.3 (4)	2.854 (5)	0.0082 (3)	0.020
Au foil	Au–Au	12 (fixed)	2.857 (2)	0.0077 (1)	0.004

[a]Fitting parameters: S_0^2 value of 0.826, determined by Au foil standard; fit range 3.0 < *k* < 12.3 and 1.5 < *R* < 3.5, number of independent points = 11.7, abs–sc = absorbing atom–scattering atom.

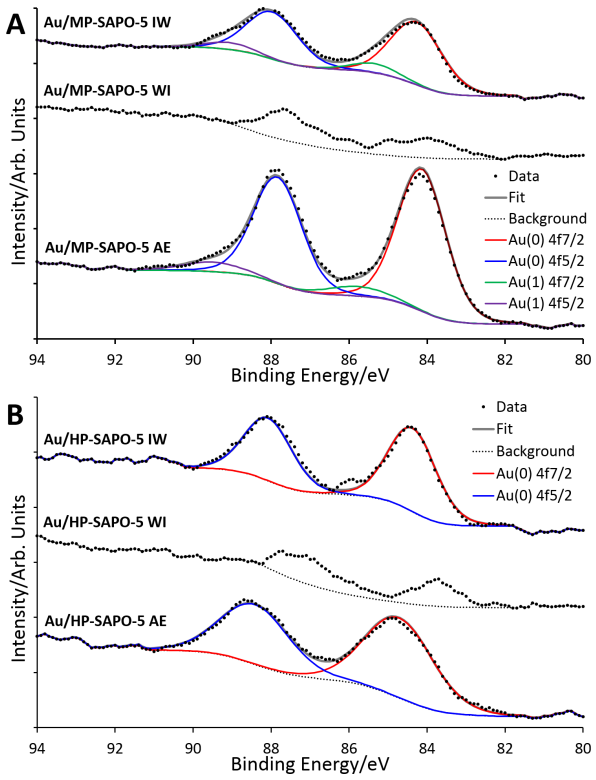


Figure 4: Stacked XPS data for Au-doped microporous MP-SAPO-5 (A) and hierarchical HP-SAPO-5 (B) showing the oxidation states present in the samples.

inclusion of mesopores, with their inherent porosity aiding nanoparticle reduction. Such materials have potential in catalytic oxidations/reductions, with Au/HP-SAPO-5 IW yielding a turn over number (TON) of 35 (Table S5, Supporting Information File 1) for the catalytic oxidation of toluene (preliminary findings). These materials offer significant potential as catalysts in their own right for C–H activation, but also as nanoparticle hosts. The dual porosity opens up the possibility of selectively isolating distinct active sites in specific-sized pores, towards intelligently designed bifunctional and tandem catalysts.

Supporting Information

Supporting Information File 1

Additional experimental data.
[https://www.beilstein-journals.org/bjnano/content/supplementary/2190-4286-10-191-S1.pdf]

Acknowledgements

Panashe Mhembere acknowledges AdvanSix and Honeywell LLC for financial support. Dr. Matthew Cooper and the Geochemistry group at the National Oceanography Centre, University of Southampton are thanked for their help performing and analysing the ICP-MS data. The UK Catalysis Hub is kindly thanked for resources and support provided via our membership of the UK Catalysis Hub Consortium and funded by EPSRC grant: EP/R026815/1. The authors wish to acknowledge the Diamond Light Source and the UK Catalysis Hub for provision of beamtime (proposal number SP19850-2). Dr. Mark Isaacs and HarwellXPS are thanked for their assistance collecting the XPS data for this work.

ORCID® iDs

Matthew E. Potter - https://orcid.org/0000-0001-9849-3306
Alice E. Oakley - https://orcid.org/0000-0002-5489-9424
Panashe M. Mhembere - https://orcid.org/0000-0002-1219-8486
June Callison - https://orcid.org/0000-0003-4506-1862
Robert Raja - https://orcid.org/0000-0002-4161-7053

Preprint

A non-peer-reviewed version of this article has been previously published as a preprint doi:10.3762/bxiv.2019.35.v1

References

1. Lohse, S. E.; Murphy, C. J. *J. Am. Chem. Soc.* **2012,** *134,* 15607–15620. doi:10.1021/ja307589n
2. Lal, S.; Link, S.; Halas, N. J. *Nat. Photonics* **2007,** *1,* 641–648. doi:10.1038/nphoton.2007.223
3. Prati, L.; Villa, A. *Acc. Chem. Res.* **2014,** *47,* 855–863. doi:10.1021/ar400170j
4. Rogers, S. M.; Catlow, C. R. A.; Chan-Thaw, C. E.; Gianolio, D.; Gibson, E. K.; Gould, A. L.; Jian, N.; Logsdail, A. J.; Palmer, R. E.; Prati, L.; Dimitratos, N.; Villa, A.; Wells, P. P. *ACS Catal.* **2015,** *5,* 4377–4384. doi:10.1021/acscatal.5b00754
5. Dimitratos, N.; Lopez-Sanchez, J. A.; Hutchings, G. J. *Chem. Sci.* **2012,** *3,* 20–44. doi:10.1039/c1sc00524c
6. Prieto, G.; Zečević, J.; Friedrich, H.; de Jong, K. P.; de Jongh, P. E. *Nat. Mater.* **2013,** *12,* 34–39. doi:10.1038/nmat3471
7. Zhu, Q.-L.; Li, J.; Xu, Q. *J. Am. Chem. Soc.* **2013,** *135,* 10210–10213. doi:10.1021/ja403330m
8. Farrusseng, D.; Tuel, A. *New J. Chem.* **2016,** *40,* 3933–3949. doi:10.1039/c5nj02608c
9. Cruz, P.; Pérez, Y.; del Hierro, I.; Fajardo, M. *Microporous Mesoporous Mater.* **2016,** *220,* 136–147. doi:10.1016/j.micromeso.2015.08.029
10. Chen, Y.; Zhu, Q.-L.; Tsumori, N.; Xu, Q. *J. Am. Chem. Soc.* **2015,** *137,* 106–109. doi:10.1021/ja511511q
11. O'Malley, A. J.; Parker, S. F.; Chutia, A.; Farrow, M. R.; Silverwood, I. P.; García-Sakai, V.; Catlow, C. R. A. *Chem. Commun.* **2016,** *52,* 2897–2900. doi:10.1039/c5cc08956e
12. Raja, R.; Potter, M. E.; Newland, S. H. *Chem. Commun.* **2014,** *50,* 5940–5957. doi:10.1039/c4cc00834k
13. Potter, M. E.; Purkis, J. M.; Perdjon, M.; Wells, P. P.; Raja, R. *Mol. Syst. Des. Eng.* **2016,** *1,* 335–344. doi:10.1039/c6me00061d
14. Newland, S. H.; Sinkler, W.; Mezza, T.; Bare, S. R.; Carravetta, M.; Haies, I. M.; Levy, A.; Keenan, S.; Raja, R. *ACS Catal.* **2015,** *5,* 6587–6593. doi:10.1021/acscatal.5b01595

15. White, R. J.; Luque, R.; Budarin, V. L.; Clark, J. H.; Macquarrie, D. J. *Chem. Soc. Rev.* **2009,** *38,* 481–494. doi:10.1039/b802654h
16. Zhu, S.; Gao, X.; Zhu, Y.; Fan, W.; Wang, J.; Li, Y. *Catal. Sci. Technol.* **2015,** *5,* 1169–1180. doi:10.1039/c4cy01148a
17. Potter, M. E.; Kezina, J.; Bounds, R.; Carravetta, M.; Mezza, T. M.; Raja, R. *Catal. Sci. Technol.* **2018,** *8,* 5155–5164. doi:10.1039/c8cy01370e
18. Wei, F.-F.; Cui, Z.-M.; Meng, X.-J.; Cao, C.-Y.; Xiao, F.-S.; Song, W.-G. *ACS Catal.* **2014,** *4,* 529–534. doi:10.1021/cs400855p
19. Mori, K.; Verma, P.; Hayashi, R.; Fuku, K.; Yamashita, H. *Chem. – Eur. J.* **2015,** *21,* 11885–11893. doi:10.1002/chem.201501361
20. Malta, G.; Kondrat, S. A.; Freakley, S. J.; Davies, C. J.; Lu, L.; Dawson, S.; Thetford, A.; Gibson, E. K.; Morgan, D. J.; Jones, W.; Wells, P. P.; Johnston, P.; Catlow, C. R. A.; Kiely, C. J.; Hutchings, G. J. *Science* **2017,** *355,* 1399–1403. doi:10.1126/science.aal3439
21. Beale, A. M.; Weckhuysen, B. M. *Phys. Chem. Chem. Phys.* **2010,** *12,* 5562–5574. doi:10.1039/b925206a
22. Casaletto, M. P.; Longo, A.; Martorana, A.; Prestianni, A.; Venezia, A. M. *Surf. Interface Anal.* **2006,** *38,* 215–218. doi:10.1002/sia.2180

License and Terms

This is an Open Access article under the terms of the Creative Commons Attribution License (http://creativecommons.org/licenses/by/4.0). Please note that the reuse, redistribution and reproduction in particular requires that the authors and source are credited.

The license is subject to the *Beilstein Journal of Nanotechnology* terms and conditions: (https://www.beilstein-journals.org/bjnano)

The definitive version of this article is the electronic one which can be found at: doi:10.3762/bjnano.10.191

BEILSTEIN JOURNAL OF NANOTECHNOLOGY

Nanostructured and oriented metal–organic framework films enabling extreme surface wetting properties

Andre Mähringer[1,2], Julian M. Rotter[1,2] and Dana D. Medina[*1,2]

Full Research Paper

Open Access

Address:
[1]Department of Chemistry, Ludwig-Maximilians-Universität (LMU), Butenandtstr. 11, 81377 Munich, Germany and [2]Nanosystems Initiative Munich (NIM) and Center for NanoScience (CeNS), Schellingstr. 4, 80799 Munich, Germany

Email:
Dana D. Medina[*] - dana.medina@cup.uni-muenchen.de

* Corresponding author

Keywords:
antifog; antifouling; biomimetic coatings; metal–organic frameworks (MOFs); superhydrophilic; superoleophobic; thin films; vapor-assisted conversion

Beilstein J. Nanotechnol. **2019,** *10,* 1994–2003.
doi:10.3762/bjnano.10.196

Received: 04 July 2019
Accepted: 20 September 2019
Published: 09 October 2019

This article is part of the thematic issue "New directions for nanoporous materials".

Guest Editor: C. T. Yavuz

© 2019 Mähringer et al.; licensee Beilstein-Institut.
License and terms: see end of document.

Abstract

We report on the synthesis of highly oriented and nanostructured metal–organic framework (MOF) films featuring extreme surface wetting properties. The Ni- and Co- derivatives of the metal–catecholate series (M-CAT-1) were synthesized as highly crystalline bulk materials and thin films. Oriented pillar-like nanostructured M-CAT-1 films exhibiting pronounced needle-like morphology on gold substrates were established by incorporating a crystallization promoter into the film synthesis. These nanostructured M-CAT-1 MOF films feature extreme wetting phenomena, specifically superhydrophilic and underwater superoleophobic properties with water and underwater oil-contact angles of 0° and up to 174°, respectively. The self-cleaning capability of the nanostructured, needle-like M-CAT-1 films was illustrated by measuring time-dependent oil droplet rolling-off a tilted surface. The deposition of the nanostructured Ni-CAT-1 film on a large glass substrate allowed for the realization of an efficient, transparent, antifog coating, enabling a clear view even at extreme temperature gaps up to ≈120 °C. This work illustrates the strong link between MOF film morphology and surface properties based on these framework materials.

Introduction

Over millions of years, plants and animals have evolved a spectrum of surface designs enabling specific wetting properties tailored for their survival in extreme conditions [1-4]. In plants, the unique surface architecture of the lotus leaf enables superhydrophobic and self-cleaning properties for sustaining efficient photosynthesis, even in polluted environments [5-7]. In the realm of animals, mosquitos utilize an antifog coating covering their eyes for clear vision in high humidity regions [8]. The fogstand beetles employ an antifog coating for enhancing water vapor harvesting abilities in dry climates [9]. In marine

life, fish protect themselves from oil-polluted environments or avoid biofouling due to oil-repellent designs and self-cleaning capabilities of their skin [10-12]. These intriguing superhydrophilic or superoleophobic surface characteristics are obtained by the combination of a precise chemical composition and hierarchical microstructuring of the surface [13-16]. Nowadays, modern surface technologies such as antifog or antifouling, oil-repellant coatings, self-cleaning surfaces and water-harvesting systems are inspired by nature's designs [17-26]. The synthesis of artificial superhydrophilic surfaces can be achieved by a variety of routes, for example, sol–gel synthesis, electrochemical deposition, anodization, electrochemical polymerization, electrospinning, plasma treatment, chemical or hydrothermal methods, vapor deposition, layer-by-layer assembly or laser ablation [19,27-39]. However, the development of a straightforward and versatile bottom-up synthesis scheme enabling tunable surface morphologies for controlled wetting properties is still challenging and highly desired.

Metal–organic frameworks (MOFs) are porous, crystalline materials featuring a great structural and chemical diversity [40-45]. Thereby, they are attractive synthesis targets for a large variety of applications, including gas storage and separation, chemical sensing, thermoelectrics, capacitors, transistors or photovoltaics [46-52]. Due to their exceptional variety of structural properties and functions, MOFs are intriguing candidates for the design and synthesis of coatings combining a superhydrophilic, superhydrophobic, superoleophilic or superoleophobic character with desired features such as light filtering, hosting cavities, electrical conductivity, etc. In the literature, the synthesis procedures of MOF powders with encoded wetting properties have been reported [53-60]. Typically, the desired wetting properties in MOFs were chemically induced by a post-synthesis modification or by including building blocks decorated with hydrocarbon side chains [58,61-64]. Very recently, a copper mesh decorated with hybrid $Cu(OH)_2$/MOF-nanobrushes showed underwater contact angles suggesting superoleophobic properties [65]. However, the use of well-defined MOF films for encoding on-surface wetting properties is yet to be revealed.

Here we report the synthesis of highly oriented, nanostructured MOF films that mimic architectures observed in nature, resulting in highly unusual, extreme surface wetting properties. For the synthesis, the Ni- and Co-derivatives of the metal–catecholate series (M-CAT-1) were selected [66]. First, these M-CAT-1 derivatives were synthesized as highly crystalline bulk materials. The M-CAT-1 surface energy was estimated by contact angle measurements using pellet samples exposing nonoriented crystallites on the surface. Next, oriented and compact Co- and Ni-CAT-1 films were deposited on gold surfaces by vapor-assisted conversion (VAC). These films showed enhanced hydrophilic and underwater oleophobic properties compared to the corresponding pressed pellet samples.

Oriented, nanostructured M-CAT-1 films exhibiting a pronounced needle-like morphology on gold substrates were obtained by adding a crystallization promotor into the VAC precursor solution. These nanostructured M-CAT-1 MOF films feature extreme wetting phenomena, specifically superhydrophilic and underwater superoleophobic properties with water and underwater oil-contact angles of 0° and up to 174°, respectively. The self-cleaning capability of the nanostructured, needle-like Ni- and Co-CAT-1 films was illustrated by measuring time-dependent oil droplet rolling-off a tilted surface. The deposition of the nanostructured Ni-CAT-1 film on large glass substrates allowed for the realization of an efficient antifog coating. These antifog coatings enabled clear vision, even at large temperature differences of up to 120 °C.

Results and Discussion

The M-CAT-1 MOFs are crystalline, microporous structures obtained by a solvothermal reaction of metal precursors and the organic building block 2,3,6,7,10,11-hexahydroxytriphenylene (HHTP) as a dark precipitate. The M-CAT-1 crystallites exhibit a hexagonally faceted, needle-like morphology with crystal cross-sections of 30–40 nm and several micrometers in length (Figure 1). In addition, the M-CAT-1 materials are electroactive featuring electrical conductivity values of up to 10^{-2}–10^{-3} S cm^{-1} for pressed powder pellets and oriented thin films, respectively [67]. However, the wetting properties of these MOFs both as pristine powders and as films have not been explored.

For our study, we focused on Ni- and the Co-CAT-1, since their structure is well-characterized and elucidated by diffraction methods, serving as a good basis for understanding their growth behavior and morphology. To assess the wetting properties of Ni- and Co-CAT-1, we investigated the interaction of the bulk materials pressed as compact pellets with different polar and apolar liquids. For this purpose, we synthesized M-CAT-1 bulk materials following our recently reported solvothermal synthesis procedure (for more details see Figure S3.1, Supporting Information File 1) [67]. Subsequently, the obtained MOF powders were collected, activated under dynamic vacuum and pressed into crystalline pellet samples (1 cm diameter, thickness 500 μm; 100 mg activated MOF, roughness (RMS): 37 nm). Scanning electron microscope (SEM) micrographs reveal densely packed and randomly oriented MOF crystallites throughout the sample (see Figure S3.2, Supporting Information File 1). For the contact angle (CA) measurements at the solid/air interface we chose diiodomethane as a nonpolar

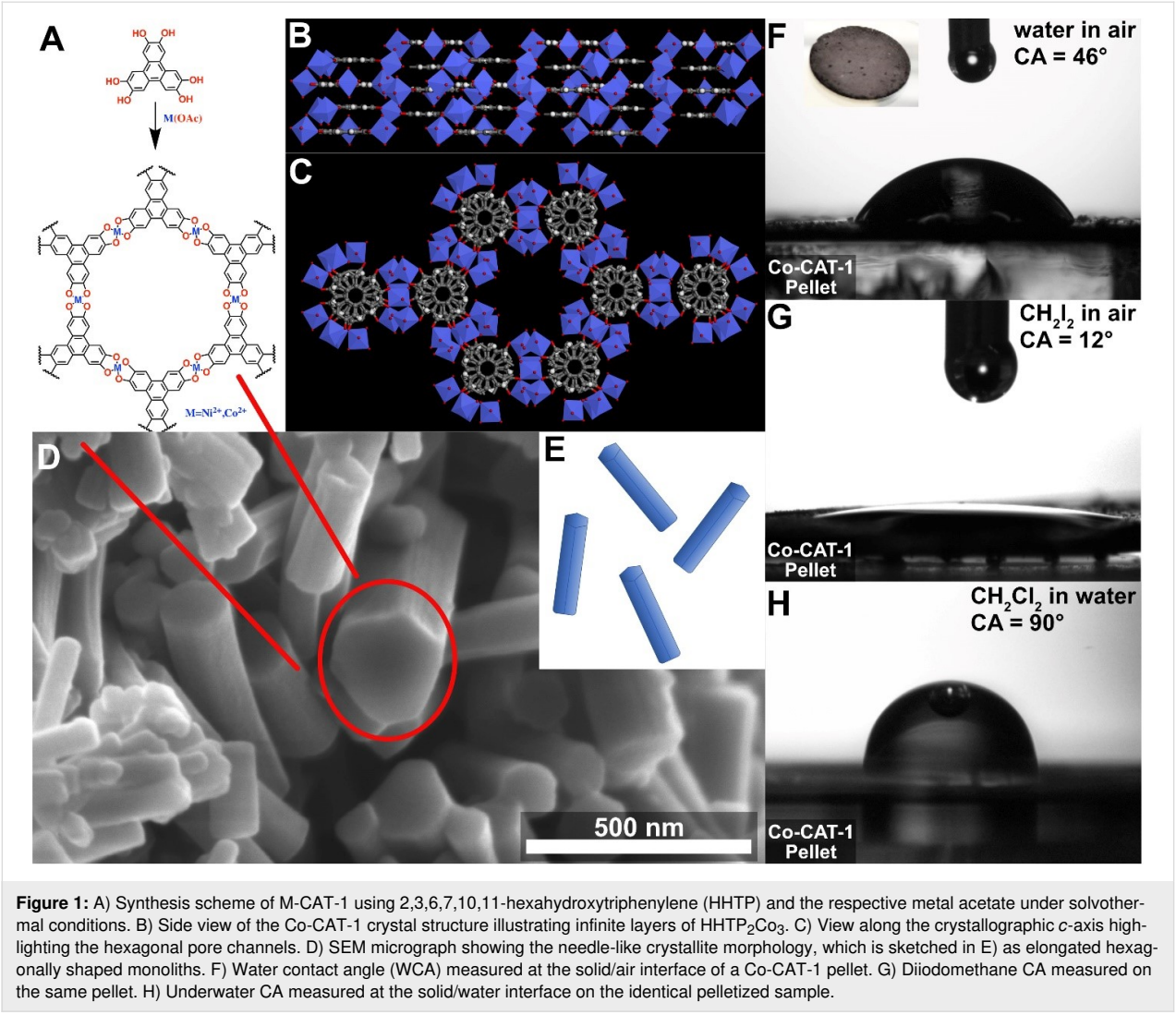


Figure 1: A) Synthesis scheme of M-CAT-1 using 2,3,6,7,10,11-hexahydroxytriphenylene (HHTP) and the respective metal acetate under solvothermal conditions. B) Side view of the Co-CAT-1 crystal structure illustrating infinite layers of $HHTP_2Co_3$. C) View along the crystallographic *c*-axis highlighting the hexagonal pore channels. D) SEM micrograph showing the needle-like crystallite morphology, which is sketched in E) as elongated hexagonally shaped monoliths. F) Water contact angle (WCA) measured at the solid/air interface of a Co-CAT-1 pellet. G) Diiodomethane CA measured on the same pellet. H) Underwater CA measured at the solid/water interface on the identical pelletized sample.

organic liquid, which exhibits a relatively high surface tension, and water as a polar liquid (see Figure 1). CA measurements on M-CAT-1 pellets reveal shallow angles of about 12° for diiodomethane and WCA values of about 46°. This illustrates that in air the M-CAT-1 materials feature an amphiphilic character, namely hydrophilic and superolephilic properties. This amphiphilic wetting property can be attributed to the high surface energy of the MOF materials. To estimate the corresponding MOF surface energy, we applied Fowker's theory, where the observed CA between a liquid and a solid is related to the sum of a polar and dispersive components of the liquid's surface tension [68]. Utilizing the measured CAs of diiodomethane exhibiting solely a dispersive component and water, having a dispersive and polar components, enabled the calculation of the overall surface energy for Ni- and Co-CAT-1 (for detailed discussion see Supporting Information File 1, Table S1). We obtained a surface energy of 64.02 and 62.38 mN/m for the Ni- and Co-CAT-1 pellet samples, respectively, as summarized in Table 1. These values are higher than the surface energy reported for oleophilic polymers which exhibit a surface energy in the range of 20–50 mN/m. However, the estimated MOF surface energy and WCAs are in good agreement with systems such as modified carbonaceous layers, showing values of about 60 mN/m and WCAs of 50° [69]. Superoleophilic wetting properties were also detected for chlorinated oils such as dichloromethane on M-CAT-1 pellets (see Figure S3.3, Supporting Information File 1). This further illustrates the amphiphilic

Table 1: Surface energy (σ_S) and the respective dispersive (σ_S^D) and polar (σ_S^P) components estimated for Ni- and Co-CAT-1 pellet samples.

M-CAT-1	σ_S [mN/m]	σ_S^D [mN/m]	σ_S^P [mN/m]
Ni-CAT-1	64.02	49.69	14.06
Co-CAT-1	62.38	50.30	12.08

nature of the M-CATs, showing hydrophilic as well as superoleophilic behavior towards several different oils. Interestingly, the underwater oil contact angle (OCA) of diiodomethane on these pellets reveals an inverse wetting phenomenon. Under these conditions, the M-CAT-1 materials reject oil and turn oleophobic with an OCA of 90° (Figure 1H).

Constructing nanostructured M-CAT-1 surfaces

According to Wenzel's model, film topography has a strong impact on the wetting properties of a surface [70]. Following this line of thought, we aimed at constructing M-CAT-1 thin films featuring distinct surface morphologies, allowing for the desired surface wetting properties to be achieved. However, on-surface control of MOF film morphology is a challenging task due to the required growth conditions for maintaining key features such as homogeneity, crystallinity and crystal orientation on the surface. In our previous reports, we have demonstrated that the use of a modulator in combination with the choice of a substrate play a crucial role in VAC synthesis and the formation of a crystalline MOF film [71]. In the present study, we introduce the use of a crystallization promoter in the VAC process, solely for inducing distinct film morphology while maintaining crystallinity and crystal orientation on a preselected substrate.

Accordingly, we employed VAC methods for producing both compact and nanostructured M-CAT-1 films (see Figure S5.1, Supporting Information File 1). Briefly, oriented thin films of Ni- and Co-CAT-1 were synthesized on gold substrates by depositing a thin layer of a precursor solution onto a gold substrate. Then, the gold substrate was placed on a glass platform above a solvent bath inside a glass autoclave. Subsequently, the reactor was sealed and placed at 85 °C in a preheated oven. After 12 h of reaction time, the reactor was removed from the oven and allowed to cool down to room temperature. The substrates were recovered, washed and dried under a N_2 stream, revealing a colored film on the gold substrate. These films typically exhibit thickness of about 150 nm, consisting of highly intergrown oriented crystallites (see Figure S5.1, Supporting Information File 1).

Next, nanostructured pillar-like M-CAT-1 films were synthesized by including carboxylic acids, which served as crystallization promotors in the drop-cast precursor solution layer. Specifically, we introduced acetic acid in the Ni-CAT-1 and salicylic acid in the Co-CAT-1 synthesis (see Figure 2A). Top-view SEM images show a homogenous film and a long-range ordered array of pillar-like structures with a cross-section of 20–30 nm and evident gaps between the pillars of about 150 nm for both samples (see Figure 2B,C).

Cross-section SEM micrographs clearly visualize an array of vertically aligned MOF needles on the surface plane. In addition, a uniform film thickness of about 800 nm is observed throughout the cross-section of both Ni- and Co-CAT-1 samples, indicating a self-terminating growth under the employed conditions (Figure 3B and Figure S5.4, Supporting Information File 1). To confirm that the defined nanostructured film is indeed crystalline and the crystallites are well-aligned orthogonal to the surface plane, X-ray grazing incidence wide-angle scattering (GIWAXS) experiments were performed (see Figure 2B,C). GIWAXS analysis of the obtained films confirmed the successful on-surface deposition of crystalline M-CAT-1 materials. The collected out-of-plane reflections at q_y = 3.9 nm^{-1} (100), q_y = 7.1 nm^{-1} (200) and q_y = 9.2 nm^{-1} (210) near q_z = 0 were indexed according to the powder X-ray diffraction pattern of Co-CAT-1. The (004) reflection, referred to as the in-plane reflection, is visible as a diffuse arc at q_z =19 nm^{-1} (for further details see Supporting Information File 1). The latter corresponds to an interlayer distance of 3.3 Å. This points toward the preferential orientation of the M-CAT-1 crystals on the surface, where the crystallographic *c*-axis is positioned normal to the surface plane.

These data show that by employing the VAC synthesis approach in the presence of a specific crystallization promotor, the fabrication of crystalline nanostructured and oriented M-CAT-1 films on gold substrates is feasible. Deviating from these optimal conditions resulted in a poorly crystalline or inhomogeneous film (see Figure S5.10, Supporting Information File 1).

Superhydrophilic and underwater superoleophobic MOF-based surfaces

Following Wenzels' equation [70], an increased surface roughness results in a decreased WCA and in an enhanced OCA. To study the impact of roughness on the wetting properties of the M-CAT-1 films, we performed WCA and underwater OCA measurements for the compact and the nanostructured M-CAT-1 films (see Figure 3 and S5.5, Supporting Information File 1).

Oriented and compact films demonstrated CAs of 32° and 26° for Ni- and Co-CAT-1, respectively, whereas oriented and nanostructured films featured a drastic decrease in the WCA (see Figures S5.5, S5.7, Supporting Information File 1). Strikingly, we observed complete water spreading on the M-CAT-1 films and a WCA of 0° for both films, thus these surfaces can be considered superhydrophilic (Figure 3D and S5.5, Supporting Information File 1). These observed surface properties were further confirmed by measuring the underwater OCA with a droplet of dichloromethane (DCM). The oriented and compact films showed enhanced oleophobic properties with an under-

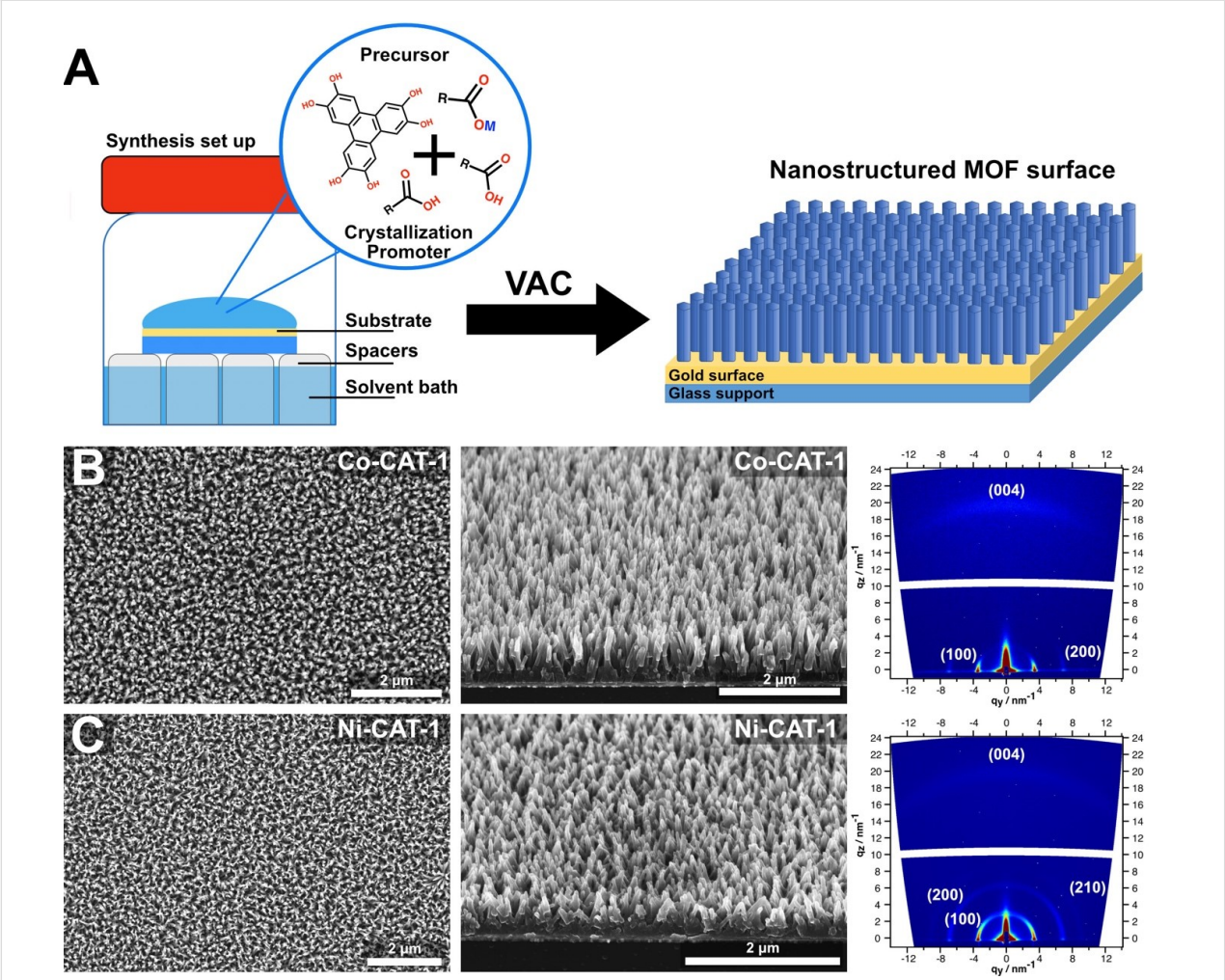


Figure 2: A) A scheme of the vapor-assisted conversion (VAC) set up and the resulting nanostructured films. B) SEM top view, 30° tilted cross-section and the related GIWAXS pattern of the Co-CAT-1 film. C) SEM top view, 30° tilted cross-section momographs and the related GIWAXS pattern of the Ni-CAT-1.

water OCA of about 130° and 133° for Ni-CAT-1 and Co-CAT-1, respectively (see Figure 3 and S5.5, Supporting Information File 1). Remarkably, for the oriented and nanostructured films, we observed a strong increase in the OCA and extreme values of 174° and 173° were determined for Ni-CAT-1 and Co-CAT-1, respectively (see Figure S5.5, Supporting Information File 1). On these films, a nearly perfect oil sphere was formed, which is hardly in contact with the surface (see Figure S5.7, Supporting Information File 1). These surface properties resemble those of surface designs found in nature. For example, referring to marine life, fish scales in air show an amphiphilic behavior due to their high surface energy, but under water they turn superoleophobic, which is of great advantage for protection against hazardous environments, for example, oil-polluted water.

The self-cleaning properties of these extremely oleophobic M-CAT-1 nanostructured surfaces were demonstrated by casting a DCM oil droplet on a marginally tilted substrate (e.g., by 1.4°). Subsequently, the motion of the droplet was recorded by a high-speed camera with 3 frames per second (see Figure 3G and S5.6, Supporting Information File 1). The obtained image series reveals that the droplet crosses the substrate and rolls out of the detection range of the high-speed camera in about 1.3 s. According to the Cassi–Baxter theory, the combination of the very low tilt-angle that is required for the droplet to roll off the substrate and the extreme underwater OCA angle suggests that the DCM sphere is in contact only with the tips of the crystalline needles, whereas the intercrystallite areas only interact with water (Figure S7.1, Supporting Information File 1) [72]. To exclude the contribution of the gold surface to the wetting properties of the MOF films, we carried out control experiments with blank gold substrates giving a WCA of 94° and underwater OCA of 52° (see Figure S4.1, Supporting Information File 1). This confirms that the observed super-

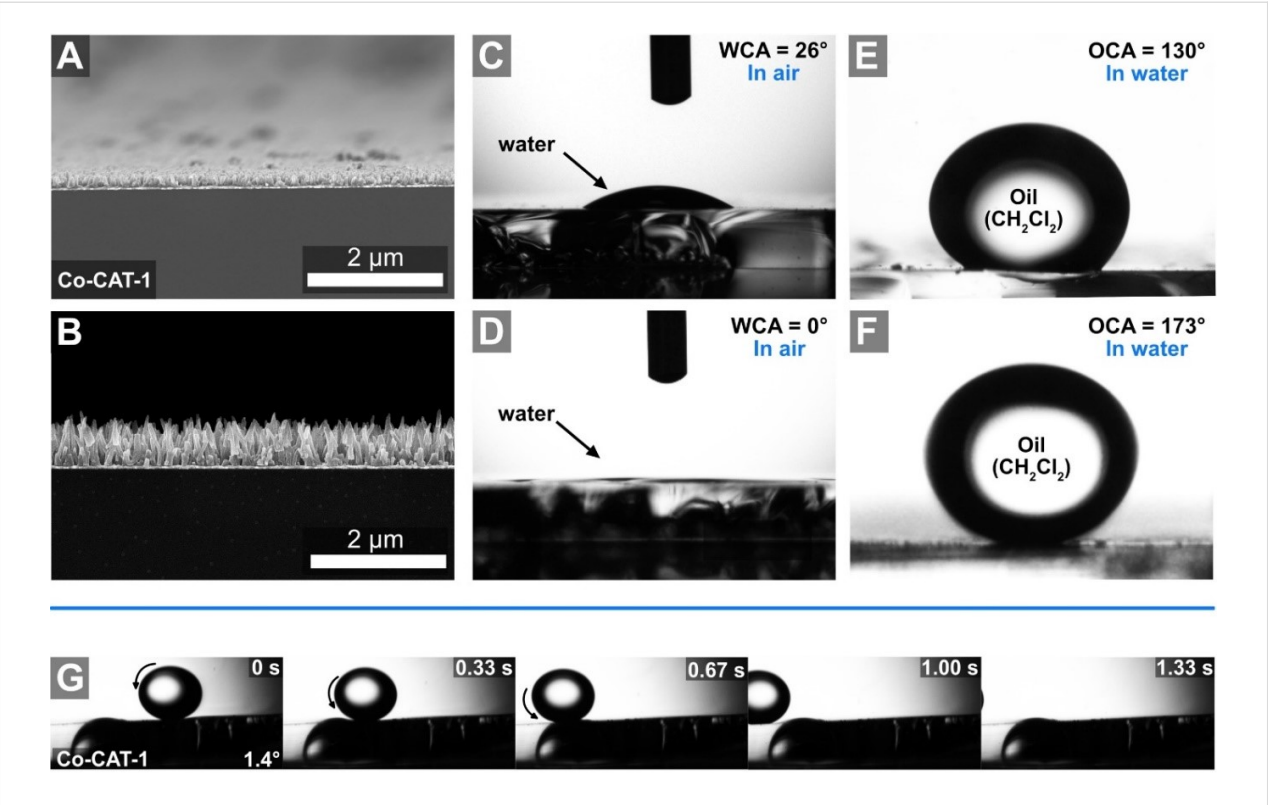


Figure 3: Cross-section SEM micrographs of A) an oriented and compact Co-CAT-1 film and B) an oriented (pillar-like) nanostructured Co-CAT-1 film. WCA of the C) compact (WCA = 26°) and the D) nanostructured (WCA = 0°) films. Underwater OCA (dichloromethane (DCM)) of the E) compact (CA = 130°) and the F) nanostructured films (CA = 173°). G) An image series of a self-cleaning surface experiment (3 frames per second) with DCM as an oil droplet placed on the nanostructured Co-CAT-1 film performed at a substrate tilt angle of 1.4°.

hydrophilic and superoleophobic behavior arises from the MOF film.

To illustrate the stability of the MOF under harsh conditions, the films were subjected to an acidic environment (pH 5, 12 h), a basic environment (pH 9, 12 h), high temperature (150 °C, 12 h), and mechanical impact (sonication in water, 20 min). GIWAXS analysis in addition to WCA and OCA measurements after the respective treatment confirmed that the crystallinity, crystal orientation and extreme wetting properties were preserved (see Figures S8.1, S8.2, Supporting Information File 1).

To establish these MOF films as superoleophobic surfaces applicable to a wide range of oils, we examined the interactions of other high-density oils with the oriented and nanostructured MOF surfaces. For this purpose, we determined the underwater OCA for different chlorinated liquids, such as dichloromethane (DCM), dichloroethane (DCE), chloroform ($CHCl_3$) and chlorobenzene (PhCl). The OCAs were recorded using the exact same described procedure for DCM, and the results are plotted as box and whisker plots in Figure 4. For all the measured oils, superoleophobic behavior was observed with extreme OCAs ranging from 155° (DCE) for Co-CAT-1 to 169° (PhCl) for Ni-CAT-1 films. Specifically, the Ni-CAT-1 film exhibits the following OCAs: 174° (DCM), 162° (DCE), 165° ($CHCl_3$) and 169° (PhCl), whereas the Co-CAT-1 film exhibits 173° (DCM),

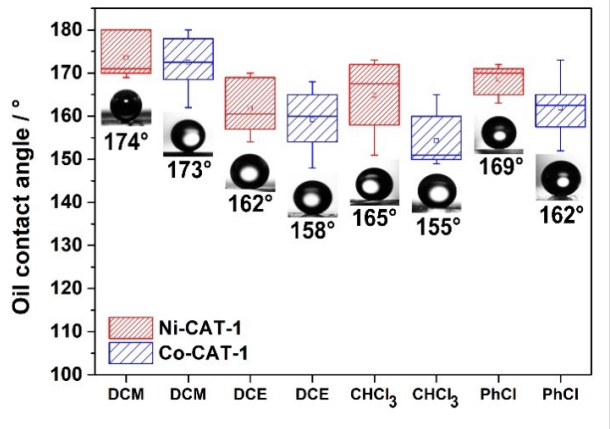


Figure 4: Box and whisker plot of the measured underwater OCAs for the nanostructured Ni-CAT-1 and Co-CAT-1 films. The employed liquids are dichloromethane (DCM), dichloroethane (DCE), chloroform ($CHCl_3$) and chlorobenzene (PhCl). For all the tested liquids,a superoleophobicity is observed with underwater OCAs > 150°.

158° (DCE), 155° ($CHCl_3$) and 162° (PhCl). These results confirm that the MOF films efficiently repel a large variety of oily liquids, hence constituting an intriguing platform for underwater superoleophobic properties.

Since MOFs are crystalline materials featuring crystal facets with distinct surface energies, the orientation of these crystallites on a surface is expected to impact the wetting properties. In the following, we discuss the case of Ni-CAT-1 as a model for the M-CAT-1 series. In the context of crystal orientation on the surface, we analyzed the Ni-CAT-1 WCAs measured for pressed pellet samples and those of oriented and compact films. Interestingly, pressed pellet samples consisting of randomly distributed crystallites on the surface exhibit greater WCAs than oriented films, although the latter shows a slightly increased surface roughness (see Figures S5.2, S5.3, S3.4, S3.5, Supporting Information File 1). We attribute this difference to the different surface character which directly impacts the surface energy, and hence, the wetting properties (see Table S1, Supporting Information File 1). We therefore conclude that the observed wetting properties are due to a combination of two different significant contributions which can be controlled by the VAC process, namely the surface roughness and the crystallite orientation on the substrate.

Antifog coating with MOF films

Water condensation on surfaces is a known phenomenon occurring at the dew point on substrates such as glass, which serves as a favorable nucleation site for water droplets. This process leads to a substantial reduction in the transparency of the glass and the vision though the glass becomes extremely limited. To avoid condensation, modifications of the glass surface with different classes of functional coatings are necessary. Motivated by the superhydrophilic properties obtained by growing nanostructured M-CAT-1 films on gold substrates, we investigated the synthesis of such films as transparent coatings on glass substrates, thereby altering their wetting character towards superhydrophilic properties. Through this approach, a thin water layer decorating the textured MOF surface is expected to form, hindering the nucleation of water droplets on the glass surface. For this purpose, we employed the newly developed methodology for the synthesis of nanostructured Ni-CAT-1 films on gold substrates with a slightly modified synthesis procedure in order to address larger substrate dimensions such as 2.5 cm × 2.5 cm. The resulting MOF films on glass substrates reveal a blue-tinted, yet transparent coating (see Figure 5C,F). A top view SEM micrograph revealed the typical orthogonally aligned needle-like nanostructures on the surface, similar to the M-CAT-1 films grown on gold surfaces. The preferential orientation of the MOF crystals on the glass substrate was further confirmed by GIWAXS measurements (see Figure S5.8, Supporting Information File 1). The WCA measurements showed superhydrophilic properties similar to those observed for gold substrates (Figure 5C). Further control experiments confirmed that the superhydrophilic wetting properties originate from the presence of the nanostructured MOF film. Blank glass substrates showed WCA of 11° and OCA of 81° (see Figure S4.2, Supporting Information File 1). Furthermore, the MOF films endow the glass substrates with light-absorbing properties while maintaining transparency (see Figure S5.9, Supporting Information File 1). In addition, we found that these MOF films are stable in acidic (pH 5, 12 h) and basic conditions and at high temperature (150 °C, 12 h) (see Figure S8.3, Supporting Information File 1).

To test the antifog properties of the Ni-CAT-1 film, a glass vessel containing a reservoir of boiling water (≈100 °C) was placed above an LMU seal, and a non-modified glass substrate was positioned on top of the open vessel (see Figure 5D,F and S6.1, Supporting Information File 1). Within seconds, the seal was no longer visible, obscured by the water droplets generated by the condensation of steam on the glass surface (Figure 5E). In contrast, using a MOF-coated glass substrate, high transparency and clear visibility through the substrate were enabled, and the seal was visible even after longer exposure times (Figure 5F,G). To examine the behavior of the antifog coating under extreme temperature differences, the MOF-modified glass substrates were cooled down to −20 °C and subsequently placed on top of the hot water reservoir. Under all examined conditions, clear vision through the glass was maintained and water vapor nucleation was not observed (see Figure S6.2, Supporting Information File 1). This striking effect is attributed to the formation of a thin water layer on the MOF films which spreads out completely on the surface. This thin water layer is clearly visible by turning the substrate upside down (Figure 5G). This set of experiments establishes the pillar-like nanostructured Ni-CAT-1 films as highly efficient, antifog coatings featuring additional desired properties such as light absorbance. Furthermore, it underlines the power of VAC in enabling controlled bottom-up fabrication of MOF films with well-defined nanoscale morphologies and associated functionality.

Conclusion

In this study, we demonstrated the controlled on-surface synthesis of crystalline, highly oriented and nanostructured M-CAT-1 films by employing a crystallization promoter in a VAC synthesis. First, the free surface energy of M-CAT-1 was calculated for pressed pellet samples, shedding light on the amphiphilic wetting properties (both hydrophilic and oleophilic) of the materials in air. Oriented and compact M-CAT-1 films exhibited enhanced wetting properties where shallower contact angles were deter-mined for water (about 32°) and a large underwater

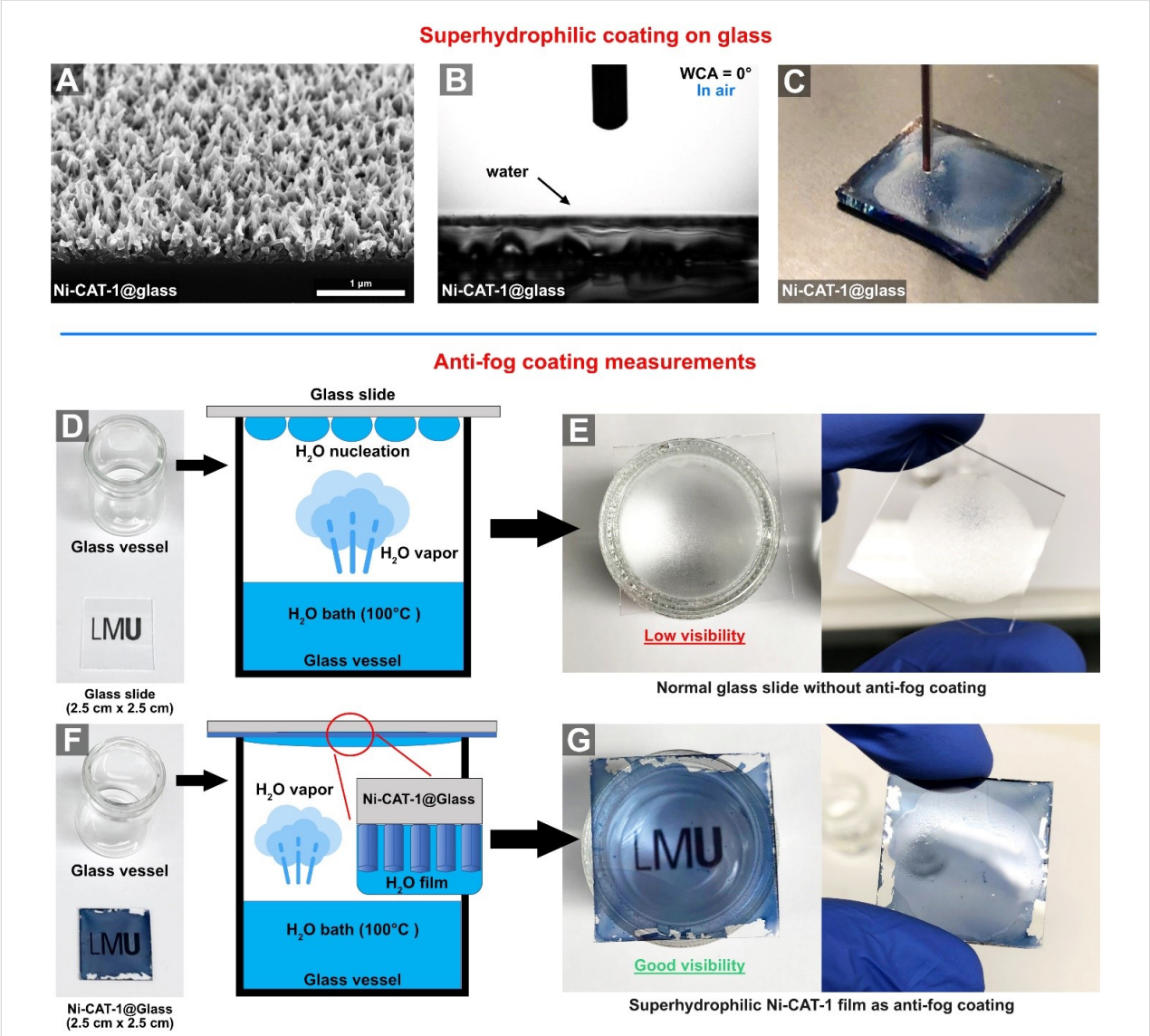


Figure 5: A) A 30° tilted SEM top view micrograph of Ni-CAT-1 film grown on glass. B) WCA on the superhydrophilic and nanostructured Ni-CAT-1 film. C) Macroscopic image of the Ni-CAT-1 on a glass substrate, showing a complete spreading of the water droplet. D) An antifog coating experiment performed with a bare glass slide that is placed above a glass vessel containing a reservoir of hot water at boiling temperature. E) The LMU seal obscured by water condensation on the bare glass. F) An antifog coating experiment performed with a MOF-coated glass above a glass vessel containing a reservoir of hot water at boiling temperature. G) High transparency and visibility through the substrate and a visible LMU seal is demonstrated.

OCA (130°), indicating oleophobic properties. The corresponding oriented and nanostructured M-CAT-1 films exhibited extreme wetting properties with a WCA of 0° and an underwater OCA of 174°, and are thus demonstrated as being superhydrophilic and superoleophobic in water.

The underwater self-cleaning ability of these films was demonstrated by depositing an oil droplet on a substrate tilted at a shallow angle of 1.4°. The effective underwater oil-repelling properties of the M-CAT-1 films were confirmed by employing a variety of different chlorinated oily liquids. Under ambient atmosphere, the water wetting properties of these systems could be drastically altered by changing the film morphology from compact to pillar-like nanostructures. This effect was also transferred onto transparent substrates such as glass, resulting in an efficient, transparent, MOF-based, antifog coating. Hence, we demonstrate that on-surface alteration of the MOF film morphology by versatile solution-based bottom-up methods such as VAC is a powerful tool for realizing the potential of MOFs in surface-based technologies such as oil–water separation systems, antioil coatings, or self-cleaning surfaces. Furthermore, the use of a MOF allows for encoding further desired sur-

face properties such as light absorption and electrical conductivity. This can be valuable for applications such as photo-electrocatalysis water splitting where a high textural surface area, water contact and light absorption are required.

Supporting Information

Supporting Information File 1

Additional experimental details.
[https://www.beilstein-journals.org/bjnano/content/supplementary/2190-4286-10-196-S1.pdf]

Acknowledgements

The authors are grateful for funding from the German Science Foundation (SPP 1928 8481830/92, Excellence Cluster NIM). Moreover, the authors thank the Free State of Bavaria for funding in the context of the Research Network SolTech. The authors thank Dr. Markus Döblinger for transmission electron microscopy experiments. The manuscript was written through contributions from all authors. All authors have given approval to the final version of the manuscript. The Authors declare no competing financial interests.

ORCID® iDs

Dana D. Medina - https://orcid.org/0000-0003-4759-8612

Preprint

A non-peer-reviewed version of this article has been previously published as a preprint https://doi.org/10.26434/chemrxiv.8191265.v2

References

1. Yong, J.; Chen, F.; Yang, Q.; Jiang, Z.; Hou, X. *Adv. Mater. Interfaces* **2018,** *5,* 1701370. doi:10.1002/admi.201701370
2. Yong, J.; Chen, F.; Yang, Q.; Huo, J.; Hou, X. *Chem. Soc. Rev.* **2017,** *46,* 4168–4217. doi:10.1039/c6cs00751a
3. Helbig, R.; Nickerl, J.; Neinhuis, C.; Werner, C. *PLoS One* **2011,** *6,* e25105. doi:10.1371/journal.pone.0025105
4. Hernandez, A.; Brebbia, C. A. *Design and Nature IV: Comparing Design in Nature With Science and Engineering;* WIT Press: Ashurst, 2012.
5. Feng, L.; Zhang, Y.; Xi, J.; Zhu, Y.; Wang, N.; Xia, F.; Jiang, L. *Langmuir* **2008,** *24,* 4114–4119. doi:10.1021/la703821h
6. Neinhuis, C.; Barthlott, W. *Ann. Bot. (Oxford, U. K.)* **1997,** *79,* 667–677. doi:10.1006/anbo.1997.0400
7. Rich, B. B.; Pokroy, B. *Soft Matter* **2018,** *14,* 7782–7792. doi:10.1039/c8sm01115j
8. Gao, X.; Yan, X.; Yao, X.; Xu, L.; Zhang, K.; Zhang, J.; Yang, B.; Jiang, L. *Adv. Mater. (Weinheim, Ger.)* **2007,** *19,* 2213–2217. doi:10.1002/adma.200601946
9. Parker, A. R.; Lawrence, C. R. *Nature* **2001,** *414,* 33–34. doi:10.1038/35102108
10. Waghmare, P. R.; Gunda, N. S. K.; Mitra, S. K. *Sci. Rep.* **2014,** *4,* 7454. doi:10.1038/srep07454
11. Bixler, G. D.; Bhushan, B. *Nanoscale* **2013,** *5,* 7685–7710. doi:10.1039/c3nr01710a
12. Liu, M.; Wang, S.; Wei, Z.; Song, Y.; Jiang, L. *Adv. Mater. (Weinheim, Ger.)* **2009,** *21,* 665–669. doi:10.1002/adma.200801782
13. Bhushan, B.; Jung, Y. C.; Koch, K. *Philos. Trans. R. Soc., A* **2009,** *367,* 1631–1672. doi:10.1098/rsta.2009.0014
14. Feng, L.; Li, S.; Li, Y.; Li, H.; Zhang, L.; Zhai, J.; Song, Y.; Liu, B.; Jiang, L.; Zhu, D. *Adv. Mater. (Weinheim, Ger.)* **2002,** *14,* 1857–1860. doi:10.1002/adma.200290020
15. Darmanin, T.; Guittard, F. *Mater. Today* **2015,** *18,* 273–285. doi:10.1016/j.mattod.2015.01.001
16. Kota, A. K.; Li, Y.; Mabry, J. M.; Tuteja, A. *Adv. Mater. (Weinheim, Ger.)* **2012,** *24,* 5838–5843. doi:10.1002/adma.201202554
17. Wen, L.; Tian, Y.; Jiang, L. *Angew. Chem.* **2015,** *127,* 3448–3462. doi:10.1002/ange.201409911
18. Jiang, L.; Zhao, Y.; Zhai, J. *Angew. Chem., Int. Ed.* **2004,** *43,* 4338–4341. doi:10.1002/anie.200460333
19. Jiang, T.; Guo, Z.; Liu, W. *J. Mater. Chem. A* **2015,** *3,* 1811–1827. doi:10.1039/c4ta05582a
20. Koch, K.; Bhushan, B.; Barthlott, W. *Prog. Mater. Sci.* **2009,** *54,* 137–178. doi:10.1016/j.pmatsci.2008.07.003
21. Liu, X.; Zhou, J.; Xue, Z.; Gao, J.; Meng, J.; Wang, S.; Jiang, L. *Adv. Mater. (Weinheim, Ger.)* **2012,** *24,* 3401–3405. doi:10.1002/adma.201200797
22. Nishimoto, S.; Bhushan, B. *RSC Adv.* **2013,** *3,* 671–690. doi:10.1039/c2ra21260a
23. Xu, L.-P.; Peng, J.; Liu, Y.; Wen, Y.; Zhang, X.; Jiang, L.; Wang, S. *ACS Nano* **2013,** *7,* 5077–5083. doi:10.1021/nn400650f
24. Cai, Y.; Lin, L.; Xue, Z.; Liu, M.; Wang, S.; Jiang, L. *Adv. Funct. Mater.* **2014,** *24,* 809–816. doi:10.1002/adfm.201302034
25. Tahk, D.; Kim, T.-i.; Yoon, H.; Choi, M.; Shin, K.; Suh, K. Y. *Langmuir* **2010,** *26,* 2240–2243. doi:10.1021/la904768e
26. Williams, D. E.; Dolgopolova, E. A.; Pellechia, P. J.; Palukoshka, A.; Wilson, T. J.; Tan, R.; Maier, J. M.; Greytak, A. B.; Smith, M. D.; Krause, J. A.; Shustova, N. B. *J. Am. Chem. Soc.* **2015,** *137,* 2223–2226. doi:10.1021/ja5131269
27. Barthwal, S.; Kim, Y. S.; Lim, S.-H. *J. Colloid Interface Sci.* **2013,** *400,* 123–129. doi:10.1016/j.jcis.2013.02.037
28. Chang, C.-J.; Wang, C.-F.; Chen, J.-K.; Hsieh, C.-C.; Chen, P.-A. *Appl. Surf. Sci.* **2013,** *286,* 280–286. doi:10.1016/j.apsusc.2013.09.071
29. Choi, H.-J.; Choo, S.; Shin, J.-H.; Kim, K.-I.; Lee, H. *J. Phys. Chem. C* **2013,** *117,* 24354–24359. doi:10.1021/jp4070399
30. Ellinas, K.; Pujari, S. P.; Dragatogiannis, D. A.; Charitidis, C. A.; Tserepi, A.; Zuilhof, H.; Gogolides, E. *ACS Appl. Mater. Interfaces* **2014,** *6,* 6510–6524. doi:10.1021/am5000432
31. Ganesh, V. A.; Dinachali, S. S.; Nair, A. S.; Ramakrishna, S. *ACS Appl. Mater. Interfaces* **2013,** *5,* 1527–1532. doi:10.1021/am302790d
32. Hayase, G.; Kanamori, K.; Hasegawa, G.; Maeno, A.; Kaji, H.; Nakanishi, K. *Angew. Chem., Int. Ed.* **2013,** *52,* 10788–10791. doi:10.1002/anie.201304169
33. Liu, J.-Q.; Bai, C.; Jia, D.-D.; Liu, W.-L.; He, F.-Y.; Liu, Q.-Z.; Yao, J.-S.; Wang, X.-Q.; Wu, Y.-Z. *RSC Adv.* **2014,** *4,* 18025–18032. doi:10.1039/c4ra01505c
34. Deng, X.; Mammen, L.; Butt, H.-J.; Vollmer, D. *Science* **2012,** *335,* 67–70. doi:10.1126/science.1207115
35. Onda, T.; Shibuichi, S.; Satoh, N.; Tsujii, K. *Langmuir* **1996,** *12,* 2125–2127. doi:10.1021/la950418o

36. Wang, R.; Hashimoto, K.; Fujishima, A.; Chikuni, M.; Kojima, E.; Kitamura, A.; Shimohigoshi, M.; Watanabe, T. *Nature* **1997,** *388,* 431–432. doi:10.1038/41233
37. Fujishima, A.; Rao, T. N.; Tryk, D. A. *Electrochim. Acta* **2000,** *45,* 4683–4690. doi:10.1016/s0013-4686(00)00620-4
38. Nakajima, A.; Fujishima, A.; Hashimoto, K.; Watanabe, T. *Adv. Mater. (Weinheim, Ger.)* **1999,** *11,* 1365–1368. doi:10.1002/(sici)1521-4095(199911)11:16<1365::aid-adma1365>3.3.co;2-6
39. Gordon, V.; Marom, G.; Magdassi, S. *Int. J. Pharm.* **2015,** *478,* 172–179. doi:10.1016/j.ijpharm.2014.11.038
40. Férey, G. *Chem. Soc. Rev.* **2008,** *37,* 191–214. doi:10.1039/b618320b
41. Furukawa, H.; Cordova, K. E.; O'Keeffe, M.; Yaghi, O. M. *Science* **2013,** *341,* 1230444. doi:10.1126/science.1230444
42. Cook, T. R.; Zheng, Y.-R.; Stang, P. J. *Chem. Rev.* **2013,** *113,* 734–777. doi:10.1021/cr3002824
43. Evans, J. D.; Garai, B.; Reinsch, H.; Li, W.; Dissegna, S.; Bon, V.; Senkovska, I.; Fischer, R. A.; Kaskel, S.; Janiak, C.; Stock, N.; Volkmer, D. *Coord. Chem. Rev.* **2019,** *380,* 378–418. doi:10.1016/j.ccr.2018.10.002
44. Haraguchi, T.; Otsubo, K.; Kitagawa, H. *Eur. J. Inorg. Chem.* **2018,** 1697–1706. doi:10.1002/ejic.201701234
45. Ko, M.; Mendecki, L.; Mirica, K. A. *Chem. Commun.* **2018,** *54,* 7873–7891. doi:10.1039/c8cc02871k
46. Meek, S. T.; Greathouse, J. A.; Allendorf, M. D. *Adv. Mater. (Weinheim, Ger.)* **2011,** *23,* 249–267. doi:10.1002/adma.201002854
47. Qiu, S.; Zhu, G. *Coord. Chem. Rev.* **2009,** *253,* 2891–2911. doi:10.1016/j.ccr.2009.07.020
48. Rowsell, J. L. C.; Yaghi, O. M. *J. Am. Chem. Soc.* **2006,** *128,* 1304–1315. doi:10.1021/ja056639q
49. Usman, M.; Mendiratta, S.; Lu, K.-L. *Adv. Mater. (Weinheim, Ger.)* **2017,** *29,* 1605071. doi:10.1002/adma.201605071
50. Sun, L.; Campbell, M. G.; Dincă, M. *Angew. Chem., Int. Ed.* **2016,** *55,* 3566–3579. doi:10.1002/anie.201506219
51. Allendorf, M. D.; Schwartzberg, A.; Stavila, V.; Talin, A. A. *Chem. – Eur. J.* **2011,** *17,* 11372–11388. doi:10.1002/chem.201101595
52. Dolgopolova, E. A.; Shustova, N. B. *MRS Bull.* **2016,** *41,* 890–896. doi:10.1557/mrs.2016.246
53. Liu, M.; Tie, L.; Li, J.; Hou, Y.; Guo, Z. *J. Mater. Chem. A* **2018,** *6,* 1692–1699. doi:10.1039/c7ta09711e
54. Ma, D.; Peh, S. B.; Han, G.; Chen, S. B. *ACS Appl. Mater. Interfaces* **2017,** *9,* 7523–7534. doi:10.1021/acsami.6b14223
55. Sun, H.; Tang, B.; Wu, P. *ACS Appl. Mater. Interfaces* **2017,** *9,* 21473–21484. doi:10.1021/acsami.7b05504
56. Du, J.; Zhou, C.; Yang, Z.; Cheng, J.; Shen, Y.; Zeng, X.; Tan, L.; Dong, L. *Surf. Coat. Technol.* **2019,** *363,* 282–290. doi:10.1016/j.surfcoat.2019.02.062
57. Zhang, X.; Zhao, Y.; Mu, S.; Jiang, C.; Song, M.; Fang, Q.; Xue, M.; Qiu, S.; Chen, B. *ACS Appl. Mater. Interfaces* **2018,** *10,* 17301–17308. doi:10.1021/acsami.8b05137
58. Tan, T. T. Y.; Reithofer, M. R.; Chen, E. Y.; Menon, A. G.; Hor, T. S. A.; Xu, J.; Chin, J. M. *J. Am. Chem. Soc.* **2013,** *135,* 16272–16275. doi:10.1021/ja407896m
59. Padial, N. M.; Quartapelle Procopio, E.; Montoro, C.; López, E.; Oltra, J. E.; Colombo, V.; Maspero, A.; Masciocchi, N.; Galli, S.; Senkovska, I.; Kaskel, S.; Barea, E.; Navarro, J. A. R. *Angew. Chem., Int. Ed.* **2013,** *52,* 8290–8294. doi:10.1002/anie.201303484
60. Ko, M.; Aykanat, A.; Smith, M. K.; Mirica, K. A. *Sensors* **2017,** *17,* 2192. doi:10.3390/s17102192
61. Du, J.; Zhang, C.; Pu, H.; Li, Y.; Jin, S.; Tan, L.; Zhou, C.; Dong, L. *Colloids Surf., A* **2019,** *573,* 222–229. doi:10.1016/j.colsurfa.2019.04.064
62. Jayaramulu, K.; Datta, K. K. R.; Rösler, C.; Petr, M.; Otyepka, M.; Zboril, R.; Fischer, R. A. *Angew. Chem., Int. Ed.* **2016,** *55,* 1178–1182. doi:10.1002/anie.201507692
63. Gao, M.-L.; Zhao, S.-Y.; Chen, Z.-Y.; Liu, L.; Han, Z.-B. *Inorg. Chem.* **2019,** *58,* 2261–2264. doi:10.1021/acs.inorgchem.8b03293
64. Jayaramulu, K.; Datta, K. K. R.; Rösler, C.; Petr, M.; Otyepka, M.; Zboril, R.; Fischer, R. A. *Angew. Chem.* **2016,** *128,* 1193–1197. doi:10.1002/ange.201507692
65. Ma, Q.; Yin, P.; Zhao, M.; Luo, Z.; Huang, Y.; He, Q.; Yu, Y.; Liu, Z.; Hu, Z.; Chen, B.; Zhang, H. *Adv. Mater. (Weinheim, Ger.)* **2019,** *31,* 1808249. doi:10.1002/adma.201808249
66. Hmadeh, M.; Lu, Z.; Liu, Z.; Gándara, F.; Furukawa, H.; Wan, S.; Augustyn, V.; Chang, R.; Liao, L.; Zhou, F.; Perre, E.; Ozolins, V.; Suenaga, K.; Duan, X.; Dunn, B.; Yamamto, Y.; Terasaki, O.; Yaghi, O. M. *Chem. Mater.* **2012,** *24,* 3511–3513. doi:10.1021/cm301194a
67. Mähringer, A.; Jakowetz, A. C.; Rotter, J. M.; Bohn, B. J.; Stolarczyk, J. K.; Feldmann, J.; Bein, T.; Medina, D. D. *ACS Nano* **2019,** *13,* 6711–6719. doi:10.1021/acsnano.9b01137
68. Fowkes, F. M. *J. Phys. Chem.* **1963,** *67,* 2538–2541. doi:10.1021/j100806a008
69. Turri, R. G.; Santos, R. M.; Rangel, E. C.; da Cruz, N. C.; Bortoleto, J. R. R.; Dias da Silva, J. H.; Antonio, C. A.; Durrant, S. F. *Appl. Surf. Sci.* **2013,** *280,* 474–481. doi:10.1016/j.apsusc.2013.05.013
70. Wenzel, R. N. *Ind. Eng. Chem.* **1936,** *28,* 988–994. doi:10.1021/ie50320a024
71. Virmani, E.; Rotter, J. M.; Mähringer, A.; von Zons, T.; Godt, A.; Bein, T.; Wuttke, S.; Medina, D. D. *J. Am. Chem. Soc.* **2018,** *140,* 4812–4819. doi:10.1021/jacs.7b08174
72. Cassie, A. B. D.; Baxter, S. *Trans. Faraday Soc.* **1944,** *40,* 546–551. doi:10.1039/tf9444000546

License and Terms

This is an Open Access article under the terms of the Creative Commons Attribution License (http://creativecommons.org/licenses/by/4.0). Please note that the reuse, redistribution and reproduction in particular requires that the authors and source are credited.

The license is subject to the *Beilstein Journal of Nanotechnology* terms and conditions: (https://www.beilstein-journals.org/bjnano)

The definitive version of this article is the electronic one which can be found at: doi:10.3762/bjnano.10.196

BEILSTEIN JOURNAL OF NANOTECHNOLOGY

Synthesis of highly active ETS-10-based titanosilicate for heterogeneously catalyzed transesterification of triglycerides

Muhammad A. Zaheer[1], David Poppitz[1], Khavar Feyzullayeva[1], Marianne Wenzel[2], Jörg Matysik[2], Radomir Ljupkovic[3], Aleksandra Zarubica[3], Alexander A. Karavaev[4], Andreas Pöppl[5], Roger Gläser[1] and Muslim Dvoyashkin[*1]

Full Research Paper

Open Access

Address:
[1]Institute of Chemical Technology, Universität Leipzig, Linnéstraße 3, 04103 Leipzig, Germany, [2]Institute of Analytical Chemistry, Universität Leipzig, Linnéstraße 3, 04103 Leipzig, Germany, [3]Faculty of Science and Mathematics, University of Nis, Visegradska 33, 18000 Nis, Serbia, [4]Gubkin Russian State University of Oil and Gas, Leninsky Prospekt 65, 119991 Moscow, Russia and [5]Felix-Bloch-Institut, Universität Leipzig, Linnéstraße 5, 04103 Leipzig, Germany

Email:
Muslim Dvoyashkin[*] - muslim.dvoyashkin@uni-leipzig.de

* Corresponding author

Keywords:
CaO; diffusion; ETS-10; nuclear magnetic resonance (NMR); transesterification

Beilstein J. Nanotechnol. **2019,** *10,* 2039–2061.
doi:10.3762/bjnano.10.200

Received: 15 July 2019
Accepted: 15 October 2019
Published: 28 October 2019

This article is part of the thematic issue "New directions for nanoporous materials".

Guest Editor: C. T. Yavuz

© 2019 Zaheer et al.; licensee Beilstein-Institut.
License and terms: see end of document.

Abstract

In this contribution, the preparation of hierarchically structured ETS-10-based catalysts exhibiting notably higher activity in the conversion of triolein with methanol compared to microporous titanosilicate is presented. Triolein, together with its unsaturated analog trilinolein, represent the most prevalent triglycerides in oils. The introduction of mesopores by post-synthetic treatment with hydrogen peroxide and a subsequent calcination step results in the generation of an additional active surface with Brønsted basic sites becoming accessible for triolein and enhancing the rate of transesterification. The resulting catalyst exhibits a comparable triolein conversion (≈73%) after 4 h of reaction to CaO (≈76%), which is reportedly known to be highly active in the transesterification of triglycerides. In addition, while CaO showed a maximum conversion of 83% after 24 h, the ETS-10-based catalyst reached 100% after 8 h, revealing its higher stability compared to CaO. The following characteristics of the catalysts were experimentally addressed – crystal structure (X-ray diffraction, transmission electron microscopy), crystal shape and size (scanning electron microscopy, laser diffraction), textural properties (N_2 sorption, Hg porosimetry), presence of hydroxyl groups and active sites (temperature-programmed desorption of NH_3 and CO_2, ^{29}Si magic angle spinning nuclear magnetic resonance (NMR)), mesopore accessibility and diffusion coefficient of adsorbed triolein (pulsed field gradient NMR), pore interconnectivity (variable temperature and exchange spectroscopy experiments using hyperpolarized ^{129}Xe NMR) and oxidation state of Ti atoms (electron paramagnetic resonance). The obtained results enabled the detailed understanding of the impact of the post-synthetic treatment applied to the ETS-10 titanosilicate with respect to the catalytic activity in the heterogeneously catalyzed transesterification of triglycerides.

Introduction

One of the available solutions to address the world's increasing energy consumption is the production of fatty acid methyl esters (FAMEs), also known as biodiesel, which are an alternative fuel similar to conventional diesel. They are usually produced from various triglycerides – components of vegetable or plant oils, animal fats and tallows [1]. Keeping in mind the critical aspect of food security (i.e., minimizing the use of edible feedstock types for fuel production) and the need for sustainability in the long run, recent developments in the use of algae as the feedstock have given the concepts of biofuel production renewed attention [2]. After several decades since the first reports on the usage of microalgae for biodiesel production [3,4], it has been determined that microalgal biofuels are promising candidates for the partial replacement of fossil fuels.

The production of microalgal biodiesel requires an efficient catalyst for initiation of the transesterification process that converts triglycerides into FAMEs. Other methods that do not require a catalyst, such as pyrolysis and utilization of supercritical fluid technology, are considered to be highly energy-intensive, inhibiting their practical implementation on the industrial scale [5].

The preparation and application of different types of catalysts for homogeneous, heterogeneous, and even enzymatic transesterification processes have been extensively investigated [6]. However, the most commonly used commercial process for biodiesel production is the homogenous transesterification of triglycerides with methanol in the presence of sodium hydroxide (NaOH) or potassium hydroxide (KOH), which is still in use on an industrial scale. Along with the obvious advantages of being highly active and relatively inexpensive (depending however on the number of washing steps and possible need for neutralization), the downsides of alkali hydroxides are long known – difficulties in separation of the K^+/Na^+ traces from the product, higher catalyst consumption compared to the solid ones and low reusability [7]. On the other hand, the reported solid catalysts can potentially resolve issues associated with catalysts used in the homogeneous process, that is, they can be prepared with a desired particle size for separation needs and can be reused. The main drawbacks are their lower activity compared to the catalysts used in homogeneous solutions (often associated with mass transfer issues [7]) and the leaching of the active phase (if supported catalysts are used [8]).

Thus, the search continues for a new generation of catalysts that ideally combine the advantages of both types of catalysts used in the homo- and heterogeneously catalyzed reactions [9-12]. In the context of biodiesel production via the transesterification of triglycerides with methanol, the challenge is to prepare a catalyst possessing the following characteristics: i) large particle size for convenient separation, ii) accessibility of the active sites for reactants, iii) minimized diffusion limitations for reaching effectiveness factors close to unity, iv) leaching resistance, v) activity at moderate temperatures (e.g., at the boiling point of methanol) being ideally comparable to KOH/NaOH catalysts and vi) stability for multiple reuse. Our approach to address this challenge is based on the preparation of bulk catalysts that are reported to be active in the transesterification reaction together with further (nano)structural modification aimed at enhancing accessibility to the active sites and improving the mass transfer characteristics for efficient reactant supply and product removal [13].

Amongst the prospective solid catalysts designed for transesterification reactions, such as calcium [14] and other metal oxides [15], metal–organic frameworks (MOFs) [10], silica-supported catalysts [16], biochar [17] and other biomass-derived catalysts [18], zeolites and molecular sieves [19,20] offer a combination of the possibility for the pore network modification (e.g., as a result of a post-synthetic treatment) and high stability (e.g., compared to MOFs) with active sites being part of a framework.

The microporous, titanosilicate ETS-10 catalyst was found to be one of the most active catalysts amongst the crystalline microporous molecular sieves (such as, e.g., zeolites) reported for the transesterification of triglycerides with methanol [20]. Its crystal structure is built up from orthogonal TiO_6 octahedra and SiO_4 tetrahedra sharing oxygen atoms and forming a three-dimensional interconnected pore system [21] consisting of channels with cross-sectional dimensions of 0.8 × 0.5 nm [22,23] (Figure 1A). Each Ti atom in a six-coordinated state bears two negative charges, which can be balanced by Na^+ or K^+ cations according to the following stoichiometry $(Na,K)_2TiSi_5O_{13}$ [22]. The high activity of ETS-10 in the transesterification reactions compared to zeolites and other molecular sieves originates presumably from its pronounced Brønsted basicity of the shared oxygen atoms [20]. For example, it has been reported that the parent ETS-10 catalyst is approximately four times more basic than the NaX zeolite based on acetone selectivity in the conversion of isopropanol to acetone and propene [24]. However, due to its microporous nature, to the best of our knowledge, in all reported studies on the transesterification of triglycerides (single-component or in mixtures/oils) for biodiesel production, the reaction took place solely on the outer crystal surface. The smallest triglyceride, triacetin, used in these studies, has a reported critical diameter of ≈1 nm [25], which appears to be too large to diffuse into the micropores.

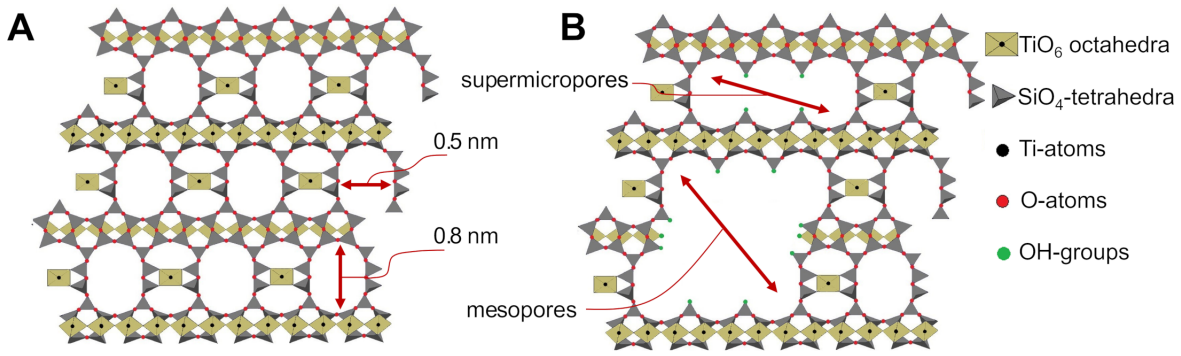


Figure 1: One of the polymorphs of the microporous ETS-10 consisting of TiO_6 octahedra and SiO_4 tetrahedra sharing oxygen atoms (A). Possible framework modification with present super-micropores and mesopores that might result from the post-synthetic treatment of ETS-10 with H_2O_2 aqueous solution according to [26] (B).

Several strategies have been attempted for a post-synthetic modification of the ETS-10: an ion-exchange method [27], acidic treatment [28,29], and treatment with hydrogen peroxide (H_2O_2) [26,30,31]. The latter approach resulted in a notable pore network modification by introducing larger micropores (≈1–2 nm) and mesopores (≈5–30 nm) in a controllable way, for example, by using different concentrations of the H_2O_2 solution and treatment times (Figure 1B). Herewith, the crystallinity and mechanical stability of the materials were well-preserved despite the experienced desilication and detitanation. This approach was followed in the present study to prepare hierarchically structured ETS-10 crystals (i.e., containing interconnected micro- and mesopores). In general, the micropores of the hierarchical catalysts mostly contribute to the catalytic process, while the function of the larger mesopores is the promotion of the reactant supply and product removal. However, for bulky triglycerides, the micropores are not expected to be accessible. In such a case, the mesopores will fulfil the task of providing access to the catalytically active sites located within them.

In the present contribution, we report the successful preparation of large crystallite (≈30 µm) ETS-10 titanosilicates with improved active site accessibility (achieved by post-synthetic treatment) for efficient transesterification of triglycerides into biodiesel. A triolein has been selected as the triglyceride due to its prevalence in, for example, microalgal oils typically used in production of 3rd and 4th generation biodiesel. Additionally, CaO catalysts, known to be highly active in the transesterification process, were prepared as references for comparison of the catalytic activity under identical reaction conditions. Prior to catalytic tests, the prepared CaO- and titanosilicate catalysts were characterized to obtain quantitative information on properties such as crystal structure by X-ray diffraction (XRD), crystal size by laser diffraction, crystal morphology by scanning electron microscopy (SEM) and transmission electron microscopy (TEM), pore width by N_2 sorption and Hg intrusion, acid and basic site density by NH_3 and CO_2 temperature-programmed desorption (TPD), presence of hydroxyl groups by ^{29}Si magic angle spinning nuclear magnetic resonance (MAS NMR), pore interconnectivity by hyperpolarized (HP) ^{129}Xe NMR, pore accessibility for triolein by ^{1}H pulsed field gradient (PFG) NMR, state of the Ti atoms before and after the treatment of titanosilicates by electron paramagnetic resonance (EPR) and thermal stability of the crystals by differential thermal analysis (DTA).

Results and Discussion

Structure characterization of an as-synthesized ETS-10 titanosilicate

Figure 2 represents XRD data obtained on an as-synthesized ETS-10 (Na,K-ETS-10) plotted together with reference diffractograms of the phases that can be formed as by-products during

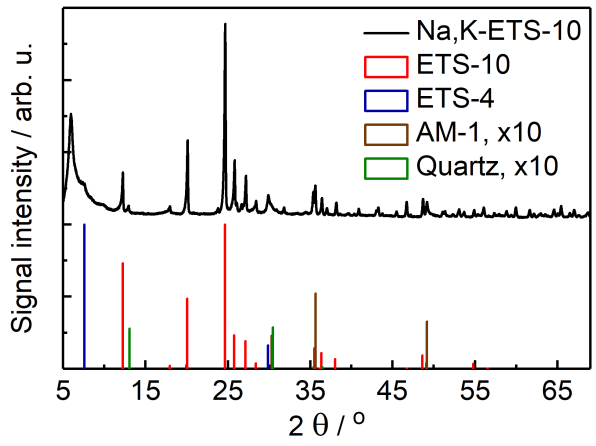


Figure 2: X-ray diffractograms of the as-synthesized ETS-10 material (Na,K-ETS-10, top) and of the reference reflections of ETS-10, ETS-4, AM-1 and quartz according to [33-36]. Signals of AM-1 and quartz are 10-fold amplified for visibility.

the synthesis of ETS-10 [30,32]. Thus, in addition to the prevalent reflections being characteristic for ETS-10, smaller quantities of ETS-4, AM-1 and quartz were detected (see also SEM data in Figure 3). The corresponding reflections at angles of 2θ are seen at, for example, 29.9° and 7.6° from ETS-4, 35.6° and 49.2° from AM-1, and 13.1° and 30.4° from quartz. The quantification of the presence of each phase in the prepared batch, as well as the results of the studies aimed at minimization of the amount of quartz and alternative titanosilicate phases employed during the synthesis of ETS-10 are described in section S6 of Supporting Information File 1. The presence of sharp peaks in the diffractogram (e.g., 0.15° FWHM for the peak at 24.63°) reflects the high crystallinity of the prepared ETS-10 material.

Data of the textural analysis by N_2 sorption into the Na,K-ETS-10 sample is presented in Figure 4. The isotherms exhibit the Type I shape [37] (revealing the presence of solely micropores) and have a specific surface area of 257 m^2 g^{-1} and micropore volume of 0.110 cm^3 g^{-1}. The pore width distribution calculated from the adsorption branches of the isotherm using the NLDFT method is presented in the inset of Figure 4. The same procedure was applied for the characterization of other (treated) titanosilicates. The Hg intrusion data shown in Figure 5 demonstrate the absence of pores in the range from 5 nm to ≈1 μm, suggesting that the amount of possible defects in the crystals is negligibly small. The textural data of all titanosilicates prepared for catalytic studies are summarized in Table 1.

The microporous nature and high crystallinity of Na,K-ETS-10 is further confirmed by TEM (Figure 6) demonstrating high order of the titanosilicate framework with parallel Ti nanowires

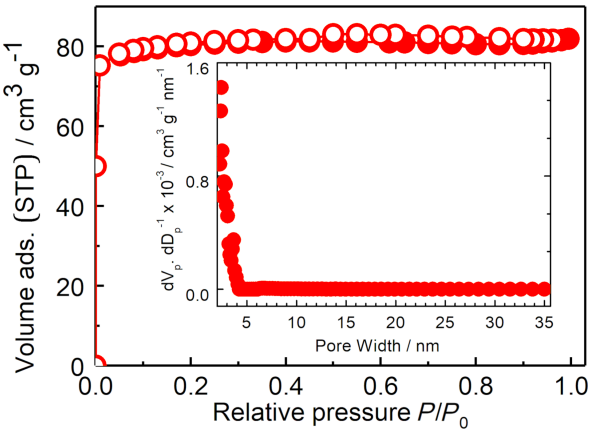


Figure 4: Nitrogen adsorption (solid circles) and desorption (open circles) isotherms of the as-synthesized Na,K-ETS-10. The inset shows the calculated pore width distribution according to the NLDFT.

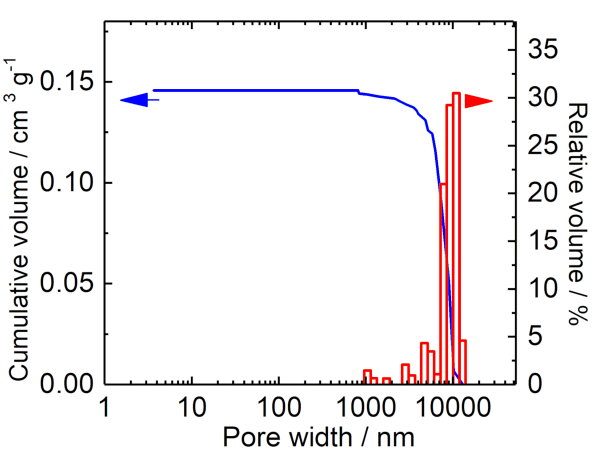


Figure 5: Hg intrusion data of the as-synthesized Na,K-ETS-10 material.

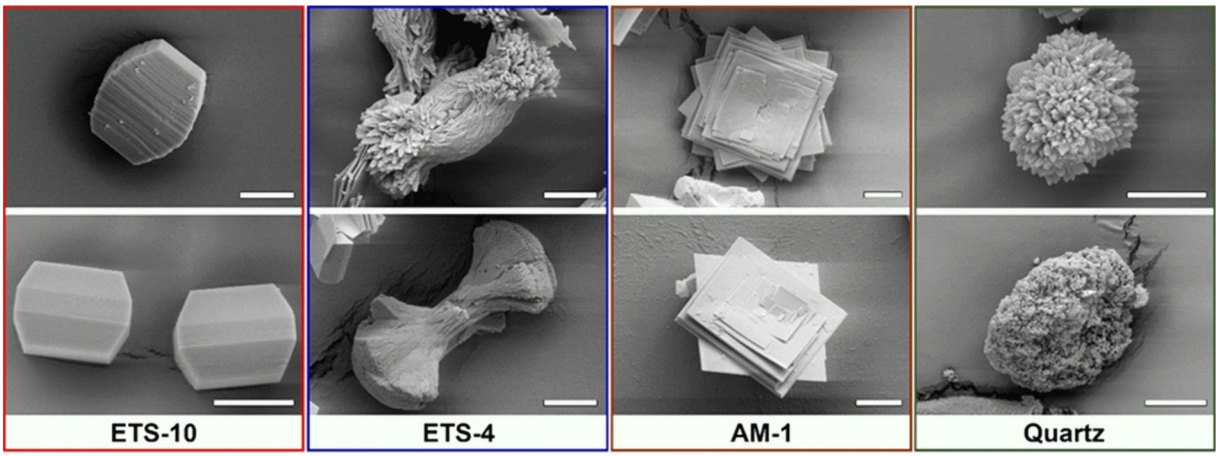


Figure 3: SEM micrographs of selected crystals representing different types of phases formed during the synthesis of titanosilicates. The assignment of each crystal shape to the corresponding phase was done based on the Si/Ti (for titanosilicates) and Si/O (for quartz) ratios obtained from the EDX analysis (see Table S8 in Supporting Information File 1). The scale bar in all images is 10 μm.

Table 1: Textural characteristics of the titanosilicates from the results of the N_2 sorption experiments.

Material	BET specific surface area / $m^2\ g^{-1}$	Specific micropore volume[a] / $cm^3\ g^{-1}$	Specific mesopore volume / $cm^3\ g^{-1}$	Specific total pore volume[b] / $cm^3\ g^{-1}$
Na,K-ETS-10	257	0.110	0.017	0.127
P-ETS-10/30	262	0.110	0.022	0.132
P-ETS-10/45	282	0.111	0.070	0.181
P-ETS-10/60	291	0.131	0.098	0.229
C-P-ETS-10/60	235	0.105	0.084	0.189

[a]Micropore volume was calculated by t-plot at a relative pressure range of P/P_0 = 0.15–0.5; [b]Total pore volume was calculated at P/P_0 = 0.99 according to the Gurvich rule, and the mesopore volume is calculated by subtracting the micropore volume from the total pore volume.

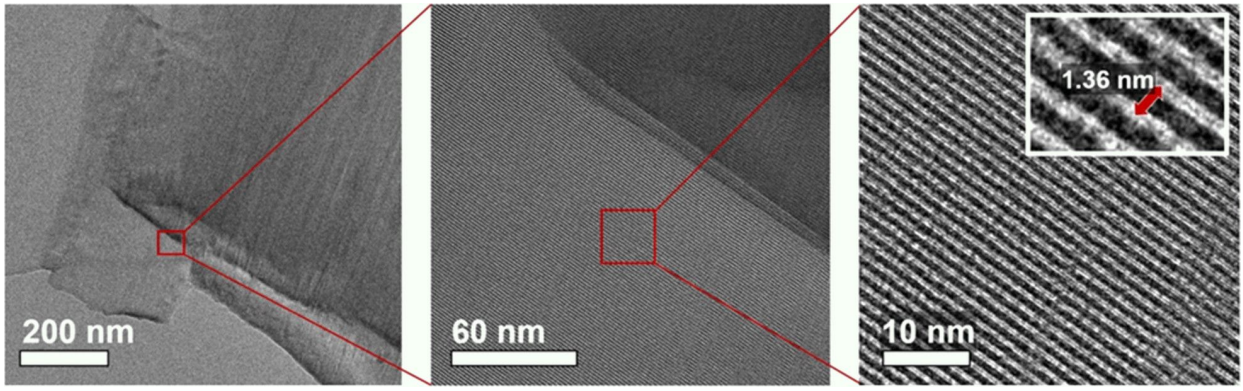


Figure 6: TEM micrographs for the Na,K-ETS-10 material obtained with different magnifications demonstrating a highly ordered ETS-10 crystal structure. Other images obtained with different ETS-10 crystals can be found in section S9 of Supporting Information File 1.

showing no visible defects on the length scale of hundreds of nanometers. The spacing between adjacent nanowires showed good agreement with literature data of 1.36 nm [38].

Impact of H_2O_2 treatment on crystallinity, textural characteristics, surface chemistry and pore interconnectivity of ETS-10 titanosilicates

The XRD data of treated samples in Figure 7A demonstrate that the treatment of titanosilicates with H_2O_2 and subsequent calcination does not notably affect the crystallinity, which is fully restored after the calcination (see Table S10 of Supporting Information File 1). However, partial removal of the framework has led to the appearance of crack-looking defects on the surface of ETS-10, less noticeable on the crystals treated for 30 min, but more pronounced for longer treatment times (Figure 8). Despite these defects, the particle size distribution probed by laser diffraction revealed minor changes suggesting that treatment neither leads to dissolution of smaller particles, nor to detectable fractioning of the larger ones (Figure 7B).

The N_2 sorption isotherms revealed an increasing impact of treatment on the textural properties of the titanosilicates with longer treatment time (Figure 9A) – the total pore volume increased from 0.127 $cm^3\ g^{-1}$ for Na,K-ETS-10 to 0.132, 0.181 and 0.229 $cm^3\ g^{-1}$ after 30, 45 and 60 min of contact time with H_2O_2, respectively. This change results from the contribution of mesopores in the range of 5–40 nm formed during the treatment (see Figure 9B and Table 1). This is consistent with the TEM images of treated samples with clear identification of mesopores presented in Figure 10. It is worth noting that the appearance of mesopores after treatment has led to the change of the isotherm shape from type I (typical for microporous solids) to a combination of types I and IV, as is expected for micro–mesoporous materials [37].

It was suggested that exposure of the ETS-10 framework to H_2O_2 solution leads to its partial removal either by the disruption of Ti–O–Ti chains and partial leaching of Ti atoms [26] or by microexplosions if elevated temperatures are used [39]. At the same time, the measured specific micropore volume either does not change (for 30 and 45 min of treatment time) or

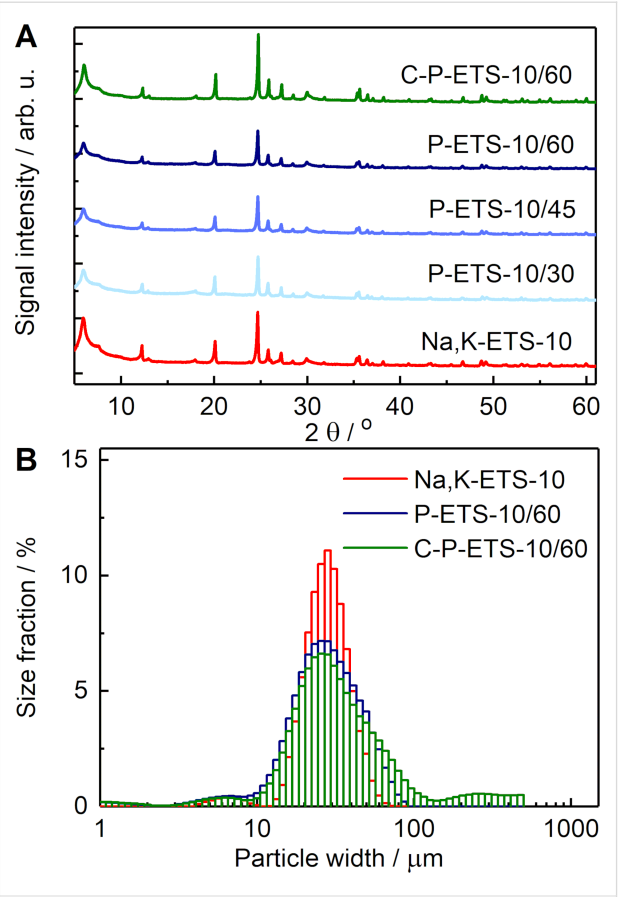


Figure 7: (A) XRD data of post-synthetically treated titanosilicates. The calculated crystallinity decreased to ≈70% for P-ETS-10/30, P-ETS-10/45 and P-ETS-10/60, and was restored to 100% for C-P-ETS-10/60 (assuming the parent material is 100%). (B) Particle size distribution obtained by laser diffraction for Na,K-ETS-10 (red), P-ETS-10/60 (blue) and C-P-ETS 10/60 (green).

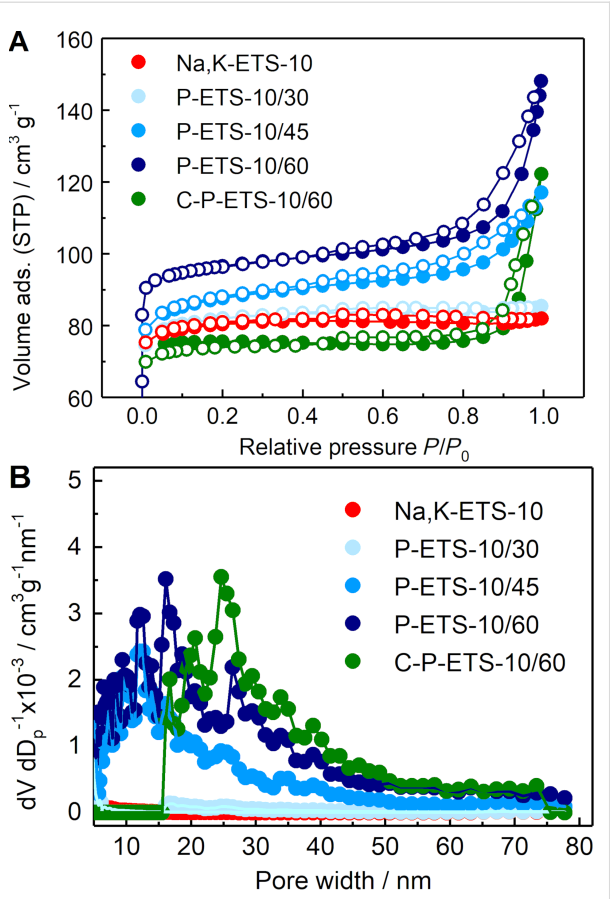


Figure 9: (A) Nitrogen adsorption and desorption isotherms of titanosilicates treated with H_2O_2 for 30 min (light blue), 45 min (blue) and 60 min (dark blue) and of the latter after calcination (green). The sorption isotherm of as-synthesized Na,K-ETS-10 (red) is shown for comparison. (B) Calculated pore width distributions using the NLDFT.

slightly increases from 0.110 $cm^3\ g^{-1}$ for the parent titanosilicate to 0.131 $cm^3\ g^{-1}$ after 60 min of treatment. The application of calcination has led to a slightly lower mesopore volume for P-ETS-10/60 (0.098 $cm^3\ g^{-1}$) and C-P-ETS-10/60 (0.084 $cm^3\ g^{-1}$) and to micropore volumes of 0.131 $cm^3\ g^{-1}$ and 0.105 $cm^3\ g^{-1}$, respectively. Referring to the XRD data, which reveals that the structure of the ETS-10 material after calcination remains intact (also preserving high crystallinity), it is not expected that the micropore volume will notably decrease. This observation can be attributed to the different interactions of the titanosilicate surface with the quadrupole momentum of N_2 for P-ETS-10/60 and C-P-ETS-10/60. In such a case, the precise analysis of the microporosity by N_2 is difficult and the use of Ar instead is recommended [26,40].

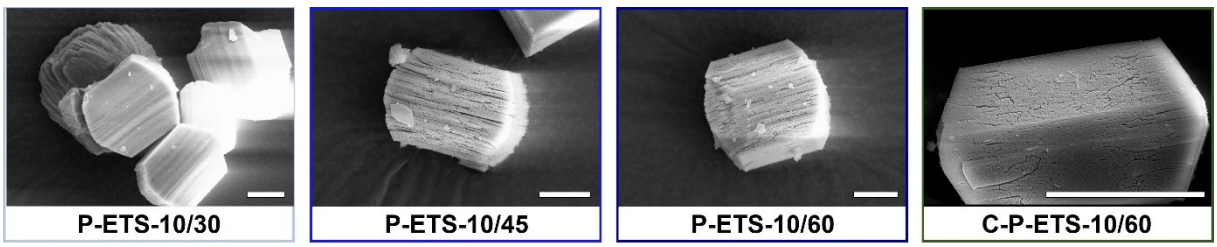


Figure 8: SEM micrographs of the titanosilicates treated with H_2O_2 for 30, 45 and 60 min (P-ETS-10/30, P-ETS-10/45, P-ETS-10/60). P-ETS-10/60 additionally underwent calcination at 873 K for 6 h. The scale bar in all images is 10 µm.

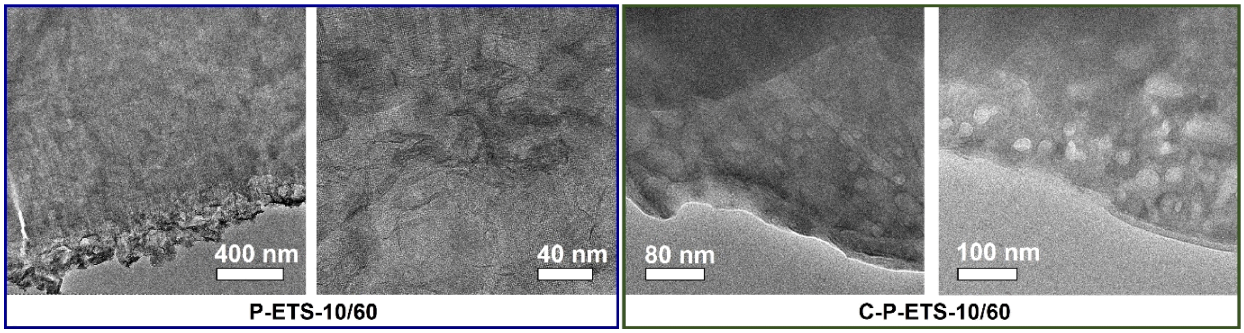


Figure 10: TEM images of the selected crystals of P-ETS-10/60 and C-P-ETS 10/60 demonstrating the presence of mesopores that appeared after treatment.

The calcination of P-ETS-10/60 has led to a visible decrease of the adsorbed volume in the range of 5–15 nm and to a shift of the maximum of the pore width distribution towards larger values. One possible explanation of this observation is the appearance of additional structural defects (to those resulting from the H_2O_2 treatment) due to exposure of the material to high temperatures (i.e., 873 K) for 6 h. Such thermal treatment might cause cracks in part of the framework, for example, separating two adjacent mesopores, leading to merging into a larger void. It was reported that the ETS-10 framework can collapse at temperatures above 920 K [41]. To determine this critical temperature, which might vary for titanosilicates prepared under different conditions, DTA was conducted where a critical temperature of ≈950 K was determined (Figure 11). This is only 77 K higher than the calcination temperature employed, which might be sufficient to introduce such cracks upon heating. On the other hand, this temperature difference seems to be large enough to prevent destruction of the framework during the calcination. The low-temperature minimum (first weight loss) is due to dehydration, while the exothermic part in the range 500–900 K can be attributed to the burning-out of the surface hydroxyl groups [42,43].

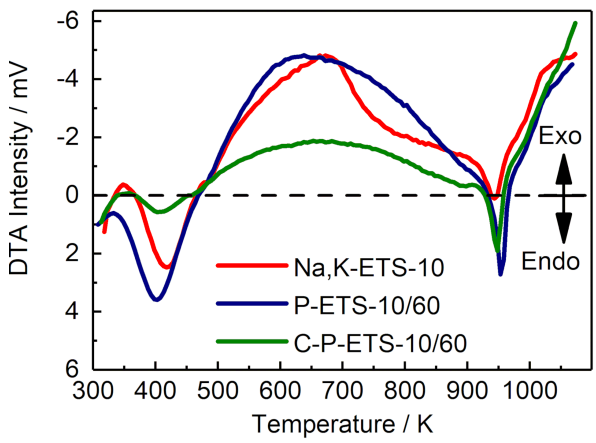


Figure 11: Differential thermal analysis of the Na,K-ETS-10 (red), P-ETS-10/60 (blue) and C-P-ETS-10/60 (green) materials. The dashed line separates regions of exothermic (exo) and endothermic (endo) processes.

Since it is expected that the active sites located inside the micropores of the catalysts are not accessible for bulky triolein, their contribution in the transesterification process is expected to be negligibly small. Thus, further analysis of the textural characteristics of the micropores by Ar was not conducted. The 60 min titanosilicate-treated P-ETS-10/60 and its calcined counterpart C-P-ETS-10/60 were selected for further characterization and catalytic studies as those exhibiting the highest mesopore volume.

Another limitation of using N_2 is the analysis of the macropores (>50 nm) [37], for which the Hg porosimetry was considered. The obtained data show a significant fraction of voids in the range of ≈1–20 µm (see Figure S11 of Supporting Information File 1), which was assigned to the interparticle spaces that can be filled by Hg after applying pressure. This is consistent with the similar crystal sizes measured by laser diffraction (Figure 7B). As expected, below 1 µm no Hg intrusion can be seen for the microporous Na,K-ETS-10, while for P-ETS-10/60 and C-P-ETS 10/60, a visible fraction in the range of mesopores and macropores is detected. The obtained specific mesopore volumes were 0.114 $cm^3\ g^{-1}$ and 0.069 $cm^3\ g^{-1}$ for P-ETS-10/60 and C-P-ETS 10/60, respectively. This appears to be in good agreement with the corresponding values obtained by N_2 sorption (Table 1, column 3). The specific surface area from the Hg intrusion was 0.1 $m^2\ g^{-1}$ for Na,K-ETS-10, 52.6 $m^2\ g^{-1}$ for P-ETS-10/60, and 24.2 $m^2\ g^{-1}$ for P-ETS-10/60. In the conducted Hg porosimetry experiments, in contrast to the N_2 sorption, the micropores were not reachable for Hg, while the macropores did contribute to the measured surface area.

Characterization of acidity and basicity of the ETS-10-based titanosilicates

NH_3 and CO_2 were used as probe molecules in TPD studies to determine the surface acid/basic site density of the prepared titanosilicates. Desorption of NH_3 presented in Figure 12A occurs in one (Na,K-ETS-10) or two (P-ETS-10/60, C-P-ETS-10/60) distinguishable steps. According to [44], the range ≈380–600 K represents temperatures of NH_3 desorption from the weak Lewis acid sites, for example, Na^+ or K^+ cations, being more pronounced in Na,K-ETS-10, which is partially due to the higher amount of present cations compared to the treated titanosilicates (Table 2, last column). In all materials this desorption step extends over ≈200 K, probably due to the presence of different cationic sites (I–V) near the titanate chains, which are described in [45] in detail. NH_3 preferentially coordinates near the type V cations located at the top of the 12 ring pore near a titanate chain. After treatment, these vacancies are partially removed due to the detitanation process. This can additionally contribute to the decrease in the observed intensities of NH_3 desorption below 600 K for treated samples compared to Na,K-ETS-10. At temperatures above 600 K, highly pronounced NH_3 desorption, presumably from the surface hydroxyl groups being strong Brønsted acid sites, appeared as a result of the H_2O_2 treatment. The calcination process leads to dehydroxylation of the surface [42], which notably reduces the NH_3 desorption for C-P-ETS-10/60 above 600 K as compared to P-ETS-10/60. Table 2 summarizes the calculated values of the surface acid/basic site density and intrinsic acid/basic adsorption capacity of the titanosilicates, as calculated by

$$\frac{\text{Surface acid (basic) site density } [\mu\text{mol g}^{-1}]}{\text{Specific surface area } [\text{m}^2\ \text{g}^{-1}]} \quad (1)$$

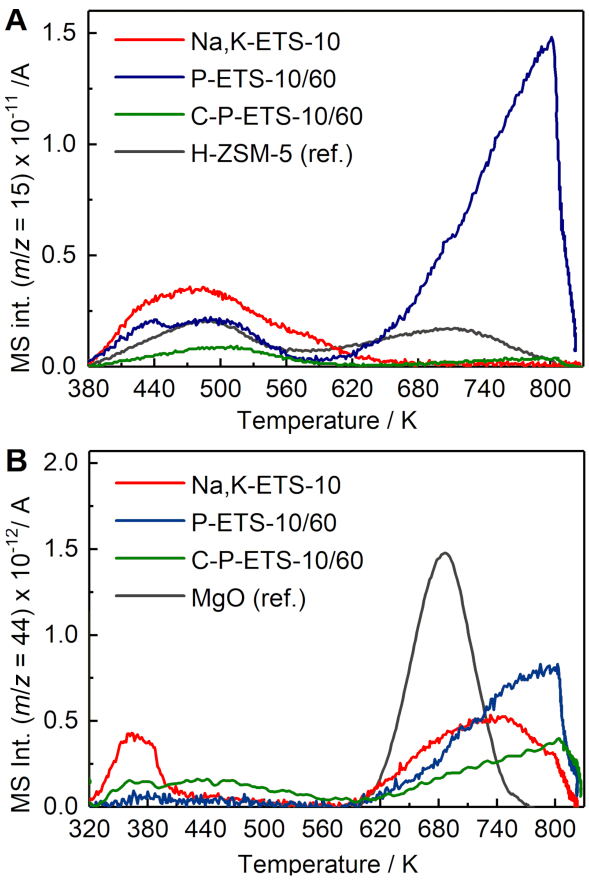


Figure 12: Temperature-programmed desorption of NH_3 (A) and CO_2 (B) in Na,K-ETS-10 (red), P-ETS-10/60 (blue) and C-P-ETS 10/60 (green) samples. For comparison, NH_3 desorption from the H-ZSM-5 zeolite with Si/Al = 27 and a known acid site density used as a reference is presented by the grey line. The curve of MgO was used as a reference in B.

Table 2: NH_3 TPD, CO_2 TPD, and ICP OES data for Na,K-ETS-10, P-ETS-10/60, and C-P-ETS-10/60. n.d. – no data.

Sample	Surface acid site density / μmol g^{-1}	Surface basic site density / μmol g^{-1}	Specific surface area / $m^2\ g^{-1}$	Intrinsic acid adsorption capacity[a] / μmol m^{-2}	Intrinsic base adsorption capacity[a] / μmol m^{-2}	wt % of elemental Ti, Na, and K[b]
Na,K-ETS-10	1324	136	257	5.15	0.52	9.7, 9.0, 0.7
P-ETS-10/60	3955	145	291	13.59	0.49	11.0, 7.0, 0.9
C-P-ETS-10/60	359	92	239	1.50	0.38	9.8, 7.0 1.1
H-ZSM-5[c]	1186	n.d.	366	3.24	n.d.	–
MgO[c]	n.d.	959	15	n.d.	63.9	–

[a]Calculated using Equation 1; [b]Experimental error in the ICP OES analysis is ≈1 wt %; [c]H-ZSM-5 and MgO were used as references with known surface acid and basic site density.

The results of the CO_2 TPD in the parent and treated titanosilicates are presented in Figure 12B. The TPD curve of Na,K-ETS-10 reveals two distinct peaks in the range ≈320–420 K and above 600 K. The desorption in the low-temperature range is presumably due to Na^+ or K^+ cations and weakly basic surface hydroxyl groups [46,47], i.e., the H-bridged Ti–OH–Si (see also Figure 3 of [31]). As a result of the post-synthetic treatment by H_2O_2, a decrease of the desorption peak in this temperature range for P-ETS-10/60 might be due to the partial removal of the cations (decrease of the Na wt % from 9 to 7 after treatment with H_2O_2, see Table 2 (last column)) and of the H-bridged surface hydroxyl groups, as is also evident from the diffuse reflectance infrared Fourier transform (DRIFT) study in [31]. After calcination, the peak below 600 K slightly increases and becomes broad.

The high-temperature range for all three titanosilicates is characterized by notable desorption from the strong Brønsted basic sites. For Na,K-ETS-10, these are the oxygen atoms shared between Si and Ti and bearing uncompensated negative charge (O^-), and the isolated hydroxyl groups forming the hydrogen carbonate species $HO–CO_2^-$ [48]. It is worth noting that probably only those O^- Brønsted sites are sensed by CO_2 which are located between the 12-membered ring pore and the Ti–O–Ti nanorods. The treatment with H_2O_2 leads to higher CO_2 desorption above 600 K, presumably due to the formation of additional isolated hydroxyl groups, e.g., after extraction of Ti atoms together with next-neighbor SiO_4 tetrahedra [26]. This is also consistent with the observed decrease of this peak after calcination due to the expected surface dehydroxylation resulting from the high-temperature treatment. The obtained surface basic site density and corresponding intrinsic adsorption capacity are presented in Table 2.

Surface characterization of the ETS-10-based titanosilicates by ^{29}Si MAS NMR

For quantitative analysis of the surface groups present in the titanosilicates before and after treatment, ^{29}Si MAS NMR was used. Figure 13A demonstrates the measured high-power decoupled (HPDEC) spectra of the ETS-10-based samples. The spectrum of the Na,K-ETS-10 exhibits three distinguishable peaks at −95.1 ppm (A2), −96.8 ppm (A3) and at −103.8 ppm (A4) with calculated relative peak areas after deconvolution of 40, 40 and 20%, respectively (see Table 3). This is consistent with the structural data provided for ETS-10 in [23]. The two resonances at −95.1 ppm and −96.8 ppm are assigned to the Si bonded via O atoms to three Si atoms and one Ti atom, i.e., Si(3Si, 1Ti). The third peak at −103.8 ppm originates from the Si coordinated through O atoms to other four Si atoms, i.e., Si(4Si, 0Ti). Due to the very low number of protons in the Na,K-ETS-10 sample, the signal is not observable in the respective cross-polarization (CP) spectrum presented in Figure 13B. It is worth mentioning that the CP technique facilitates polarization transfer from protons to silicon to acquire spectra of the latter.

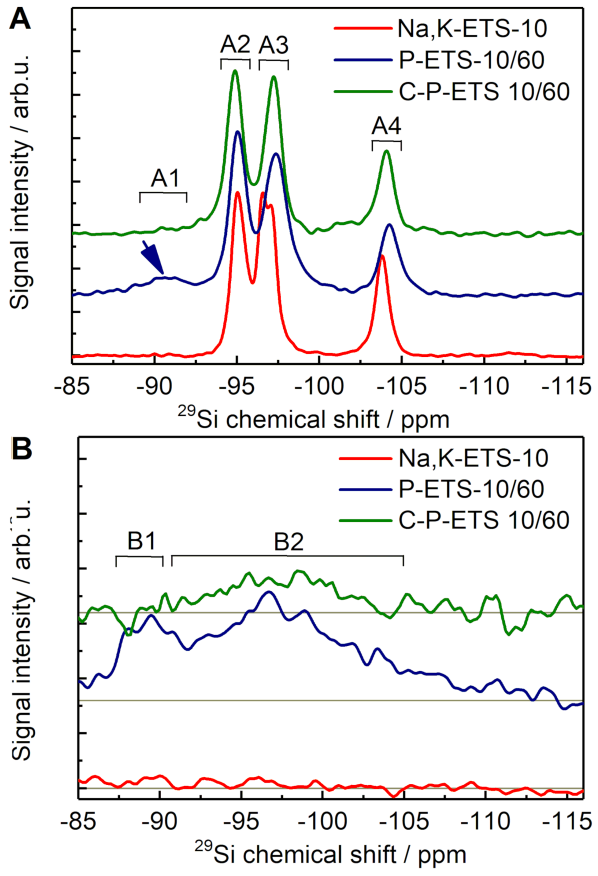


Figure 13: The HPDEC (A) and CP (B) ^{29}Si MAS NMR spectra obtained for Na,K-ETS-10 (red), P-ETS-10/60 (blue) and C-P-ETS 10/60 (green) at 12 kHz and 298 K. The arrow in (A) indicates a detectable signal centered at 90 ppm.

The HPDEC spectrum of the P-ETS-10/60 sample in Figure 13A shows four peaks in the range between −85 and −110 ppm, where the tetracoordinated Si might occur [49]. The presence of an additional peak at −90 ppm (A1) and a relative area of 6% was assigned to Si (2Si, 1Ti, 1OH) resulting from the intense surface hydroxylation after treatment of the titanosilicate with H_2O_2. This hypothesis was confirmed by efficient cross-polarization from the protons of the OH groups, accompanied by a significant enhancement of the signal at 90.0 ppm (B1) in Figure 13B. The rest of the signals in the CP spectrum of P-ETS-10/60 (B2) originate from the Si(3Si, 1Ti). The peaks at −95.0 ppm and −97.4 ppm of the HPDEC spectrum are similar to those seen for Na,K-ETS-10, i.e., coordinated as Si(3Si, 1Ti). They show relative areas of 43% and 34%, respectively. In comparison to the spectrum of Na,K-ETS-10,

Table 3: Assignment and estimated relative peak areas of the ^{29}Si MAS NMR peaks presented in Figure 13A.

Titanosilicate	Chemical shift / ppm	Peak labelling	Si coordination	Relative peak area[a]
Na,K-ETS-10	−90.0	A1	Si (2Si, 1Ti, 1OH)	0.002
	−95.0	A2	Si (3Si, 1Ti)	0.400
	−97.1	A3	Si (3Si, 1Ti)	0.401
	−103.9	A4	Si (4Si, 0Ti)	0.197
P-ETS-10/60	−90.0	A1	Si (2Si, 1Ti, 1OH)	0.058
	−95.0	A2	Si (3Si, 1Ti)	0.430
	−97.3	A3	Si (3Si, 1Ti)	0.339
	−104.2	A4	Si (4Si, 0Ti)	0.172
C-P-ETS-10/60	−90.0	A1	Si (2Si, 1Ti, 1OH)	0.023
	−95.0	A2	Si (3Si, 1Ti)	0.486
	−97.3	A3	Si (3Si, 1Ti)	0.307
	−104.2	A4	Si (4Si, 0Ti)	0.184

[a]Calculated after peak deconvolution.

the intensity of the peak centered at −97.3 ppm is reduced due to the partial hydroxylation of the silicon atoms after treatment. In the CP spectrum, the hydroxylated species of Si(3Si, 0Ti, 1OH) exhibit a broad peak at −96.4 ppm, while in the HPDEC spectrum they are not visible, probably due to the low intensity and the resonance overlap with the highly abundant Si(3Si, 1Ti) species. The peak at −104.2 ppm is assigned to Si(4Si, 0Ti) and has a slightly reduced relative area of 17%. The loss in silicon atoms with this resonance comes mainly from the hydroxylation that shifts the peak of the resulting species to −96.4 ppm.

The HPDEC spectrum of the C-P-ETS-10/60 material in Figure 13A clearly shows that the Si(2Si, 1Ti, 1OH) species at −90.0 ppm have vanished. In the CP spectrum in Figure 13B, this is confirmed by the absence of the respective peak at −90 ppm. Within the detection limit of the experiments, this suggests that the OH groups have been removed during the calcination for the case of Si(2Si, 1Ti, 1OH). At the same time, the signal at −95.0 ppm reached an area of 49%. This increase after calcination presumably comes from the formation of Si(3Si, 1Ti) at a chemical shift of −95.0 ppm from the available number of Si(2Si, 1Ti, 1OH) species. The area of the peak at −96.2 ppm is lower compared to the same one measured for P-ETS-10/60 due to smaller overlapping signal of Si(3Si, 0Ti, 1OH) seen after calcination. In the CP spectrum, the impact of the polarization transfer to the species of Si(3Si, 0Ti, 1OH) from the OH groups is still seen, leading to a broad peak at −95.5 ppm with lower intensity than prior to calcination. This suggests that dehydroxylation of Si with adjacent Ti is more effective than for the species surrounded by four Si atoms. In the HPDEC spectrum, the peak at −104.2 ppm, which is assigned to Si(4Si, 0Ti), has a slightly higher relative area of 18% after calcination. This increase might come from the additional formation of Si(4Si, 0Ti) from the previously hydroxylated species after calcination. For convenience, the assigned elements are illustrated in Figure S13 (A-C) of Supporting Information File 1.

The state of Ti sites probed by EPR spectroscopy

It has been demonstrated that application of post-synthetic treatment to titanosilicates can change the state of titanium atoms from Ti(IV) to catalytically active Ti(III) [50]. Such a reduction to paramagnetic Ti in ETS-10 titanosilicates can occur as a result of high-temperature treatment under vacuum [51], treatment with H_2 or CO at moderate to high temperatures [52], ion exchange [53,54], UV [55] or γ-irradiation [51]. To characterize the state of Ti in the titanosilicates participating in catalytic tests and the possible presence of impurities, the EPR spectra of these samples were measured at 70 K (Figure 14).

The spectrum of the parent K,Na-ETS-10 expectedly showed no signals of Ti(III) around 3500 G due to its oxidation state Ti(IV), which is diamagnetic and thus EPR-silent. Both samples, C-P-ETS-10/60 and P-ETS-10/60, display a typical signal of high spin Fe(III) of dispersed paramagnetic centers. Their g-value of 4.3 is indicative of a large axial zero-field splitting (ZFS) parameter (D >> 10 GHz) and a ratio between rhombic and axial ZFS of 1/3. Such Fe(III) centers have been commonly observed in zeolite and silica materials and were assigned to iron sites with a distorted tetrahedral coordination geometry [56,57]. In addition, P-ETS-10/60 exhibits signals at g = 2.069 and g = 2.008, which can be assigned to peroxy radicals Si–O–O$^{\bullet}$ (peak EPR-1) and non-bridging oxygen Si–O$^{\bullet}$ (peak EPR-2) resulting from the desilication process [58], respective-

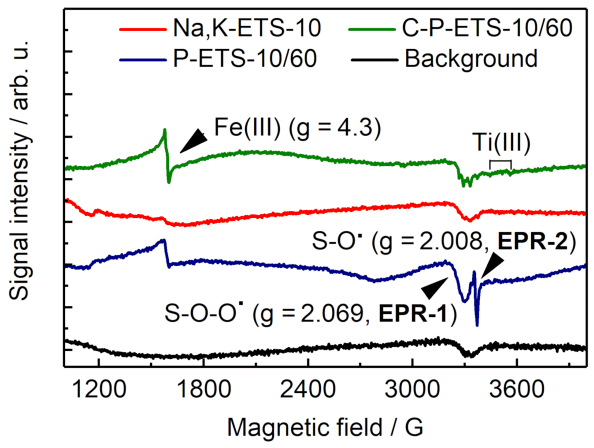


Figure 14: The EPR spectra measured with Na,K-ETS-10 (red), P-ETS-10/60 (blue) and C-P-ETS-10/60 (green) at 70 K. The background spectrum taken on an empty sample tube is presented for comparison (black).

ly. It is worth noting that no EPR signals from Ti(III) species with typical g values in the range of 1.89–1.97 were observed for all investigated materials. This suggests that the presence of the paramagnetic Ti(III) in the treated titanosilicates is negligibly small.

Variable temperature and 2D-exchange hyperpolarized ^{129}Xe NMR experiments for probing the interconnectivity between micro-, meso- and macropores in titanosilicates

The introduction of mesopores after the post-synthetic treatment into initially microporous material does not necessarily lead to the organization of micro- and mesopores in a hierarchical manner. A prominent example is the dealumination of the USY zeolite by steaming as reported in [59], which leads to the appearance of separated domains of micropores and mesopores as large as several micrometers. In such a case, it is expected that a significant portion of the mesopores might be not accessible for bulky reactants, such as triolein, being too large to diffuse through the micropores. In the case of treatment of ETS-10 titanosilicates with H_2O_2 at elevated temperatures, if accompanied by microexplosions [39], the appearance of such domains is possible. To address this, a number of NMR experiments with adsorbed Xe possessing a polarizability that is high enough to distinguish between micro-, meso-, and macropores were conducted [60]. The respective signals of Xe differing by the chemical shift, under the assumption of a slow or moderate chemical exchange between different types of pores, would deliver quantitative information on their interconnectivity [61,62].

Figure 15 represents the spectra from variable temperature experiments using the hyperpolarized ^{129}Xe gas. The signals at 0 ppm are assigned to free Xe gas in the detectable part of the space above the sample compartment and to Xe located be-

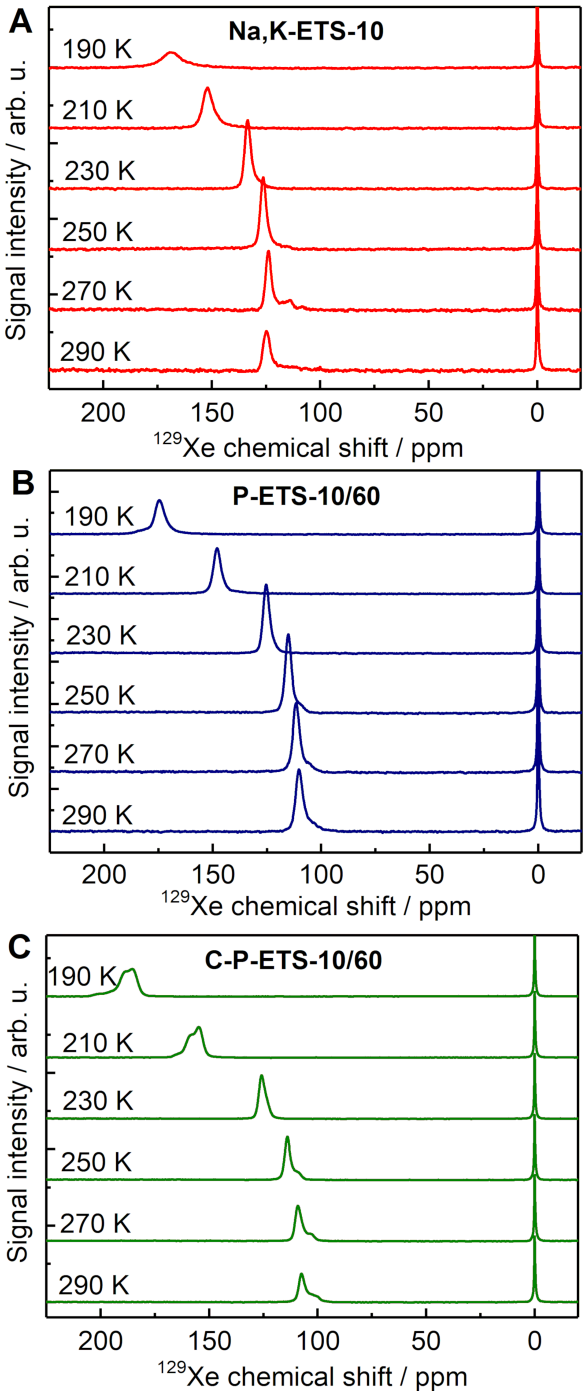


Figure 15: Variable temperature HP ^{129}Xe NMR spectra acquired on Na,K-ETS-10 (A, red), P-ETS-10/60 (B, blue) and C-P-ETS-10/60 (C, green). The chemical shift scale is referenced to the signal of free Xe gas measured in an empty tube at 290 K.

tween the crystals. Other signals at higher ppm values are assigned to Xe adsorbed inside pores of titanosilicates. In the case of Na,K-ETS-10 (Figure 15A), the chemical shift of adsorbed Xe shifts monotonically from 125 ppm at 290 K to 169 ppm at 190 K due to growing Xe density with decreasing temperature. The peak is assigned to Xe adsorbed in the 12-member rings, while the 7-member ring, according to [63], is not accessible. For P-ETS-10/60, for all temperature ranges studied, one peak with a chemical shift extending from 110 ppm to 174 ppm is observed (Figure 15B). If the presence of mesopores can be confirmed by N_2 sorption and Hg porosimetry, this result might originate solely from the rapid Xe exchange between micro- and mesopores highly interconnected to each other. An alternative explanation that the appearance of mesopores with multiple surface hydroxyl groups are not accessible for Xe due to too low hydrophobicity seems to be improbable. A similar observation is seen for C-P-ETS-10/60 with a Xe chemical shift variation from 108 ppm to 185 ppm, as presented in Figure 15C. However, another signal with a very close chemical shift value can be identified. This signal might originate from Xe penetration into the 7-member ring pores, and the amount of present OH groups of which might decrease after calcination, thus enhancing their accessibility. Earlier, it was demonstrated that Xe can squeeze into the pores with dimension as small as 0.37 nm [64]. Two-dimensional exchange spectroscopy (EXSY) experiments were conducted to probe the exchange between the micro-/mesopores and of the space between the crystals. The aim here was to investigate the possible presence of barriers on diffusion for molecules entering or exiting the pore space of the titanosilicate crystals [65]. All studied titanosilicates demonstrated detectable cross-peaks for 100 ms mixing time originating from the entering and exiting Xe, suggesting sufficient exchange on this time scale (see Figures S12 of Supporting Information File 1).

Probing the mesopore accessibility for triolein using PFG NMR with ultrahigh gradients

Post-synthetic modification has resulted in the appearance of a fraction of mesopores ranging from a few to a few tens of nanometers (see, e.g., Figure 9B). This size is large enough to accommodate the long-chain triolein or methyl oleate with a largest dimension of ≈2.5 nm of a single aliphatic part and a certain degree of chain flexibility [66]. However, the data of N_2 sorption or CO_2-/NH_3-TPD do not guarantee that the mesopores will become accessible for these molecules in a reaction. In our recent study [67], we demonstrated the applicability of pulsed-field gradient (PFG) NMR spectroscopy for measuring self-diffusion coefficients of the long-chain hydrocarbons (up to C19) confined to the nanopores of a catalyst. Here, we attempted to use this approach for clarification of the mesopore accessibility by the direct diffusion measurement using triolein. Due to the unique design of the probe (combination of the ultrahigh field gradients with the possibility of temperature control up to 463 K), it became possible to probe diffusion of nanoscopically confined triolein ($C_{57}H_{104}O_6$) at 403 K resembling temperature used during the catalytic tests.

Figure 16 demonstrates the measured diffusion attenuation curve for triolein in C-P-ETS-10/60, which could be satisfactorily fitted using Equation 2 and a sum of three diffusion modes. The result of the fitting procedure is presented in Table 4. In the utilized oversaturated sample, that is, when the bulk excess was present, one component (the fastest amongst all others and labelled as "1") shall be assigned to the diffusion of the bulk triolein. This value was also measured in a separate experiment with triolein only, resulting in 2.0×10^{-10} m^2 s^{-1} (see the dashed line in Figure 16) and was fixed during the fitting procedure. The second mode "2" (with diffusivity 2.9×10^{-11} m^2 s^{-1}) presumably originates from the diffusion between the ETS-10 crystals and the film diffusion on the surface of the crystals. It is approximately one order of magnitude lower than the bulk diffusivity. The mode revealing the slowest diffusion (1.9×10^{-12} m^2 s^{-1}) was assigned to triolein located within the mesopores of ETS-10 crystals. The root mean squared displacement (RMSD) estimated using the Einstein relation resulted in 0.5 µm, which is much smaller than the average crystal size measured by laser diffraction (≈30 µm). This suggests that the mode "3" represents intrinsic intracrystalline diffusivity with a negligibly small influence of the possible diffusion exchange with the intercrystalline space during the used diffusion time (20 ms). It is worth mentioning that in both catalysts, microporous Na,K-ETS-10 and micro–mesoporous P-ETS-10/60, the amount of triolein was below the detection

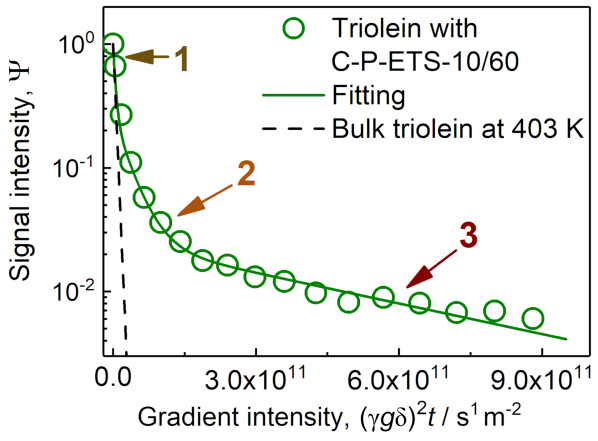


Figure 16: ^{1}H PFG NMR diffusion attenuation curves of bulk triolein (dashed line) and triolein in oversaturated C-P-ETS-10/60 titanosilicate at 403 K. The solid line represents converged fitting using Equation 2 with i = 3. The ranges where the corresponding diffusion mode dominates are shown by the arrows.

limit. While for the microporous titanosilicate it was expected that the too small pores prohibit accommodation of triolein molecules. For P-ETS-10/60 this might result from the decreased surface hydrophobicity (as seen by the ^{29}Si NMR and indirectly by the NH_3-TPD), preventing efficient diffusion into the mesopores of the crystals. The discussed scenarios are illustrated in Figure 17 with representation of the respective diffusion modes. To the best of our knowledge, this study represents the first direct measurement of the self-diffusion coefficient of (any) triglyceride or oil (as their mixture) confined to nanopores of (any) catalyst.

Table 4: Result of the fitting of the data presented in Figure 16: the self-diffusion coefficients and the resulting root mean squared displacements (RMSDs).

Diffusion mode	Self-diffusion coefficient / $m^2\ s^{-1}$	RMSD / μm
1 (fast)	2.0×10^{-10}	4.91
2 (intermediate)	$(2.9 \pm 0.2) \times 10^{-11}$	1.9 ± 0.1[a]
3 (slow)	$(1.9 \pm 0.3) \times 10^{-12}$	0.5 ± 0.1[a]

[a]The upper uncertainty limit of the RMSD is taken to be equal to the lower one, which is larger.

Based on the results of NH_3-TPD, CO_2-TPD, ^{29}Si MAS NMR, EPR and PFG NMR, the structures of the titanosilicates with summarized significant elements (e.g., acid and basic sites as seen by TPD, structural defects caused by post-synthetic treatment, presence of hydroxyl groups, pore accessibility for triolein) are presented in Figure S13 of Supporting Information File 1.

Transesterification of triolein to methyl oleate over the CaO- and ETS-10-based catalysts

Prior to catalytic experiments with titanosilicates, the conversion of triolein was tested over CaO as the reference and well-studied for transesterification of various triglycerides with methanol, mostly for biodiesel production [68-74]. Additionally, the goal was to have the identical reaction conditions in experiments with titanosilicates for the possibility of direct comparison. Depending on the activation (calcination) conditions, the activity of the CaO-based catalysts was observed to depend strongly on the calcination temperature. In [74], an increase in the yield of FAME from 17 to 85% after 5.5 h of reaction time was observed upon the change of the calcination temperature from 773 to 1173 K. This trend was observed in multiple reports in which CaO was used [73]. It is associated with the minimization of $Ca(OH)_2$ and $CaCO_3$ during calcination, which have lower activity compared to CaO. However, after a certain calcination temperature corresponding to the highest possible activity, a decrease in the activity for the catalyst calcined at even higher temperatures was reported [70,71]. This decrease is attributed to the loss of accessible surface area resulting from the partial sintering of CaO crystals at high calcination temperatures (usually above 1100 K). A similar observation was found for catalysts prepared and used in the present study. In Figure 18A, the catalyst CaO-800 calcined at 1073 K exhibited the highest conversion of triolein amongst those tested, that is, 79% after 4 h of reaction. This value is consistent with the reported FAME yields in the transesterification of sunflower oil with methanol at 393 K over the catalyst identically prepared and calcined at 1173 K (presented by squares for comparison). The CaO-900 and Ca-1000 reached 57% and 51% of conver-

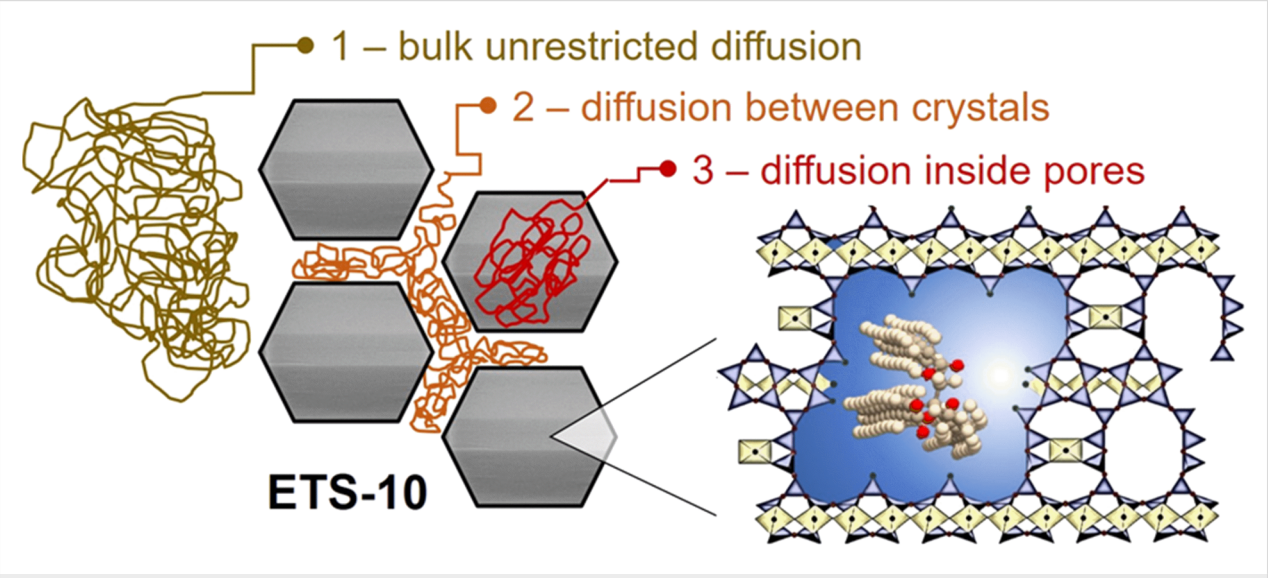


Figure 17: Schematic representation of the diffusion modes denoted as 1, 2 and 3 in the Figure 16 as observed by PFG NMR. The inset represents part of the treated ETS-10 framework with triolein inside it. The sketched trajectories are not to scale – see Table 4 for measured RMSD values.

sion after 4 h, respectively. The observed lower conversion with increasing catalyst calcination temperature is consistent with the SEM and N_2 sorption results, demonstrating a decrease in the specific surface area (see Table S4 of Supporting Information File 1).

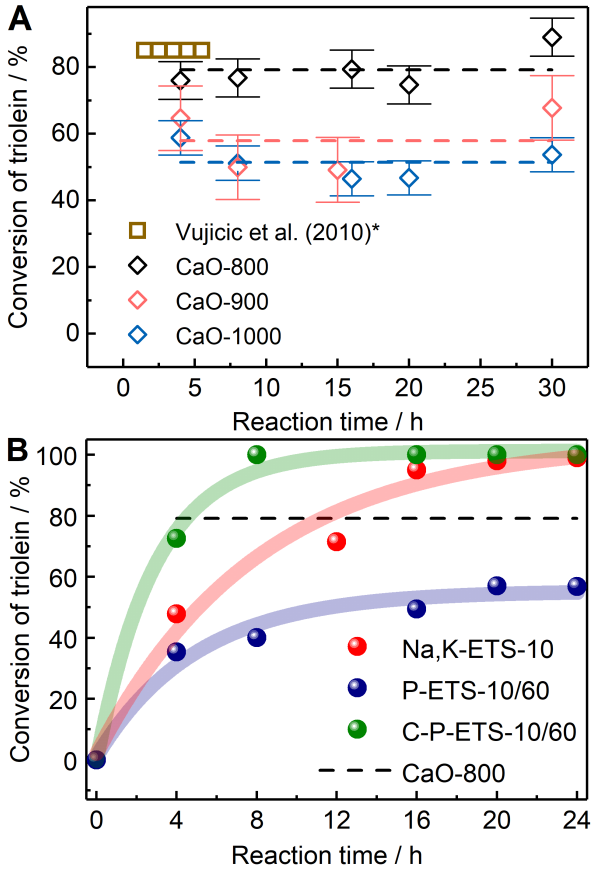


Figure 18: Conversion of triolein over CaO- (A) and ETS-10-based (B) catalysts at 403 K measured for different reaction times. The dashed lines in A represents an average conversion for each catalyst calculated from the values obtained for different times assuming no time dependence. For comparison, the data obtained on the transesterification of sunflower oil (*recalculated for conversion of oil) at 393 K over CaO from [74] are presented. The dashed line in B was adapted from A and represents the conversion over the most active CaO catalyst (CaO-800). Semitransparent lines and conversions in B at time 0 h are used to guide the eye.

No further change in conversion was observed for reaction times higher than 4 h. The transesterification is a reversible process with possible back reactions to form mono-, di-, or triglycerides. In [75], it was demonstrated that the biodiesel yield over the CaO catalyst can be improved by introducing excess amounts of methanol to force the reaction towards the formation of biodiesel, that is, by increasing the methanol-to-triglyceride molar ratio. When this ratio reached 9:1, the yield reached the maximum value with no further increase. In the present study, a 36:1 ratio was selected to assure negligible impact of the back reaction on the measured triolein conversions. Thus, the observed catalyst deactivation was attributed to the problem of catalyst leaching during the course of the reaction [76].

The results of the catalytic studies with the prepared titanosilicates are presented in Figure 18B. The parent Na,K-ETS-10 showed 48% of conversion after 4 h of reaction. The conversion continued to increase, reaching 100% after 20 h. This activity seems to be slightly lower than those reported in the literature, in which ETS-10 catalysts were used in transesterification reactions with various triglycerides at comparable temperatures [20,77,78]. For example, in [20], 80% of the conversion has been achieved after 2 h at 393 K. It should be mentioned, however, that it was achieved under the permanent stirring conditions and with the catalyst from the former Engelhard Corporation (Iselin, NJ) having an average crystal size ranging from a few hundred nanometers [50] to a few micrometers [79]. In the conducted catalytic tests, the tube was shaken only once and left undisturbed for the entire reaction time. In addition, the average crystal size of the prepared Na,K-ETS-10 was 30 µm, reducing the accessible surface area outside the crystal per mass of a catalyst compared to the commercial ones.

The introduction of mesopores by treatment with H_2O_2 aimed at increasing the total accessible surface area of the catalysts; for P-ETS-10, it led to the lower activity compared to the microporous Na,K-ETS-10. The maximum conversion of 57% was reached only after 20 h of reaction. This observation, being counterintuitive at a first glance, can be explained by the reduced hydrophobicity of the surface after treatment, also on the outer crystal surface. This is consistent with the absence of detectable adsorbed triolein inside the pores of P-ETS-10. A similar effect has been observed in [80] for the methyl oleate epoxidation with H_2O_2 over the parent (microporous) and alkaline treated (hierarchical) titanium silicalite-1. Despite the mesopores present in the treated sample, the conversion of methyl oleate decreased by ≈50%, which has been attributed to the decreased hydrophobicity after treatment. To address this effect directly, further studies including the measurement of water sorption isotherms to obtain the "hydrophilicity index" according to Thommes et al. [81] are planned.

In the case of the calcined hierarchical titanosilicate C-P-ETS-10, a dramatic increase in activity is observed, as compared to Na,K-ETS-10 and P-ETS-10/60, showing full conversion already after 8 h. After 4 h, the conversion of triolein reaches ≈73%, becoming comparable to that of CaO-800 (≈76%). The latter remains unchanged over the time, while the C-P-ETS-10 exhibits a further increase up to 100%. The observation of such activity appeared despite the lowest surface

basic site density and intrinsic base adsorption capacity amongst the tested titanosilicates measured by CO_2-TPD. It is worth mentioning that CO_2-TPD does not distinguish between the surface of micro- and mesopores, while the active sites (the Brønsted strong basic sites) located only in mesopores can be accessible during the reaction. Thus, the "effective" basicity seen by the reactants might differ from the measured values. In addition to this, as is evident from the results of DTA and ^{29}Si NMR, calcination leads to the partial surface dehydroxylation. This might improve the accessibility of mesopores for triolein via the increased surface hydrophobicity. Additionally, the hydrophobicity of the outer crystal surface is expected to be restored after calcination, adding to the resulting activity of the C-P-ETS-10/60 catalyst.

Using the obtained self-diffusion coefficient of pure triolein inside the mesopores of C-P-ETS-10 at 403 K, a simple estimate results in ≈150 s for the upper time limit needed to cross a crystal with 30 μm size. This value, which under the reaction conditions might become lower due to the presence of methyl oleate and methanol, is much smaller than the time needed to reach full conversion (8 h). As it has been reported in [82], for the hydrogenation of 1,3,5-triisopropylbenzene with a critical diameter of ≈0.95 nm over the Pt supported on controlled pore glass with 80 nm pore width and particle size of 50–100 μm at 373 K, a clear indication of diffusion limitation was observed. Thus, with the larger size of triolein and the smaller average mesopore size (≈30 nm) of C-P-ETS-10/60, it can be expected that the reaction will be diffusion limited under the applied conditions. However, in order to properly address this question, further studies with a variation of the particle sizes and more frequent sampling for obtaining the initial reaction rates are needed.

Conclusion

The applied hydrothermal synthesis of the microporous ETS-10 titanosilicate (Na,K-ETS-10) resulted in crystals with an average size of ≈30 μm without structural defects visible by SEM and TEM, but with the presence of a small fraction (less than 5%) of alternative phases (such as ETS-4, AM-1, or quartz) appearing as side products. This was confirmed by X-ray diffractograms and TEM, revealing the high crystallinity of the material.

Post-synthetic treatment with H_2O_2 at 423 K led to the successful introduction of mesopores in the range of 4–40 nm interconnected with the micropores in a hierarchical manner. The latter has been confirmed in the hyperpolarized ^{129}Xe NMR experiments by monitoring the fast Xe exchange between micro- and mesopores on a timescale of microseconds. Along with this, such a treatment is accompanied by the appearance of additional OH groups on the surface of the created mesopores originating from the partial removal of TiO_6 octahedra and SiO_4 tetrahedra from the framework and subsequent protonation of the oxygen radicals. The quantitative information of the surface modification was obtained from the ^{29}Si MAS NMR experiments. This step led to a 2.6-fold increase of the intrinsic acid adsorption capacity of the treated catalyst (P-ETS-10/60) compared to the Na,K-ETS-10 as probed by NH_3-TPD, presumably due to intense surface hydroxylation, and therefore, reduction in hydrophobicity. The latter has led to an even lower activity compared to the parent titanosilicate. The basicity probed by CO_2-TPD exhibited two peaks for Na,K-ETS-10 that were assigned to the Na,K-cations as weak Lewis bases in the low-temperature region and to the strong Brønsted basic oxygen atoms coordinated as Si–O–Ti in the framework. The application of the H_2O_2 treatment only slightly affected the intrinsic base adsorption capacity, while shifting the CO_2 desorption to temperatures above 600 K.

The subsequent calcination of the H_2O_2 treated titanosilicate has led to notable surface dehydroxylation while preserving mechanical stability, high material crystallinity and a hierarchical pore network. The surface basicity after calcination as probed by CO_2-TPD was found to be the lowest amongst other titanosilicates. Despite this, the activity of the catalyst in the triolein transesterification was observed to be higher than that of the Na,K-ETS-10 and P-ETS-10/60. This result was assigned to the drastically improved accessibility of the active sites on the surface of the mesopores for reactants, which was also confirmed by the direct diffusion measurements using PFG NMR with ultrahigh gradients. Further comparison of the triolein conversion with CaO-based catalysts tested under the same conditions revealed comparable values after 4 h of the reaction course, i.e., 73% and 76% for the calcined hierarchical ETS-10 and CaO catalysts, respectively. Remarkably, while the conversion over the latter did not further change due to stability issues, an ETS-10-based catalyst revealed achievement of 100% already after 8 h. This observation suggests that the ETS-10 titanosilicates, when appropriately treated, exhibit comparable behavior to the CaO catalysts activity in the heterogeneously catalyzed transesterification of triglycerides, but may outperform them in terms of stability and ability for regeneration.

Experimental

Materials and chemicals used in the preparation of CaO- and ETS-10-based catalysts

Calcium oxide of technical grade (Centrochem Co., Serbia) was used as a precursor in the preparation of CaO-based catalysts. For the preparation of ETS-10, sodium silicate (Na_2SiO_3,

34.5–36.0 wt % SiO_2, 17–19 wt % Na_2O, donated by PQ corporation), titanium isopropoxide (TIP, 97 wt %, Sigma-Aldrich), hydrochloric acid (HCl, 35–37 wt %, VWR Chemicals), sodium chloride (high-purity grade, VWR Chemicals), and potassium fluoride (KF, ≥99 wt %, Fluka, Sigma-Aldrich) were used. In the post-synthetic treatment of ETS-10, hydrogen peroxide (H_2O_2, 30 wt %, Merck Millipore) and distilled deionized water (DDW, 0.055 µS conductivity, PureLab flex 3 & 4 water purification systems) were used.

Chemicals used in the transesterification reaction and gas chromatography

Triolein (>99 wt %, Sigma-Aldrich) and methanol (99 wt %, VWR corporation) were used in the transesterification reaction. Methyl oleate (>99 wt %, Sigma-Aldrich), 1,3-diolein (>99 wt %, Sigma-Aldrich), 1-oleoyl-*rac*-glycerol (≥99 wt % monolein, Sigma-Aldrich), and glycerol (99 wt %, Sigma-Aldrich) were used for calibration of analytes. All mentioned materials and chemicals were used without further purification.

Preparation of the CaO-based catalysts

The CaO precursors were activated at temperatures of 1073 K, 1173 K, and 1273 K for 3 h under static air conditions in the Elektron Co. furnace. After calcination, the catalysts were kept in a desiccator. The obtained catalysts were denoted according to the applied calcination temperatures as CaO-800, CaO-900, and CaO-1000, respectively.

The CaO-based catalysts were then shaped into pellets by using a hydraulic press (Womax Co.) at a pressure of 5 t. Afterwards, the pellets were ground and sieved in order to obtain fractions between 1.0 and 1.5 µm.

Preparation of ETS-10-based catalysts

ETS-10 molecular sieves were prepared by hydrothermal synthesis following a reported procedure [32]. Initially, a visually transparent silica-containing solution was prepared by dilution of the 9.8 mL aqueous solution of 51–55 wt % Na_2SiO_3 with 45.2 mL of DDW in a 250 mL flask. An aqueous solution of NaCl (3.4 g of NaCl dissolved in 10.0 mL of DDW) was subsequently added into the flask with the silica-containing solution in it. A titania-containing solution was prepared by dissolving 5.4 mL TIP and 3.0 mL HCl in 12.6 mL DDW in a 100 mL flask. Both the silica- and titania-containing solutions were prepared under vigorous stirring for 2 h at room temperature.

The prepared titania-containing solution was then added dropwise using a pipette into the silica-containing solution while stirring, resulting in the appearance of an opaque mixture. After this, the mixture was stirred for 1 h at room temperature. A KF-solution was prepared by dissolution of 0.1 g of KF in 2.5 mL of DDW, resulting in a 0.0011 g mL^{-1} concentration. The prepared amount of a KF solution was further added into 87.5 mL of the titania/silica-containing solution. The resulting molar composition of the obtained 90 mL solution is the following $SiO_2/TiO_2/HCl/Na_2O/NaCl/KF/H_2O$ = 5.56:1:1.94:2.64:3.22:0.09:216.

The solution was then further aged for 16 h in a flask at room temperature for polymerization to obtain –[–Ti–O–Ti–]–, –[–Si–O–Si–]–, and –[–Ti–O–Si–]– containing seeds. After aging, the 90 mL solution was divided into two 45 mL parts, each of which was placed into the 70 mL polytetrafluoroethylene (PTFE) reactor. The reactor was closed with a PTFE cap and inserted into a homemade stainless steel autoclave. The design of the autoclave is similar to a standard acid digestion vessel. The autoclave was then closed with a stainless steel screw-tightened cap. Both autoclaves were placed simultaneously into a preheated (473 K) VWR dry air convection oven and kept inside for 96 h at this temperature. Afterwards, the autoclaves were removed from the oven and quenched in cold water down to room temperature. A white powder was observed at the bottom of the reactor. The solutions from the reactor containers were transferred to 50 mL centrifuge tubes for further centrifugation for 10 min at 3000 rpm in a Thermoscientifc Heraeus Megafuge 8 centrifuge. Three washing steps with DDW and a subsequent centrifugation step were taken for the removal of residual components remaining after synthesis. In a final step, the powder was dried in a convection oven at 423 K for 24 h. Then, the pre-dried powder was placed into the vacuum oven and kept inside at 1 kPa pressure and 373 K for 24 h to remove residual moisture, which might be present inside the pores. The obtained titanosilicate was denoted as Na,K-ETS-10.

A graphical sketch of the synthesis procedure and calculations of the mixture volumes are provided in section S1 of Supporting Information File 1.

Variation of KF- and HCl during synthesis

The ETS-4 phases were minimized in the as-synthesized ETS-10 by varying the HCl concentration from 0.033, 0.044, 0.047 to 0.05 g mL^{-1} (3, 4, 4.2, 4.6 mL) in the solution (see section S6 of Supporting Information File 1). This implies that four 90 mL solutions were prepared with four different HCl concentrations. The procedure followed was reported by Lv et al. [29]. The addition of a HCl step was carried out similar as mentioned in the section before. After preparing the 90 mL solution, the pH value was determined using a Mettler-Toledo Seven Go DuoPro with a Mettler Toledo InLab Expert Pro ISM IP67 sensor probe. The remaining steps for the preparation were similar as mentioned in the section before.

Another investigation was also carried out to minimize AM-1 along with ETS-4 in the Na,K-ETS-10 (see section S7 of Supporting Information File 1). The crystallization of different titanosilicate phases were observed by varying the concentration of KF and HCl in the different synthesis solutions. The concentration for HCl was varied from 0.026 g mL^{-1} to 0.068 g mL^{-1} in the 90 mL solution while keeping the KF concentration constant. Similarly, the concentration of KF was varied from 0.007 g mL^{-1} to 0.026 g mL^{-1} in the 90 mL solution while keeping HCl constant. Table 5 summarizes the concentrations of KF and HCl and corresponding pH values.

Procedure of the post-synthetic treatment with H_2O_2

Post-synthetic treatment by H_2O_2 was performed following the procedure reported in [26]. 200 mg of predried as-synthesized ETS-10 powder and 20 mL of 30 wt % aqueous H_2O_2 solution were loaded into a 90 mL PTFE reactor, which was inserted into a stainless steel autoclave and closed. The autoclave was put into the preheated to 423 K oven. The treatment was carried out in three autoclaves separately over 30 min, 45 min and 60 min. After the required duration, each autoclave was quenched with cold water down to room temperature and opened. The mixture in the reactor had a yellow color. Each sample was transferred to the centrifuge tube, washed with DDW and centrifuged at 3000 rpm three times. The centrifuged powders were finally dried in a convection oven at 423 K for 24 h. Afterwards, they were placed in a vacuum oven and further dried at 1 kPa and 373 K for 24 h to remove possible residual moisture. The post-synthetically treated samples were denoted as P-ETS-10/30, P-ETS-10/45, P-ETS-10/60 (where "P" stands for post-synthetically treated) according to corresponding treatment times of 30, 45 and 60 min, respectively.

Calcination procedure

The catalyst P-ETS-10/60 underwent calcination (≈1 g) in a ceramic crucible. The calcination took place inside a NaberTherm® P 300 muffle oven. The catalyst was not exposed to any thermal treatment prior to calcination. The calcination temperature of 873 K was reached with a ramp rate of 10 K min^{-1}, after which the target temperature was held for 6 h. After this, the ramp rate for cooling was set at 10 K min^{-1}. After room temperature was reached, the crucible was taken out of the muffle oven. The resulting material was labelled as C-P-ETS-10/60.

Catalytic experiments

The catalytic reaction procedure was identical for all catalysts used in the transesterification reaction (CaO-800, CaO-900, CaO-1000, Na,K-ETS-10, P-ETS-10/60 and C-P-ETS-10/60). The reaction was carried out in sealed glass cylindrical tubes with a 7 mm inner diameter and 70 mm length resulting in 2.4 mL of available volume. A similar procedure was used in [20] to prevent methanol from evaporating during the course of reaction. The constituents of the reaction were added, after which the tube was quickly (<30 s) flame-sealed. 54 mg of a solid predried catalyst, 0.54 mL of triolein and 0.85 mL of methanol (measured at room temperature), resulting in a methanol/triolein molar ratio of 36:1, were used in all catalytic experiments.

After the glass tube was sealed, it was hand-shaken once during 15 s and loaded by ≈50 mm into the silicone oil bath preheated to 403 K; from this moment, the timing starts. The homogeneous heating of an oil bath (270 mL, 136 mm in diameter, 70 mm height) is provided by the 30 mm magnetic rod stirred using the IKA RCT basic magnetic stirrer at 600 rpm. An IKA ETS-D5 thermometer was used to control the temperature of the oil bath. After the desired reaction time, the tube was taken out

Table 5: Concentration of KF and HCl and the resulting pH values used for different batches (from A to T).

Batch	KF conc. / g mL^{-1}	HCl conc. / g mL^{-1}	pH (±0.2)	Batch	KF conc. / g mL^{-1}	HCl conc. / g mL^{-1}	pH (±0.2)
A	0.027	0.027	11.65	K	0.014	0.027	11.67
B	0.027	0.037	11.60	L	0.014	0.038	11.50
C	0.027	0.048	11.26	M	0.014	0.048	11.26
D	0.027	0.058	11.07	N	0.013	0.058	11.00
E	0.026	0.068	10.15	O	0.013	0.068	10.24
F	0.021	0.027	11.67	P	0.007	0.027	11.63
G	0.020	0.038	11.37	Q	0.007	0.038	11.48
H	0.020	0.048	11.27	R	0.007	0.048	11.11
I	0.020	0.058	10.80	S	0.007	0.058	10.70
J	0.020	0.068	10.05	T	0.007	0.068	9.97

of the bath, cooled down to room temperature and opened for further chromatographic analysis. Due to the initially poor miscibility of the triolein/methanol mixture, it is possible that after stopping the reaction, the mixture might remain still partly separated. This effect is expected to be less pronounced with the higher amount of methyl oleate formed. Thus, shortly before taking samples for analysis, the tube was again intensively shaken to minimize extraction of samples either from the triolein- or methanol-rich phases. After this, 10 µL of the reaction mixture was transferred to a centrifuge vial, preloaded with 3.2 mL of toluene and 0.013 mL dodecane. Toluene was used to promote dissolution of the reaction components, while dodecane was added as an internal standard for GC analysis. The solution, after the centrifugation for separation of the remaining catalyst, was transferred to another vial and analyzed by GC. To avoid the negative impact of sampling on the continuation of the reaction, the separate tubes were prepared (under the same contusions) for every reaction time studied.

Gas chromatographic analysis of the reaction mixtures used in the catalytic experiments was performed using a Shimadzu GC-2010 gas chromatograph equipped with a flame ionization detector (FID). For the separation of triolein and methyl oleate, an Rtx-Biodiesel TG capillary column (Restek, 10 m long, 0.32 mm inner diameter, 0.1 µm film thickness) was used. Nitrogen was used as the carrier gas at a flow rate of 2.14 mL min^{-1} with a purge flow rate of 3 mL min^{-1}. The calibration procedure is described in section S2 of Supporting Information File 1.

Powder X-ray diffraction

Powder X-ray diffraction (XRD) analysis of the CaO-based catalysts was performed using a Philips APD-1700 diffractometer with a monochromator and Cu anticathode in an angle diffraction span between 10 and 80° working at 55 mA and 40 kV. The crystallite sizes were calculated based on the data of the full width at diffraction line half maximum by using Scherrer's equation.

The XRD patterns of the titanosilicates were acquired on a Siemens D5000 diffractometer operating with Cu Kα radiation (λ = 0.15418 nm). The data were recorded in the 2θ range of 4–90° with a step of 0.05°. Approximately 100 mg of the solid sample was used in each experiment. The Miller indices of reflections obtained in the XRD patterns were analyzed using the "Match!" software.

Scanning electron microscopy

Scanning electron microscopy (SEM) of the CaO-based catalysts was performed on a JEOL JSM-6460LV microscope at an accelerating voltage of 25 kV and different magnifications up to 100,000×. The samples were prepared for measurement by coating with gold nanolayers using the ion-sputtering chamber.

The SEM images of the titanosilicates were acquired using a LEO GEMINI 1530 device by Zeiss GmbH operating at an acceleration voltage between 5 and 30 kV. Approximately 1 mg of the solid samples was utilized for microscopy. The samples were analyzed on a carbon film on top of an aluminum stub. The samples were sputtered with a gold film using a BALZERS CED 030 sputter coater. The "Image J" software was used to analyze the microscopy images. SEM was carried out at the IMKM, Universität Leipzig.

Energy dispersive X-ray spectroscopy (EDX) was carried out with an Oxford Instruments (Model No. 7426) device with an energy resolution of 138 eV. The system utilizes the "INCA" software for creating EDX energy maps. EDX was utilized to determine the silicon (Si), titanium (Ti), oxygen (O), sodium (Na) and potassium (K) amount in atomic percent (atom %). Each determination of the atomic composition was based on four measurements by calculating the average atom %. The samples were sputtered with a carbon film.

Transmission electron microscopy

Transmission electron microscopy (TEM) was carried out using a JEM-2100Plus instrument from JEOL operating at an accelerating voltage of 200 kV. The images were taken with a 4K CMOS camera from TVIPS. The TEM is equipped with a LaB_6 cathode and high-resolution pole piece to achieve a point resolution in the TEM mode of 0.23 nm. The sample preparation was performed by grinding the sample in a mortar and pestle in ethanol and the dispersed particles were supported on a TEM lacey carbon grid.

Nitrogen sorption experiments

N_2 sorption isotherms were recorded at 77 K using a Micromeritics ASAP 2000 instrument. Before the measurements, the samples were degassed in vacuum (3×10^{-11} MPa) at 623 K for 8 h. The pore width distribution (PWD) in the mesopore range was calculated from the adsorption isotherms. The non-local density functional theory (NLDFT) kernel on silica (cylindrical pore, adsorption branch) in the "ASIQwin" software from Quantachrome Instruments was used for this purpose. In N_2 adsorption experiments, 51 points were measured in the range of relative pressure between P/P_0 = 0.05 (40 Torr) and P/P_0 = 0.99 (760 Torr). The Brunauer–Emmett–Teller (BET) method was applied to calculate the specific surface area (S_{BET}) from the adsorption branch of the isotherm in the relative pressure range of P/P_0 = 0.06–0.30. The specific micropore volume (V_{micro}) was deter-

mined using the *t*-plot method according to De Boer et al. [83] in the relative pressure range of P/P_0 = 0.15–0.50. The total pore volume (V_{Total}) was measured with the help of the Gurvich rule [84] at P/P_0 = 0.99. The mesopore volume (V_{meso}) was calculated by subtracting the V_{Total} by V_{micro}.

Mercury intrusion porosimetry

Mercury (Hg) intrusion porosimetry was carried out using a PASCAL 440 instrument reaching a maximum pressure of 400 MPa. Approximately 100 mg of a solid sample was used for characterization. The pore widths were calculated using the Washburn equation [85].

Laser diffraction

Particle size analysis was carried out using the CILAS 1064 diffractometer. Approximately 200 mg were used for each measurement. The obscurity level was maintained at three. The measurement of a background signal was done prior to each experiment. An intense rinsing of the suspension with water was carried out after every measurement to remove residual particles from the previous measurements.

Temperature-programmed desorption

Temperature-programmed desorption (TPD) experiments were carried out using an online Pfeiffer Vacuum quadrupole mass spectrometer (MS). The surface acid site and basic site density were determined using ammonia (NH_3) and carbon dioxide (CO_2) as probe molecules, respectively. After switching between probe gases, the instrument was flushed with the required gas for 24 h. The samples were flushed with 40 mL min^{-1} of (99 vol %) helium (He) from Air Liquide throughout the measurement process.

Prior to the TPD studies, ≈50 mg of the solid was placed into the reactor and pretreated at 573 K for 30 min. The sample was cooled down to different temperatures after pretreatment – to 363 K and 303 K in the case of NH_3 and CO_2, respectively. Loading with NH_3/CO_2 was carried out by purging the sample six times with doses of 1 mL min^{-1} for 1 min and then pulsing for 6 min. After purging, the samples were kept at that temperatures for 1.5 h to remove physisorbed NH_3/CO_2. For measuring the TPD profiles, the samples were heated at 10 K min^{-1} to 830 K, held for 30 min at 830 K and cooled to 303 K.

The desorbing gases were detected by a Pfeiffer Vacuum QME 200 mass spectrometer. For the detection of NH_3, the mass fragment with m/z = 15 was recorded. For the NH_3 oxidation products, N_2O and NO mass fragments with m/z = 44 and 30, respectively, were recorded. The surface acid site densities were calculated from the amounts of desorbed NH_3, N_2O and NO under the assumption that desorbed N_2O and NO were adsorbed as NH_3 in the catalyst before they were oxidized. For the detection of CO_2, the mass fragment with m/z = 44 was recorded. The surface basic site densities were calculated from the amount of desorbed CO_2. The accuracy of the TPD-NH_3/CO_2 method was estimated to be ±5%.

Differential thermal analysis

Differential thermal analysis was performed with 50 mg of the sample. The measurements were carried out on a Netzsch STA 409 TG/DTA cell coupled with a Balzers QMS 421 mass spectrometer equipped with a QMA 125 quadrupole analyzer system. The samples were analyzed in the temperature range of 283–1173 K with a heating rate of 278 K min^{-1} under an air stream.

Optical emission spectrometry by inductively coupled plasma spectroscopy

Inductively coupled plasma optical emission spectrometry (ICP-OES) was used to determine elemental composition (wt %) of Ti, Na and K in the samples. The PerkinElmer OPTIMA 8000 ICP-OES instrument includes a CCD array detector that captures the full wavelength range at a high speed but does not allow simultaneous wavelength measurements. The sample introduction system used was a Cross Flow / Scott atomizer. Prior to analysis, the powdered samples (maximum 50 mg) were digested in a PTFE vessel in a mixture of 2 mL hydrofluoric acid, 3 mL nitric acid and 3 mL hydrochloric acid. The digestion occurred with the help of an Anton Parr Multiwave 3000 microwave oven having 8 XF100 rotors for chemical extraction. The microwave oven was kept at 1400 W, producing an internal temperature in the PTFE reactor of 448 K for 70 min. After digestion, 12 mL of boric acid were added for the complexation of hydrofluoric acid. The mixture was again treated for 10 min at 448 K in the microwave oven. After further microwave treatment, a clear solution was obtained and diluted with distilled deionized water to reach 50 mL for the ICP-OES analysis.

^{1}H pulsed field gradient NMR

The diffusion experiments were performed using ^{1}H NMR on a wide-bore 9.4 T Bruker BioSpin spectrometer. It was equipped with a home-built gradient unit, producing ultrahigh *z*-gradients of up to 35 T/m in a 7 mm (outer diameter) NMR sample compartment.

Around 180 mg of the material (C-P-ETS-10/60) was loaded into the glass tube. The latter was then connected to a custom-built vacuum system, and the samples were activated under high vacuum (10^{-3} Pa) at 400 K overnight. After cooling to room temperature, the sample was saturated under vacuum by injection of triolein (99 wt %, Sigma-Aldrich). The amount of

liquid was chosen to be sufficient to cover the particles of the samples completely, i.e., oversaturated. This was done to ensure that all mesopores were completely filled. After loading, the NMR tubes were detached from the vacuum system and flame-sealed.

A 13-interval pulse sequence [86] was applied with the following parameters of the pulse sequence: τ = 2 ms, δ = 0.8 ms, and Δ = 20 ms. Here, τ is the spacing between the first two ($\pi/2$) pulses, δ is the effective duration of the gradient pulses, and Δ is the gradient pulse separation. The diffusion time t_d in this case is ≈20 ms. The signal accumulation was performed with a repetition of 5 times of T_1, where T_1 is the nuclear magnetic spin-lattice relaxation time of the component having the longest relaxation in the system.

The decrease of the measured NMR signal (Ψ) caused by diffusion for a system containing molecular ensembles (p_i) with different diffusion coefficients (D_i) and being in the slow (compared to the time of the experiment) diffusion exchange can be presented in the form [87]:

$$\Psi(g\delta,t_d) = \sum_i p_i \exp\left(-D_i\gamma^2 g^2 {t_d}^2\right) \quad (2)$$

where γ is the gyromagnetic ratio of the nucleus that is observed, g and δ are the amplitude and the duration of the gradient pulses, respectively, t_d is the effective diffusion time ($\Delta-\delta/6-\tau/2$ in the case of the 13-interval pulse sequence). Equation 2 gives a poly-exponential decay of the observed NMR signal, if i > 1.

^{29}Si solid-state magic angle spinning NMR

The ^{29}Si NMR spectra were recorded on a Bruker DRX-400 WB spectrometer (Bruker Biospin, Karlsruhe, Germany) with a 4 mm MAS BB/1H probe at a Larmor frequency of 79.49 MHz for ^{29}Si and 400.15 MHz for protons, respectively. All of the spectra were acquired at a spinning speed of 12 kHz and at a temperature of 293 K. The spectra were referenced externally to tetramethylsilane (TMS).

The $\pi/2$ pulse was calibrated at a radio-frequency (rf) field strength of 100 kHz for ^{1}H and 42 kHz for ^{29}Si, respectively. For the CP experiments, 1024 scans were accumulated using an acquisition time of 25 ms. For the CP transfer, a linear rf field of 42 kHz for ^{29}Si and a linearly ramped rf field ranging from 43 kHz to 62 kHz for protons within a contact time of 8 ms were applied. A recycle delay of 1 s was used. The spectral width was set to 32 kHz and the offset was placed at −50 ppm. During the acquisition, heteronuclear decoupling was achieved using a SW_f-TPPM [88] at an rf frequency of 100 kHz.

For the HPDEC experiments, 256 scans were accumulated at an rf field strength of 42 kHz as a $\pi/2$ pulse on ^{29}Si during an acquisition time of 25 ms. The spectra were obtained at a spinning speed of 12 kHz and a recycle delay of 40 s at a temperature of 293 K. The spectral width was set to 32 kHz and the offset was placed at −50 ppm. During the acquisition, heteronuclear decoupling was achieved using a SW_f-TPPM at an rf frequency of 100 kHz.

Hyperpolarized ^{129}Xe NMR

The hyperpolarized (HP) ^{129}Xe NMR spectra were recorded on a Bruker DRX-600 MHz spectrometer (Bruker Biospin, Karlsruhe, Germany) with a 5 mm TBI probe at a Larmor frequency of 166 MHz for ^{129}Xe. The hyperpolarization of Xe nuclei was achieved by spin-exchange optical pumping (SEOP) using a home-built polarizer in continuous-flow mode as described elsewhere [89]. The gas mixture consisted of 1.1% Xe (natural isotopic portions, Air Liquide, purity: 99.998%), 27.5% N_2 (Air Liquide, purity: 99.999%) and 71.4% He (Air Liquide, purity: 99.999%). The optical pumping cell contained rubidium (AlphaAesar, purity >99%). During the pumping process, the temperature was set to 423 K. The samples were dried for 14 h at 393 K and directly transferred to a standard 5 mm NMR tube equipped with a home-built gas insertion cap for continuous gas delivery.

For one-dimensional spectra, 32 scans were accumulated with an acquisition time of 60 ms, employing an rf field strength of 11 kHz for the ^{129}Xe $\pi/2$ pulse and a recycle delay of 15 s. The spectral width was set to 42 kHz and the offset was placed at 30 ppm. The temperature calibration for the variable-temperature (VT) experiments was performed based on the proton chemical shift of a methanol calibration sample provided by Bruker. The temperature points were set to 190 K, 210 K, 230 K, 250 K, 270 K and 290 K.

The EXSY experiments were recorded at a temperature of 293 K where 8 scans were acquired for each of the 32 points in the F1 dimension. The mixing times were set to 1 ms and 100 ms, respectively. The rf field strength of the 90° pulse on ^{129}Xe was 11 kHz, while the recycle delay was set to 7 s. The spectral width was set to 42 kHz and the offset was placed at 30 ppm in both dimensions.

For all spectra, the free gas signal was set to 0 ppm for referencing the chemical shifts. Due to alterations in filling height, packing density and polarization rate, the comparison of the absolute signal intensities between the samples cannot be made.

Electron paramagnetic resonance

CW EPR measurements were carried out using a Bruker EMXmicro X-band spectrometer (≈9.41 GHz) equipped with a Bruker ER4119HS cylindrical cavity resonator. For low-temperature measurements, an Oxford ESR 900 flow cryostat was used. All spectra were recorded at T = 70 K with a modulation amplitude of 0.4 mT and a microwave power of 2.0 mW. Before and during the measurements, the samples were kept under ambient atmosphere.

Supporting Information

Supporting Information File 1

Preparation and characterization of catalysts and performance of catalytic tests.
[https://www.beilstein-journals.org/bjnano/content/supplementary/2190-4286-10-200-S1.pdf]

Acknowledgements

M.D. gratefully acknowledges the DFG research grants DV 58/2-1 and DV 58/2-2 for financial support. M.A.Z. acknowledges the DAAD scholarship programme GSSP 57034101. A.Z. and R.Lj. acknowledge the Erasmus+ Key Action 1 programme and Prof. Dr. Evamarie Hey-Hawkins for the financial support. Discussions with Alexander Grimm are gratefully acknowledged. The bottle graphics and the molecules in the graphical abstract are reproduced from PixelSquid (https://learn.pixelsquid.com/pixelsquid-royalty-free-license/).

ORCID® iDs

Muhammad A. Zaheer - https://orcid.org/0000-0002-6872-2486
Marianne Wenzel - https://orcid.org/0000-0001-9092-0879
Jörg Matysik - https://orcid.org/0000-0002-7800-7443
Radomir Ljupkovic - https://orcid.org/0000-0002-5828-1816
Alexander A. Karavaev - https://orcid.org/0000-0002-3258-9126
Roger Gläser - https://orcid.org/0000-0002-8134-4280
Muslim Dvoyashkin - https://orcid.org/0000-0003-4411-1952

References

1. Gebremariam, S. N.; Marchetti, J. M. *Energy Convers. Manage.* **2018,** *168,* 74–84. doi:10.1016/j.enconman.2018.05.002
2. Shuba, E. S.; Kifle, D. *Renewable Sustainable Energy Rev.* **2018,** *81,* 743–755. doi:10.1016/j.rser.2017.08.042
3. Mata, T. M.; Martins, A. A.; Caetano, N. S. *Renewable Sustainable Energy Rev.* **2010,** *14,* 217–232. doi:10.1016/j.rser.2009.07.020
4. Chisti, Y. *Biotechnol. Adv.* **2007,** *25,* 294–306. doi:10.1016/j.biotechadv.2007.02.001
5. Ambat, I.; Srivastava, V.; Sillanpää, M. *Renewable Sustainable Energy Rev.* **2018,** *90,* 356–369. doi:10.1016/j.rser.2018.03.069
6. Aarthy, M.; Saravanan, P.; Gowthaman, M. K.; Rose, C.; Kamini, N. R. *Chem. Eng. Res. Des.* **2014,** *92,* 1591–1601. doi:10.1016/j.cherd.2014.04.008
7. Mbaraka, I. K.; Shanks, B. H. *J. Am. Oil Chem. Soc.* **2006,** *83,* 79–91. doi:10.1007/s11746-006-1179-x
8. Noiroj, K.; Intarapong, P.; Luengnaruemitchai, A.; Jai-In, S. *Renewable Energy* **2009,** *34,* 1145–1150. doi:10.1016/j.renene.2008.06.015
9. Baskar, G.; Aberna Ebenezer Selvakumari, I.; Aiswarya, R. *Bioresour. Technol.* **2018,** *250,* 793–798. doi:10.1016/j.biortech.2017.12.010
10. Dhakshinamoorthy, A.; Asiri, A. M.; Alvaro, M.; Garcia, H. *Green Chem.* **2018,** *20,* 86–107. doi:10.1039/c7gc02260c
11. Xie, W.; Huang, M. *Energy Convers. Manage.* **2018,** *159,* 42–53. doi:10.1016/j.enconman.2018.01.021
12. Xie, W.; Wan, F. *Fuel* **2018,** *220,* 248–256. doi:10.1016/j.fuel.2018.02.014
13. Gheorghiu, S.; Coppens, M.-O. *AIChE J.* **2004,** *50,* 812–820. doi:10.1002/aic.10076
14. Marinković, D. M.; Stanković, M. V.; Veličković, A. V.; Avramović, J. M.; Miladinović, M. R.; Stamenković, O. O.; Veljković, V. B.; Jovanović, D. M. *Renewable Sustainable Energy Rev.* **2016,** *56,* 1387–1408. doi:10.1016/j.rser.2015.12.007
15. Mardhiah, H. H.; Ong, H. C.; Masjuki, H. H.; Lim, S.; Lee, H. V. *Renewable Sustainable Energy Rev.* **2017,** *67,* 1225–1236. doi:10.1016/j.rser.2016.09.036
16. Su, F.; Guo, Y. *Green Chem.* **2014,** *16,* 2934–2957. doi:10.1039/c3gc42333f
17. Lee, J.; Kim, K.-H.; Kwon, E. E. *Renewable Sustainable Energy Rev.* **2017,** *77,* 70–79. doi:10.1016/j.rser.2017.04.002
18. Abdullah, S. H. Y. S.; Hanapi, N. H. M.; Azid, A.; Umar, R.; Juahir, H.; Khatoon, H.; Endut, A. *Renewable Sustainable Energy Rev.* **2017,** *70,* 1040–1051. doi:10.1016/j.rser.2016.12.008
19. Mansir, N.; Taufiq-Yap, Y. H.; Rashid, U.; Lokman, I. M. *Energy Convers. Manage.* **2017,** *141,* 171–182. doi:10.1016/j.enconman.2016.07.037
20. Suppes, G. *Appl. Catal., A* **2004,** *257,* 213–223. doi:10.1016/j.apcata.2003.07.010
21. Casado, C.; Amghouz, Z.; García, J. R.; Boulahya, K.; González-Calbet, J. M.; Téllez, C.; Coronas, J. *Mater. Res. Bull.* **2009,** *44,* 1225–1231. doi:10.1016/j.materresbull.2009.01.015
22. Anderson, M. W.; Terasaki, O.; Ohsuna, T.; Malley, P. J. O.; Philippou, A.; Mackay, S. P.; Ferreira, A.; Rocha, J.; Lidin, S. *Philos. Mag. B* **1995,** *71,* 813–841. doi:10.1080/01418639508243589
23. Anderson, M. W.; Terasaki, O.; Ohsuna, T.; Philippou, A.; Mackay, S. P.; Ferreira, A.; Rocha, J.; Lidin, S. *Nature (London)* **1994,** *367,* 347–351. doi:10.1038/367347a0
24. Philippou, A.; Rocha, J.; Anderson, M. W. *Catal. Lett.* **1999,** *57,* 151–153. doi:10.1023/a:1019099616405
25. Konwar, L. J.; Mäki-Arvela, P.; Begum, P.; Kumar, N.; Thakur, A. J.; Mikkola, J.-P.; Deka, R. C.; Deka, D. *J. Catal.* **2015,** *329,* 237–247. doi:10.1016/j.jcat.2015.05.021
26. Pavel, C. C.; Park, S.-H.; Dreier, A.; Tesche, B.; Schmidt, W. *Chem. Mater.* **2006,** *18,* 3813–3820. doi:10.1021/cm052261j
27. Pavel, C. C.; Zibrowius, B.; Löffler, E.; Schmidt, W. *Phys. Chem. Chem. Phys.* **2007,** *9,* 3440–3446. doi:10.1039/b701773a
28. Goa, Y.; Yoshitake, H.; Wu, P.; Tatsumi, T. *Microporous Mesoporous Mater.* **2004,** *70,* 93–101. doi:10.1016/j.micromeso.2004.03.007

29. Lv, L.; Lee, F. Y.; Zhou, J.; Su, F.; Zhao, X. S. *Microporous Mesoporous Mater.* **2006,** *96,* 270–275. doi:10.1016/j.micromeso.2006.07.006
30. Pavel, C. C.; Schmidt, W. *Chem. Commun.* **2006,** 882–884. doi:10.1039/b515720j
31. Pavel, C.; Palkovitz, R.; Schuth, F.; Schmidt, W. *J. Catal.* **2008,** *254,* 84–90. doi:10.1016/j.jcat.2007.11.020
32. Datta, S. J.; Yoon, K. B. *Catal. Today* **2013,** *204,* 60–65. doi:10.1016/j.cattod.2012.08.006
33. Wang, X.; Jacobson, A. J. *Chem. Commun.* **1999,** 973–974. doi:10.1039/a901280j
34. Nair, S.; Jeong, H.-K.; Chandrasekaran, A.; Braunbarth, C. M.; Tsapatsis, M.; Kuznicki, S. M. *Chem. Mater.* **2001,** *13,* 4247–4254. doi:10.1021/cm0103803
35. Ferdov, S.; Kolitsch, U.; Lengauer, C.; Tillmanns, E.; Lin, Z.; Sá Ferreira, R. A. *Acta Crystallogr., Sect. E: Struct. Rep. Online* **2007,** *63,* i186. doi:10.1107/s160053680704812x
36. Foster, M. D.; Delgado Friedrichs, O.; Bell, R. G.; Almeida Paz, F. A.; Klinowski, J. *J. Am. Chem. Soc.* **2004,** *126,* 9769–9775. doi:10.1021/ja037334j
37. Cychosz, K. A.; Guillet-Nicolas, R.; García-Martínez, J.; Thommes, M. *Chem. Soc. Rev.* **2017,** *46,* 389–414. doi:10.1039/c6cs00391e
38. Jeong, N. C.; Lee, M. H.; Yoon, K. B. *Angew. Chem., Int. Ed.* **2007,** *46,* 5868–5872. doi:10.1002/anie.200701676
39. Zhang, B.; Zhang, Y.; Hu, Y.; Shi, Z.; Azhati, A.; Xie, S.; He, H.; Tang, Y. *Chem. Mater.* **2016,** *28,* 2757–2767. doi:10.1021/acs.chemmater.6b00503
40. Groen, J. C.; Peffer, L. A. A.; Moulijn, J. A.; Pérez-Ramírez, J. *Chem. – Eur. J.* **2005,** *11,* 4983–4994. doi:10.1002/chem.200500045
41. Yang, X.; Paillaud, J.-L.; van Breukelen, H. F. W. J.; Kessler, H.; Duprey, E. *Microporous Mesoporous Mater.* **2001,** *46,* 1–11. doi:10.1016/s1387-1811(01)00267-0
42. Landmesser, H. *Solid State Ionics* **1997,** *101–103,* 271–277. doi:10.1016/s0167-2738(97)84042-8
43. Valtchev, V. P. *J. Chem. Soc., Chem. Commun.* **1994,** 261. doi:10.1039/c39940000261
44. Bagnasco, G.; Turco, M.; Busca, G.; Armaroli, T.; Nastro, A.; De Luca, P. *Adsorpt. Sci. Technol.* **2003,** *21,* 683–696. doi:10.1260/026361703772776466
45. Anderson, M. W.; Agger, J. R.; Luigi, D.-P.; Baggaley, A. K.; Rocha, J. *Phys. Chem. Chem. Phys.* **1999,** *1,* 2287–2292. doi:10.1039/a900863b
46. Xiang, M.; Wu, D. *RSC Adv.* **2018,** *8,* 33473–33486. doi:10.1039/c8ra06811a
47. Park, S. W.; Yun, Y. H.; Kim, S. D.; Yang, S. T.; Ahn, W. S.; Seo, G.; Kim, W. J. *J. Porous Mater.* **2010,** *17,* 589–595. doi:10.1007/s10934-009-9328-x
48. Lavalley, J. C. *Catal. Today* **1996,** *27,* 377–401. doi:10.1016/0920-5861(95)00161-1
49. Stebbins, J. F.; Poe, B. T. *Geophys. Res. Lett.* **1999,** *26,* 2521–2523. doi:10.1029/1999gl008364
50. Llabrés i Xamena, F. X.; Calza, P.; Lamberti, C.; Prestipino, C.; Damin, A.; Bordiga, S.; Pelizzetti, E.; Zecchina, A. *J. Am. Chem. Soc.* **2003,** *125,* 2264–2271. doi:10.1021/ja027382o
51. Prakash, A. M.; Kevan, L. Electron spin resonance study on the nature of titanium in titanosilicate ets-10 molecular sieve. In *Science and Technology in Catalysis 1998, Proceedings of the Third Tokyo Conference on Advanced Catalytic Science and Technology,* Studies in Surface Science and Catalysis; Elsevier, 1999; pp 233–238. doi:10.1016/s0167-2991(99)80072-x
52. Bal, R.; Chaudhari, K.; Srinivas, D.; Sivasanker, S.; Ratnasamy, P. *J. Mol. Catal. A: Chem.* **2000,** *162,* 199–207. doi:10.1016/s1381-1169(00)00290-9
53. Krishna, R. M.; Prakash, A. M.; Kurshev, V.; Kevan, L. *Phys. Chem. Chem. Phys.* **1999,** *1,* 4119–4124. doi:10.1039/a903461g
54. Tiscornia, I.; Irusta, S.; Prádanos, P.; Téllez, C.; Coronas, J.; Santamaría, J. *J. Phys. Chem. C* **2007,** *111,* 4702–4709. doi:10.1021/jp070044v
55. Krisnandi, Y. K.; Howe, R. F. *Appl. Catal., A* **2006,** *307,* 62–69. doi:10.1016/j.apcata.2006.03.008
56. Goldfarb, D.; Bernardo, M.; Strohmaier, K. G.; Vaughan, D. E. W.; Thomann, H. *J. Am. Chem. Soc.* **1994,** *116,* 6344–6353. doi:10.1021/ja00093a039
57. Devadas, M.; Kröcher, O.; Elsener, M.; Wokaun, A.; Mitrikas, G.; Söger, N.; Pfeifer, M.; Demel, Y.; Mussmann, L. *Catal. Today* **2007,** *119,* 137–144. doi:10.1016/j.cattod.2006.08.018
58. Giamello, E.; Fubini, B.; Volante, M.; Costa, D. *Colloids Surf.* **1990,** *45,* 155–165. doi:10.1016/0166-6622(90)80019-z
59. Kortunov, P.; Vasenkov, S.; Kärger, J.; Valiullin, R.; Gottschalk, P.; Fé Elía, M.; Perez, M.; Stöcker, M.; Drescher, B.; McElhiney, G.; Berger, C.; Gläser, R.; Weitkamp, J. *J. Am. Chem. Soc.* **2005,** *127,* 13055–13059. doi:10.1021/ja053134r
60. Meersmann, T.; Brunner, E., Eds. *Hyperpolarized Xenon-129 Magnetic Resonance;* New Developments in NMR; Royal Society of Chemistry: Cambridge, United Kingdom, 2015. doi:10.1039/9781782628378
61. Oschatz, M.; Hoffmann, H. C.; Pallmann, J.; Schaber, J.; Borchardt, L.; Nickel, W.; Senkovska, I.; Rico-Francés, S.; Silvestre-Albero, J.; Kaskel, S.; Brunner, E. *Chem. Mater.* **2014,** *26,* 3280–3288. doi:10.1021/cm501102y
62. Keenan, C. D.; Herling, M. M.; Siegel, R.; Petzold, N.; Bowers, C. R.; Rössler, E. A.; Breu, J.; Senker, J. *Langmuir* **2013,** *29,* 643–652. doi:10.1021/la304502r
63. Yang, X.; Truitt, R. E. *J. Phys. Chem.* **1996,** *100,* 3713–3718. doi:10.1021/jp952203t
64. Bowers, C. R.; Dvoyashkin, M.; Salpage, S. R.; Akel, C.; Bhase, H.; Geer, M. F.; Shimizu, L. S. *ACS Nano* **2015,** *9,* 6343–6353. doi:10.1021/acsnano.5b01895
65. Hibbe, F.; Chmelik, C.; Heinke, L.; Pramanik, S.; Li, J.; Ruthven, D. M.; Tzoulaki, D.; Kärger, J. *J. Am. Chem. Soc.* **2011,** *133,* 2804–2807. doi:10.1021/ja108625z
66. Berman, P.; Meiri, N.; Colnago, L. A.; Moraes, T. B.; Linder, C.; Levi, O.; Parmet, Y.; Saunders, M.; Wiesman, Z. *Biotechnol. Biofuels* **2015,** *8,* 12. doi:10.1186/s13068-014-0194-7
67. Dvoyashkin, M.; Wilde, N.; Haase, J.; Gläser, R. *RSC Adv.* **2018,** *8,* 38941–38944. doi:10.1039/c8ra07434h
68. Correia, L. M.; Saboya, R. M. A.; de Sousa Campelo, N.; Cecilia, J. A.; Rodríguez-Castellón, E.; Cavalcante, C. L., Jr.; Vieira, R. S. *Bioresour. Technol.* **2014,** *151,* 207–213. doi:10.1016/j.biortech.2013.10.046
69. Granados, M. L.; Poves, M. D. Z.; Alonso, D. M.; Mariscal, R.; Galisteo, F. C.; Moreno-Tost, R.; Santamaría, J.; Fierro, J. L. G. *Appl. Catal., B* **2007,** *73,* 317–326. doi:10.1016/j.apcatb.2006.12.017
70. Cho, Y. B.; Seo, G.; Chang, D. R. *Fuel Process. Technol.* **2009,** *90,* 1252–1258. doi:10.1016/j.fuproc.2009.06.007
71. Veljković, V. B.; Stamenković, O. S.; Todorović, Z. B.; Lazić, M. L.; Skala, D. U. *Fuel* **2009,** *88,* 1554–1562. doi:10.1016/j.fuel.2009.02.013
72. Kouzu, M.; Yamanaka, S.-y.; Hidaka, J.-s.; Tsunomori, M. *Appl. Catal., A* **2009,** *355,* 94–99. doi:10.1016/j.apcata.2008.12.003
73. Kouzu, M.; Hidaka, J.-s. *Fuel* **2012,** *93,* 1–12. doi:10.1016/j.fuel.2011.09.015

74. Vujicic, D.; Comic, D.; Zarubica, A.; Micic, R.; Boskovic, G. *Fuel* **2010,** *89,* 2054–2061. doi:10.1016/j.fuel.2009.11.043
75. Wu, H.; Zhang, J.; Wei, Q.; Zheng, J.; Zhang, J. *Fuel Process. Technol.* **2013,** *109,* 13–18. doi:10.1016/j.fuproc.2012.09.032
76. Chen, G.-Y.; Shan, R.; Yan, B.-B.; Shi, J.-F.; Li, S.-Y.; Liu, C.-Y. *Fuel Process. Technol.* **2016,** *143,* 110–117. doi:10.1016/j.fuproc.2015.11.017
77. López, D. E.; Goodwin, J. G., Jr.; Bruce, D. A.; Lotero, E. *Appl. Catal., A* **2005,** *295,* 97–105. doi:10.1016/j.apcata.2005.07.055
78. Al-Ani, A.; Drijfhout, F.; Crickett, S.; Zholobenko, V. *J. Porous Mater.* **2019,** *26,* 69–76. doi:10.1007/s10934-018-0610-7
79. Borello, E.; Lamberti, C.; Bordiga, S.; Zecchina, A.; Areán, C. O. *Appl. Phys. Lett.* **1997,** *71,* 2319–2321. doi:10.1063/1.120060
80. Wilde, N.; Pelz, M.; Gebhardt, S. G.; Gläser, R. *Green Chem.* **2015,** *17,* 3378–3389. doi:10.1039/c5gc00406c
81. Thommes, M.; Mitchell, S.; Pérez-Ramírez, J. *J. Phys. Chem. C* **2012,** *116,* 18816–18823. doi:10.1021/jp3051214
82. Goepel, M.; Kabir, H.; Küster, C.; Saraçi, E.; Zeigermann, P.; Valiullin, R.; Chmelik, C.; Enke, D.; Kärger, J.; Gläser, R. *Catal. Sci. Technol.* **2015,** *5,* 3137–3146. doi:10.1039/c4cy01665c
83. de Boer, J. H.; Lippens, B. C.; Linsen, B. G.; Broekhoff, J. C. P.; van den Heuvel, A.; Osinga, T. J. *J. Colloid Interface Sci.* **1966,** *21,* 405–414. doi:10.1016/0095-8522(66)90006-7
84. Lowell, S.; Shields, J. E.; Thomas, M. A.; Thommes, M. *Characterization of Porous Solids and Powders: Surface Area, Pore Size and Density;* Scarlett, B., Ed.; Particle Technology Series, Vol. 16; Springer: Dordrecht, Netherlands, 2004. doi:10.1007/978-1-4020-2303-3
85. Washburn, E. W. *Phys. Rev.* **1921,** *17,* 273–283. doi:10.1103/physrev.17.273
86. Cotts, R. M.; Hoch, M. J. R.; Sun, T.; Markert, J. T. *J. Magn. Reson. (1969-1992)* **1989,** *83,* 252–266. doi:10.1016/0022-2364(89)90189-3
87. Kärger, J.; Pfeifer, H.; Heink, W. *Adv. Magn. Reson.* **1988,** *12,* 1–89. doi:10.1016/b978-0-12-025512-2.50004-x
88. Thakur, R. S.; Kurur, N. D.; Madhu, P. K. *Chem. Phys. Lett.* **2006,** *426,* 459–463. doi:10.1016/j.cplett.2006.06.007
89. Puente-Urbina, A.; Hollenbach, J.; Céspedes-Camacho, I. F.; Matysik, J.; Valle-Bourrouet, G. *J. Porous Mater.* **2016,** *23,* 1439–1449. doi:10.1007/s10934-016-0204-1

License and Terms

This is an Open Access article under the terms of the Creative Commons Attribution License (http://creativecommons.org/licenses/by/4.0). Please note that the reuse, redistribution and reproduction in particular requires that the authors and source are credited.

The license is subject to the *Beilstein Journal of Nanotechnology* terms and conditions: (https://www.beilstein-journals.org/bjnano)

The definitive version of this article is the electronic one which can be found at: doi:10.3762/bjnano.10.200

BEILSTEIN JOURNAL OF NANOTECHNOLOGY

Adsorption and desorption of self-assembled L-cysteine monolayers on nanoporous gold monitored by in situ resistometry

Elisabeth Hengge[*1], Eva-Maria Steyskal[1], Rupert Bachler[1], Alexander Dennig[2], Bernd Nidetzky[2] and Roland Würschum[1]

Letter

Open Access

Address:
[1]Insitute of Materials Physics, Graz University of Technology, Petersgasse 16, A-8010 Graz, Austria and [2]Institute of Biotechnology and Biochemical Engineering, Graz University of Technology, Petersgasse 12, A-8010 Graz, Austria

Email:
Elisabeth Hengge[*] - e.hengge@tugraz.at

* Corresponding author

Keywords:
L-cysteine; in situ resistometry; nanoporous gold; self-assembled monolayer (SAM); voltammetry

Beilstein J. Nanotechnol. **2019,** *10,* 2275–2279.
doi:10.3762/bjnano.10.219

Received: 14 August 2019
Accepted: 31 October 2019
Published: 18 November 2019

This article is part of the thematic issue "New directions for nanoporous materials".

Guest Editor: C. T. Yavuz

© 2019 Hengge et al.; licensee Beilstein-Institut.
License and terms: see end of document.

Abstract

Surface modifications of nanoporous metals have become a highly attractive research field as they exhibit great potential for various applications, especially in biotechnology. Using self-assembled monolayers is one of the most promising approaches to modify a gold surface. However, only few techniques are capable of characterizing the formation of these monolayers on porous substrates. Here, we present a method to in situ monitor the adsorption and desorption of self-assembled monolayers on nanoporous gold by resistometry, using cysteine as example. During the adsorption an overall relative change in resistance of 18% is detected, which occurs in three distinct stages. First, the cysteine molecules are adsorbed on the outer surface. In the second stage, they are adsorbed on the internal surfaces and in the last stage the reordering accompanied by additional adsorption takes place. The successful binding of cysteine on the Au surface was confirmed by cyclic voltammetry, which showed a significant decrease of the double-layer capacitance. Also, the electrochemically controlled desorption of cysteine was monitored by concomitant in situ resistometry. From the desorption peak related to the (111) surface of the structure, which is associated with a resistance change of 4.8%, an initial surface coverage of 0.48 monolayers of cysteine could be estimated.

Findings

Nanoporous gold, produced by selective etching of the less noble component of a AuAg master alloy (also known as de-alloying), is a very promising material in many applications due to its three-dimensional nanoporous structure. Among many other technological applications as sensing [1,2] and energy storage [3], nanoporous metals exhibit great potential in

biochemical applications [4]. In addition to their various useful intrinsic characteristics, such as high surface-to-volume ratio and tunable mechanical properties, some applications require a modification of the surface, e.g., by using the well-known spontaneous formation of self-assembled monolayers (SAMs) on gold substrates [5]. These layers usually consist of three groups: a thiol as the head group, a carbon chain as the backbone and an end group that can be chosen according to the requirements for subsequent application. For planar Au surfaces, self-assembly processes are known to occur in adsorption and ordering (also known as "standing up") stages [6]. The adsorption and ordering of such monolayers has been subject to experimental as well as theoretical investigation for many years, mostly studying the deposition on single crystalline surfaces. Using nanoporous substrates for modification with SAMs, however, is more complicated, as the applicable techniques for characterization are very limited, whereby electrochemical methods seem most promising [7,8].

Here, we present a new method to monitor and characterize the ad-/desorption of SAMs on nanoporous gold (npAu), based on our experience on in situ resistometry as a highly sensitive diagnosis tool for ad-/desorption processes [9]. The selected SAM material for this study is cysteine, due to its beneficial properties such as the short carbon backbone, the solubility in water and the easy handling.

The npAu substrate material was fabricated by electrochemically assisted dealloying of $Ag_{75}Au_{25}$. The alloy was prepared by arc melting, homogenized at 800 °C for 12 h under argon atmosphere, rolled to a sheet of 220 µm in thickness, annealed again at 600 °C for 1 h, and cut in rectangular pieces sized 10 × 5 mm. Two representative samples are presented here, referred to as sample A (91 mg) and sample B (86 mg). Given weights refer to the master alloy.

Each sample was contacted by five flattened Au wires, attached in line. The mid-positioned wire served as connection to an Autolab PGSTAT204 potentiostat, the others for four-point resistance measurements with a Keithley 2400 Source Meter. For a more detailed description of the resistometry setup, the reader is referred to our previous work [9]. An electrochemical cell was set up in three-electrode geometry, using a commercial Ag/AgCl reference electrode (saturated KCl with a 3 M KNO_3 salt bridge), relative to which all potentials will be stated in the following. Whenever the cell electrolyte was changed, the setup was immersed in distilled water for several hours for rinsing.

Dealloying was performed in 0.1 M $HClO_4$ with a Pt-wire counter electrode under chronoamperometric conditions at $U_{Ag/AgCl}$ = 1100 mV until the current had fallen below 50 µA. For all following procedures, a carbon fabric served as the counter electrode. After dealloying, the sample was cleaned from the primary oxide [10] by cyclic voltammetry (CV) in 0.1 M $HClO_4$ solution. The SAMs were deposited from a 20 mM cysteine solution (ROTH company, L-cysteine ≥98% in ultrapure water). Sample A was immersed directly into 20 mL of the cysteine solution, while sample B was first immersed in 10 mL ultrapure water, then 10 mL of 40 mM cysteine solution was added. Both samples were transferred directly from the rinsing solution, the different immersion procedures were chosen for detailed comparison of the resistance behavior caused by the cysteine molecules. The samples were exposed to cysteine solution for a total timespan of approximately 95 h.

Figure 1 shows the in situ resistance measurement during SAM formation, which yields a total resistance increase of approximately 18%. Both samples exhibit a similar trend, demonstrating the high reproducibility. This overall resistance change is well in line with ex situ studies on npAu in the literature, reporting a relative change in resistance of 6% for propanethiol and 22% for cysteamine monolayer assembly after 24 h [11]. In Figure 1, we can distinguish between three regimes of different slope (denoted as (I) to (III)). Regimes (I) and (III) can be correlated to stages in the adsorption process on planar gold, whereas regime (II) exhibits a behavior unique for nanoporous gold. The steep regime (I) yields an increase of about 4% in about 50 min, which is assigned to cysteine molecules being chemisorbed on the easily accessible outer surfaces. This chemisorption has been reported in the literature to take 30 min for planar Au [7]. Regime (III) shows a very slow increase of the resistance, assigned to reordering of the monolayer, which is known to take several days [12]. After 72 h a total change between 17% and 18% is observed with a fading slope, which

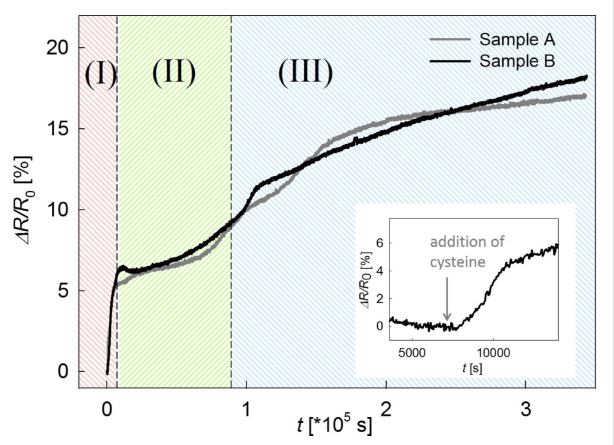


Figure 1: Relative change in electrical resistance measured in situ during the exposure of npAu in 20 mM cysteine solution. Inset: Enlarged first few hours of the resistance change of sample B. After 2 h in ultrapure water, cysteine was added (marked by the grey arrow).

yet dropped to less than 1% in 2 days. In the intermediate regime (II), which takes approximately 24 h, the resistance increases by about 5% with a moderate slope. As, to the knowledge of the authors, there is no equivalent stage reported for planar Au [6], we assume this stage to be specific for nanoporosity, representing adsorption on internal surfaces.

In the inset of Figure 1, the first few hours of the resistance change of sample B are shown enlarged. The sample was first stored in water for 2 h prior to the addition of cysteine. Interestingly, the resistance increase attributed to stage (I) starts with a certain delay (about 600 s) after cysteine adding (grey arrow). This delay is attributed to a physisorption step prior to chemisorption (reported to take few minutes for planar Au [13]), which does not significantly change the electronic structure and thus the resistance of the substrate.

Since SAMs are known to decrease the double-layer capacitance of the substrate [14], Figure 2 compares CVs in 1 M KOH of sample A under cysteine-free conditions (before SAM assembly) and after different treatments. The SAMs can be considered stable between −400 mV (SAM desorption) and −50 mV (cysteine oxidation). At −300 mV, a double-layer capacitance of 48 µF/cm^2 under cysteine-free conditions (Figure 2a,b, black curve) and 8 µF/cm^2 after cysteine assembly (Figure 2b, solid green curve) can be estimated. When the lower limit of the CV is extended to −900 mV (limited by gas evolution that might cause sample damage), a desorption peak in the first cathodic scan is observed at about −820 mV (Figure 2b, dashed red curve), which does not reappear in the following cycles (Figure 2b, dashed grey curve). For planar Au, several distinct peaks occur during cysteine desorption, which can be assigned to different low-index crystal planes. The weakest bound cysteine molecules desorb at around −700 mV on planar Au, which is attributed to the desorption from the (111) plane [15,16]. It was shown that the desorption of any SAM shifts by about −100 mV when using a nanoporous instead of a planar sample [17]. Thus, based on literature, the cathodic peak at −820 mV in Figure 2b can be attributed to cysteine desorption from the (111) planes of our npAu sample, meaning that the SAM was only partially desorbed. Desorption of stronger bound cysteine was not possible to examine as scanning to even more negative potential would have risked sample damage.

After this desorption peak, significantly higher currents flow near the upper potential limit (Figure 2b, dashed red and grey curves), which are assigned to cysteine oxidation in the solution [18] as the desorbed cysteine is now dissolved in the electrolyte. The double-layer capacitance now amounts to 20 µF/cm^2 (Figure 2b, solid blue curve), which is still significantly lower than the initial value.

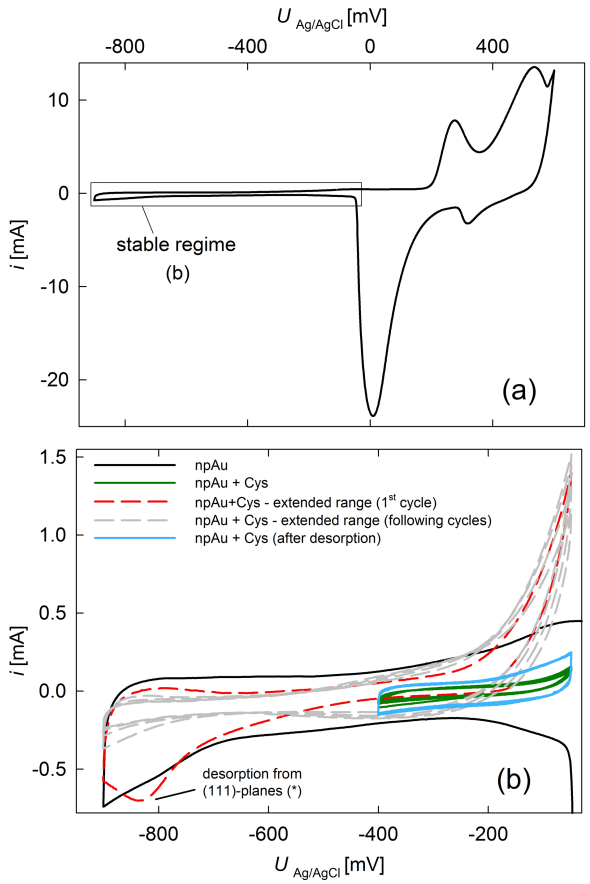


Figure 2: Cyclic voltammetry of sample A. (a) Measurement of the cysteine-free npAu between 600 and −900 mV, (b) CVs recorded after modification with cysteine together with a part of the curve from (a) for reference. In (b), the double layer CV (solid curves) were recorded between −50 and −400 mV and the electrochemical desorption (dashed curves) between −50 and −900 mV. (*)The peak was correlated to the desorption from the (111) plane based on [15]. The blue solid curve was recorded after the dashed curves. All CVs were conducted in 1 M KOH at a scan rate of 1 mV/s. Please note the change in *x*-axis scale between (a) and (b).

The relative change in electrical resistance during cysteine desorption from the (111) planes and subsequent cycling between −900 and −50 mV was monitored in situ for sample B, as shown in Figure 3. It demonstrates good reproducibility of the desorption peak at −820 mV.

During desorption, the resistance (Figure 3b) strongly decreases by about 7.2%. In subsequent cycles it varies in a range of 4%, matching our earlier results for double-layer charging of npAu [19]. A slight drift during repeated cycling is most likely caused by sample degradation.

The charge transfer of 0.15 C during desorption is a superposition of actual cysteine desorption and double-layer charging (with an increasing contribution as cysteine is desorbed). When we assume the double-layer capacitance to increase roughly

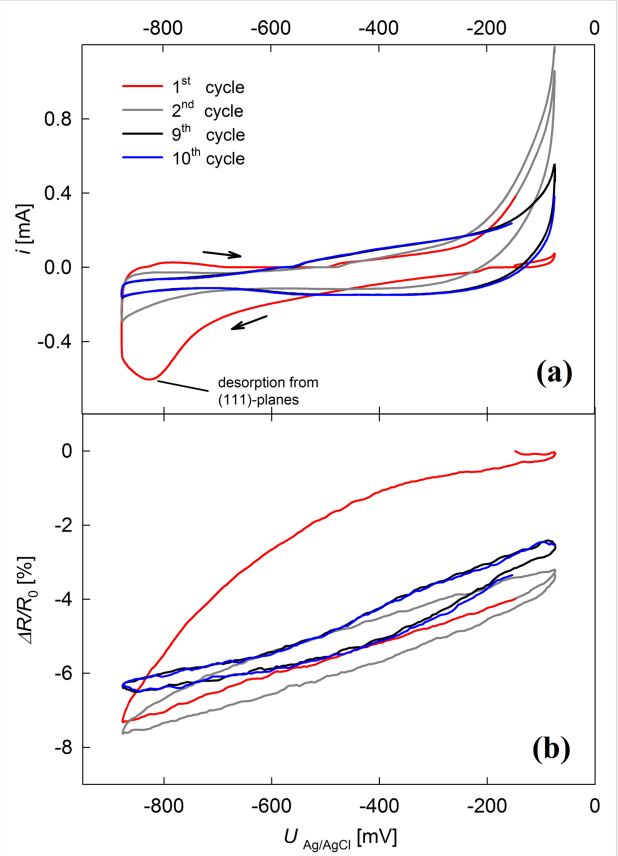


Figure 3: Cyclic voltammetry of sample B modified with cysteine (a) and concomitantly measured change in relative electrical resistance (b). The potential was varied between −900 and −50 mV with a scan rate of 1 mV/s in 1 M KOH.

proportionally to the total charge transfer, this yields contributions of 0.06 C for the double layer and 0.09 C for the cysteine desorption. This charge transfer can be associated with a resistance variation of 2.4% (estimated from the variations upon double-layer charging in following cycles) and 4.8%, respectively. Assuming equal contributions of desorption from different crystallographic planes to the resistance change and a transfer of one electron per cysteine molecule, the total amount of cysteine (3.5×10^{-6} mol) on the npAu can be deduced from the initial resistance increase of 18% during the assembly. With a specific surface area of 10 m^2/g (determined following [20]), an initial surface coverage of 0.48 monolayers can be estimated. This value agrees well with SAM surface coverages reported in the literature [21-23].

The sensitivity of resistance measurements towards ad-/desorption can be expressed by the charge coefficient, which relates the relative resistance variations to the imposed charge per mole. Here, a value of 9.1×10^{-5} mol/C is obtained for cysteine, which is approximately twice as high as that obtained for the ad-/desorption of oxygen on npAu [19], approving this technique to be suitable for sensitively detecting even small amounts of SAMs on npAu.

In conclusion, in situ resistometry proved to be a highly sensitive tool for dynamically monitoring the formation process of self-assembled monolayers, exemplarily using cysteine. The assembly takes place with a total resistance increase of about 18% in three clearly distinguishable regimes. The three regimes can be assigned to the adsorption on easily accessible outer surfaces, followed by adsorption on internal surfaces of the nanoporous structure and finally a reordering stage, taking several days. In cyclic voltammetry, a desorption of the SAM could be achieved from the crystallographic (111) planes, along with a resistance decrease of 4.8%, determined by in situ resistometry. From this, an initial surface coverage of 0.48 cysteine monolayers could be estimated. As an outlook, influencing parameters such as the cysteine concentration in solution, which would affect the time period of the adsorption [24], and the pH value of the solution, which would impact the stability of the SAMs [25], could be examined further.

Acknowledgements

The authors thank Nadiia Mameka (Helmholtz-Zentrum Geesthacht) and Egbert Zojer (Institute of Solid State Physics, University of Technology Graz) for the fruitful discussion. The work was financially supported by the Lead Project (LP-03) Porous Materials @ Work at the University of Technology, Graz. This work was performed in the framework of the inter-university cooperation of TU Graz and Uni Graz on natural sciences (NAWI Graz).

ORCID® iDs

Elisabeth Hengge - https://orcid.org/0000-0002-7954-008X
Eva-Maria Steyskal - https://orcid.org/0000-0003-0752-9997
Rupert Bachler - https://orcid.org/0000-0002-7953-4712
Alexander Dennig - https://orcid.org/0000-0003-4721-5095
Bernd Nidetzky - https://orcid.org/0000-0002-5030-2643
Roland Würschum - https://orcid.org/0000-0003-4624-4433

References

1. Xiao, X.; Li, H.; Wang, M.; Zhang, K.; Si, P. *Analyst* **2014,** *139,* 488–494. doi:10.1039/c3an01670f
2. Meng, F.; Yan, X.; Liu, J.; Gu, J.; Zou, Z. *Electrochim. Acta* **2011,** *56,* 4657–4662. doi:10.1016/j.electacta.2011.02.105
3. Lang, X. Y.; Yuan, H. T.; Iwasa, Y.; Chen, M. W. *Scr. Mater.* **2011,** *64,* 923–926. doi:10.1016/j.scriptamat.2011.01.038
4. Xiao, X.; Si, P.; Magner, E. *Bioelectrochemistry* **2016,** *109,* 117–126. doi:10.1016/j.bioelechem.2015.12.008
5. Mameka, N.; Lührs, L.; Heissler, S.; Gliemann, H.; Wöll, C. *ACS Appl. Nano Mater.* **2018,** *1,* 6613–6621. doi:10.1021/acsanm.8b01368

6. Vericat, C.; Vela, M. E.; Benitez, G.; Carro, P.; Salvarezza, R. C. *Chem. Soc. Rev.* **2010,** *39,* 1805–1834. doi:10.1039/b907301a
7. Qingwen, L.; Hong, G.; Yiming, W.; Guoan, L.; Jie, M. *Electroanalysis* **2001,** *13,* 1342–1346. doi:10.1002/1521-4109(200111)13:16<1342::aid-elan1342>3.0.co;2-b
8. Hakamada, M.; Takahashi, M.; Furukawa, T.; Tajima, K.; Yoshimura, K.; Chino, Y.; Mabuchi, M. *Phys. Chem. Chem. Phys.* **2011,** *13,* 12277–12284. doi:10.1039/c0cp02553d
9. Steyskal, E.-M.; Qi, Z.; Pölt, P.; Albu, M.; Weissmüller, J.; Würschum, R. *Langmuir* **2016,** *32,* 7757–7764. doi:10.1021/acs.langmuir.6b01734
10. Jin, H.-J.; Parida, S.; Kramer, D.; Weissmüller, J. *Surf. Sci.* **2008,** *602,* 3588–3594. doi:10.1016/j.susc.2008.09.038
11. Hakamada, M.; Kato, N.; Mabuchi, M. *Appl. Surf. Sci.* **2016,** *387,* 1088–1092. doi:10.1016/j.apsusc.2016.07.059
12. Sumi, T.; Wano, H.; Uosaki, K. *J. Electroanal. Chem.* **2003,** *550–551,* 321–325. doi:10.1016/s0022-0728(03)00141-4
13. Torrelles, X.; Vericat, C.; Vela, M. E.; Fonticelli, M. H.; Daza Millone, M. A.; Felici, R.; Lee, T.-L.; Zegenhagen, J.; Muñoz, G.; Martín-Gago, J. A.; Salvarezza, R. C. *J. Phys. Chem. B* **2006,** *110,* 5586–5594. doi:10.1021/jp054879m
14. Campuzano, S.; Pedrero, M.; Montemayor, C.; Fatás, E.; Pingarrón, J. M. *J. Electroanal. Chem.* **2006,** *586,* 112–121. doi:10.1016/j.jelechem.2005.09.007
15. Arihara, K.; Ariga, T.; Takashima, N.; Arihara, K.; Okajima, T.; Kitamura, F.; Tokuda, K.; Ohsaka, T. *Phys. Chem. Chem. Phys.* **2003,** *5,* 3758–3761. doi:10.1039/b305867k
16. Huang, J.-F.; Sun, I.-W. *Adv. Funct. Mater.* **2005,** *15,* 989–994. doi:10.1002/adfm.200400382
17. Chu, Y.; Seo, B.-R.; Kim, J.-W. *Bull. Korean Chem. Soc.* **2010,** *31,* 3407–3410. doi:10.5012/bkcs.2010.31.11.3407
18. Fawcett, W. R.; Fedurco, M.; Kováčová, Z.; Borkowska, Z. *J. Electroanal. Chem.* **1994,** *368,* 265–274. doi:10.1016/0022-0728(93)03060-3
19. Wahl, P.; Traußnig, T.; Landgraf, S.; Jin, H.-J.; Weissmüller, J.; Würschum, R. *J. Appl. Phys.* **2010,** *108,* 073706. doi:10.1063/1.3490789
20. Lakshmanan, C.; Viswanath, R.; Polaki, S.; Rajaraman, R. *AIP Conf. Proc.* **2015,** *1665,* 140033. doi:10.1063/1.4918242
21. Widrig, C. A.; Chung, C.; Porter, M. D. *J. Electroanal. Chem. Interfacial Electrochem.* **1991,** *310,* 335–359. doi:10.1016/0022-0728(91)85271-p
22. Love, J. C.; Estroff, L. A.; Kriebel, J. K.; Nuzzo, R. G.; Whitesides, G. M. *Chem. Rev.* **2005,** *105,* 1103–1170. doi:10.1021/cr0300789
23. Cortes, E.; Rubert, A. A.; Benitez, G.; Carro, P.; Vela, M. E.; Salvarezza, R. C. *Langmuir* **2009,** *25,* 5661–5666. doi:10.1021/la804251a
24. Han, Y.; Uosaki, K. *Electrochim. Acta* **2008,** *53,* 6196–6201. doi:10.1016/j.electacta.2008.04.016
25. Kong, B.-K.; Kim, Y.-S.; Choi, I. S. *Bull. Korean Chem. Soc.* **2008,** *29,* 1843–1846. doi:10.5012/bkcs.2008.29.9.1843

License and Terms

This is an Open Access article under the terms of the Creative Commons Attribution License (http://creativecommons.org/licenses/by/4.0). Please note that the reuse, redistribution and reproduction in particular requires that the authors and source are credited.

The license is subject to the *Beilstein Journal of Nanotechnology* terms and conditions: (https://www.beilstein-journals.org/bjnano)

The definitive version of this article is the electronic one which can be found at:
doi:10.3762/bjnano.10.219

BEILSTEIN JOURNAL OF NANOTECHNOLOGY

Air oxidation of sulfur mustard gas simulants using a pyrene-based metal–organic framework photocatalyst

Ghada Ayoub[1,2], Mihails Arhangelskis[1], Xuan Zhang[2], Florencia Son[2], Timur Islamoglu[2], Tomislav Friščić[*1] and Omar K. Farha[*2,3]

Full Research Paper

Open Access

Address:
[1]Department of Chemistry, McGill University, Montreal, Quebec, H3A 0B8, Canada, [2]International Institute of Nanotechnology, Department of Chemistry, Northwestern University, 2145 Sheridan Rd, Evanston, IL 60208, USA and [3]Department of Chemical & Biological Engineering, Northwestern University, 2145 Sheridan Rd, Evanston, IL 60208, USA

Email:
Tomislav Friščić[*] - tomislav.friscic@mcgill.ca; Omar K. Farha[*] - o-farha@northwestern.edu

* Corresponding author

Keywords:
metal-organic frameworks; oxidation; photocatalysis; singlet oxygen; sulfur mustard gas

Beilstein J. Nanotechnol. **2019,** *10,* 2422–2427.
doi:10.3762/bjnano.10.232

Received: 26 August 2019
Accepted: 03 December 2019
Published: 09 December 2019

This article is part of the thematic issue "New directions for nanoporous materials".

Guest Editor: C. T. Yavuz

© 2019 Ayoub et al.; licensee Beilstein-Institut.
License and terms: see end of document.

Abstract

We demonstrate a microporous metal–organic framework NU-400 based on a 2,7-disubstituted pyrene linker as a highly efficient photosensitizer for generating singlet oxygen and subsequent oxidative degradation of chemical warfare agents (CWAs). The high activity of NU-400 permits photocatalytic conversion of the 2-chloroethyl ethyl sulfide (CEES) mustard gas simulant into a benign sulfoxide derivative, in air, with less than 15 minutes' half-life. This is a considerable improvement to NU-1000, based on a 1,3,6,8-tetrasubstituted pyrene unit, demonstrating how variation of the substitution pattern of a metal–organic framework linker permits modification of its photoactive behavior.

Introduction

Sulfur mustard gas also known as mustard gas, HD, or Yperite belongs to a class of chemical warfare agents (CWAs) known as vesicants, which have detrimental effects on humans, including the blistering of skin upon contact [1]. Even at a low dosage [2], this chemical can be fatal. Although in 1993 at the Chemical Weapon Convention (CWC) 192 nations signed an agreement to outlaw the production, stockpiling, and deployment of chemical weapons, sulfur mustard gas has continuously been used against civilians and soldiers over the past several decades [3], including as recently as 2018 in Syria [4-7]. Therefore, it is imperative to design and develop novel methods for the detoxification of sulfur mustard gas in stockpiles as well as in the battle field.

There are several routes for the detoxification of sulfur mustard gas, including: 1) hydrolysis [8,9], 2) oxidation, and 3) dehy-

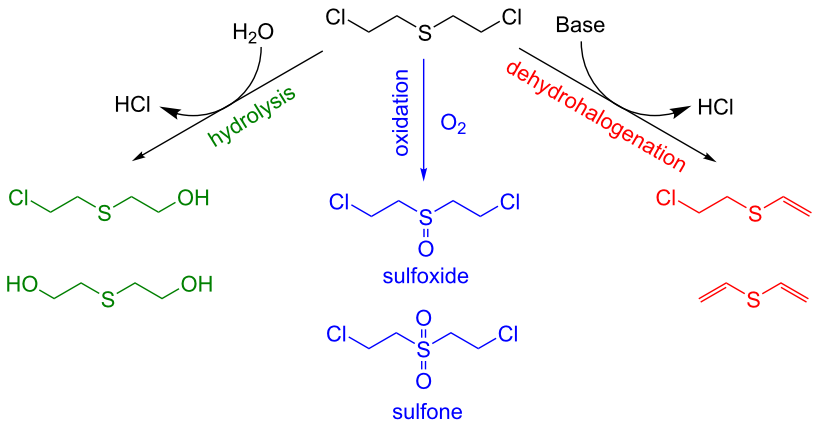
drohalogenation [10-12] (Scheme 1). The hydrolysis route is limited to small scales because of the hydrophobicity of sulfur mustard gas. The mechanism of degradation by dehydrohalogenation mechanism is still poorly understood and not efficient enough for real-world applications. So far, the oxidative degradation [13-19] route has been shown to be the most promising but relies on the use of oxidants highly selective for the formation of sulfoxides, as further oxidation to a sulfone leads to a product of toxicity comparable to sulfur mustard gas [20].

While oxidative detoxification of sulfur mustard gas has traditionally relied on bleaching powders, such reagents come with significant drawbacks, including corrosiveness and loss of activity over time [21,22]. Ideal candidates for the oxidation of mustard gas should be mild oxidants that will selectively produce the partially oxidized sulfoxide. In that context, a promising approach is the use of singlet oxygen ($^1O_2$) generated by photosensitization of ground-state molecular oxygen ($^3O_2$) via an electronically excited chromophore. The chromophores can be compounds with significant quantum yields and whose absorption wavelengths span the ultraviolet–visible spectrum. Moreover, singlet oxygen could be generated from homogenous [23] or heterogeneous catalysts, the latter of which will allow for the ease of separation at the end of the reaction, recyclability of the catalyst, wide selection of solvent choices since solubility of the chromophore does not need to be considered, and lower probability of photobleaching [24,25].

Metal–organic frameworks (MOFs), porous crystalline materials comprised of metal nodes and organic linkers, have attracted tremendous attention in heterogeneous catalysis due to their structural and chemical tunability [26-36]. In that context, zirconium-based MOFs have demonstrated particularly high stability under a range of conditions, enabling their application for efficient, rapid hydrolytic or oxidative degradation of nerve gas agents [37-42].

Here, we describe the preparation of NU-400 [43], a zirconium-based MOF based on a judiciously chosen pyrene-based linker and utilized it as a photosensitizer for the efficient production of $^1O_2$ and hence photocatalytic conversion of the sulfur mustard simulant 2-chloroethyl ethyl sulfide (CEES) into a benign sulfoxide product, using ambient air as the oxygen source. We selected a Zr_6-based MOF because of its outstanding stability under a wide range of thermal and chemical conditions. As pyrene has been known as an efficient photosensitizer that is capable of producing singlet oxygen upon exposure to UV light [44,45], we anticipated that a MOF with isolated pyrene linkers would be a good candidate catalyst for the photocatalytic oxidation of sulfur mustard.

The NU-400 material (Figure 1) was synthesized from the pyrene-2,7-dicarboxylic acid (Py-DCA) linker, $ZrCl_4$ metal salt, and acetic acid as a modulator, in DMF at 120 °C (see section S.3, Supporting Information File 1 for synthetic details). Different from the reported synthesis of pyrene-2,7-dicarboxylic acid linker [46], which required an organolithium reagent, a more benign Pd-catalyzed carbonylation reaction was utilized with 2,7-dibromopyrene as the starting material [46]. Powder X-ray diffraction (PXRD) analysis of the as-synthesized materials revealed that NU-400 is isostructural to the related UiO-67 framework based on 4,4'-biphenyldicarboxylate linkers. Subsequently, the structure of NU-400 (see section S.2.1, Table S1 in Supporting Information File 1 for crystal structure details) was established from PXRD data, by Rietveld refinement (Figure S1, Supporting Information File 1) of a model generated from UiO-67 (CCDC code WIZMAV03). The morphology of the materials was confirmed by scanning electron microscopy



Scheme 1: Detoxification routes of sulfur mustard gas: hydrolysis (green); oxidation to sulfoxide (blue) and dehydrohalogenation (red).

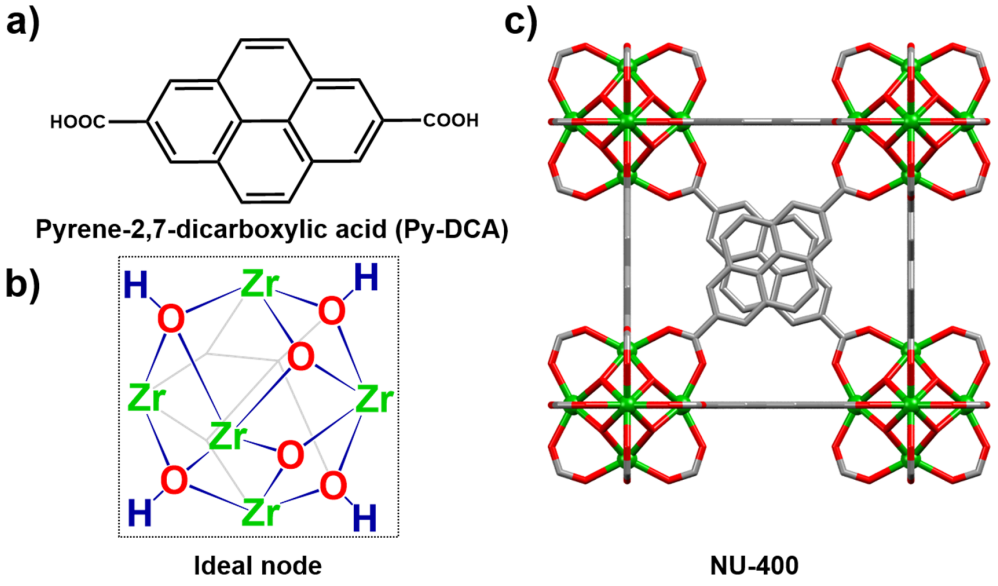


Figure 1: NU-400 constituents: a) the pyrene-based linker, pyrene-2,7-dicarboxylic acid and b) Zr_6 metal node. c) Fragment of the crystal structure of NU-400, established from PXRD data. Hydrogen atoms and disorder of pyrene groups are not shown for clarity. Zr: green, O: red, and C: grey.

(SEM) images showing that bulk NU-400 material consists of octahedral crystals ranging in sizes from 1 to 5 microns (Figure S3, Supporting Information File 1). The microporous nature of NU-400 was established by N_2 sorption measurements at 77 K, which revealed a Brunauer–Emmet–Teller (BET) surface area of 1325 m^2/g (Figure S4, Supporting Information File 1) [44]. The pore size analysis using DFT model revealed pores of approximately 11 Å, which is suitable for diffusion of CEES molecules into the pores of NU-400.

The solid-state UV–vis spectrum of NU-400 reveals that the strongest absorption bands lie below 400 nm (see Figure S5, Supporting Information File 1), leading us to use two commercially available ultraviolet light emitting diodes (UV-LEDs) with λ_{max} = 390–400 nm as a means to excite the MOF for $^1O_2$ production.

Results and Discussion

As our first entry into investigating the efficiency of NU-400 as a photosensitizer for singlet oxygen generation, we used 1 mol % (2 μmol, 4.75 mg) of the MOF under oxygen saturation conditions and UV irradiation (see section S.3.3 in Supporting Information File 1 for the detailed procedure). Aliquots were taken at various time points, filtered using syringe filters and, after dilution with dichloromethane, analyzed by GC-FID to monitor the reaction kinetics. Oxidation products were analyzed by NMR spectroscopy using deuterated methanol as a solvent. Under these conditions, reaction monitoring revealed that complete and selective conversion of CEES into CEESO was achieved over a period of 50 minutes, with a half-life of 10.2 minutes (Figure 2). During control experiments designed to evaluate the significance of each parameter in the process of $^1O_2$ production, we unexpectedly found that conducting the photocatalytic oxidation under the same conditions of irradiation, and the same MOF content, but in the absence of O_2 saturation step, also led to complete conversion of CEES into the sulfoxide. Specifically, under such conditions the complete conversion of CEES was observed after 2 hours, with a half-life of 13.5 minutes (Figure 2). Achieving complete oxidation of CEES without the O_2 saturation represents a milestone for the potential deployment of MOFs as an active detoxification catalyst and, consequently, we focused on detailed exploration of the activity of NU-400 in air, without oxygen purging.

Given that NU-400 is an active photocatalyst, where the pyrene-based linkers are expected to play the role of photosensitizers responsible for singlet oxygen production under UV irradiation, several control studies were performed to firmly establish the role of the linker. We explored the ability of pure linker precursor to act as the photosensitizer by performing the oxidation in the presence of 1 mol % Py-DCA (3.4 mg, 11.5 μmol) under air and in the presence of UV light, leading to a 75% conversion of CEES to CEESO after 2 hours (Figure 2). This observation implies that incorporation into the MOF structure enhanced the catalytic activity of Py-DCA, most likely due to the heterogeneous nature of the MOF, which assembles the pyrene linkers periodically within a robust three-dimensional framework, preventing their deactivation through aggregation. In all cases the $^1O_2$ acted as a highly selective oxidant for the formation of the target sulfoxide species, as no overoxidation to

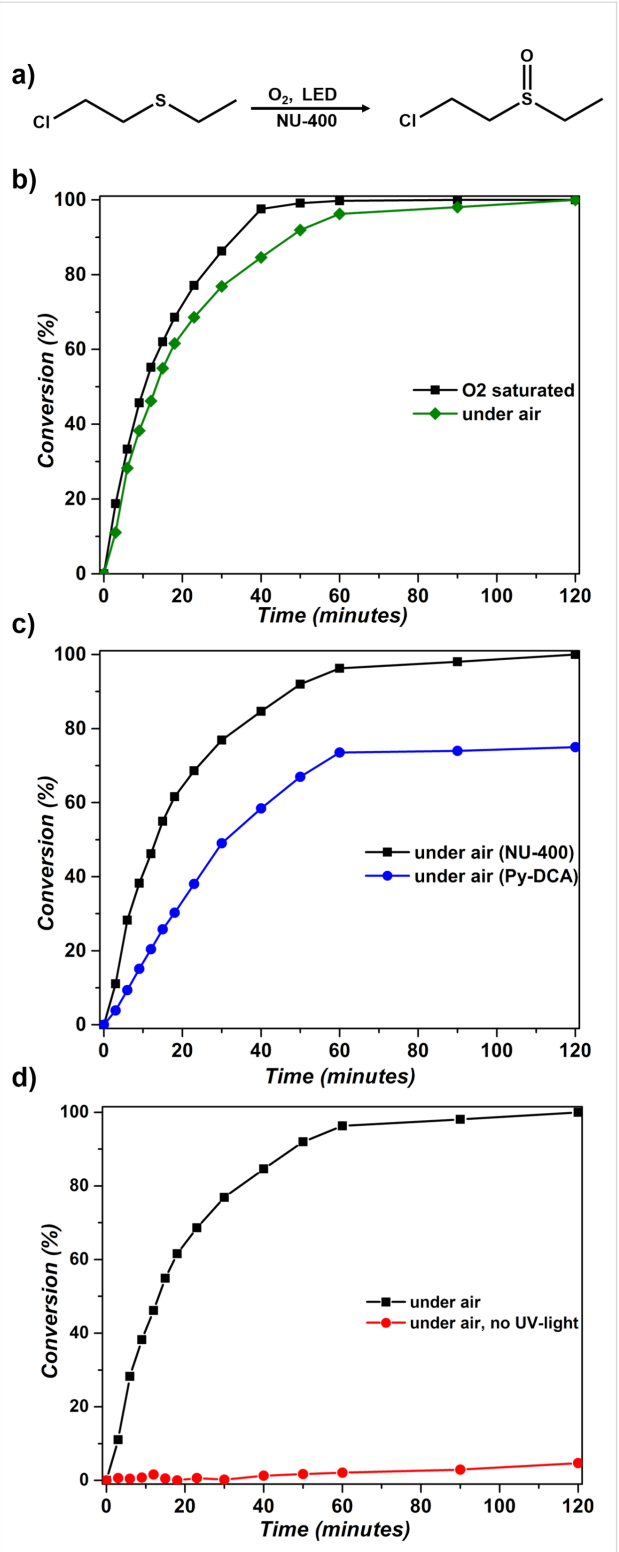


Figure 2: Conversion of CEES to CEESO under different conditions: (a) reaction scheme; (b) in the presence of NU-400 with O_2 saturation and under air; (c) in the presence of Py-DCA with O_2 saturation and under air, and (d) in the presence or absence of UV-light, under air. One mol % (based on Py-DCA) catalyst loading was used for all reactions.

form a more toxic sulfone analogue was observed (Figure S6, Supporting Information File 1). Finally, we explored the possibility of the reaction occurring in the absence of UV light. Under these conditions, in the presence of 1 mol % (12 µmol, 3.4 mg) of the MOF, no conversion of CEES was detected (Figure 2), confirming the role of NU-400 as a photocatalyst.

The photocatalytic activity of NU-400 in air, without oxygen presaturation, is significantly higher compared to the previously explored mesoporous NU-1000 MOF, which is based on a different, tetratopic pyrene-based linker 4,4',4'',4'''-(pyrene-1,3,6,8-tetrayl)tetrabenzoate (H_4TBApy). Using 1 mol % (5.2 mg) NU-1000 as a photocatalyst enabled the full conversion of CEES into CEESO with a half-life of only 6.2 minutes under conditions of O_2 saturation. However, the process was significantly slower, with a half-life of 24.5 minutes (Figure 3), when the reaction vessel was not saturated with oxygen. The superior performance of NU-400 (half-life of 13.5 minutes) under air can be attributed to the higher density of pyrene linkers in NU-400 (0.101 g/cm^3) compared to NU-1000 (0.0506 g/cm^3) which is responsible for $^1O_2$ generation.

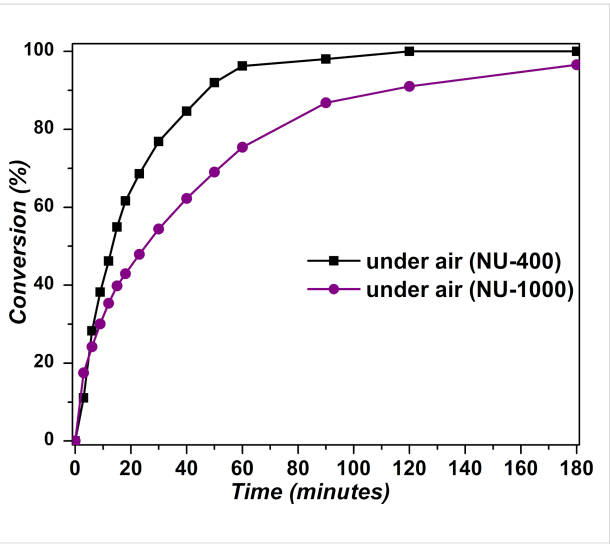


Figure 3: Selective oxidation of CEES to CEESO using 1 mol % catalyst of NU-400 (black) versus NU-1000 (purple).

Finally, we investigated to recyclability of NU-400 by adding multiple injections of CEES (0.2 µmol) into the microwave vial after one cycle of full conversion of CEES to CEESO. As the reaction was carried out using the oxygen available in atmosphere, without any additional O_2 purging, opening the microwave vial upon the addition of CEES ensured the presence of fresh air needed for the reaction. This recyclability test was repeated three times, and the reaction progress was monitored using GC-FID in order to calculate the conversion of the reaction after each injection (Figure 4).

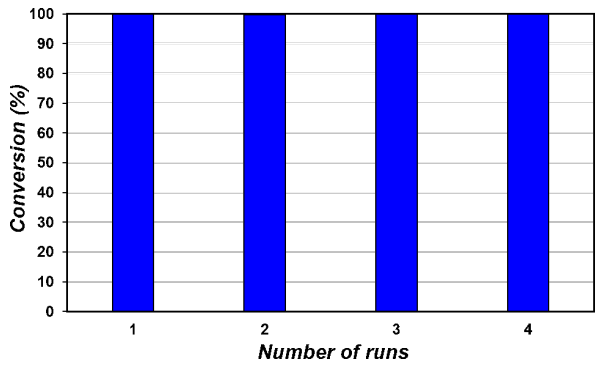


Figure 4: The reusability of the catalyst NU-400 MOF over four successive injections of CEES (0.2 mmol) into the same reaction vial.

The photocatalytic oxidation reaction takes place without noticeable degradation of NU-400, as evidenced by PXRD analysis following four cycles of CEES to CEESO oxidation, which reveals a high degree of crystallinity (see Figure S7, Supporting Information File 1). At the same time, no overoxidation of CEES to 2-chloroethyl ethyl sulfone ($CEESO_2$) was observed, as demonstrated by ^1H NMR spectroscopy (Figure S6, Supporting Information File 1).

Conclusion

In summary, we demonstrated NU-400, a microporous MOF based on a pyrene-2,7-dicarboxylate linker as a highly effective platform for singlet oxygen production and photocatalytic degradation of mustard gas simulant. In contrast to previously reported NU-1000, based on a 1,3,6,8-tetrasubstituted pyrene unit, which required saturation with oxygen to achieve effective high singlet oxygen production, the herein reported NU-400 is effective without oxygen saturation. The photocatalytic activity of NU-400 enabled singlet oxygen-induced conversion of CEES to CEESO with a half-life of 13.5 minutes under air, a milestone in the development of MOFs as new, highly efficient catalysts for mustard gas degradation.

Supporting Information

Supporting Information File 1

Methods and materials, ligand and MOF synthesis details and additional characterization data.
[https://www.beilstein-journals.org/bjnano/content/supplementary/2190-4286-10-232-S1.pdf]

Acknowledgements

O.K.F. gratefully acknowledges support from the Defense Threat Reduction Agency (HDTRA1-19-1-0007 for synthesis of fcu topology NU-400 and HDTRA1-18-1-0003 for catalysis study). T. F. acknowledges financial support of the National Science and Engineering Research Council (NSERC) Discovery Grant (RGPIN-2017-06467), NSERC E.W.R. Steacie Memorial Fellowship (SMFSU 507347-17) and McGill University Graduate Student Mobility Award (for GA), and Northwestern University.

ORCID® iDs

Ghada Ayoub - https://orcid.org/0000-0002-5864-8681
Mihails Arhangelskis - https://orcid.org/0000-0003-1150-3108
Xuan Zhang - https://orcid.org/0000-0001-8214-7265
Florencia Son - https://orcid.org/0000-0002-7524-3774
Timur Islamoglu - https://orcid.org/0000-0003-3688-9158
Tomislav Friščić - https://orcid.org/0000-0002-3921-7915
Omar K. Farha - https://orcid.org/0000-0002-9904-9845

Preprint

A non-peer-reviewed version of this article has been previously published as a preprint https://doi.org/10.26434/chemrxiv.9717011.v1

References

1. Fitzgerald, G. J. *Am. J. Public Health* **2008,** *98,* 611–625. doi:10.2105/ajph.2007.111930
2. Sidell, F. R.; Borak, J. *Ann. Emerg. Med.* **1992,** *21,* 865–871. doi:10.1016/s0196-0644(05)81036-4
3. Organisation for the Prohibition of Chemical Weapons. Chemical Weapons Convention. https://www.opcw.org/chemical-weapons-convention (accessed Aug 19, 2016).
4. Hess, G. UN says Syria and Islamic State used chemical weapons, Chemical and Engineering News, August 2016. (accessed Nov 3, 2019). https://cen.acs.org/articles/94/web/2016/08/UN-says-Syria-Islamic-State.html
5. Fassihi, F. U. N. Report Finds Chemical Weapons Used by Syrian Regime, Islamic State. The Wall Street Journal, 2016; https://www.wsj.com/articles/u-n-report-finds-chemical-weapons-used-by-syrian-regime-islamic-state-1472092954 (accessed Dec 4, 2019).
6. Sezigen, S.; Eyison, R. K.; Kenar, L. *Gulhane Med. J.* **2019,** *61,* 64–68. doi:10.26657/gulhane.00056
7. Irvine, D. A.; Earley, J. P.; Cassidy, D. P.; Harvey, S. P. *Water Sci. Technol.* **1997,** *35,* 67–74. doi:10.2166/wst.1997.0014
8. Wang, Q.-Q.; Begum, R. A.; Day, V. W.; Bowman-James, K. *Org. Biomol. Chem.* **2012,** *10,* 8786–8793. doi:10.1039/c2ob26482j
9. Wagner, G. W.; Bartram, P. W.; Koper, O.; Klabunde, K. J. *J. Phys. Chem. B* **1999,** *103,* 3225–3228. doi:10.1021/jp984689u
10. Wagner, G. W.; Koper, O. B.; Lucas, E.; Decker, S.; Klabunde, K. J. *J. Phys. Chem. B* **2000,** *104,* 5118–5123. doi:10.1021/jp000101j
11. Horcajada, P.; Surblé, S.; Serre, C.; Hong, D.-Y.; Seo, Y.-K.; Chang, J.-S.; Grenèche, J.-M.; Margiolaki, I.; Férey, G. *Chem. Commun.* **2007,** 2820–2822. doi:10.1039/b704325b
12. Popiel, S.; Nawała, J. *Enzyme Microb. Technol.* **2013,** *53,* 295–301. doi:10.1016/j.enzmictec.2013.06.002
13. Price, C. C.; Bullitt, O. H. *J. Org. Chem.* **1947,** *12,* 238–248. doi:10.1021/jo01166a006
14. Gall, R. D.; Faraj, M.; Hill, C. L. *Inorg. Chem.* **1994,** *33,* 5015–5021. doi:10.1021/ic00100a028

15. Richardson, D. E.; Yao, H.; Frank, K. M.; Bennett, D. A. *J. Am. Chem. Soc.* **2000,** *122,* 1729–1739. doi:10.1021/ja9927467
16. Boring, E.; Geletii, Y. V.; Hill, C. L. *J. Am. Chem. Soc.* **2001,** *123,* 1625–1635. doi:10.1021/ja0033133
17. Ringenbach, C. R.; Livingston, S. R.; Kumar, D.; Landry, C. C. *Chem. Mater.* **2005,** *17,* 5580–5586. doi:10.1021/cm051372f
18. Wagner, G. W.; Yang, Y.-C. *Ind. Eng. Chem. Res.* **2002,** *41,* 1925–1928. doi:10.1021/ie010732f
19. Hirade, J.; Ninomiya, A. *J. Biochem.* **1950,** *37,* 19–34. doi:10.1093/oxfordjournals.jbchem.a126178
20. Yang, Y. C.; Baker, J. A.; Ward, J. R. *Chem. Rev.* **1992,** *92,* 1729–1743. doi:10.1021/cr00016a003
21. Jang, Y. J.; Kim, K.; Tsay, O. G.; Atwood, D. A.; Churchill, D. G. *Chem. Rev.* **2015,** *115,* PR1–PR76. doi:10.1021/acs.chemrev.5b00402
22. DeRosa, M. C.; Crutchley, R. J. *Coord. Chem. Rev.* **2002,** *233–234,* 351–371. doi:10.1016/s0010-8545(02)00034-6
23. Griesbeck, A. G.; El-Idreesy, T. T.; Bartoschek, A. *Adv. Synth. Catal.* **2004,** *346,* 245–251. doi:10.1002/adsc.200303181
24. Roman, E. S. Heterogeneous Singlet Oxygen Sensitizers. In *Singlet Oxygen: Applications in Biosciences and Nanosciences;* Nonell, S.; Flors, C., Eds.; **Comprehensive Series in Photochemical & Photobiological Sciences**, Vol. 1; Royal Society of Chemistry: Cambridge, United Kingdom, 2016; pp 183–208. doi:10.1039/9781782622208-00183
25. Li, H.; Eddaoudi, M.; O'Keeffe, M.; Yaghi, O. M. *Nature* **1999,** *402,* 276–279. doi:10.1038/46248
26. Férey, G. *Chem. Soc. Rev.* **2008,** *37,* 191–214. doi:10.1039/b618320b
27. Cooper, A. I.; Rosseinsky, M. J. *Nat. Chem.* **2009,** *1,* 26–27. doi:10.1038/nchem.157
28. Shimizu, G. K. H.; Vaidhyanathan, R.; Taylor, J. M. *Chem. Soc. Rev.* **2009,** *38,* 1430–1449. doi:10.1039/b802423p
29. Zhou, H.-C.; Long, J. R.; Yaghi, O. M. *Chem. Rev.* **2012,** *112,* 673–674. doi:10.1021/cr300014x
30. Chen, Z.; Hanna, S. L.; Redfern, L. R.; Alezi, D.; Islamoglu, T.; Farha, O. K. *Coord. Chem. Rev.* **2019,** *386,* 32–49. doi:10.1016/j.ccr.2019.01.017
31. Denny, M. S., Jr.; Moreton, J. C.; Benz, L.; Cohen, S. M. *Nat. Rev. Mater.* **2016,** *1,* 16078–16085. doi:10.1038/natrevmats.2016.78
32. Smaldone, R. A.; Forgan, R. S.; Furukawa, H.; Gassensmith, J. J.; Slawin, A. M.; Yaghi, O. M.; Stoddart, J. F. *Angew. Chem., Int. Ed.* **2010,** *49,* 8630–8634. doi:10.1002/anie.201002343
33. Campbell, M. G.; Liu, S. F.; Swager, T. M.; Dincă, M. *J. Am. Chem. Soc.* **2015,** *137,* 13780–13783. doi:10.1021/jacs.5b09600
34. Orellana-Tavra, C.; Baxter, E. F.; Tian, T.; Bennett, T. D.; Slater, N. K. H.; Cheetham, A. K.; Fairen-Jimenez, D. *Chem. Commun.* **2015,** *51,* 13878–13881. doi:10.1039/c5cc05237h
35. Lee, J.; Farha, O. K.; Roberts, J.; Scheidt, K. A.; Nguyen, S. T.; Hupp, J. T. *Chem. Soc. Rev.* **2009,** *38,* 1450–1459. doi:10.1039/b807080f
36. Ayoub, G.; Islamoglu, T.; Goswami, S.; Friščić, T.; Farha, O. K. *ACS Appl. Mater. Interfaces* **2019,** *11,* 15788–15794. doi:10.1021/acsami.9b02764
37. Howarth, A. J.; Liu, Y.; Li, P.; Li, Z.; Wang, T. C.; Hupp, J. T.; Farha, O. K. *Nat. Rev. Mater.* **2016,** *1,* 15018. doi:10.1038/natrevmats.2015.18
38. Feng, D.; Gu, Z.-Y.; Li, J.-R.; Jiang, H.-L.; Wei, Z.; Zhou, H.-C. *Angew. Chem., Int. Ed.* **2012,** *51,* 10307–10310. doi:10.1002/anie.201204475
39. Liu, Y.; Howarth, A. J.; Vermeulen, N. A.; Moon, S.-Y.; Hupp, J. T.; Farha, O. K. *Coord. Chem. Rev.* **2017,** *346,* 101–111. doi:10.1016/j.ccr.2016.11.008
40. Buru, C. T.; Majewski, M. B.; Howarth, A. J.; Lavroff, R. H.; Kung, C.-W.; Peters, A. W.; Goswami, S.; Farha, O. K. *ACS Appl. Mater. Interfaces* **2018,** *10,* 23802–23806. doi:10.1021/acsami.8b05792
41. Gil-San-Millan, R.; López-Maya, E.; Hall, M.; Padial, N. M.; Peterson, G. W.; DeCoste, J. B.; Rodríguez-Albelo, L. M.; Oltra, J. E.; Barea, E.; Navarro, J. A. R. *ACS Appl. Mater. Interfaces* **2017,** *9,* 23967–23973. doi:10.1021/acsami.7b06341
42. DeCoste, J. B.; Peterson, G. W. *Chem. Rev.* **2014,** *114,* 5695–5727. doi:10.1021/cr4006473
43. Lv, X.-L.; Yuan, S.; Xie, L.-H.; Darke, H. F.; Chen, Y.; He, T.; Dong, C.; Wang, B.; Zhang, Y.-Z.; Li, J.-R.; Zhou, H.-C. *J. Am. Chem. Soc.* **2019,** *141,* 10283–10293. doi:10.1021/jacs.9b02947
44. Liu, Y.; Buru, C. T.; Howarth, A. J.; Mahle, J. J.; Buchanan, J. H.; DeCoste, J. B.; Hupp, J. T.; Farha, O. K. *J. Mater. Chem. A* **2016,** *4,* 13809–13813. doi:10.1039/c6ta05903a
45. Bobbitt, N. S.; Mendonca, M. L.; Howarth, A. J.; Islamoglu, T.; Hupp, J. T.; Farha, O. K.; Snurr, R. Q. *Chem. Soc. Rev.* **2017,** *46,* 3357–3385. doi:10.1039/c7cs00108h
46. Zhang, X.; Huang, Z.; Ferrandon, M.; Yang, D.; Robison, L.; Li, P.; Wang, T. C.; Delferro, M.; Farha, O. K. *Nat. Catal.* **2018,** *1,* 356–362. doi:10.1038/s41929-018-0069-6

License and Terms

This is an Open Access article under the terms of the Creative Commons Attribution License (http://creativecommons.org/licenses/by/4.0). Please note that the reuse, redistribution and reproduction in particular requires that the authors and source are credited.

The license is subject to the *Beilstein Journal of Nanotechnology* terms and conditions: (https://www.beilstein-journals.org/bjnano)

The definitive version of this article is the electronic one which can be found at: doi:10.3762/bjnano.10.232

BEILSTEIN JOURNAL OF NANOTECHNOLOGY

Adsorptive removal of bulky dye molecules from water with mesoporous polyaniline-derived carbon

Hyung Jun An‡, Jong Min Park‡, Nazmul Abedin Khan and Sung Hwa Jhung*

Full Research Paper

Open Access

Address:
Department of Chemistry and Green-Nano Materials Research Center, Kyungpook National University, Daegu 41566, Republic of Korea

Email:
Sung Hwa Jhung* - sung@knu.ac.kr

* Corresponding author ‡ Equal contributors

Keywords:
acid red 1; adsorption; bulky dye molecules; Janus green B; polyaniline-derived carbon; water purification

Beilstein J. Nanotechnol. **2020,** *11,* 597–605.
doi:10.3762/bjnano.11.47

Received: 24 December 2019
Accepted: 16 March 2020
Published: 08 April 2020

This article is part of the thematic issue "New directions for nanoporous materials".

Guest Editor: C. T. Yavuz

© 2020 An et al.; licensee Beilstein-Institut.
License and terms: see end of document.

Abstract

Polyaniline-derived carbon (PDC) was obtained via pyrolysis of polyaniline under different temperatures and applied for the purification of water contaminated with dye molecules of different sizes and charge by adsorption. With increasing pyrolysis temperature, it was found that the hydrophobicity, pore size and mesopore volume increased. A mesoporous PDC sample obtained via pyrolysis at 900 °C showed remarkable performance in the adsorption of dye molecules, irrespective of dye charge, especially in the removal of bulky dye molecules, such as acid red 1 (AR1) and Janus green B (JGB). For example, the most competitive PDC material showed a Q_0 value (maximum adsorption capacity) 8.1 times that of commercial, activated carbon for AR1. The remarkable adsorption of AR1 and JGB over KOH-900 could be explained by the combined mechanisms of hydrophobic, π–π, electrostatic and van der Waals interactions.

Introduction

Dyes have been widely used in a wide range of industries including textile, leather and paper, causing serious concern worldwide mainly because of the contamination of water resources. For example, around 700,000 tons of textile dyes are produced annually; and a considerable quantity of the produced dyes is discharged into waste water [1]. Such dyes are usually toxic or are converted into toxic substances after further treatment [1,2], and dyes discarded in waste water inevitably increase the biochemical oxygen demand (BOD) and chemical oxygen demand (COD) levels. Additionally, dyes decrease sunlight penetration through water, decreasing the natural restoration activity of rivers. Moreover, dyes in waste water are also considered problematic in the aesthetic sense, since the absorbance of dyes is usually very high (therefore, even small quantity of dyes can affect the color of the water).

The removal of dye molecules from contaminated water is very important and has been carried out via various methods such as

oxidation [3,4], including advanced oxidation processing (AOP), photocatalysis [5], biological treatment, coagulation, and membrane separation [2,6,7]. However, these techniques are not very satisfactory for applications on a large scale. For example, dyes are very resistant against degradation by catalysis, with a common example given by the stable characteristics of dyes under even sunlight. Recently, adsorption has been regarded to be very effective and attractive because of its operation under mild conditions and no need of oxidant, active catalyst, and irradiation [8,9]. Therefore, adsorption with carbon nanotubes, activated carbon (AC), biomass, and metallic–organic frameworks (MOFs) has been actively studied for the removal of dye molecules from water [10-15]. However, adsorbents with high adsorption capacity, structural integrity, low cost and facile recyclability are required for the practical operations or commercial applications.

So far, the development of various adsorbents has been successful because of functional carbon materials (graphene [16] or porous carbon [17]), mesoporous materials [18] and MOFs [19-22]. For example, MOFs [23-25], carbonaceous materials (such as carbon nanotubes, graphene, biochar and activated carbon) [26] and clay [27] have been applied in adsorptive removal of contaminants of emerging concern, hazardous organics and persistent organic pollutants. Carbonaceous materials have been particularly attractive in the purification of contaminated water via adsorption because of the easy preparation of carbon materials [26], especially from waste materials [28]. Moreover, highly porous carbon materials, especially with high nitrogen content, have been produced from various precursors including organic polymers [29-33] and MOFs [34-38].

Polyaniline (PANI), prepared from aniline, is a useful polymer in various fields because of its facile synthesis, high conductivity and nitrogen content. Porous carbon materials, with high porosity and nitrogen content, have also been obtained from PANI. In other words, functional carbon, for catalysts and supercapacitors can be derived from high temperature carbonization of PANI, especially in the co-presence of activating agents such as KOH, H_3PO_4 or $ZnCl_2$ [39]. Even though PANI-derived carbon (PDC) was used in gas-phase adsorption [40,41], it has been scarcely applied in liquid phase adsorption. Only recently we applied PDC for the possible purification of water contaminated with organics and fuel containing dibenzothiophene or dimethyldibenzothiophene [42,43]. However, further research is required to utilize the highly porous PDC materials for the purification of water contaminated with organics such as dyes.

Herein, we utilized PDC, prepared especially at high temperature, for the purification of water contaminated with dyes, such as acid red 1 (AR1), Janus green B (JGB), methyl orange (MO) and methylene blue (MB), via adsorption. AR1 is a large anionic dye which is toxic and widely applied in the paper industry [44]. Janus green B (JGB) is one of the most typical large cationic dyes that is widely used in several industries [42]. MO and MB are widely applied anionic and cationic dyes, respectively [45]. The chemical structures of the studied dyes are shown in Supporting Information File 1, Figure S1.

A PDC, obtained from PANI at 900 °C, showed remarkable performance in the adsorption of bulky dye molecules such as AR1 and JGB. For example, the PDC material developed in this work shows the highest adsorption capacity compared with any reported results, so far. Moreover, the adsorption capacity of the PDC material is more than 8 times that of a commercial, activated carbon. However, the adsorptive performance of the PDC for small dye molecules, such as MO and MB, was not very impressive, albeit quite competitive against similar reported results. The adsorption mechanisms could be suggested based on the physical properties (including hydrophobicity) of PDC materials and adsorption of AR1 and JGB under a wide range of pH values (from 2 to 12).

Results and Discussion

Characterization of polyaniline-derived carbon (PDC)

The porosity and pore size distribution of the adsorbents were characterized with nitrogen adsorption at 77 K. As shown in Figure 1a, the porosity of the PDC materials was considerable when the pyrolysis temperature was equal to or higher than 700 °C. The detailed porosity data are summarized in Supporting Information File 1, Table S1. With increasing pyrolysis temperature up to 800 °C, the BET surface area, total pore volume and mesopore volume increased. However, all of the porosity data (BET surface area, and total, micro- and mesopore volumes) decreased with further increasing temperature from 800 to 900 °C. Therefore, 800 °C was the optimum temperature to derive PDC materials with the highest porosity, excluding the micropore volume (for this, 750 °C was the most effective). Importantly, the pore size distribution patterns presented in Figure 1b show that the pore size of PDC increased with increasing pyrolysis temperature; and KOH-900, a PDC material that was obtained via pyrolysis of PANI at 900 °C, has an average pore size of ≈3 nm, which is very effective in adsorption of bulky dye molecules (vide infra). On the contrary, the pore size of activated carbon (AC) is very small (or mainly in microporous region); therefore, it might not be effective in adsorption of bulky dye molecules.

The hydrophobicity or hydrophilicity of PDC was estimated by checking the adsorbed quantity of water and *n*-octane [46]. The

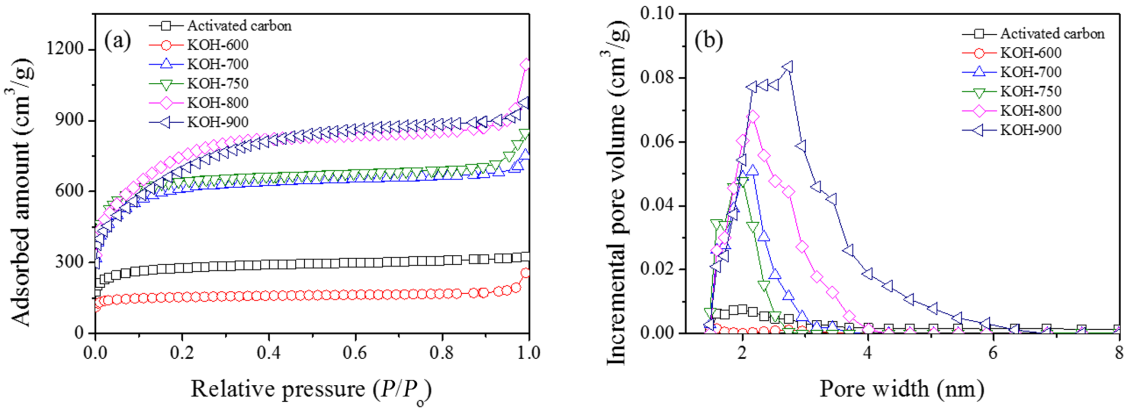


Figure 1: (a) N_2 adsorption isotherms and (b) pore size distribution of PDC materials and activated carbon (AC) .

quantity of adsorbed water decreased with increasing pyrolysis temperature, as shown in Figure 2a. On the contrary, the adsorbed *n*-octane showed the very opposite trend (Figure 2b). The adsorbed *n*-octane was in the order: KOH-900 > KOH-800 > KOH-750 > KOH-700 > KOH-600. The ratio of adsorbed vapors (*n*-octane/water, mol/mol) is shown as Figure 2c, and the ratio increased monotonically with increasing pyrolysis temperature. Therefore, it could be confirmed that the hydrophobicity of PDC increased with increasing pyrolysis temperature. This is understandable based on the enrichment of carbon (or successive removal of heteroatoms such as nitrogen and oxygen) with increasing pyrolysis temperature [42,43]. The best adsorbent (vide infra) KOH-900 was analyzed further with Raman spectroscopy. As shown in Supporting Information File 1, Figure S1, KOH-900 is composed of both graphitic and defect phases. Therefore, KOH-900 might be useful for adsorp-

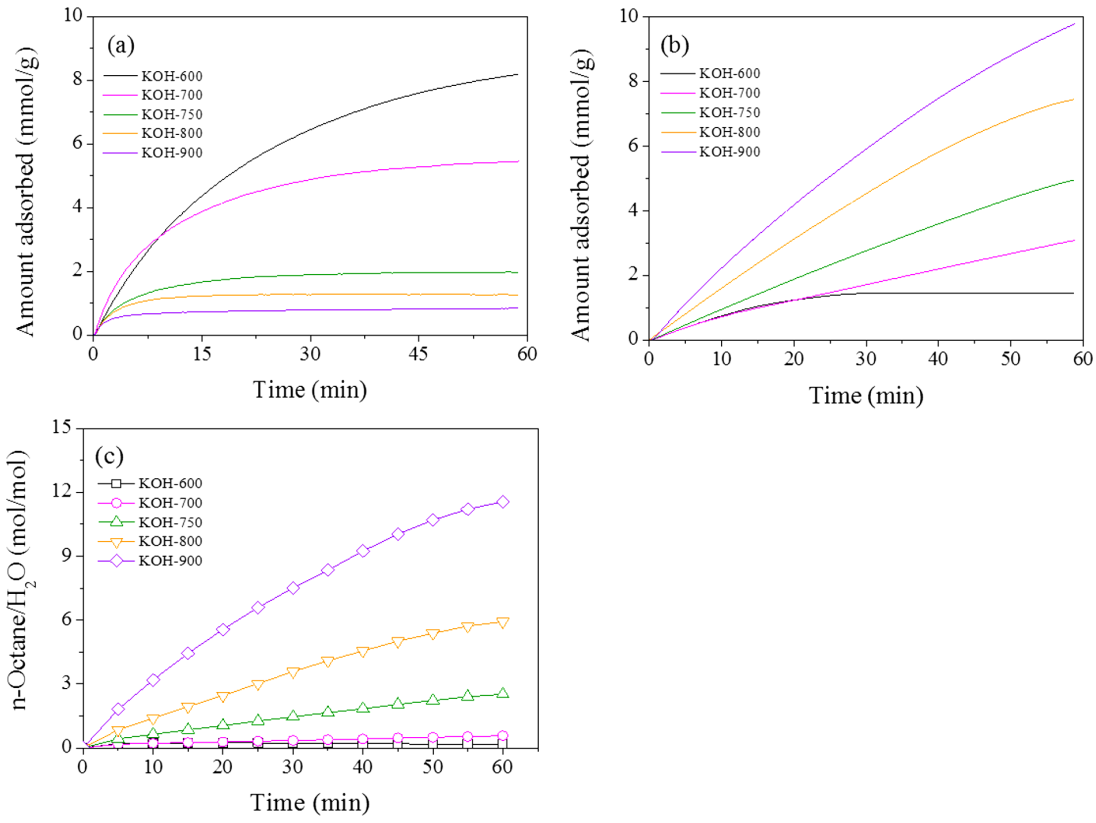


Figure 2: Amount of adsorbed (a) H_2O and (b) *n*-octane over PDC materials. (c) Ratios of adsorbed amounts of *n*-octane/H_2O over PDC materials.

tion because of defects and the graphitic layers (with π-electrons).

Dye adsorption over polyaniline-derived carbon (PDC)

Firstly, adsorption of AR1 over PDC and AC was carried out for 6 h. As illustrated in Figure 3a, the adsorbed quantity (q_{6h}, in mg/g) decreased in the order: KOH-900 > KOH-800 > KOH-750 > KOH-700 > AC > KOH-600. Therefore, the PDC materials are very competitive in AR1 adsorption compared to AC when the pyrolysis temperature is at 700 °C or higher. Considering the dominant role of porosity in adsorption [47], the q_{6h} values were calculated based on the BET surface area of adsorbents. Curiously, as presented in Figure 3b, the q_{6h} (in mg/m^2) for AR1 showed a tendency similar to that of the quantity based on unit weight of adsorbents or PDC (q_{6h} in mg/g). Therefore, it should be emphasized that there is another important contribution, excluding simple porosity, to explain the performance of the PDC materials in AR1 adsorption.

Considering that the best performance was found with KOH-900 (based on both unit weight and BET surface area), further experiments were done with KOH-900 and AC, as a standard adsorbent. Similar to AR1, other dye molecules (with different charge and size) were also adsorbed for 6 h over KOH-900 and AC. As presented in Figure 4, KOH-900 had a much higher q_{6h} than AC for the four dyes studied, namely AR1, MO, MB, and JGB. However, the ratio of adsorbed quantity [q_{6h} (KOH-900)/q_{6h} (AC)] was very much dependent on the size of the adsorbed dye, as summarized in Supporting Information File 1, Table S2. KOH-900 showed much higher efficiency than AC especially in the adsorption of bulky dye molecules, such as AR1 and JGB.

Inspired by the remarkable performance of KOH-900 in the adsorption of bulky dye molecules, adsorption experiments

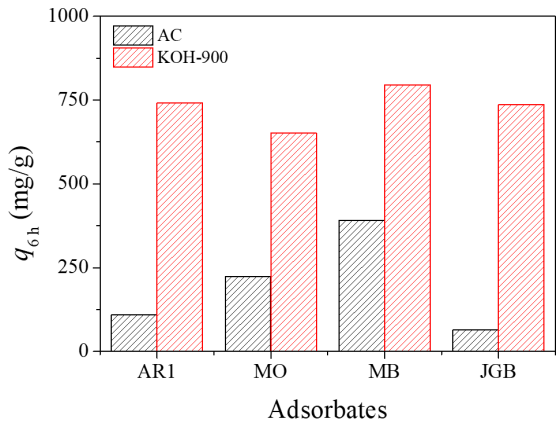


Figure 4: Adsorbed quantities of acid red 1 (AR1), methyl orange (MO), methylene blue (MB) and Janus green B (JGB) over AC and KOH-900.

were further carried out for AR1 and JGB over KOH-900 and AC for a wide range of adsorption times from 0.5 to 6 h. As illustrated in Figure 5, KOH-900 had a much higher adsorption capacity than AC for AR1 and JGB, irrespective of the adsorption time and the type of adsorbate or dye. In order to determine the maximum adsorption capacity of KOH-900 and AC for AR1, adsorption isotherms were obtained from adsorption for 6 h with a wide range of AR1 concentrations. The adsorption isotherms and Langmuir plots are illustrated in Figure 6a and 6b, respectively. The high correlation coefficients (R^2 > 0.99) shown on Figure 6b confirm that the Langmuir equation can be adequately applied to interpret the observed adsorptions. As summarized in Table 1, KOH-900 had a Q_0 (for AR1) value 8.1 times as that of commercial, activated carbon.

Adsorption mechanism

Understanding the adsorption mechanism is helpful to develop a competitive adsorption technology and to further improve the

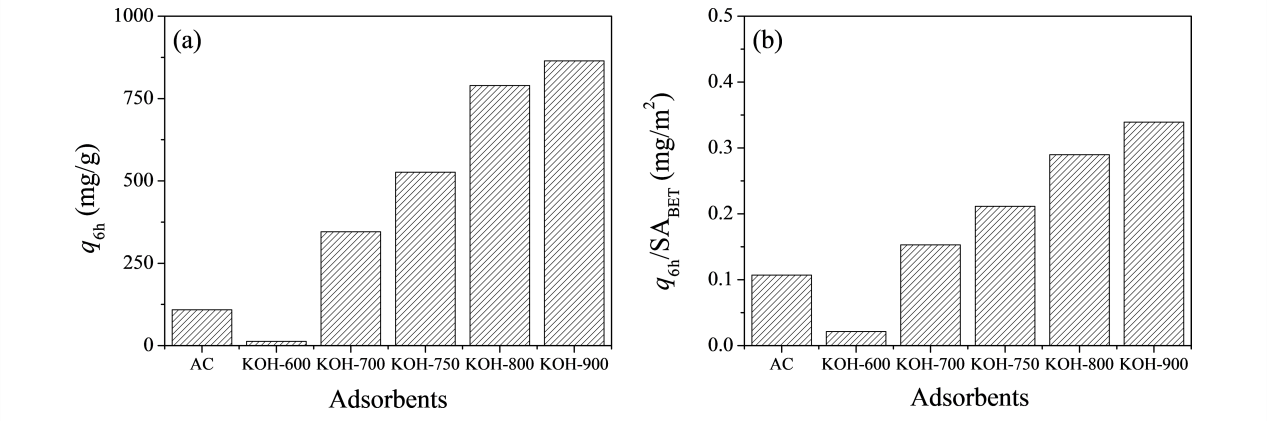


Figure 3: Adsorbed quantities of acid red 1 (AR1) over AC, KOH-600, KOH-700, KOH-750, KOH-800 and KOH-900 based on (a) unit weight and (b) unit BET surface area.

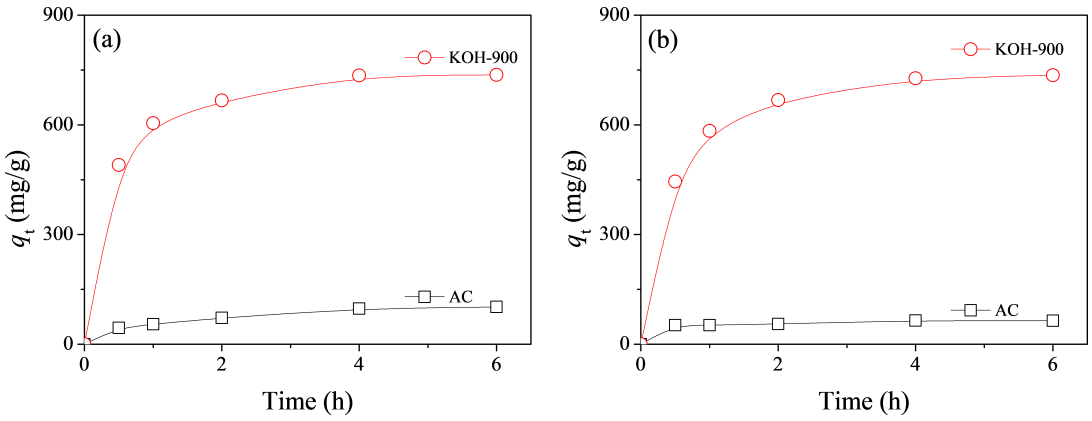


Figure 5: Effect of contact time on (a) AR1 and (b) JGB adsorption over AC and KOH-900.

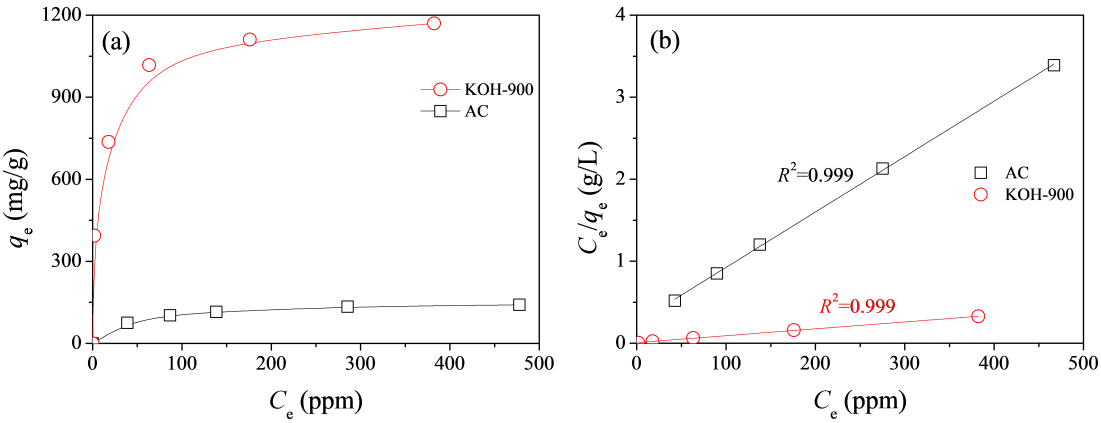


Figure 6: (a) Adsorption isotherms and (b) Langmuir plots for the adsorption of AR1 from water over AC and KOH-900.

Table 1: Maximum adsorption capacity (Q_0) of some reported adsorbents for the adsorption of AR1 from water.

Adsorbents	SA_{BET} ($m^2 \cdot g^{-1}$)	Solution pH	Q_0 ($mg \cdot g^{-1}$)	Ref.
coal FA	9	6.0	93	[67]
Mg-Al-LDH	104	–	108	[68]
MH-1000	799	6.0	11.2	[69]
TNTs (HDTMA-modified version) treated with 0.0001 N acid	45	–	396	[70]
Fe_3O_4/MIL-101(Cr)	1790	5.0	143	[44]
chitosan–alunite composite	–	3.0	589	[71]
PCN-222(Fe)	2476	7.0	371	[72]
commercial activated carbon	1016	7.0	148	this work
KOH-900	2549	7.0	1192	this work

performance of an adsorbent. So far, several mechanisms [48], such as electrostatic [49,50], π–π [51-54], acid–base interactions [55,56], and hydrogen bonding [57-59], were applied to interpret various adsorption events. In order to understand the plausible mechanism, especially in aqueous phase, adsorption over a wide range of pH conditions is very effective [60] since both the adsorbate and adsorbent can be changed in terms of charge or functional group (for example, via protonation or deprotonation) under different conditions of acidity/basicity.

In this study, the q_{6h} values were checked over KOH-900 for AR1 and JBG under pH 2–12. As shown in Figure 7, the q_{6h} for

AR1 decreased monotonously with increasing pH of the solution; however, the adsorption of JGB showed an opposite trend. This very opposite trend, observed in anionic AR1 and cationic JGB, could be explained via electrostatic interactions considering the opposite charges on the studied dyes. Moreover, the studied PDC or KOH-900 might have both positive and negative charges, depending on pH, since the surface charge of porous carbon generally decreases (from positive to negative) with increasing pH of the adsorption solution [61-63]. Therefore, the negative AR1 should have a favorable interaction at low pH; on the contrary, the adsorption of the positive JGB will be more effective at higher pH if the electrostatic interaction is considered.

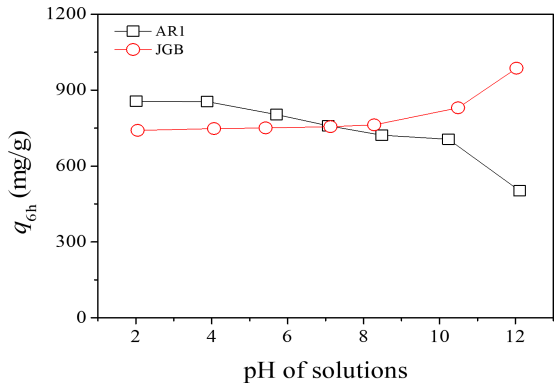


Figure 7: Effect of pH on the adsorbed amounts of AR1 and JGB over KOH-900.

However, there should be other dominant mechanisms since the q_{6h} values are quite high under a wide range of pH conditions. At first, the very high hydrophobicity of KOH-900, as shown in Figure 2, can be considered. Compared with any other adsorbent, KOH-900 showed the highest performance in AR1 adsorption, as shown in Figure 3. Therefore, hydrophobic interaction can be suggested as a plausible mechanism for AR1 and JGB adsorption. This mechanism, which has been suggested earlier in adsorption of malachite green [52], aromatics [64], benzotriazole/benzimidazole [53], bisphenol A [65] and pharmaceutical and personal care products (PPCPs) [66], is acceptable considering the relatively small impact of pH on the q_{6h}. Moreover, π–π interaction [51-54] might be another possible explanation considering that this interaction is hardly dependent on the pH (when aromatic rings are maintained under the studied pH); and both studied dyes (AR1 and JGB) and KOH-900 have ample aromatic rings with π electrons. Finally, the contribution of pore size should be mentioned. As illustrated in Figure 4 and Supporting Information File 1, Table S2, the KOH-900 sample is very effective in the adsorption of bulky dye molecules, as compared with the adsorption of small dyes such as MO and MB. This might be explained by the relatively large pore size of KOH-900, as shown in Figure 1b. Another explanation is that the pore size of KOH-900 is too large for effective adsorption of small MO or MB since van der Waals interactions rely on adequate matching between pore and adsorbates. On the contrary, bulky dye molecules such as AR1 and JGB can interact effectively with KOH-900 via van der Waals interactions, which relies on the suitable pore size of KOH-900 for the bulky dye molecules. In summary, the remarkable adsorption of AR1 and JGB over KOH-900 can be explained by the combined mechanisms of hydrophobic, π–π, electrostatic and van der Waals interactions.

Competitiveness of KOH-900 in adsorption of dyes

Based on the remarkable performance of KOH-900 in the adsorption of AR1 and JGB, the performance of KOH-900 PDC was compared with earlier results, as shown in Table 1 [44,67-72] and Table 2 [73-77] for AR1 and JGB, respectively. As summarized in Table 1, KOH-900 had a Q_0 value (for AR1) 8.1 times that of commercial, activated carbon. Moreover, KOH-900 had the highest Q_0, compared with any reported adsorbent, so far. Additionally, KOH-900 showed a Q_0 of more than 2 times that of a chitosan–alunite composite (previously the highest Q_0) [71] even though the pH of adsorption solution was not the same. If the pH effect (vide supra, including Figure 7) is considered, the difference in Q_0 between KOH-900 and chitosan–alunite composite will increase.

Table 2: Maximum adsorption capacity (Q_0) of some reported adsorbents for the adsorption of JGB from water.

Adsorbents	SA_{BET} ($m^2 \cdot g^{-1}$)	Solution pH	Q_0 ($mg \cdot g^{-1}$)	Ref.
magnetic-modified MWCNTs	145	7.0	250	[73]
ZnO/$Zn(OH)_2$-NP-AC	–	7.0	98	[74]
$Ni_{0.5}Zn_{0.5}Fe_2O_4$	–	7.0	333	[75]
mesoporous silica	659	–	62	[76]
TiO_2 (254 nm)	–	–	294	[77]
commercial activated carbon	1016	7.0	64[a]	this work
KOH-900	2549	7.0	736[a]	this work

[a]q_{6h}.

Based on Table 2, KOH-900 was also very competitive in JGB adsorption against the reported adsorbents. To begin with, KOH-900 had a q_{6h} for JGB 11.5 times that of AC. The q_{6h} of KOH-900 for JGB is more than 2 times that of the Q_0 of the $Ni_{0.5}Zn_{0.5}Fe_2O_4$ adsorbent. The difference in Q_0 should increase if the actual Q_0 of KOH-900 is reached (in this work, q_{6h} of KOH-900 was used in comparison) since Q_0 is always higher than any q_t value. Therefore, it could be confirmed that KOH-900 is remarkably effective in the removal of bulky dye molecules such as AR1 and JGB, irrespective of charge, mainly because of the large pores, high porosity and high hydrophobicity.

The Q_0 or q_t values of the reported adsorbents for MO and MB are compared in Supporting Information File 1, Tables S3 and S4, respectively. Even though KOH-900 is not very competitive in the adsorption of MO and MB (as compared with the adsorption of AR1 and JGB), the new adsorbent is also attractive in the removal of small dyes like MO and MB. Additionally, KOH-900 showed the second best performance in adsorption of MO or MB, partially because of its high porosity.

Conclusion

PANI-derived carbon materials were prepared from pyrolysis of PANI under a wide range of temperatures and applied in the adsorption of dyes from water. The hydrophobicity, pore size and mesopore volume were found to increase monotonously with increasing pyrolysis temperature. In addition, the best PDC (KOH-900) was very effective in the adsorption of dyes, especially those of a large size such as AR1 and JGB. For example, KOH-900 had a Q_0 (for AR1) value 8.1 times that of commercial, activated carbon. Moreover, KOH-900 showed a Q_0 value of more than 2 times that of a chitosan–alunite composite which previously showed the highest Q_0 to date. The remarkable adsorption of AR1 and JGB over KOH-900 could be explained with combined mechanisms such as hydrophobic, π–π, electrostatic and van der Waals interactions. Finally, the PDC materials presented in this work could be suggested as a potential adsorbent to purify water contaminated with dye molecules, irrespective of size and charge.

Materials and Methods

Chemicals

AR1 (60%), JGB (65%), MO (85%), MB (82%) and aniline hydrochloride (C_6H_8ClN, 97%) were acquired from Sigma-Aldrich. Activated carbon (2–3 mm, granule, practical grade) was obtained from Duksan Pure Chemical Co., Ltd. Other chemicals used in this research were of analytical grade and were purchased from commercial venders and applied without any purification.

Preparation of polyaniline-derived carbon (PDC) materials

The PDC materials were obtained via pyrolysis of PANI, derived from aniline hydrochloride, in two steps, following earlier reports [42,43]. In brief, PANI was firstly pyrolyzed at 550 °C for 2 h under nitrogen flow. The pyrolyzed product was mixed well with KOH (the weight of KOH was 2 times that of the pyrolyzed product) and carbonized again at 600–900 °C for 1 h under nitrogen flow. The PDC samples were named KOH-x where x represents the pyrolysis temperature in the second step.

Characterization of polyaniline-derived carbon (PDC) samples

PDC and AC were characterized by nitrogen adsorption (Micromeritics, Tristar II 3020) to understand their porosity characteristics. Nitrogen adsorption was carried out at 77 K after evacuation of samples at 150 °C for 12 h. The Brunauer−Emmett−Teller (BET) equation and t-plot were applied to calculate the surface area and micropore volume, respectively, of the adsorbents. The pore size distributions were calculated with nonlocal density functional theory (NLDFT). The hydrophobicity of the studied adsorbents was evaluated by measuring the relative quantities of adsorbed water and n-octane at 30 °C with thermogravimetric analysis (TGA, Perkin-Elmer TGA 4000 system), similar to a previous work [46]. In brief, an adsorbed quantity of water was measured for up to 60 min by feeding water vapor with the help of a nitrogen carrier. The adsorbed quantity of n-octane was determined similarly, and the relative quantity (n-octane/water, mol/mol) was calculated accordingly.

Adsorption of dye molecules

The adsorption of the dye molecules was carried out with model solution at pH 7.0, considering the usual pH of rainwater and river water [78]. Detailed methods to calculate the adsorbed quantity at time t in h (q_t) and maximum adsorption capacity (Q_0) [79] are shown in Supporting Information File 1. In order to understand the adsorption mechanism, the solution pH for AR1 and JGB was controlled (up to 2–12) with aqueous solution of NaOH or HCl (0.1 M each).

Supporting Information

Supporting Information File 1

Additional experimental procedure "Adsorption of dyes from water" and additional experimental results.
[https://www.beilstein-journals.org/bjnano/content/supplementary/2190-4286-11-47-S1.pdf]

Funding

This research was supported by Kyungpook National University Development Project Research Fund, 2019.

ORCID® iDs

Sung Hwa Jhung - https://orcid.org/0000-0002-6941-1583

References

1. Asghar, A.; Raman, A. A. A.; Daud, W. M. A. W. *J. Cleaner Prod.* **2015,** *87,* 826–838. doi:10.1016/j.jclepro.2014.09.010
2. Gupta, V. K.; Kumar, R.; Nayak, A.; Saleh, T. A.; Barakat, M. A. *Adv. Colloid Interface Sci.* **2013,** *193–194,* 24–34. doi:10.1016/j.cis.2013.03.003
3. Mezohegyi, G.; van der Zee, F. P.; Font, J.; Fortuny, A.; Fabregat, A. *J. Environ. Manage.* **2012,** *102,* 148–164. doi:10.1016/j.jenvman.2012.02.021
4. Gupta, V. K.; Khamparia, S.; Tyagi, I.; Jaspal, D.; Malviya, A. *Global J. Environ. Sci. Manage.* **2015,** *1,* 71–94. doi:10.7508/GJESM.2015.01.007
5. Reza, K. M.; Kurny, A. S. W.; Gulshan, F. *Appl. Water Sci.* **2017,** *7,* 1569–1578. doi:10.1007/s13201-015-0367-y
6. Pavithra, K. G.; Kumar, P. S.; Jaikumar, V.; Rajan, P. S. *J. Ind. Eng. Chem. (Amsterdam, Neth.)* **2019,** *75,* 1–19. doi:10.1016/j.jiec.2019.02.011
7. Holkar, C. R.; Jadhav, A. J.; Pinjari, D. V.; Mahamuni, N. M.; Pandit, A. B. *J. Environ. Manage.* **2016,** *182,* 351–366. doi:10.1016/j.jenvman.2016.07.090
8. Jiang, D.; Chen, M.; Wang, H.; Zeng, G.; Huang, D.; Cheng, M.; Liu, Y.; Xue, W.; Wang, Z. *Coord. Chem. Rev.* **2019,** *380,* 471–483. doi:10.1016/j.ccr.2018.11.002
9. Gusain, R.; Kumar, N.; Ray, S. S. *Coord. Chem. Rev.* **2020,** *405,* 213111. doi:10.1016/j.ccr.2019.213111
10. Rajabi, M.; Mahanpoor, K.; Moradi, O. *RSC Adv.* **2017,** *7,* 47083–47090. doi:10.1039/c7ra09377b
11. Zare, K.; Gupta, V. K.; Moradi, O.; Makhlouf, A. S. H.; Sillanpää, M.; Nadagouda, M. N.; Sadegh, H.; Shahryari-ghoshekandi, R.; Pal, A.; Wang, Z.-j.; Tyagi, I.; Kazemi, M. *J. Nanostruct. Chem.* **2015,** *5,* 227–236. doi:10.1007/s40097-015-0158-x
12. Anastopoulos, I.; Kyzas, G. Z. *J. Mol. Liq.* **2014,** *200,* 381–389. doi:10.1016/j.molliq.2014.11.006
13. Hadi, P.; Xu, M.; Ning, C.; Lin, C. S. K.; McKay, G. *Chem. Eng. J.* **2015,** *260,* 895–906. doi:10.1016/j.cej.2014.08.088
14. Adeyemo, A. A.; Adeoye, I. O.; Bello, O. S. *Toxicol. Environ. Chem.* **2012,** *94,* 1846–1863. doi:10.1080/02772248.2012.744023
15. Kumar, P.; Agnihotri, R.; Wasewar, K. L.; Uslu, H.; Yoo, C. *Desalin. Water Treat.* **2012,** *50,* 226–244. doi:10.1080/19443994.2012.719472
16. Lazar, P.; Karlický, F.; Jurečka, P.; Kocman, M.; Otyepková, E.; Šafářová, K.; Otyepka, M. *J. Am. Chem. Soc.* **2013,** *135,* 6372–6377. doi:10.1021/ja403162r
17. Benzigar, M. R.; Talapaneni, S. N.; Joseph, S.; Ramadass, K.; Singh, G.; Scaranto, J.; Ravon, U.; Al-Bahily, K.; Vinu, A. *Chem. Soc. Rev.* **2018,** *47,* 2680–2721. doi:10.1039/c7cs00787f
18. Suib, S. L. *Chem. Rec.* **2017,** *17,* 1169–1183. doi:10.1002/tcr.201700025
19. Kirchon, A.; Feng, L.; Drake, H. F.; Joseph, E. A.; Zhou, H.-C. *Chem. Soc. Rev.* **2018,** *47,* 8611–8638. doi:10.1039/c8cs00688a
20. Adil, K.; Belmabkhout, Y.; Pillai, R. S.; Cadiau, A.; Bhatt, P. M.; Assen, A. H.; Maurin, G.; Eddaoudi, M. *Chem. Soc. Rev.* **2017,** *46,* 3402–3430. doi:10.1039/c7cs00153c
21. Silva, P.; Vilela, S. M. F.; Tomé, J. P. C.; Almeida Paz, F. A. *Chem. Soc. Rev.* **2015,** *44,* 6774–6803. doi:10.1039/c5cs00307e
22. Li, J.; Wang, X.; Zhao, G.; Chen, C.; Chai, Z.; Alsaedi, A.; Hayat, T.; Wang, X. *Chem. Soc. Rev.* **2018,** *47,* 2322–2356. doi:10.1039/c7cs00543a
23. Dhaka, S.; Kumar, R.; Deep, A.; Kurade, M. B.; Ji, S.-W.; Jeon, B.-H. *Coord. Chem. Rev.* **2019,** *380,* 330–352. doi:10.1016/j.ccr.2018.10.003
24. Gao, Q.; Xu, J.; Bu, X.-H. *Coord. Chem. Rev.* **2019,** *378,* 17–31. doi:10.1016/j.ccr.2018.03.015
25. Li, J.; Wang, H.; Yuan, X.; Zhang, J.; Chew, J. W. *Coord. Chem. Rev.* **2020,** *404,* 213116. doi:10.1016/j.ccr.2019.213116
26. Sophia A., C.; Lima, E. C. *Ecotoxicol. Environ. Saf.* **2018,** *150,* 1–17. doi:10.1016/j.ecoenv.2017.12.026
27. Unuabonah, E. I.; Nöske, R.; Weber, J.; Günter, C.; Taubert, A. *Beilstein J. Nanotechnol.* **2019,** *10,* 119–131. doi:10.3762/bjnano.10.11
28. Yahya, M. A.; Al-Qodah, Z.; Ngah, C. W. Z. *Renewable Sustainable Energy Rev.* **2015,** *46,* 218–235. doi:10.1016/j.rser.2015.02.051
29. Dutta, S.; Bhaumik, A.; Wu, K. C.-W. *Energy Environ. Sci.* **2014,** *7,* 3574–3592. doi:10.1039/c4ee01075b
30. Kou, J.; Sun, L.-B. *Ind. Eng. Chem. Res.* **2016,** *55,* 10916–10925. doi:10.1021/acs.iecr.6b02857
31. Xu, G.; Ding, B.; Nie, P.; Shen, L.; Wang, J.; Zhang, X. *Chem. – Eur. J.* **2013,** *19,* 12306–12312. doi:10.1002/chem.201301352
32. Kou, J.; Sun, L.-B. *J. Mater. Chem. A* **2016,** *4,* 17299–17307. doi:10.1039/c6ta07305k
33. Schneidermann, C.; Otto, P.; Leistenschneider, D.; Grätz, S.; Eßbach, C.; Borchardt, L. *Beilstein J. Nanotechnol.* **2019,** *10,* 1618–1627. doi:10.3762/bjnano.10.157
34. Wang, C.; Kim, J.; Tang, J.; Kim, M.; Lim, H.; Malgras, V.; You, J.; Xu, Q.; Li, J.; Yamauchi, Y. *Chem* **2020,** *6,* 19–40. doi:10.1016/j.chempr.2019.09.005
35. Yang, W.; Li, X.; Li, Y.; Zhu, R.; Pang, H. *Adv. Mater. (Weinheim, Ger.)* **2019,** *31,* 1804740. doi:10.1002/adma.201804740
36. Chen, Y.-Z.; Zhang, R.; Jiao, L.; Jiang, H.-L. *Coord. Chem. Rev.* **2018,** *362,* 1–23. doi:10.1016/j.ccr.2018.02.008
37. Bhadra, B. N.; Vinu, A.; Serre, C.; Jhung, S. H. *Mater. Today* **2019,** *25,* 88–111. doi:10.1016/j.mattod.2018.10.016
38. Lin, K.-Y. A.; Chang, H.-A.; Chen, B.-J. *J. Mater. Chem. A* **2016,** *4,* 13611–13625. doi:10.1039/c6ta04619c
39. Ćirić-Marjanović, G.; Pašti, I.; Gavrilov, N.; Janošević, A.; Mentus, S. *Chem. Pap.* **2013,** *67,* 781–813. doi:10.2478/s11696-013-0312-1
40. Zhang, Z.; Zhou, J.; Xing, W.; Xue, Q.; Yan, Z.; Zhuo, S.; Qiao, S. Z. *Phys. Chem. Chem. Phys.* **2013,** *15,* 2523–2529. doi:10.1039/c2cp44436d
41. Silvestre-Albero, A.; Silvestre-Albero, J.; Martínez-Escandell, M.; Rodríguez-Reinoso, F. *Ind. Eng. Chem. Res.* **2014,** *53,* 15398–15405. doi:10.1021/ie5013129
42. Khan, N. A.; An, H. J.; Yoo, D. K.; Jhung, S. H. *J. Hazard. Mater.* **2018,** *360,* 163–171. doi:10.1016/j.jhazmat.2018.08.001
43. Yoo, D. K.; An, H. J.; Khan, N. A.; Hwang, G. T.; Jhung, S. H. *Chem. Eng. J.* **2018,** *352,* 71–78. doi:10.1016/j.cej.2018.06.144
44. Wang, T.; Zhao, P.; Lu, N.; Chen, H.; Zhang, C.; Hou, X. *Chem. Eng. J.* **2016,** *295,* 403–413. doi:10.1016/j.cej.2016.03.016
45. Ma, J.; Yu, F.; Zhou, L.; Jin, L.; Yang, M.; Luan, J.; Tang, Y.; Fan, H.; Yuan, Z.; Chen, J. *ACS Appl. Mater. Interfaces* **2012,** *4,* 5749–5760. doi:10.1021/am301053m

46. Bhadra, B. N.; Seo, P. W.; Khan, N. A.; Jhung, S. H. *Inorg. Chem.* **2016,** *55,* 11362–11371. doi:10.1021/acs.inorgchem.6b01882
47. Ahmed, I.; Khan, N. A.; Jhung, S. H. *Inorg. Chem.* **2013,** *52,* 14155–14161. doi:10.1021/ic402012d
48. Joseph, L.; Jun, B.-M.; Jang, M.; Park, C. M.; Muñoz-Senmache, J. C.; Hernández-Maldonado, A. J.; Heyden, A.; Yu, M.; Yoon, Y. *Chem. Eng. J.* **2019,** *369,* 928–946. doi:10.1016/j.cej.2019.03.173
49. Jung, B. K.; Hasan, Z.; Jhung, S. H. *Chem. Eng. J.* **2013,** *234,* 99–105. doi:10.1016/j.cej.2013.08.110
50. Hu, Y.; Guo, T.; Ye, X.; Li, Q.; Guo, M.; Liu, H.; Wu, Z. *Chem. Eng. J.* **2013,** *228,* 392–397. doi:10.1016/j.cej.2013.04.116
51. Akpinar, I.; Drout, R. J.; Islamoglu, T.; Kato, S.; Lyu, J.; Farha, O. K. *ACS Appl. Mater. Interfaces* **2019,** *11,* 6097–6103. doi:10.1021/acsami.8b20355
52. Lin, K.-Y. A.; Chang, H.-A. *Chemosphere* **2015,** *139,* 624–631. doi:10.1016/j.chemosphere.2015.01.041
53. Sarker, M.; Bhadra, B. N.; Seo, P. W.; Jhung, S. H. *J. Hazard. Mater.* **2017,** *324,* 131–138. doi:10.1016/j.jhazmat.2016.10.042
54. Kim, T. K.; Lee, J. H.; Moon, D.; Moon, H. R. *Inorg. Chem.* **2013,** *52,* 589–595. doi:10.1021/ic3011458
55. Hasan, Z.; Choi, E.-J.; Jhung, S. H. *Chem. Eng. J.* **2013,** *219,* 537–544. doi:10.1016/j.cej.2013.01.002
56. Zhang, K.-D.; Tsai, F.-C.; Ma, N.; Xia, Y.; Liu, H.-L.; Zhan, X.-Q.; Yu, X.-Y.; Zeng, X.-Z.; Jiang, T.; Shi, D.; Chang, C.-J. *Materials* **2017,** *10,* 205. doi:10.3390/ma10020205
57. Ahmed, I.; Jhung, S. H. *Chem. Eng. J.* **2017,** *310,* 197–215. doi:10.1016/j.cej.2016.10.115
58. Song, J. Y.; Jhung, S. H. *Chem. Eng. J.* **2017,** *322,* 366–374. doi:10.1016/j.cej.2017.04.036
59. Li, C.; Xiong, Z.; Zhang, J.; Wu, C. *J. Chem. Eng. Data* **2015,** *60,* 3414–3422. doi:10.1021/acs.jced.5b00692
60. Hasan, Z.; Jhung, S. H. *J. Hazard. Mater.* **2015,** *283,* 329–339. doi:10.1016/j.jhazmat.2014.09.046
61. Bhadra, B. N.; Lee, J. K.; Cho, C.-W.; Jhung, S. H. *Chem. Eng. J.* **2018,** *343,* 225–234. doi:10.1016/j.cej.2018.03.004
62. Ahmed, I.; Bhadra, B. N.; Lee, H. J.; Jhung, S. H. *Catal. Today* **2018,** *301,* 90–97. doi:10.1016/j.cattod.2017.02.011
63. Bhadra, B. N.; Ahmed, I.; Kim, S.; Jhung, S. H. *Chem. Eng. J.* **2017,** *314,* 50–58. doi:10.1016/j.cej.2016.12.127
64. Bhadra, B. N.; Song, J. Y.; Lee, S.-K.; Hwang, Y. K.; Jhung, S. H. *J. Hazard. Mater.* **2018,** *344,* 1069–1077. doi:10.1016/j.jhazmat.2017.11.057
65. Zhou, X.; Wei, J.; Liu, K.; Liu, N.; Zhou, B. *Langmuir* **2014,** *30,* 13861–13868. doi:10.1021/la502816m
66. An, H. J.; Bhadra, B. N.; Khan, N. A.; Jhung, S. H. *Chem. Eng. J.* **2018,** *343,* 447–454. doi:10.1016/j.cej.2018.03.025
67. Hsu, T.-C. *Fuel* **2008,** *87,* 3040–3045. doi:10.1016/j.fuel.2008.03.026
68. Shan, R.-r.; Yan, L.-g.; Yang, Y.-m.; Yang, K.; Yu, S.-j.; Yu, H.-q.; Zhu, B.-c.; Du, B. *J. Ind. Eng. Chem. (Amsterdam, Neth.)* **2015,** *21,* 561–568. doi:10.1016/j.jiec.2014.03.019
69. Dávila-Jiménez, M. M.; Elizalde-González, M. P.; Hernández-Montoya, V. *Bioresour. Technol.* **2009,** *100,* 6199–6206. doi:10.1016/j.biortech.2009.06.105
70. Lee, C.-K.; Liu, S.-S.; Juang, L.-C.; Wang, C.-C.; Lyu, M.-D.; Hung, S.-H. *J. Hazard. Mater.* **2007,** *148,* 756–760. doi:10.1016/j.jhazmat.2007.07.010
71. Akar, S. T.; San, E.; Akar, T. *Carbohydr. Polym.* **2016,** *143,* 318–326. doi:10.1016/j.carbpol.2016.01.066
72. Sarker, M.; Shin, S.; Jeong, J. H.; Jhung, S. H. *Chem. Eng. J.* **2019,** *371,* 252–259. doi:10.1016/j.cej.2019.04.039
73. Madrakian, T.; Afkhami, A.; Ahmadi, M.; Bagheri, H. *J. Hazard. Mater.* **2011,** *196,* 109–114. doi:10.1016/j.jhazmat.2011.08.078
74. Mittal, H.; Mishra, S. B. *Carbohydr. Polym.* **2014,** *101,* 1255–1264. doi:10.1016/j.carbpol.2013.09.045
75. Afkhami, A.; Sayari, S.; Moosavi, R.; Madrakian, T. *J. Ind. Eng. Chem. (Amsterdam, Neth.)* **2015,** *21,* 920–924. doi:10.1016/j.jiec.2014.04.033
76. Huang, C.-H.; Chang, K.-P.; Ou, H.-D.; Chiang, Y.-C.; Wang, C.-F. *Microporous Mesoporous Mater.* **2011,** *141,* 102–109. doi:10.1016/j.micromeso.2010.11.002
77. Madrakian, T.; Afkhami, A.; Haryani, R.; Ahmadi, M. *RSC Adv.* **2014,** *4,* 44841–44847. doi:10.1039/c4ra06421f
78. Song, J. Y.; Bhadra, B. N.; Jhung, S. H. *Microporous Mesoporous Mater.* **2017,** *243,* 221–228. doi:10.1016/j.micromeso.2017.02.024
79. Hasan, Z.; Jeon, J.; Jhung, S. H. *J. Hazard. Mater.* **2012,** *209–210,* 151–157. doi:10.1016/j.jhazmat.2012.01.005

License and Terms

This is an Open Access article under the terms of the Creative Commons Attribution License (http://creativecommons.org/licenses/by/4.0). Please note that the reuse, redistribution and reproduction in particular requires that the authors and source are credited.

The license is subject to the *Beilstein Journal of Nanotechnology* terms and conditions: (https://www.beilstein-journals.org/bjnano)

The definitive version of this article is the electronic one which can be found at:
doi:10.3762/bjnano.11.47

BEILSTEIN JOURNAL OF NANOTECHNOLOGY

Nanoporous and nonporous conjugated donor–acceptor polymer semiconductors for photocatalytic hydrogen production

Zhao-Qi Sheng[1], Yu-Qin Xing[1], Yan Chen[1], Guang Zhang[*2], Shi-Yong Liu[*1] and Long Chen[2]

Review

Open Access

Address:
[1]College of Materials, Metallurgical and Chemistry, Jiangxi University of Science and Technology, Ganzhou, 341000, China, and
[2]Department of Chemistry, Tianjin University, Tianjin 300072, China

Email:
Guang Zhang[*] - gzhdream@live.com;
Shi-Yong Liu[*] - chelsy@zju.edu.cn

* Corresponding author

Keywords:
π-conjugated polymeric photocatalysts; donor–acceptor junctions; nanostructure semiconductors; photocatalytic hydrogen production

Beilstein J. Nanotechnol. **2021,** *12,* 607–623.
https://doi.org/10.3762/bjnano.12.50

Received: 12 March 2021
Accepted: 13 June 2021
Published: 30 June 2021

This article is part of the thematic issue "New directions for nanoporous materials".

Associate Editor: C. T. Yavuz

© 2021 Sheng et al.; licensee Beilstein-Institut.
License and terms: see end of document.

Abstract

Conjugated polymers (CPs) as photocatalysts have evoked substantial interest. Their geometries and physical (e.g., chemical and thermal stability and solubility), optical (e.g., light absorption range), and electronic properties (e.g., charge carrier mobility, redox potential, and exciton binding energy) can be easily tuned via structural design. In addition, they are of light weight (i.e., mainly composed of C, N, O, and S). To improve the photocatalytic performance of CPs and better understand the catalytic mechanisms, many strategies with respect to material design have been proposed. These include tuning the bandgap, enlarging the surface area, enabling more efficient separation of electron–hole pairs, and enhancing the charge carrier mobility. In particular, donor–acceptor (D–A) polymers were demonstrated as a promising platform to develop high-performance photocatalysts due to their easily tunable bandgaps, high charge carrier mobility, and efficient intramolecular charge transfer. In this minireview, recent advances of D–A polymers in photocatalytic hydrogen evolution are summarized with a particular focus on modulating the optical and electronic properties of CPs by varying the acceptor units. The challenges and prospects associated with D–A polymer-based photocatalysts are described as well.

Introduction

To date, fossil fuels still are the predominant energy source around the world. This leads to severe environmental problems, such as the ever-worsening global warming due to the excessive emission of greenhouse gases and the pollution by poisonous gases and particles generated during the incomplete combustions of fossil fuels. In addition, fossil fuels are limited

and will be depleted. Regarding clean and sustainable energy resources, in particular solar energy has become a candidate to eventually replace fossil fuels. Among the various strategies, hydrogen production by photocatalytic water splitting is emerging as a promising approach and hot research topic. Hydrogen is regarded as a clean and recyclable energy source, which can be obtained from water and, in turn, generates water as the only product after consumption [1-3]. Inspired by natural photosynthetic systems that can convert solar energy into chemical fuels, Fujishima and Honda [4] reported the first example of hydrogen production by photocatalytic water splitting in 1972, using TiO_2 as the photocatalyst under ultraviolet-light irradiation. Since then, numerous semiconductors have been explored for photocatalytic hydrogen production (PHP) by water splitting, which are primarily inorganic materials, such as metal oxides and sulfides [5].

Inorganic photocatalysts, however, have some inherent drawbacks. Harsh synthetic conditions, such as high pressure and temperature, are required [5]. Moreover, many reported inorganic photocatalysts contain heavy metal elements, for example, La, Bi, and Ta, which are often rare, toxic, and expensive [6]. Also, expensive noble metal-based cocatalysts (e.g., Pt) are required to improve the photocatalytic performance. As such, an ideal photocatalyst for water splitting reaction should fit the following criteria: suitable bandgap energy, high stability, wide light-absorption range, and sufficient catalytically active sites [7].

Conjugated polymers (CPs) are one of the most promising alternatives to the traditional inorganic photocatalysts. Their geometries and physical (e.g., chemical and thermal stability and solubility), optical (e.g., light absorption range), and electronic properties (e.g., charge carrier mobility, redox potential and exciton binding energy) can be easily tuned via structural design. In addition, they are of light weight (i.e., mainly composed of C, N, O, and S) [8-10]. In 1985, the first CP-based photocatalyst (i.e., poly(*p*-phenylene)) for PHP was reported, but did not attract much attention due to the low hydrogen evolution rate (HER) [11]. In 2009, Wang et al. reported a novel metal-free polymeric photocatalyst (i.e., graphitic carbon nitride (g-C_3N_4)), which could efficiently reduce protons to generate hydrogen under visible-light irradiation, for the first time. After that, g-C_3N_4 triggered substantial research interest [12-14]. Various strategies have been developed to improve the PHP activity of g-C_3N_4, such as introducing heterojunctions [15-17], copolymerization [18-20], doping with other elements [21-23], and the control of end groups [24]. Meanwhile, various types of CPs have been applied for PHP, including conjugated porous polymers (CPPs) [25-27], linear conjugated polymers (LCPs) [28-30], conjugated triazine frameworks (CTFs) [31-33], and covalent organic frameworks (COFs) [34]. Notably, a record HER of up to 307 $mmol \cdot h^{-1} \cdot g^{-1}$ has been achieved with a pyrene–bithiophene-based porous polymer as the photocatalyst [35].

During PHP by water splitting, first, the photocatalyst is excited by photons, and photoexcited electrons hop into the lowest unoccupied molecular orbital (LUMO) or conduction band (CB), while holes remain in the highest occupied molecular orbital (HOMO) or valence band (VB). Second, the electron–hole pairs are transferred to the surface through thermodynamic driving forces and are captured by H^+ and a sacrificial electron donor (SED) in water, which eventually produces H_2 [36,37]. Accordingly, three important factors, that is, light-harvesting ability, mobility of the photogenerated charge carriers, and electron–hole separation efficiency, need to be considered simultaneously to design efficient photocatalysts.

Organic photocatalysts with narrow bandgap and high charge carrier mobility could, therefore, facilitate light harvesting and the reduction of protons [38]. In terms of structural design, D–A polymers are a good platform to narrow the bandgap, enhance the charge carrier mobility and promote electron–hole separation (Figure 1) by selectively tuning the donor and acceptor parts within the conjugated backbones [39,40]. The D–A architecture has been widely employed in high-performance organic optoelectronic devices, such as organic photovoltaics, organic field-effect transistors, nonlinear optics, and organic light-emitting diodes (OLEDs) [41]. However, it was only in recent years that researchers have started to use D–A design strategy to develop CP-based photocatalysts for PHP. As there is growing interests in this field, a timely review article about this area would be quite instructive and necessary [42].

This minireview article summarizes D–A-type conjugated polymers as photocatalysts for PHP, including LCPs, CPPs, CTFs, and COFs with a particular focus on modulating the electron-accepting segments, that is, triazine, pyridine, benzothiadiazole, dibenzothiophene-*S*,*S*-dioxide, and cyano moieties. By tailoring the functional groups and geometries of the polymer framework, the influence of different factors on the photocatalytic activity can be systematically investigated and, consequently, the structure–performance relationships are unveiled. Herein, the donor and acceptor fragments in the polymer structures are highlighted in red and blue, respectively.

Review

Donor–acceptor conjugated polymers

Triazine-based conjugated polymers

s-Triazine and tri-*s*-triazine (heptazine), as the building blocks of carbon nitride, represent two of the most widely studied

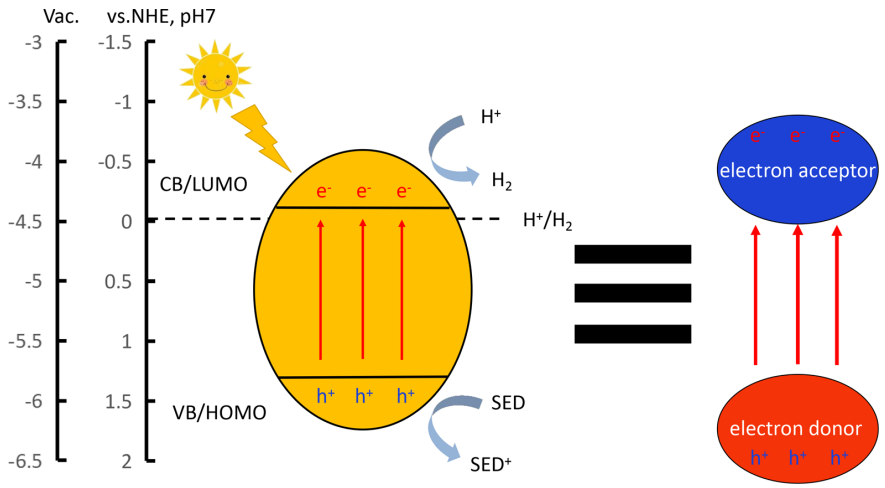


Figure 1: (Left) Schematic diagram of the mechanism of semiconducting catalyst-mediated photocatalytic hydrogen production (CB: conduction band, VB: valence band, SED: sacrificial electron donors). (Right) Charge separation in a CP-based semiconductor via photoinduced D→A charge transfer.

acceptor units [43,44]. In contrast to the conventional trimerization of nitrile under harsh conditions [43], Tan et al. developed a new condensation reaction of aldehydes with amidines to construct covalent triazene frameworks (CTFs) under mild conditions [45]. They investigated the effects of donor units with different heteroatoms on the photocatalytic performance of CTFs. The carbazole–triazine-containing CTF **P1** (Figure 2) triggered a strong intramolecular charge transfer (ICT) and achieved a high HER of 538 μmol·h^{-1} (50 mg).

Bojdys and co-workers reported a series of CTFs with diverse functional moieties (e.g., heterocycles containing S and/or N) at the edges of the frameworks to delicately tune the bandgaps of conjugated polymers. Among them, three polymers, that is, **P2**, **P3**, and **P4** (Figure 2), showed suitable bandgaps of ca. 2.2 eV, and conferred HERs of 4.72, 9.15, and 2.90 μmol·h^{-1} (10 mg), respectively, under visible-light irradiation [46,47]. The bandgaps of the CTFs can be easily tuned to optimize the photocatalytic activity by introducing different functional groups. Besides using a single kind of electron acceptor, researchers also attempted to incorporate multiple electron acceptors to construct CPs for PHP. For instance, Thomas et al. [48] prepared several porous polymers with benzothiadiazole and heptazine moieties as the acceptors and an aminobenzene segment as the donor. By adjusting the molar ratio between the monomers, secondary (**P5**, benzothiadiazole/heptazine = 2:3) or tertiary amine-linked polymers (**P6**, benzothiadiazole/heptazine = 4:3) (Figure 2) were obtained. **P5** exhibited a smaller bandgap of 1.99 eV. Moreover, the photoluminescence spectra indicated an improved separation efficiency of photogenerated charges of **P5**. A stable H_2 evolution rate of 32 μmol·h^{-1} (20 mg) was achieved for HMP-3_2:3, which was several times higher than those of the triazine-amine-based **P7** (Figure 2) and bulk g-C_3N_4. Hence, incorporation of more than one kind of electron acceptors in the polymer structure could enhance the photocatalytic efficiency.

In addition, Tan et al. [49] developed several D–A CPs with carbazole (D), benzothiadiazole (A1) and triazine (A2) fragments. The photocatalytic activities of CPs with different D/A1 ratios were systematically investigated and compared. For example, **P8** (D/A1 = 3:7) (Figure 2) yielded the highest HER (966 μmol·h^{-1}, 50 mg), which was consistent with the highest photocurrent response, smallest bandgap, and suppressed recombination of charge carriers in **P8**. The electron density distributions of three kinds of triazine-based fragments containing carbazole (**M1**), or both carbazole and benzothiadiazole (**M2**), and benzothiadiazole (**M3**) (Figure 3) were further calculated to support these results. **M1** and **M2** showed better charge separation than **M3**. In particular, **M2** exhibited superior charge separation when considering spatial effects among the three fragments. Consequently, increasing the fraction of **M2** in the polymers could be beneficial to the photocatalytic efficiency.

He et al. developed two pyrazole-triazine-based CTFs, that is, **P9** (A–D–A) and **P10** (D–A) (Figure 2) by a metal-free catalyzed approach [50]. Compared with **P10**, introducing a benzothiadiazole unit into **P9** effectively reduced the optical bandgap from 2.94 eV to the ideal value of 2.33 eV. They further probed the influence of substituting the S atom in the benzothiadiazole group with O or Se atoms on the optoelectronic and photocatalytic properties of the CTFs **P11** and **P12** (Figure 2) [51]. Introducing an O atom boosted the ICT and electron–hole separation due to the higher electron negativity; but it lowered the LUMO level, which as a result, suppressed the PHP reaction. Incorporating a Se atom led to a redshifted

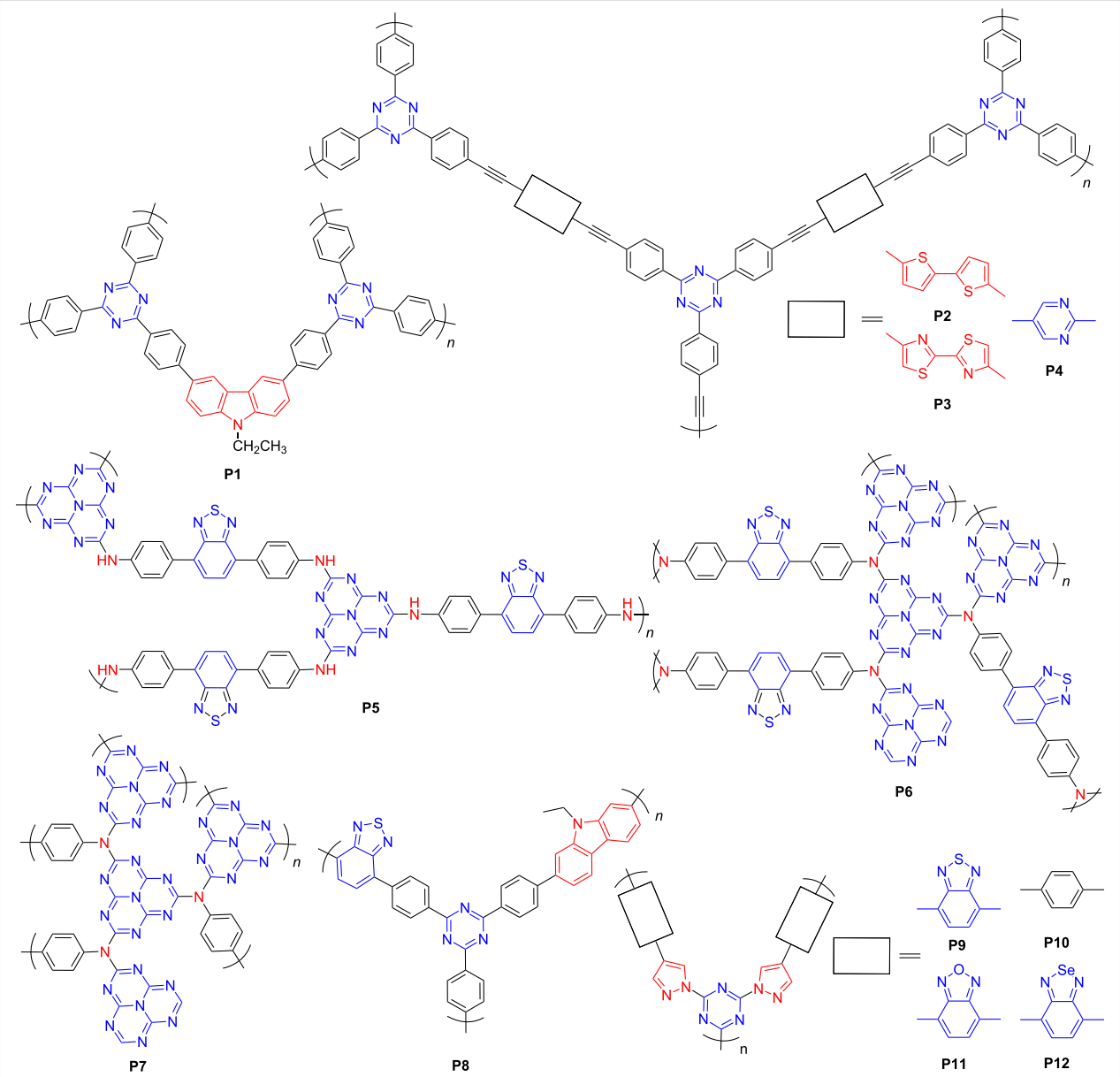


Figure 2: Structures of triazine-based conjugated polymers.

light absorption, but decreased the charge carrier mobility due to the reduced aromaticity of the architecture. Consequently, the HERs declined in both cases. These results reveal that slight structural changes could significantly modulate the properties and photocatalytic activities of CTFs.

Pyridine-based conjugated polymers

Pyridine, as a nitrogen-containing benzene analogue, was incorporated into linear conjugated polymers as early as in the 1990s. The CPs exhibited distinctive photocatalytic activity for H_2 production under visible light [52]. With the extensive studies of nitrogen-rich triazine- and heptazine-based photocatalysts for hydrogen production, pyridine and its derivatives as nitrogen-containing acceptors have attracted great interest again, and D–A architectures for photocatalytic water splitting were synthesized.

In 2015, Lotsch et al. [53] reported four COFs with benzene, pyridine, pyrimidine, and triazine as the core to disclose the effects of nitrogen atoms on the photocatalytic activities of these COFs. It showed a linear correlation between HER and the content of nitrogen atoms in the COF skeleton. However, HER is affected by the interplay of several factors, including surface area, light absorption range, crystallinity, charge transfer, and separation. Two azine-linked COFs with three pyridine segments neighboring the central benzene or triazine

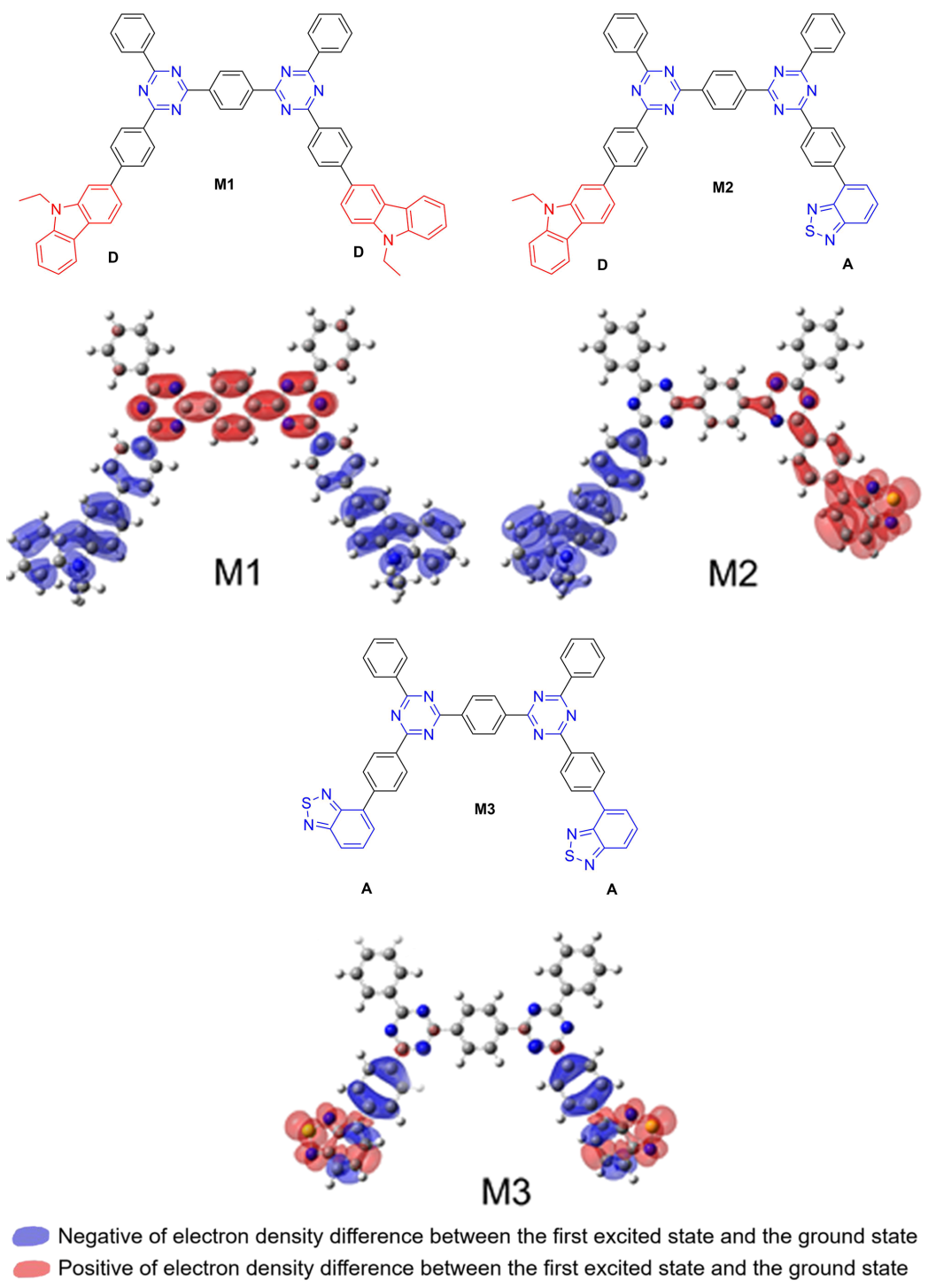


Figure 3: Proposed model fragments and electron density differences of **M1**–**M3** in **P8**. Adapted with permission from [49]. Copyright (2019) American Chemical Society. This content is not subject to CC BY 4.0.

fragment were prepared to make comparisons, that is, the 1,3,5-tri(pyridin-2-yl)benzene based COF **P13** and the benzene-triazine-based **P14** (Figure 4). Both of them showed a similar AA eclipsed stacking in the crystal structures, but the lower symmetry of **P13** resulted in worse crystallinity. Particularly, the D–A interactions between the pyridine and the benzene rings gave rise to disorder and reduced crystallinity even further. As a result, the HER of **P13** (0.42 μmol·h^{-1}, 5 mg) was one order of magnitude lower than that of **P14** (8.52 μmol·h^{-1}, 5 mg) [53].

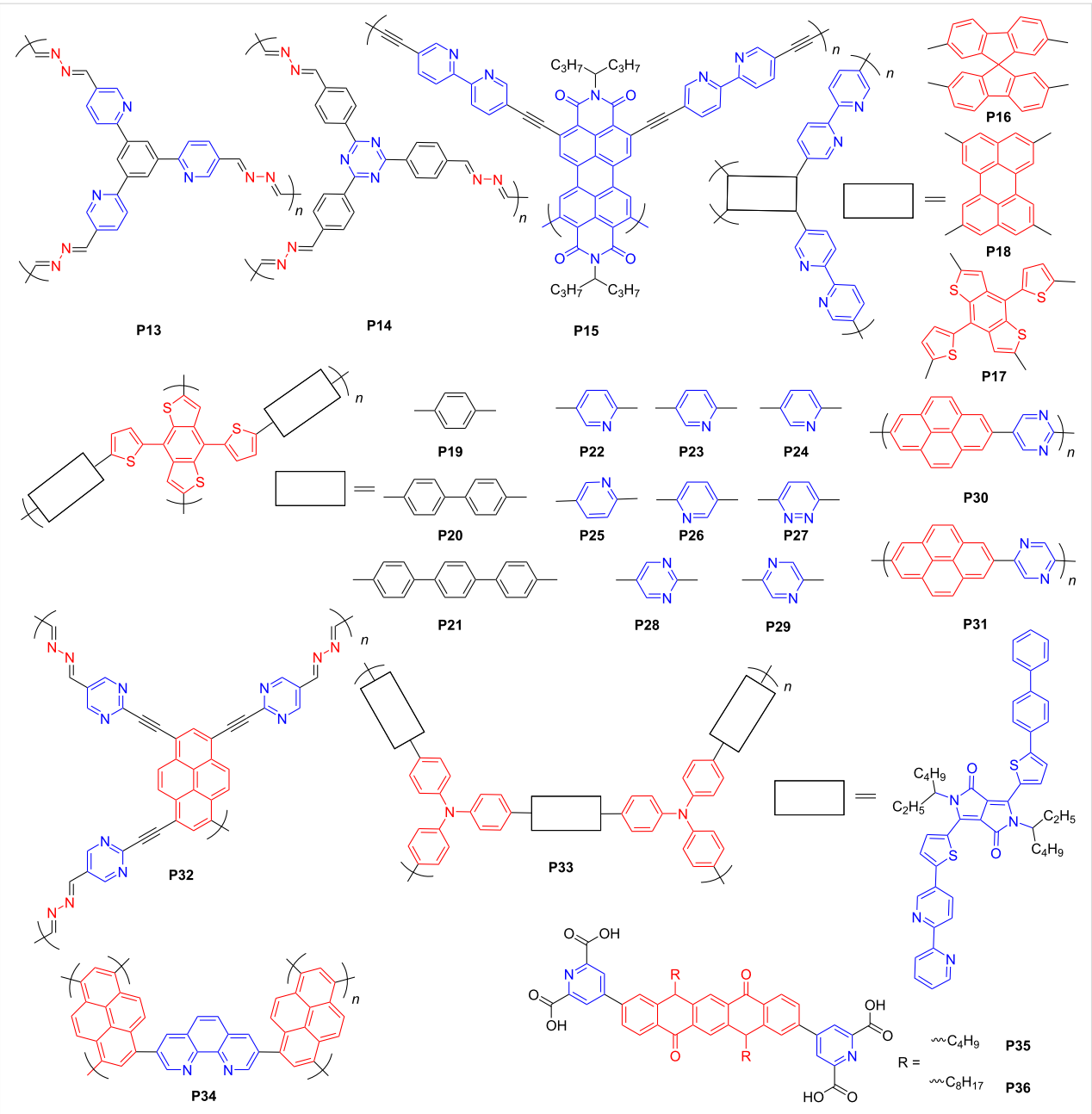


Figure 4: Schematic representation of structures of pyridine-contained conjugated polymers.

Cai et al. [54] reported a series of perylene diimide (PDI)-based n-type porous CPs (Figure 4). The HERs of the polymers with phenyl or biphenyl moieties as donors were lower than that of the pure acceptor polymer **P15** (7.2 μmol·h^{-1}, 3.5 mg). Although the benzene group could serve as a weak donor in some cases, it is difficult to render effective D–A interactions. For instance, Yu and co-workers [55] combined electron-deficient PDI or electron-rich chromophores (including spirofluorene, perylene, and 4,8-di(thiophen-2-yl)benzo[1,2-*b*:4,5-*b*']dithiophene (DTBDT) with bipyridine moieties to form several porous polymers (**P15**–**P18**) (Figure 4) to investigate the relationship between D–A interactions and photocatalytic properties. PDI-containing polymers, such as **P15,** normally confer smaller HERs than the others. **P18**, composed of strong electron-donating and bipyridine segments, rendered the best HER, which was attributed to its enhanced light absorption, better wettability, and more efficient charge separation. Based on DTBDT monomer, many porous polymers (**P19**–**P29**) (Figure 4) were further prepared to study the effects of different acceptors on the photocatalytic performance during water splitting [56]. PCPs incorporating nitrogen-containing heterocycles showed a better photocatalyt-

ic performance than those with oligophenylene moieties, which is due to the favorable internal polarization and coordinating sites rendered by nitrogen-containing heterocycles. Among them, the DTBDT–pyrazine-based **P29** achieved the best HER of 106.9 μmol·h^{-1} (12 mg) due to the suitable N substitution.

Pyrene as a well-known chromophore has been widely used in OLEDs and fluorescent probes due to its high photoluminescent quantum yield. Jiang et al. [57] introduced various sorts of nitrogen-containing fragments in pyrene-based polymers to investigate their photocatalytic performance, for example, **P30** and **P31** (Figure 4). Interestingly, different from the above examples, the pyrimidine-containing **P30** (18.7 μmol·h^{-1}, 50 mg) exhibited a much higher HER than **P31** with pyrazine moieties (8.6 μmol·h^{-1}, 50 mg). Lotsch et al. [58] also developed several pyrene-based COFs with peripheral nitrogen-containing or nitrogen-free aromatic units, among which the pyrene–pyrimidine-based **P32** (Figure 4) with the lowest nitrogen content showed the highest HER. Nitrogen heterocycles within polymers could optimize wettability, bandgap, charge transport, and separation.

Motivated by the planar configuration and strong electron-acceptor capability of diketopyrrolopyrrole (DPP) [59-61], Li and co-workers [62] combined DPP with triphenylamine and bipyridine groups to synthesize D–A polymers. A HER of 9.73 μmol·h^{-1} (3.5 mg) was achieved for **P33** (Figure 4) due to the wide spectral range of the photoresponse. The apparent quantum yield (AQY), as a vital experimental parameter for photocatalytic performance, exceeded 9% at 420 nm, which is, to date, the highest among all reported conjugated polymer-based photocatalysts. In addition, phenanthroline–pyrene-based D–A polymers were studied [63], with polymer **P34** (phenanthroline/pyrene = 1/3) (Figure 4) exhibiting the highest HER of 42 μmol·h^{-1} (10 mg). Additionally, Hua et al. [64] constructed two D–A supramolecular architectures with different alkane chains, that is, **P35** and **P36** with n-butyl and n-octyl chains, respectively (Figure 4), by self-assembling quinacridone and pyridine-2,6-dicarboxylic acid. It was revealed that the longer alkyl chain was harmful to the D–A interactions in CPs. Thus, nitrogen-containing aromatic segments can effectively mediate the internal polarization of the polymeric framework and thus enhance the PHP performance.

Benzothiadiazole-based conjugated polymers

The benzothiadiazole (BT) moiety as a strong electron acceptor features high planarity and good wettability due to incorporating N and S atoms. In 2016, Wang and co-workers [65] investigated the properties of a linear conjugated polymer and a 3D counterpart by varying the substitution position on the benzene ring. Interestingly, the linear polymer exhibited more effective D–A interactions than the 3D counterpart due to the enhanced conjugation of the former with a planar architecture.

Two ethynyl-linked benzene–benzothiadiazole-based porous polymers, that is, **P39** and **P40** (Figure 5) were synthesized to investigate the influence of fluorine substitution at BT on the charge carrier mobility and catalytic activity [66]. The mechanism of proton-coupled electron transfer (PCET) (Figure 6) was offered. It suggests for both linear and 3D polymers that single meta-F substitution renders a higher photocatalytic activity than double F substitution, and the polymer with the methoxy group at the meta site and the F atom at the para site yields the highest HER due to the excellent mobility of photogenerated charge carriers and the broad light absorption range. DFT calculations also verified that incorporating F on the para carbon atom of the BT unit strengthens the intermolecular interactions and thus enhances the charge transfer effect among the polymer chains. This is due to the interaction between two p orbitals from the meta carbon atom on one molecule and a N atom on the other. In addition, a methoxy group at the meta position intensified the intermolecular interaction, which, however, was weakened by F substitution at the meta position. Consequently, the linear **P39** (Figure 5) with both methoxy group and F on BT afforded the highest HER of 399 μmol·h^{-1} (30 mg). This suggests that selectively functionalizing the BT unit with F could greatly enhance the charge transfer in BT-based polymers.

Besides fluorine substitution, several halogenated BT-based imine-linked COFs were reported by Chen et al. [67] to investigate the effects of halogen atoms on the photocatalytic performance. The Cl-substituted COF with pyrene and BT exhibited the best HER (177.50 μmol·h^{-1}, 20 mg) due to low charge recombination and strong photoinduced charge transfer. Furthermore, DFT calculations (Figure 7) indicated that incorporating halogen atoms in both **P43** and **P44** (Figure 5) reduces the energy barrier for forming H* intermediates on polymer surface. Consequently, halogen substitution on the polymer is an approach to evoke enhanced charge separation and improve the HER of CPs.

In 2018, Jiang et al. [68] systematically studied the effects of π-linking groups, that is, benzene or biphenyl moieties in pyrene–benzothiadiazole-based polymers, for example, **P45** (Figure 5). The D–π–A-type compound **P45** possesses an extended π-conjugation along the backbone and consequently has an enlarged visible-light absorption and enhanced electronic conductivity compared with π-linker-free pyrene–benzothiadiazole-based polymers. After deposition of Pt as the cocatalyst, **P45** exhibited the most prominent photocatalytic activity for H_2 evolution (29.6 μmol·h^{-1}, 100 mg) under visible light. These

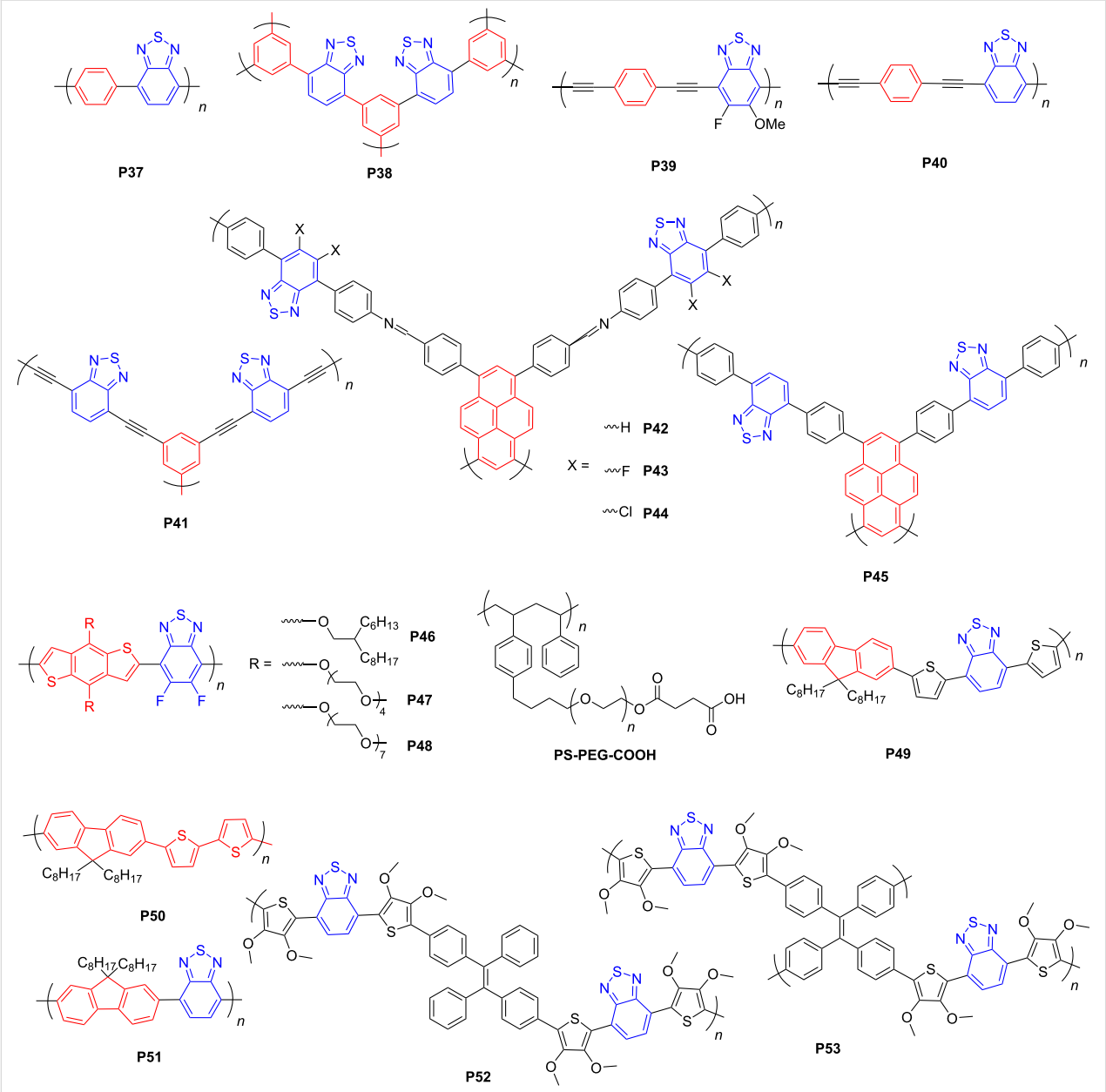


Figure 5: Schematic representation of structures of benzothiadiazole-based conjugated polymers.

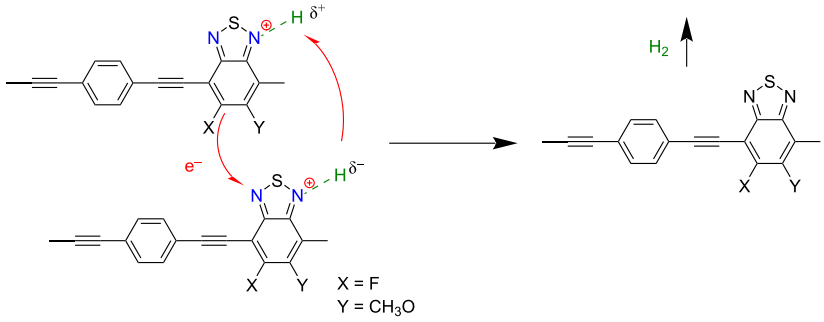


Figure 6: The mechanism of PCET-enhanced H_2 formation; see [66].

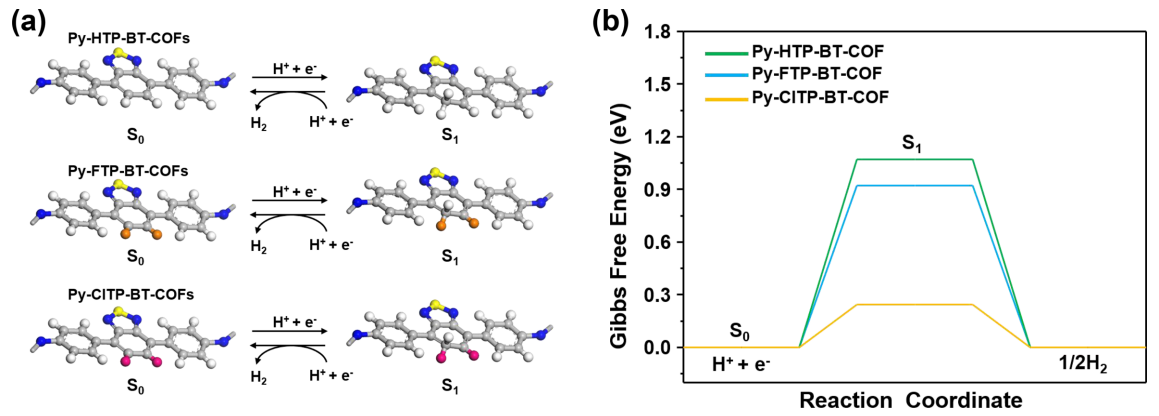


Figure 7: (a) Proposed reaction pathway for H_2 evolution (single-site reaction) on the halogen-substituted carbon atom of **P42**–**P44** (grey: C; white: H; yellow: S; blue: N; orange: F; pink: Cl). (b) Free-energy diagrams for H_2 evolution via a single-site reaction pathway at 0 V vs RHE on the halogen-substituted carbon atom of COFs. Reproduced from [67]. Copyright © 2020 Wiley-VCH GmbH. Used with permission from Chen et al., Modulating Benzothiadiazole-Based Covalent Organic Frameworks via Halogenation for Enhanced Photocatalytic Water Splitting, Angew. Chem. Int. Ed., John Wiley and Sons. This content is not subject to CC BY 4.0.

results suggest that the D–π–A architecture might be better than the conventional D–A counterpart for designing high-performance polymer-based photocatalysts for H_2 evolution.

Although the BT group can increase the wettability of polymers [50], most BT-based polymers are difficult to disperse in water. To overcome the issue of poor dispersibility of BT-based polymers, Huang et al. [69] synthesized two BT-based linear CPs with oxygen-containing branched side chains. Different from long alkyl chains, the polymers incorporating the oligo(ethylene glycol) side chains (**P48**) (Figure 5) showed considerably improved charge separation and transport and could be dispersed in water without any co-solvent. Similar to the N atoms in BT units, oxygen atoms can also adsorb H^+ in water to form the polymer/water interface.

Tian et al. [70] prepared several BT-based polymer dots (Pdots) with functionalized polystyrene (PS-PEG-COOH) (Figure 5) to improve the wettability of polymers. In contrast to the pristine BT-based polymers (**P49**–**P51**) (Figure 5), the Pdots were dispersed in water. The Pdots of **P49** rendered one of the highest HER (150 μmol·h^{-1}, 3 mg) among all Pdots, which was attributed to the water solubility, broad light absorption and abundant catalytic sites of BT-based Pdots. In addition, Hu et al. [71] synthesized hyper-branched Pdots by co-assembling pristine polymers (**P52** and **P53**) and hydrophilic PEG_{45}-*b*-$PMMA_{103}$ (Figure 5). The hyperbranched Pdots yielded higher HERs (as high as 16.8 μmol·h^{-1} (20 mg) for **P53**) than the linear Pdot **P52**, due to the shortened charge transport pathway, 3D transport, and more negative reduction potentials of the hyperbranched Pdots. Araujo et al. [72] studied several BT-containing small molecules with A–D–A architectures through theoretical calculations. They found that small molecules could also mediate photocatalytic water splitting into hydrogen and oxygen.

Dibenzothiophene-*S*,*S*-dioxide-based conjugated polymers

Recently, dibenzothiophene-*S*,*S*-dioxide (FSO) has been extensively applied to construct D–A CPs due to its planar architecture, matched energy levels, and strong electron withdrawal property. The sulfonyl groups could not only increase the wettability through the O···H hydrogen bonding, but also function as the sites for photocatalytic proton reduction in water [73]. Cooper and co-workers [74] first reported FSO-based CPs as catalysts for PHP in 2016. The linear FSO–phenyl-based polymer **P54** (Figure 8) yielded a moderate HER of 92 μmol·h^{-1} (25 mg) under visible light.

Subsequently, Wang et al. [75] combined FSO with biphenyl, dibenzothiophene, or fluorene segments to construct D–A CPs (**P55**–**P57**). Experimental studies showed that the dibenzothiophene-containig polymer **P56** (Figure 8) exhibited an outstanding AQY of 6.8% at 420 nm. Both dibenzothiophene and fluorene moieties possess planar structures compared with biphenyl group, yet dibenzothiophene has a more extended conjugation than fluorene due to the existence of a saturated 9-C atom in fluorene. Therefore, **P56** with the most extended conjugation facilitated more efficient charge transfer and separation. High planarity and extended conjugation of a polymer skeleton are crucial to realize efficient photocatalytic water splitting. Liu et al. [76] integrated FSO with fluorene or 9,9-diphenylfluorene segments to prepare two D–A polymers (**P57** and **P58**) (Figure 8). The photocatalytic activities of these D–A polymers increased with enhancing the planarity of the polymer backbones, due to improved charge transfer and increased light

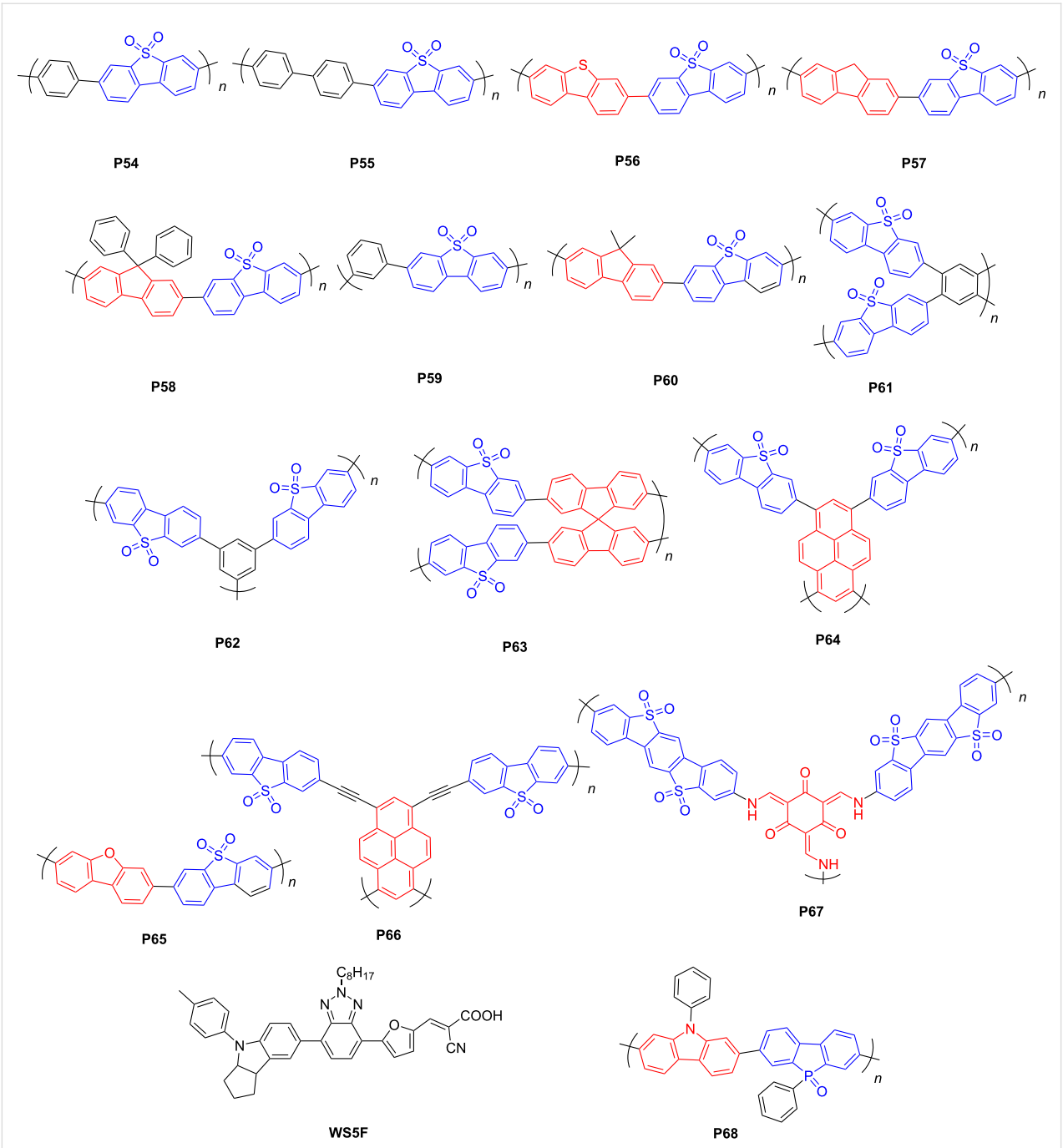


Figure 8: Schematic representation of structures of dibenzothiophene-*S*,*S*-dioxide-based CPs.

absorption in more planar conjugated systems. Therefore, the fluorene-containing polymer **P57** (Figure 8) exhibited the best performance among the three D–A polymers with a HER of 50.4 μmol·h^{-1} (10 mg).

Comparing the photocatalytic performance of linear CPs and their 3D counterparts, many research articles claimed that linear CPs render higher HERs than porous CPs due to the superior charge carrier mobility of linear polymers [65,66,71]. However, Cooper et al. [77] reasoned that porous polymers might be better than linear counterparts to promote photocatalytic hydrogen evolution as long as the charge carrier transport was not compromised by the 3D structures. This claim was exemplified by the 9,9'-spirobifluorene–FSO-based porous polymer **P63** (Figure 8), which exhibited the best catalytic performance under visible light among the linear and porous polymers in that work,

with a HER of 77.65 μmol·h^{-1} (25 mg). Jiang et al. [78] reported two pyrene–FSO-based porous CPs with different linking positions with respect to dibenzothiophene-*S*,*S*-dioxide, for example, the 3,7-position-linked polymer **P64** (Figure 8). **P64** afforded a higher HER of 284.85 μmol·h^{-1} (50 mg) under visible light without cocatalyst than the 2,8-position-linked compound due to the more extended conjugation and enhanced coplanarity of **P64**. As outlined above, judiciously selecting donor and acceptor components and designing 3D polymers could give rise to impressive performances during PHP.

Recently, Cooper and co-workers studied the effects of replacing the C9 of the fluorene moiety in polymer **P57** with heteratoms [79]. The oxygen-containing dibenzo[*b*,*d*]furan–FSO-based polymer **P65** (Figure 8) showed a higher HER (147.1 mol·h^{-1}, 25 mg) than **P57** under visible light. This was attributed to the improved wettability of **P65** induced by the additional electronegative O atom and to the decreased ionization potential of trimethylamine (TEA) accelerating its oxidation through the higher driving force of **P65** for overall TEA oxidation [79]. In addition, Wang et al. [80] prepared a porous polymer with pyrene core and F atom-functionalized FSO segments (Figure 8). Different from the BT-based polymers mentioned above, incorporating F atoms at the FSO moiety resulted in a decreased HER. The authors reasoned that **P64** with the sulfonyl group could efficiently concentrate as well as output electrons and build excellent electron-output "tentacles" and therefore increase the HER. Chen et al. [81] reported an ethynyl-bridged FSO–pyrene-based polymer (**P66**) (Figure 8) to further extend the conjugation. The water contact angle measurements showed that the wettability was enhanced with increasing the content of FSO units. **P66** achieved an AQY of 8.5%.

Cooper et al. [82] systematically investigated the influence of plasma treatments on conjugated polymers as photocatalysts, for example, the fluorine–FSO-based **P60** (Figure 8). For **P60**, a short time of plasma treatment significantly enhanced the wettability and photocatalytic performance due to the plasma oxidizing the polymer. In addition, they [83] prepared a crystalline benzo[1,2-*b*:4,5-*b*']bis[1]benzothiophene sulfone-containing covalent organic framework (**P67**) (Figure 8), which exhibited a higher HER than its amorphous or semicrystalline counterparts. Dye sensitization further enhanced the photocatalytic activity of **P67**. Remarkably, incorporating a near-infrared absorbing dye (**WS5F**) into **P67** (252.5 μmol·h^{-1}, 25 mg) further improved the HER to 497.5 mmol·h^{-1} (25 mg), which was attributed to the enhanced light absorption and photoinduced **WS5F**-to-**P67** charge transfer. Similar to the works on the FSO moiety, Chou et al. explored the phenylbenzo[*b*]phosphindole 5-oxide-containing polymer **P68** (Figure 8), which exhibited the highest AQY of 14.92% at 420 nm due to its suitable light absorption range [84].

Cyano-containing conjugated polymers

As summarized above, the D–A architecture is a fundamental design principle toward high-performance polymer-based photocatalysts, and selecting proper donor and acceptor components significantly influences the eventual photocatalytic activity. Apart from the aforementioned acceptors, the cyano moiety as a strong electron-withdrawing group, has been widely used to design organic semiconductors for diverse applications, such as organic solar cells [85], organic light-emitting diodes [86], and organic field-effect transistors [87]. Researchers have also incorporated cyano moieties into the design of D–A polymers for PHP applications. For instance, Zhuang et al. [88] developed several cyano-substituted porous polymers, which, however, only led to moderate HERs, such as **P71** (Figure 9) with a HER of 45.4 μmol·h^{-1} under visible light. Subsequently, Wang et al. reported two olefin-linked, cyano-substituted, benzene–1,3,6,8-tetrephenylpyrene-based 2D polymers (**P73** and **P74**). **P74** rendered a higher HER of 106 μmol·h^{-1} (50 mg) than **P73** (68 μmol·h^{-1}, 50 mg) due to the strongly electron-withdrawing 3-ethylrhodanine fragments in the periphery [89].

CP-based heterojunctions for PHP applications

Besides D–A polymers, heterojunctions between CPs and other semiconductors have also been developed to facilitate the intermolecular charge transfer and transport. The interactions between the CPs and various semiconductors in the heterojunctions could involve strong covalent bonds, ionic bonds, or hydrogen bonds [90,91]. Researchers have also attempted to use heterojunctions as photocatalysts for PHP. For example, Wang et al. combined a pyrene-based polymer (**P75**) (Figure 10) with g-C_3N_4 to form a heterojunction [92]. The interface between **P75** and g-C_3N_4 restrained charge recombination and promoted proton reduction. Peng et al. also prepared a photocatalyst with a surficial heterojunction composed of **P76** (Figure 10) and g-C_3N_4 by facile rotary evaporation [93]. Using ascorbic acid as the sacrificial agent, the AQY of the heterojunction increased to 59.4% at 500 nm. It suggests that polymer/polymer heterojunctions could effectively improve the intermolecular charge transfer and suppress charge recombination. In addition, Tian et al. developed a series of polymer/polymer heterojunctions with CPs and g-C_3N_4 [94]. In particular, the heterojunction between benzotriazole–fluorene-based **P77** (Figure 10) and g-C_3N_4 endowed a high AQT of 33.5% at 450 nm.

Inspire by the architectures of organic solar cells, Cooper et al. selected a ITIC-based polymer as acceptor and a BT–carbazole-based one as donor to form polymer/polymer heterojunctions

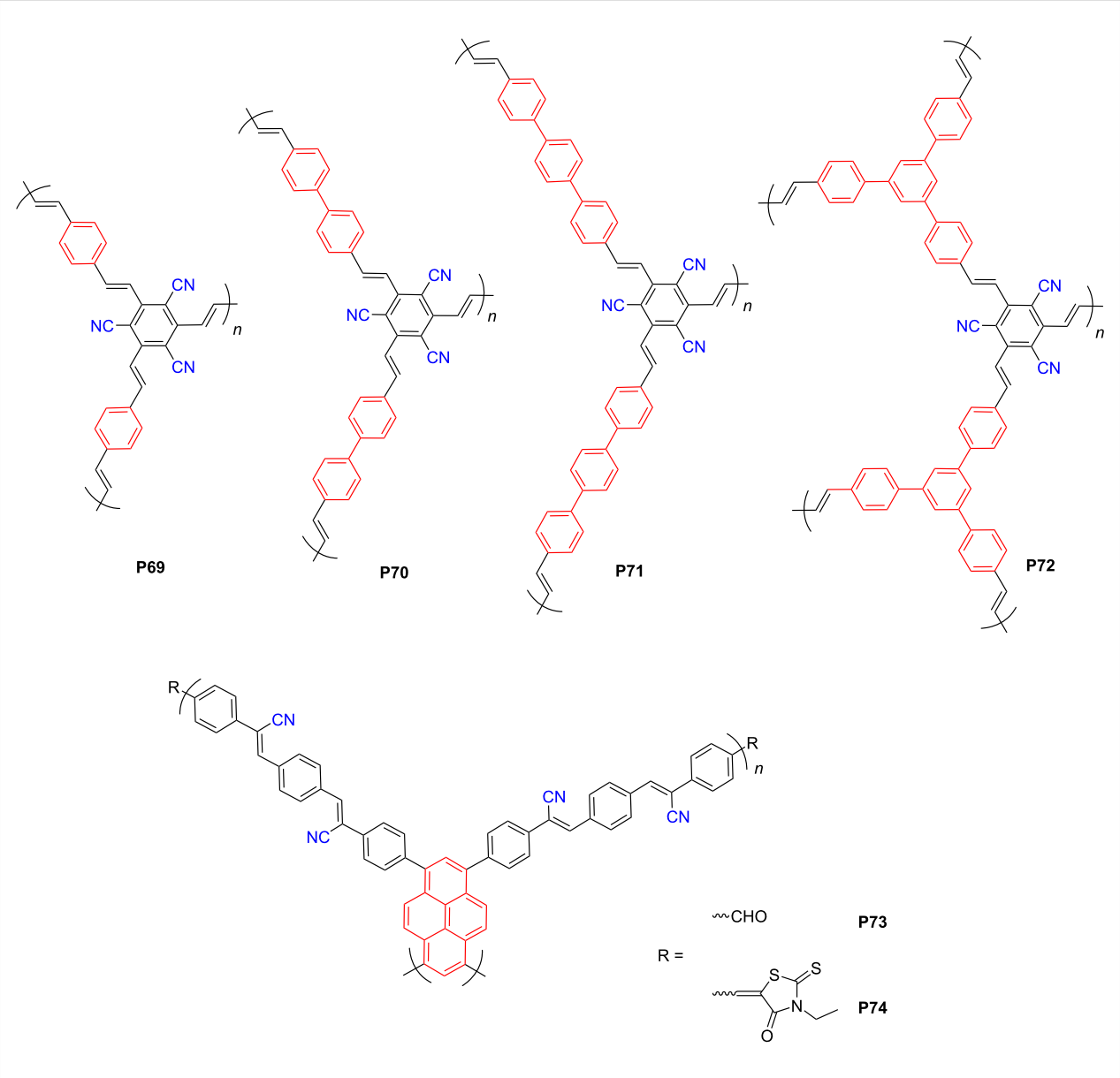


Figure 9: Schematic representation of structures of cyano-based CPs.

[95]. Due to the formation of abundant donor–acceptor interfaces, **P78**/**P79** (Figure 10) exhibited the highest HER of 191.82 μmol·h^{-1} (1.15 mg) [95]. Recently, McCulloch and co-workers discovered another D/A heterojunction (**P80**/**P81**) (Figure 10) as photocatalyst for hydrogen evolution. By stabilizing the surfactant employed during synthesis of the heterojunction, ITIC-containing **P80** as the acceptor could intimately blend with the donor **P81**, which rendered HERs up to 128.85 μmol·h^{-1} (2 mg) [96].

Regarding heterojunctions with TiO_2, for instance, Hua et al. used two indeno[1,2-*b*]thiophene-based organic dyes (**P82** and **P83**) (Figure 10) to sensitize TiO_2 to harvest near-infrared light [97]. Consequently, the average HERs of **P82**/TiO_2 and **P83**/TiO_2 with Pt as cocatalyst dramatically increased to 11.3 and 3.9 times, respectively, as high as that of using TiO_2 only. Chen et al. attempted to incorporate several CPs, that is, **P37**, **P40,** and **P84** (Figure 5 and Figure 10), with TiO_2 and formed binary composites [98-100]. Compared with pristine CPs as photocatalysts, the photocatalytic activities of the heterojunctions increased by around 18, 7, and 2 times, respectively. Subsequently, the same research group developed a **P40** flake/CdS heterojunction with broad visible light absorption (400–700 nm) and high photogenerated charge separation rate [101]. This heterojunction realized an AQY of up to 7.5% at 420 nm. By in situ solvothermal growth of CdS nanoparticles

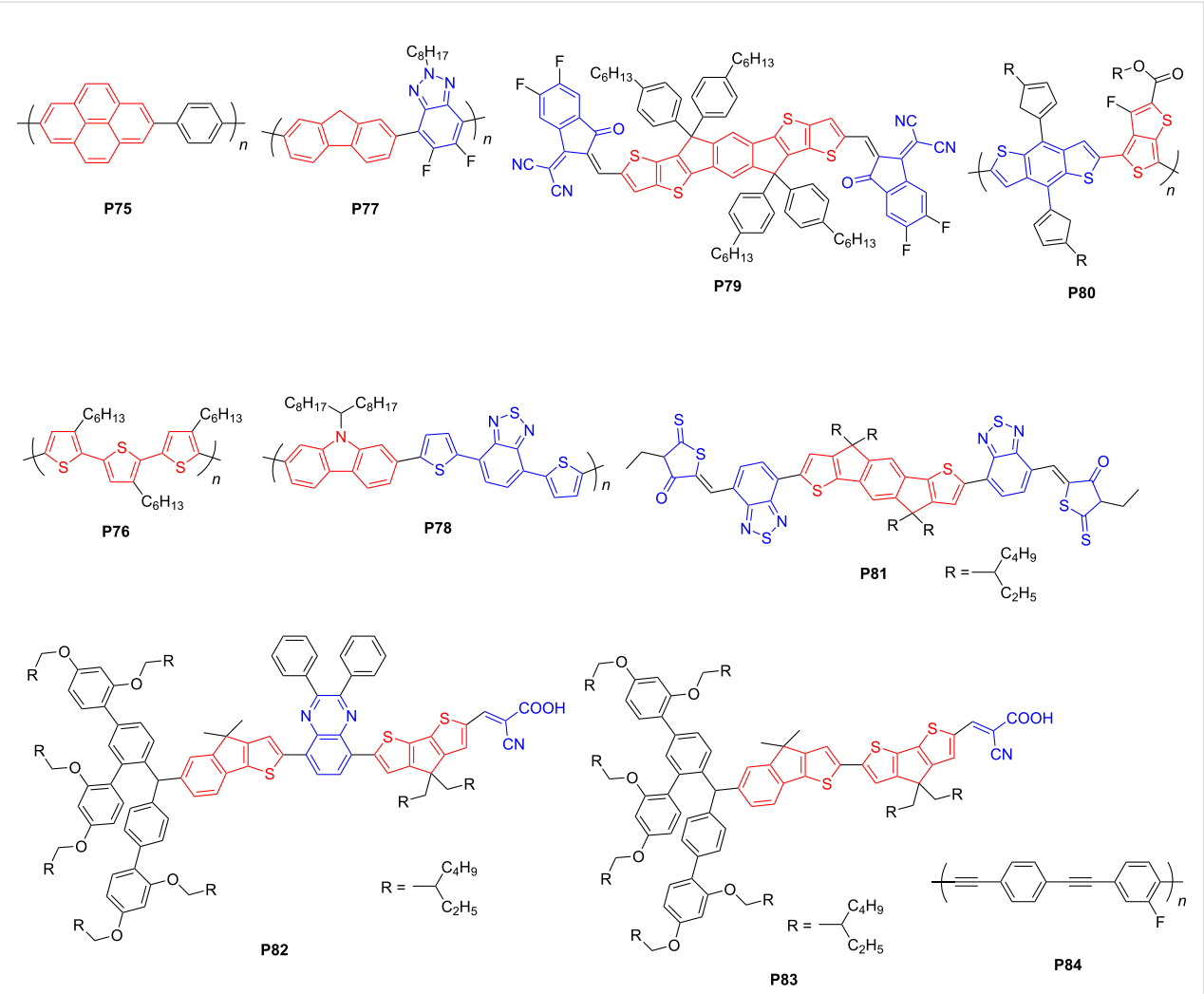


Figure 10: Schematic representation of structures of CPs for heterojunctions.

on ultrathin polyimide (PI) nanosheets, Zou et al. [102] achieved a HER of 30.65 μmol h^{-1} (50 mg) with 15% CdS/PI as the photocatalyst, which was nearly 5 and 60 times as high as the performance of pristine CdS and 1% Pt/PI, respectively. This suggests that organic/inorganic heterojunctions show higher photocatalytic performance than the single components of CPs.

Table 1 summarizes the main optoelectronic properties and HERs of the CP-based photocatalysts introduced in this review article.

Conclusion

Donor–acceptor interactions facilitate the ICT effect and decrease the optical bandgaps of D–A polymers. Correspondingly, they improve both charge carrier mobility and light harvesting, which makes D–A polymers potential photocatalysts for hydrogen production from water. In this minireview article, we systematically summarized the recent developments of the emerging diverse D–A polymers as photocatalysts for hydrogen evolution by water splitting. Several key messages could be concluded: (1) Architectures with multiple kind of acceptors, for example, D–A–A can improve the HER compared with simple D–A structures. (2) Incorporating heteroatoms, such as N, S, and O, into the polymer backbone can effectively modulate the physicochemical properties of the polymers. (3) Attaching side chains or functional groups, such as FSO and cyano groups, not only improve the solubility of CPs in water, but also tune the photoelectric properties of the polymers. Although the properties of CPs can be easily mediated by choosing different D and A building blocks, a good counterbalance between narrow bandgap and enough thermodynamic driving force for proton reduction is still hard to achieve for a single CP component.

Table 1: Summary of the bandgaps, cocatalysts, and properties related to H_2 evolution of quintessential CP photocatalysts.

CPs	Bandgap (eV)	LUMO/HOMO (eV)	Cocatalyst	SED	HER (μmol·h^{-1})	HER (μmol·g^{-1}·h^{-1})	AQY (%)	Ref.
P1	2.17	−0.86/1.31	Pt	TEOA	538[a]	10760[a]	4.07	[45]
P3	2.21	—	Pt	TEOA	ca. 2.90[b]	ca. 290[b]	—	[46]
P4	2.16	—	Pt	TEOA	9.15[b]	915±10[b]	—	[47]
P5	1.99	—	Pt	TEOA	32[b]	1600[b]	—	[48]
P8	2.11	−0.76/1.35	Pt	TEOA	966[a]	19320[a]	22.8	[49]
P9	2.33	−0.42/1.91	Pt	TEOA	50[a]	1000[a]	3.6	[50]
P11	2.37	−0.44/1.93	Pt	TEOA	22[a]	440[a]	1.43	[51]
P13	2.1	—	Pt	TEOA	0.42[c]	83.83[c]	4.15	[53]
P15	2.4	−0.90/1.5	—	TEA	7.2[c]	2057[c]	—	[54]
P18	2.45	—	Pt	TEA	6.5[a]	1857[a]	0.34	[55]
P29	ca. 1.9	ca. −1.88/0.7	—	TEA	106.9[c]	8908.3[c]	—	[56]
P30	2.53	−1.00/1.33	Pt	TEOA	18.7[d]	374[d]	1.1	[57]
P32	1.94	−0.8/1.14	Pt	TEOA	0.98[c]	98[c]	—	[58]
P33	2.32	−1.3/0.9	—	TEOA	9.73[a]	2780[a]	9.60	[62]
P34	1.85	−0.39/1.46	Pt	TEOA	42[b]	4200[b]	1.5	[63]
P35	1.76	−0.96/0.8	—	AA	19.68[b]	656[b]	—	[64]
P37	2.17	−0.89/1.28	Pt	TEOA	116[a]	2320[a]	4.01	[65]
P39	2.12	−0.55/1.57	—	TEOA	399[a]	13300[a]	5.7	[66]
P44	2.36	−1.58/0.78	Pt	AA	177.50[a]	8875[a]	8.45	[67]
P45	2.21	−1.00/1.22	Pt	TEOA	29.6[a]	296[a]	—	[68]
P48	1.69	−0.76/0.93	—	AA	32[a]	12800[a]	0.3	[69]
P49	1.98	−0.90/1.08	—	AA	150[a]	50000[a]	0.6	[70]
P53	1.97	−0.82/1.15	—	AA	16.8[a]	840[a]	0.9	[71]
P54	2.70	—	—	TEOA	92[a]	3680[a]	—	[74]
P56	3.64	−1.77/1.87	—	TEOA	170[a]	3400[a]	6.8	[75]
P57	2.07	−0.99/1.06	—	TEA	50.4[a]	5040[a]	2.31	[76]
P63	2.56	—	—	TEA	77.65[a]	3106[a]	13.2	[77]
P64	2.37	−1.02/1.35	Pt	TEOA	284.85[a]	5697[a]	6.1	[78]
P65	2.99	−1.86/1.15	—	TEA	147.1[a]	5884[a]	—	[79]
P64	2.31	−1.06/1.80	—	TEOA	400[a]	8000[a]	8.5	[80]
P66	1.95	−0.85/1.10	—	TEOA	366[a]	12200[a]	3.7	[81]
P67	1.85	—	Pt	AA	252.5[a]	10100[a]	0.6	[83]
P68	2.88	−1.79/1.09	—	TEA	30.66[b]	6132[b]	14.92	[84]
P71	2.12	−0.62/1.52	Pt	TEOA	45.4[a]	910[a]	2	[88]
P74	2.03	−0.69/1.34	Pt	TEOA	106[a]	2120[a]	0.48	[89]

[a]Light source: λ > 420 nm; [b]light source: λ > 400 nm; [c]light source: full-arc irradiation; [d]light source: λ > 300 nm.

In this respect, the combination of CPs with other semiconductors to form heterojunctions can further enhance the catalytic performance. Fabricating inorganic/polymer composites with complementary absorption ranges is an efficient strategy to extend the light-responsive region and offer enough thermodynamic driving force compared to single semiconductors. Besides, molecular heterostructures produced by two covalently bonded polymers could be a promising strategy because of effective charge carrier separation and small interfacial charge transfer resistance [103].

Consequently, we envisage the diverse kinds of CPs, in conjunction with inorganic semiconductors, promise enormous potential in PHP applications in the near future. Nevertheless, there is still a large potential for further improving D–A-type CPs for PHP applications. Large-scale and low-cost production of D–A CPs still remains a substantial challenge. Seeking atom- and step-economic synthetic alternatives [104] to traditional C-M/C-Br (M = B or Sn) coupling for preparing CPs ought to be a common goal. Furthermore, besides the PHP activity, studies regarding the long-term stability of CPs are still needed.

ORCID® iDs

Shi-Yong Liu - https://orcid.org/0000-0002-3569-3826

References

1. Jayakumar, J.; Chou, H.-H. *ChemCatChem* **2020,** *12,* 689–704. doi:10.1002/cctc.201901725
2. Tachibana, Y.; Vayssieres, L.; Durrant, J. R. *Nat. Photonics* **2012,** *6,* 511–518. doi:10.1038/nphoton.2012.175
3. Hammarström, L.; Hammes-Schiffer, S. *Acc. Chem. Res.* **2009,** *42,* 1859–1860. doi:10.1021/ar900267k
4. Fujishima, A.; Honda, K. *Nature* **1972,** *238,* 37–38. doi:10.1038/238037a0
5. Maeda, K.; Domen, K. *J. Phys. Chem. C* **2007,** *111,* 7851–7861. doi:10.1021/jp070911w
6. Tong, H.; Ouyang, S.; Bi, Y.; Umezawa, N.; Oshikiri, M.; Ye, J. *Adv. Mater. (Weinheim, Ger.)* **2012,** *24,* 229–251. doi:10.1002/adma.201102752
7. Luo, S.; Zeng, Z.; Zeng, G.; Liu, Z.; Xiao, R.; Xu, P.; Wang, H.; Huang, D.; Liu, Y.; Shao, B.; Liang, Q.; Wang, D.; H, e. Q.; Qin, L.; Fu, Y. *J. Mater. Chem. A* **2020,** *8,* 6434–6470. doi:10.1039/d0ta01102a
8. Vilela, F.; Zhang, K.; Antonietti, M. *Energy Environ. Sci.* **2012,** *5,* 7819–7832. doi:10.1039/c2ee22002d
9. Lee, J.-S. M.; Cooper, A. I. *Chem. Rev.* **2020,** *120,* 2171–2214. doi:10.1021/acs.chemrev.9b00399
10. Banerjee, T.; Podjaski, F.; Kroger, J.; Biswal, B. P.; Lotsch, B. V. *Nat. Rev. Mater.* **2021,** *6,* 168–190. doi:10.1038/s41578-020-00254-z
11. Yanagida, S.; Kabumoto, A.; Mizumoto, K.; Pac, C.; Yoshino, K. *J. Chem. Soc., Chem. Commun.* **1985,** 474–475. doi:10.1039/c39850000474
12. Wang, X.; Maeda, K.; Thomas, A.; Takanabe, K.; Xin, G.; Carlsson, J. M.; Domen, K.; Antonietti, M. *Nat. Mater.* **2009,** *8,* 76–80. doi:10.1038/nmat2317
13. Wang, X.; Blechert, S.; Antonietti, M. *ACS Catal.* **2012,** *2,* 1596–1606. doi:10.1021/cs300240x
14. Schwinghammer, K.; Tuffy, B.; Mesch, M. B.; Wirnhier, E.; Martineau, C.; Taulelle, F.; Schnick, W.; Senker, J.; Lotsch, B. V. *Angew. Chem., Int. Ed.* **2013,** *52,* 2435–2439. doi:10.1002/anie.201206817
15. Sui, Y.; Liu, J.; Zhang, Y.; Tian, X.; Chen, W. *Nanoscale* **2013,** *5,* 9150–9155. doi:10.1039/c3nr02413j
16. Fu, J.; Tian, Y.; Chang, B.; Xi, F.; Dong, X. *J. Mater. Chem.* **2012,** *22,* 21159–21166. doi:10.1039/c2jm34778d
17. Zhang, J.; Zhang, M.; Sun, R.-Q.; Wang, X. *Angew. Chem., Int. Ed.* **2012,** *51,* 10145–10149. doi:10.1002/anie.201205333
18. Zhang, J.; Chen, X.; Takanabe, K.; Maeda, K.; Domen, K.; Epping, J. D.; Fu, X.; Antonietti, M.; Wang, X. *Angew. Chem., Int. Ed.* **2010,** *49,* 441–444. doi:10.1002/anie.200903886
19. Zhang, J.; Zhang, G.; Chen, X.; Lin, S.; Möhlmann, L.; Dołęga, G.; Lipner, G.; Antonietti, M.; Blechert, S.; Wang, X. *Angew. Chem., Int. Ed.* **2012,** *51,* 3183–3187. doi:10.1002/anie.201106656
20. Zhang, G.; Wang, X. *J. Catal.* **2013,** *307,* 246–253. doi:10.1016/j.jcat.2013.07.026
21. Zhang, J.; Sun, J.; Maeda, K.; Domen, K.; Liu, P.; Antonietti, M.; Fu, X.; Wang, X. *Energy Environ. Sci.* **2011,** *4,* 675–678. doi:10.1039/c0ee00418a
22. Jiang, L.; Yuan, X.; Pan, Y.; Liang, J.; Zeng, G.; Wu, Z.; Wang, H. *Appl. Catal., B* **2017,** *217,* 388–406. doi:10.1016/j.apcatb.2017.06.003
23. Wang, Y.; Di, Y.; Antonietti, M.; Li, H.; Chen, X.; Wang, X. *Chem. Mater.* **2010,** *22,* 5119–5121. doi:10.1021/cm1019102
24. Lau, V. W.; Moudrakovski, I.; Botari, T.; Weinberger, S.; Mesch, M. B.; Duppel, V.; Senker, J.; Blum, V.; Lotsch, B. V. *Nat. Commun.* **2016,** *7,* 12165. doi:10.1038/ncomms12165
25. Sprick, R. S.; Jiang, J.-X.; Bonillo, B.; Ren, S.; Ratvijitvech, T.; Guiglion, P.; Zwijnenburg, M. A.; Adams, D. J.; Cooper, A. I. *J. Am. Chem. Soc.* **2015,** *137,* 3265–3270. doi:10.1021/ja511552k
26. Sprick, R. S.; Bonillo, B.; Sachs, M.; Clowes, R.; Durrant, J. R.; Adams, D. J.; Cooper, A. I. *Chem. Commun.* **2016,** *52,* 10008–10011. doi:10.1039/c6cc03536a
27. Wang, L.; Wan, Y.; Ding, Y.; Niu, Y.; Xiong, Y.; Wu, X.; Xu, H. *Nanoscale* **2017,** *9,* 4090–4096. doi:10.1039/c7nr00534b
28. Woods, D. J.; Sprick, R. S.; Smith, C. L.; Cowan, A. J.; Cooper, A. I. *Adv. Energy Mater.* **2017,** *7,* 1700479. doi:10.1002/aenm.201700479
29. Zong, X.; Miao, X.; Hua, S.; An, L.; Gao, X.; Jiang, W.; Qu, D.; Zhou, Z.; Liu, X.; Sun, Z. *Appl. Catal., B* **2017,** *211,* 98–105. doi:10.1016/j.apcatb.2017.04.033
30. Sprick, R. S.; Aitchison, C. M.; Berardo, E.; Turcani, L.; Wilbraham, L.; Alston, B. M.; Jelfs, K. E.; Zwijnenburg, M. A.; Cooper, A. I. *J. Mater. Chem. A* **2018,** *6,* 11994–12003. doi:10.1039/c8ta04186e
31. Bi, J.; Fang, W.; Li, L.; Wang, J.; Liang, S.; He, Y.; Liu, M.; Wu, L. *Macromol. Rapid Commun.* **2015,** *36,* 1799–1805. doi:10.1002/marc.201500270
32. Schwinghammer, K.; Hug, S.; Mesch, M. B.; Senker, J.; Lotsch, B. V. *Energy Environ. Sci.* **2015,** *8,* 3345–3353. doi:10.1039/c5ee02574e
33. Kuecken, S.; Acharjya, A.; Zhi, L.; Schwarze, M.; Schomacker, R.; Thomas, A. *Chem. Commun.* **2017,** *53,* 5854–5857. doi:10.1039/c7cc01827d
34. Stegbauer, L.; Schwinghammer, K.; Lotsch, B. V. *Chem. Sci.* **2014,** *5,* 2789–2793. doi:10.1039/c4sc00016a
35. Cheng, J.-Z.; Liu, L.-L.; Liao, G.; Shen, Z.-Q.; Tan, Z.-R.; Xing, Y.-Q.; Li, X.-X.; Yang, K.; Chen, L.; Liu, S.-Y. *J. Mater. Chem. A* **2020,** *8,* 5890–5899. doi:10.1039/c9ta13514f
36. Cheng, C.; Wang, X.; Lin, Y.; He, L.; Jiang, J.-X.; Xu, Y.; Wang, F. *Polym. Chem.* **2018,** *9,* 4468–4475. doi:10.1039/c8py00722e
37. Xu, C.; Zhang, W.; Tang, J.; Pan, C.; Yu, G. *Front. Chem. (Lausanne, Switz.)* **2018,** *6,* 592. doi:10.3389/fchem.2018.00592
38. Zhang, G.; Lan, Z.-A.; Wang, X. *Angew. Chem., Int. Ed.* **2016,** *55,* 15712–15727. doi:10.1002/anie.201607375
39. Schroeder, B. C.; Li, Z.; Brady, M. A.; Faria, G. C.; Ashraf, R. S.; Takacs, C. J.; Cowart, J. S.; Duong, D. T.; Chiu, K. H.; Tan, C.-H.; Cabral, J. T.; Salleo, A.; Chabinyc, M. L.; Durrant, J. R.; McCulloch, I. *Angew. Chem., Int. Ed.* **2014,** *53,* 12870–12875. doi:10.1002/anie.201407310
40. Gu, C.; Huang, N.; Chen, Y.; Zhang, H.; Zhang, S.; Li, F.; Ma, Y.; Jiang, D. *Angew. Chem., Int. Ed.* **2016,** *55,* 3049–3053. doi:10.1002/anie.201510723
41. Wang, L.; Fernández-Terán, R.; Zhang, L.; Fernandes, D. L. A.; Tian, L.; Chen, H.; Tian, H. *Angew. Chem., Int. Ed.* **2016,** *55,* 12306–12310. doi:10.1002/anie.201607018
42. Damas, G. B.; Marchiori, C. F. N.; Araujo, C. M. *J. Phys. Chem. C* **2019,** *123,* 25531–25542. doi:10.1021/acs.jpcc.9b06057
43. Martin, D. J.; Reardon, P. J. T.; Moniz, S. J. A.; Tang, J. *J. Am. Chem. Soc.* **2014,** *136,* 12568–12571. doi:10.1021/ja506386e
44. Liu, G.; Wang, T.; Zhang, H.; Meng, X.; Hao, D.; Chang, K.; Li, P.; Kako, T.; Ye, J. *Angew. Chem., Int. Ed.* **2015,** *54,* 13561–13565. doi:10.1002/anie.201505802

45. Guo, L.; Niu, Y.; Xu, H.; Li, Q.; Razzaque, S.; Huang, Q.; Jin, S.; Tan, B. *J. Mater. Chem. A* **2018,** *6,* 19775–19781. doi:10.1039/c8ta07391k
46. Schwarz, D.; Kochergin, Y. S.; Acharjya, A.; Ichangi, A.; Opanasenko, M. V.; Čejka, J.; Lappan, U.; Arki, P.; He, J.; Schmidt, J.; Nachtigall, P.; Thomas, A.; Tarábek, J.; Bojdys, M. J. *Chem. – Eur. J.* **2017,** *23,* 13023–13027. doi:10.1002/chem.201703332
47. Schwarz, D.; Acharja, A.; Ichangi, A.; Lyu, P.; Opanasenko, M. V.; Goßler, F. R.; König, T. A. F.; Čejka, J.; Nachtigall, P.; Thomas, A.; Bojdys, M. J. *Chem. – Eur. J.* **2018,** *24,* 11916–11921. doi:10.1002/chem.201802902
48. Kailasam, K.; Mesch, M. B.; Möhlmann, L.; Baar, M.; Blechert, S.; Schwarze, M.; Schröder, M.; Schomäcker, R.; Senker, J.; Thomas, A. *Energy Technol.* **2016,** *4,* 744–750. doi:10.1002/ente.201500478
49. Guo, L.; Niu, Y.; Razzaque, S.; Tan, B.; Jin, S. *ACS Catal.* **2019,** *9,* 9438–9445. doi:10.1021/acscatal.9b01951
50. Yu, J.; Sun, X.; Xu, X.; Zhang, C.; He, X. *Appl. Catal., B* **2019,** *257,* 117935. doi:10.1016/j.apcatb.2019.117935
51. Yu, J.; Chang, S.; Xu, X.; He, X.; Zhang, C. *J. Mater. Chem. C* **2020,** *8,* 8887–8895. doi:10.1039/d0tc00942c
52. Matsuoka, S.; Kohzuki, T.; Kuwana, Y.; Nakamura, A.; Yanagida, S. *J. Chem. Soc., Perkin Trans. 2* **1992,** 679–685. doi:10.1039/p29920000679
53. Haase, F.; Banerjee, T.; Savasci, G.; Ochsenfeld, C.; Lotsch, B. V. *Faraday Discuss.* **2017,** *201,* 247–264. doi:10.1039/c7fd00051k
54. Li, L.; Cai, Z. *Polym. Chem.* **2016,** *7,* 4937–4943. doi:10.1039/c6py00972g
55. Li, L.; Cai, Z.; Wu, Q.; Lo, W.-Y.; Zhang, N.; Chen, L. X.; Yu, L. *J. Am. Chem. Soc.* **2016,** *138,* 7681–7686. doi:10.1021/jacs.6b03472
56. Li, L.; Lo, W.-y.; Cai, Z.; Zhang, N.; Yu, L. *Macromolecules* **2016,** *49,* 6903–6909. doi:10.1021/acs.macromol.6b01764
57. Wang, Z.; Mao, N.; Zhao, Y.; Yang, T.; Wang, F.; Jiang, J.-X. *Polym. Bull.* **2019,** *76,* 3195–3206. doi:10.1007/s00289-018-2535-3
58. Stegbauer, L.; Zech, S.; Savasci, G.; Banerjee, T.; Podjaski, F.; Schwinghammer, K.; Ochsenfeld, C.; Lotsch, B. V. *Adv. Energy Mater.* **2018,** *8,* 1703278. doi:10.1002/aenm.201703278
59. Liu, H.; Zhang, X.-F.; Cheng, J.-Z.; Zhong, A.-G.; Wen, H.-R.; Liu, S.-Y. *Molecules* **2019,** *24,* 1760. doi:10.3390/molecules24091760
60. Liu, S.-Y.; Liu, H.; Shen, Z.-Q.; Huang, W.-Y.; Zhong, A.-G.; Wen, H.-R. *Dyes Pigm.* **2019,** *162,* 640–646. doi:10.1016/j.dyepig.2018.10.075
61. Zhang, X.-F.; Cheng, J.-Z.; Liu, H.; Shan, Q.; Jia, G.-X.; Wen, H.-R.; Liu, S.-Y. *Dyes Pigm.* **2020,** *172,* 107819. doi:10.1016/j.dyepig.2019.107819
62. Xiao, W.-J.; Wang, Y.; Wang, W.-R.; Li, J.; Wang, J.; Xu, Z.-W.; Li, J.; Yao, J.; Li, W.-S. *Macromolecules* **2020,** *53,* 2454–2463. doi:10.1021/acs.macromol.9b02488
63. Liu, Y.; Liao, Z.; Ma, X.; Xiang, Z. *ACS Appl. Mater. Interfaces* **2018,** *10,* 30698–30705. doi:10.1021/acsami.8b10022
64. Xu, M.; Kong, K.; Ding, H.; Chu, Y.; Zhang, S.; Yu, F.; Ye, H.; Hu, Y.; Hua, J. *J. Mater. Chem. C* **2020,** *8,* 930–934. doi:10.1039/c9tc04175c
65. Yang, C.; Ma, B. C.; Zhang, L.; Lin, S.; Ghasimi, S.; Landfester, K.; Zhang, K. A. I.; Wang, X. *Angew. Chem., Int. Ed.* **2016,** *55,* 9202–9206. doi:10.1002/anie.201603532
66. Xiang, Y.; Wang, X.; Rao, L.; Wang, P.; Huang, D.; Ding, X.; Zhang, X.; Wang, S.; Chen, H.; Zhu, Y. *ACS Energy Lett.* **2018,** *3,* 2544–2549. doi:10.1021/acsenergylett.8b01535
67. Chen, W.; Wang, L.; Mo, D.; He, F.; Wen, Z.; Wu, X.; Xu, H.; Chen, L. *Angew. Chem., Int. Ed.* **2020,** *59,* 16902–16909. doi:10.1002/anie.202006925
68. Xu, Y.; Mao, N.; Zhang, C.; Wang, X.; Zeng, J.; Chen, Y.; Wang, F.; Jiang, J.-X. *Appl. Catal., B* **2018,** *228,* 1–9. doi:10.1016/j.apcatb.2018.01.073
69. Hu, Z.; Wang, Z.; Zhang, X.; Tang, H.; Liu, X.; Huang, F.; Cao, Y. *iScience* **2019,** *13,* 33–42. doi:10.1016/j.isci.2019.02.007
70. Pati, P. B.; Damas, G.; Tian, L.; Fernandes, D. L. A.; Zhang, L.; Pehlivan, I. B.; Edvinsson, T.; Araujo, C. M.; Tian, H. *Energy Environ. Sci.* **2017,** *10,* 1372–1376. doi:10.1039/c7ee00751e
71. Zhao, P.; Wang, L.; Wu, Y.; Yang, T.; Ding, Y.; Yang, H. G.; Hu, A. *Macromolecules* **2019,** *52,* 4376–4384. doi:10.1021/acs.macromol.9b00551
72. Damas, G. B.; von Kieseritzky, F.; Hellberg, J.; Marchiori, C. F. N.; Araujo, C. M. *J. Phys. Chem. C* **2019,** *123,* 30799–30808. doi:10.1021/acs.jpcc.9b07721
73. Bai, Y.; Wilbraham, L.; Slater, B. J.; Zwijnenburg, M. A.; Sprick, R. S.; Cooper, A. I. *J. Am. Chem. Soc.* **2019,** *141,* 9063–9071. doi:10.1021/jacs.9b03591
74. Sprick, R. S.; Bonillo, B.; Clowes, R.; Guiglion, P.; Brownbill, N. J.; Slater, B. J.; Blanc, F.; Zwijnenburg, M. A.; Adams, D. J.; Cooper, A. I. *Angew. Chem., Int. Ed.* **2016,** *55,* 1792–1796. doi:10.1002/anie.201510542
75. Lan, Z.-A.; Zhang, G.; Chen, X.; Zhang, Y.; Zhang, K. A. I.; Wang, X. *Angew. Chem., Int. Ed.* **2019,** *58,* 10236–10240. doi:10.1002/anie.201904904
76. Dai, C.; Xu, S.; Liu, W.; Gong, X.; Panahandeh-Fard, M.; Liu, Z.; Zhang, D.; Xue, C.; Loh, K. P.; Liu, B. *Small* **2018,** *14,* 1801839. doi:10.1002/smll.201801839
77. Sprick, R. S.; Bai, Y.; Guilbert, A. A. Y.; Zbiri, M.; Aitchison, C. M.; Wilbraham, L.; Yan, Y.; Woods, D. J.; Zwijnenburg, M. A.; Cooper, A. I. *Chem. Mater.* **2019,** *31,* 305–313. doi:10.1021/acs.chemmater.8b02833
78. Zhao, Y.; Ma, W.; Xu, Y.; Zhang, C.; Wang, Q.; Yang, T.; Gao, X.; Wang, F.; Yan, C.; Jiang, J.-X. *Macromolecules* **2018,** *51,* 9502–9508. doi:10.1021/acs.macromol.8b02023
79. Bai, Y.; Woods, D. J.; Wilbraham, L.; Aitchison, C. M.; Zwijnenburg, M. A.; Sprick, R. S.; Cooper, A. I. *J. Mater. Chem. A* **2020,** *8,* 8700–8705. doi:10.1039/d0ta02599b
80. Lan, Z.-A.; Ren, W.; Chen, X.; Zhang, Y.; Wang, X. *Appl. Catal., B* **2019,** *245,* 596–603. doi:10.1016/j.apcatb.2019.01.010
81. Wang, X.; Chen, B.; Dong, W.; Zhang, X.; Li, Z.; Xiang, Y.; Chen, H. *Macromol. Rapid Commun.* **2019,** *40,* 1800494. doi:10.1002/marc.201800494
82. Sprick, R. S.; Cheetham, K. J.; Bai, Y.; Alves Fernandes, J.; Barnes, M.; Bradley, J. W.; Cooper, A. I. *J. Mater. Chem. A* **2020,** *8,* 7125–7129. doi:10.1039/d0ta01200a
83. Wang, X.; Chen, L.; Chong, S. Y.; Little, M. A.; Wu, Y.; Zhu, W.-H.; Clowes, R.; Yan, Y.; Zwijnenburg, M. A.; Sprick, R. S.; Cooper, A. I. *Nat. Chem.* **2018,** *10,* 1180–1189. doi:10.1038/s41557-018-0141-5
84. Wang, W.-H.; Ting, L.-Y.; Jayakumar, J.; Chang, C.-L.; Lin, W.-C.; Chung, C.-C.; Elsayed, M. H.; Lu, C.-Y.; Elewa, A. M.; Chou, H.-H. *Sustainable Energy Fuels* **2020,** *4,* 5264–5270. doi:10.1039/d0se00928h
85. Patil, Y.; Misra, R. *Chem. – Asian J.* **2018,** *13,* 220–229. doi:10.1002/asia.201701493
86. Uoyama, H.; Goushi, K.; Shizu, K.; Nomura, H.; Adachi, C. *Nature* **2012,** *492,* 234–238. doi:10.1038/nature11687

87. Jones, B. A.; Facchetti, A.; Marks, T. J.; Wasielewski, M. R. *Chem. Mater.* **2007,** *19,* 2703–2705. doi:10.1021/cm0704579
88. Bi, S.; Lan, Z.-A.; Paasch, S.; Zhang, W.; He, Y.; Zhang, C.; Liu, F.; Wu, D.; Zhuang, X.; Brunner, E.; Wang, X.; Zhang, F. *Adv. Funct. Mater.* **2017,** *27,* 1703146. doi:10.1002/adfm.201703146
89. Jin, E.; Lan, Z.; Jiang, Q.; Geng, K.; Li, G.; Wang, X.; Jiang, D. *Chem* **2019,** *5,* 1632–1647. doi:10.1016/j.chempr.2019.04.015
90. Hu, B. J.; Sun, Q.; Zuo, C. Y.; Pei, Y. X.; Yang, S. W.; Zheng, H.; Liu, F. M. *Beilstein J. Nanotechnol.* **2019,** *10,* 1157–1165. doi:10.3762/bjnano.10.115
91. Kaushik, A.; Kumar, R.; Arya, S. K.; Nair, M.; Malhotra, B. D.; Bhansali, S. *Chem. Rev.* **2015,** *115,* 4571–4606. doi:10.1021/cr400659h
92. Zang, S.; Zhang, G.; Yang, P.; Zheng, D.; Wang, X. *Chem. – Eur. J.* **2019,** *25,* 6102–6107. doi:10.1002/chem.201900414
93. Zhang, X.; Peng, B.; Zhang, S.; Peng, T. *ACS Sustainable Chem. Eng.* **2015,** *3,* 1501–1509. doi:10.1021/acssuschemeng.5b00211
94. Ye, H.; Wang, Z.; Yu, F.; Zhang, S.; Kong, K.; Gong, X.; Hua, J.; Tian, H. *Appl. Catal., B* **2020,** *267,* 118577. doi:10.1016/j.apcatb.2019.118577
95. Yang, H.; Li, X.; Sprick, R. S.; Cooper, A. I. *Chem. Commun.* **2020,** *56,* 6790–6793. doi:10.1039/d0cc00740d
96. Kosco, J.; Bidwell, M.; Cha, H.; Martin, T.; Howells, C. T.; Sachs, M.; Anjum, D. H.; Gonzalez Lopez, S.; Zou, L.; Wadsworth, A.; Zhang, W.; Zhang, L.; Tellam, J.; Sougrat, R.; Laquai, F.; DeLongchamp, D. M.; Durrant, J. R.; McCulloch, I. *Nat. Mater.* **2020,** *19,* 559–565. doi:10.1038/s41563-019-0591-1
97. Ding, H.; Xu, M.; Zhang, S.; Yu, F.; Kong, K.; Shen, Z.; Hua, J. *Renewable Energy* **2020,** *155,* 1051–1059. doi:10.1016/j.renene.2020.04.009
98. Hou, H.-J.; Zhang, X.-H.; Huang, D.-K.; Ding, X.; Wang, S.-Y.; Yang, X.-L.; Li, S.-Q.; Xiang, Y.-G.; Chen, H. *Appl. Catal., B* **2017,** *203,* 563–571. doi:10.1016/j.apcatb.2016.10.059
99. Xiang, Y.; Wang, X.; Zhang, X.; Hou, H.; Dai, K.; Huang, Q.; Chen, H. *J. Mater. Chem. A* **2018,** *6,* 153–159. doi:10.1039/c7ta09374h
100. Chen, B.; Wang, X.; Dong, W.; Zhang, X.; Rao, L.; Chen, H.; Huang, D.; Xiang, Y. *Chem. – Eur. J.* **2019,** *25,* 3362–3368. doi:10.1002/chem.201805740
101. Zhang, X.; Xiao, J.; Hou, M.; Xiang, Y.; Chen, H. *Appl. Catal., B* **2018,** *224,* 871–876. doi:10.1016/j.apcatb.2017.11.038
102. Hu, Y.; Hao, X.; Cui, Z.; Zhou, J.; Chu, S.; Wang, Y.; Zou, Z. *Appl. Catal., B* **2020,** *260,* 118131. doi:10.1016/j.apcatb.2019.118131
103. Huang, W.; He, Q.; Hu, Y.; Li, Y. *Angew. Chem., Int. Ed.* **2019,** *58,* 8676–8680. doi:10.1002/anie.201900046
104. Huang, W.-Y.; Shen, Z.-Q.; Cheng, J.-Z.; Liu, L.-L.; Yang, K.; Chen, X.; Wen, H.-R.; Liu, S.-Y. *J. Mater. Chem. A* **2019,** *7,* 24222–24230. doi:10.1039/c9ta06444c

License and Terms

This is an Open Access article under the terms of the Creative Commons Attribution License (https://creativecommons.org/licenses/by/4.0). Please note that the reuse, redistribution and reproduction in particular requires that the author(s) and source are credited and that individual graphics may be subject to special legal provisions.

The license is subject to the *Beilstein Journal of Nanotechnology* terms and conditions: (https://www.beilstein-journals.org/bjnano/terms)

The definitive version of this article is the electronic one which can be found at: https://doi.org/10.3762/bjnano.12.50